Control over Cooperative Supramolecular Polymerization by Regulating Molecular Conformation

January 2017

Mitsuaki Yamauchi
Graduate School of Engineering
CHIBA UNIVERSITY

（千葉大学審査学位論文）

Control over Cooperative Supramolecular Polymerization by Regulating Molecular Conformation

January 2017

Mitsuaki Yamauchi
Graduate School of Engineering
CHIBA UNIVERSITY

Contents

Chapter 3.

Phototriggered Supramolecular Polymerizations from Supermacrocycles of Barbiturated Naphthalene-Azobenzene Dyad

Chapter 4.

Photoresponsive Helical Supramolecular Polymers Exhibiting Morphology Transition upon Thermal Reconstruction

Chapter 5.

Conclusion and Perspectives

Chapter 6.

Acknowledgement

Chapter 7.

Appendix

7-1. Abbreviation

7-2. List of Publications

Chapter 1.

General Introduction

1-1. Noncovalent Interactions in Nature

In nature, noncovalent interactions[1], such as hydrogen-bonding, π–π stacking, van der Waals force and hydrophobic interaction, work throughout and contribute to maintaining the three-dimensional (3D) conformation of biomolecules. For example, deoxyribonucleic acid (DNA) double helix is constructed by self-complementary multiple hydrogen-bonding between DNA bases, *i.e.* combination of adenine and thymine or guanine and cytosine (Figure 1-1).[2] The helical structure[3] is further stabilized by π–π stacking between these DNA bases pairs. Such cooperative stabilization of the double helical structure plays an important role to realize the outstanding functions associated with storage and transcription of genetic information.

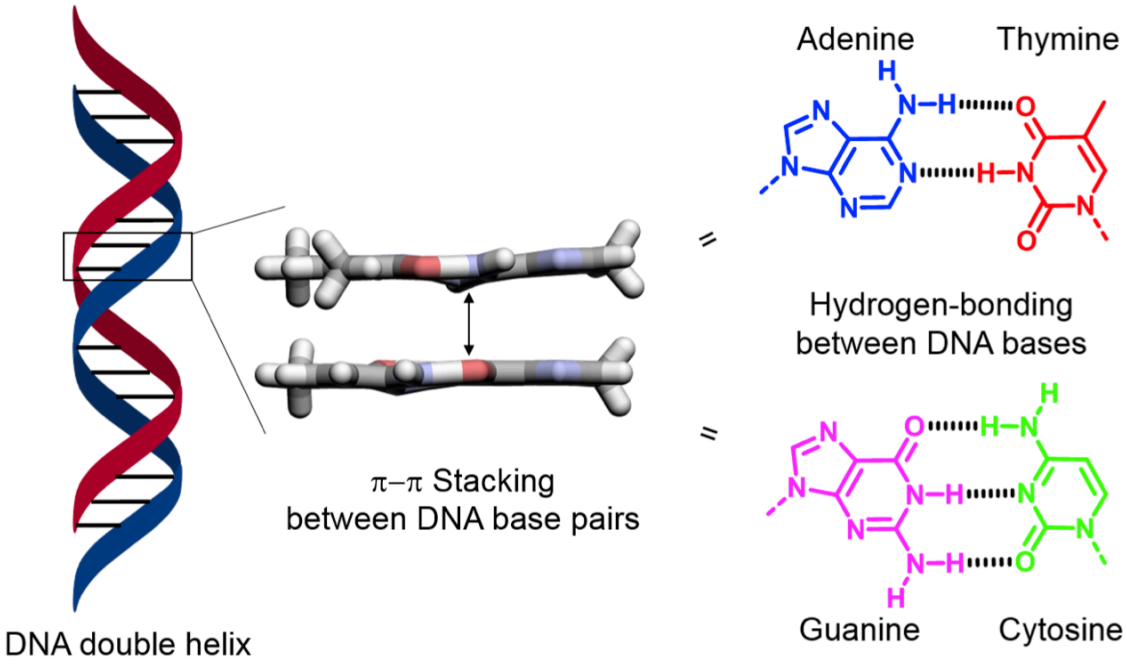

Figure 1-1. Schematic representation of DNA double helix formation.

As another important example, self-assembly of polypeptides into higher-order 3D structures via folding is often discussed owing to the sophisticated structures and functions of naturally occurring proteins. Polypeptide chains as primary structures form domains composed

of secondary structures such as α-helix and β-sheet through intramolecular hydrogen-bonding between amide groups, and they further fold into tertiary structures to form protein monomers. These protein monomers can further assemble via multiple interactions to provide functional nanostructures as quaternary structures. In the self-assembly of polypeptides via folding, both conformations of the resulting proteins and formation of oligomeric units (well-defined protein oligomers) are of great important.[4] An archetypal example is tobacco mosaic virus (TMV) capsid proteins, which undergo a cooperative nucleation-elongation self-assembly process by complexing with ribonucleic acid (RNA) to form tube-shaped nanostructures, which is one of the simplest viruses infecting a tobacco leaf (Figure 1-2).[5] In the first step, the folded protein monomers assemble into a two-layer circular disk structure composed of 17 monomers. In the second step, upon interacting with RNA, the closed circular disk shape-shifts into an open lockwasher-shaped structure as a nucleus (Figure 1-2b), and then the dispersed protein monomers stack on this open ring structures to elongate until the RNA chain is covered fully, which results in TMV tubes with uniform length.

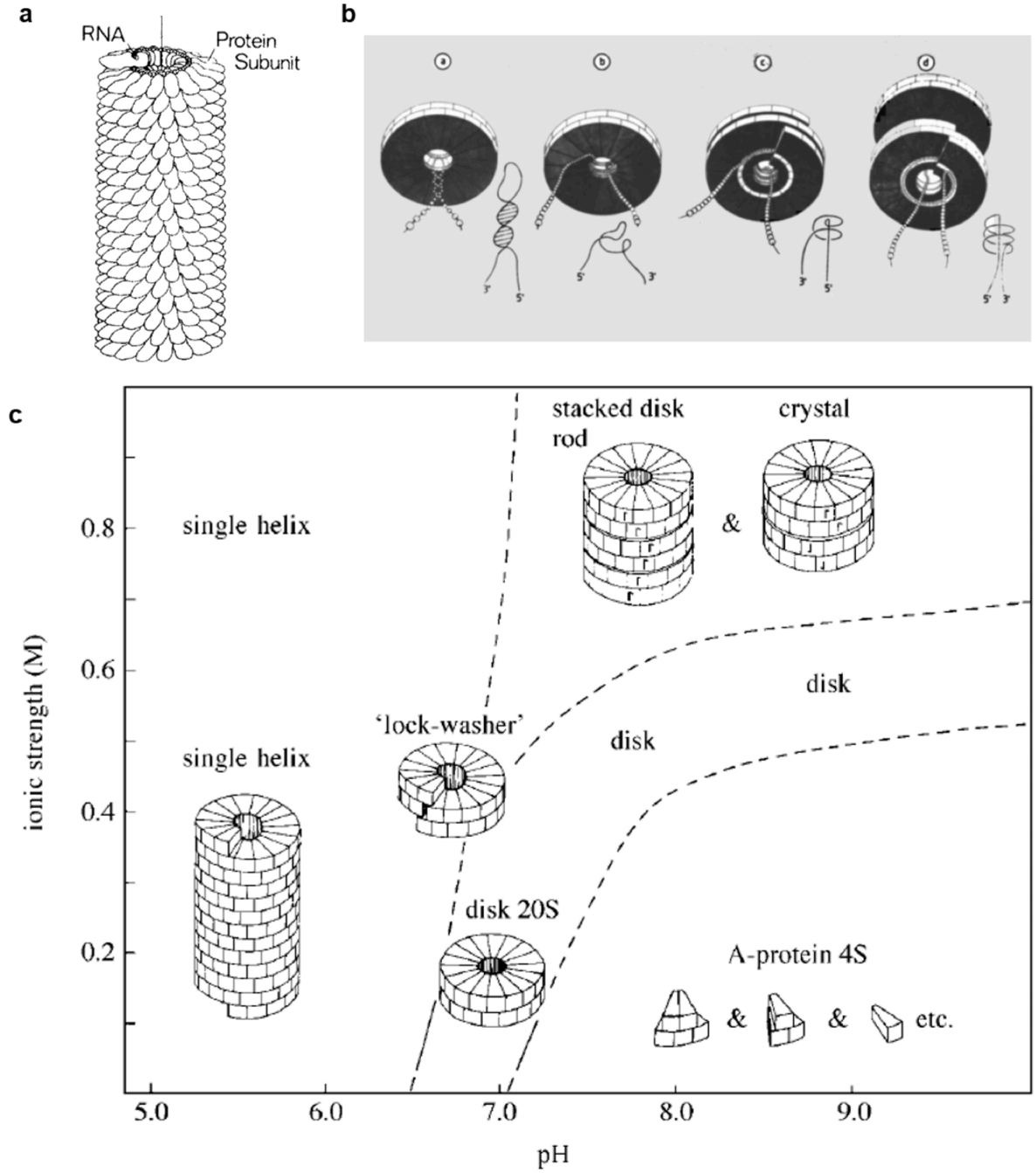

Figure 1-2. (a) Schematic illustration of the tube-shaped nanostructure of TMV. (b) Schematic representation of conformational change from circular disk to lockwasher-shaped ring in the nucleation of TMV self-assembly with RNA. (c) Schematic representation of phase diagram for self-assembly of TMV single helix through the nucleation in which the lockwasher-shaped structure is formed as nucleus. (Reprinted with permission from ref. 5a. Copyright 1983 Wiley-VCH Verlag GmbH & Co. KGaA.)

1-2. Self-assembly in Artificial System

Inspired by the aforementioned biological self-assembly systems, various supramolecular assemblies consisting of synthetic molecules have been reported so far.[6] Self-assembly of synthetic organic small molecules driven by non-covalent interactions is one of the most powerful tools to create intricate nanoarchitectures that can further organize into functional organic materials.[7] In comparison with conventional top-down approaches such as lithography by which designed patterns can be constructed in micro- and nano-scales, the bottom-up approach by means of the self-assembly enables well-defined and dynamic control of dimension-controlled nanostructures exhibiting unique properties. In many reported examples, aromatic π-conjugated units, such as perylene and oligo(phenylene vinylene), have been used as core interactive moieties of building blocks due to their directional π–π stacking interactions and abundant optical properties.[7,8] Once well-defined nanostructures are created, they are discussed by being categorized based on their architectures (Figure 1-3). As a unique example of nanostructured supramolecular assemblies, the research group of S. Yagai reported a ring-shaped 0D nanostructure that is formed via the complexation of melamine-functionalized oligo(*p*-phenylene ethynylene) derivative **5** and cyanurate derivative **6** (Figure 1-3a).[9] Among enormous examples of molecular assemblies, one-dimensionally stacked columnar assemblies of π-conjugated molecules have been explored most actively. For instance, the research group of E. W. Meijer reported a 1D fibrous nanostructure constructed via the helical stacking of C_3-symmetrical discotic molecule **7** (Figure 1-3b).[10] On the other hand, the research group of M. Lee constructed a 2D sheet-like nanostructure formed via self-assembly of amphiphilic molecule **8** possessing hepta(*p*-phenylene) aromatic unit, and the sheet can transform into a tubular structure by thermal control (Figure 1-3c).[11] Furthermore, the research group of A. Ajayaghosh reported a 3D vesicle nanostructure formed via the self-assembly of oligo(*p*-phenylene ethynylene) molecule **9**, and upon mixing the similar chiral derivative **10** the vesicle

can transform into helical nanostructures through coassembly (Figure 1-3d).[12]

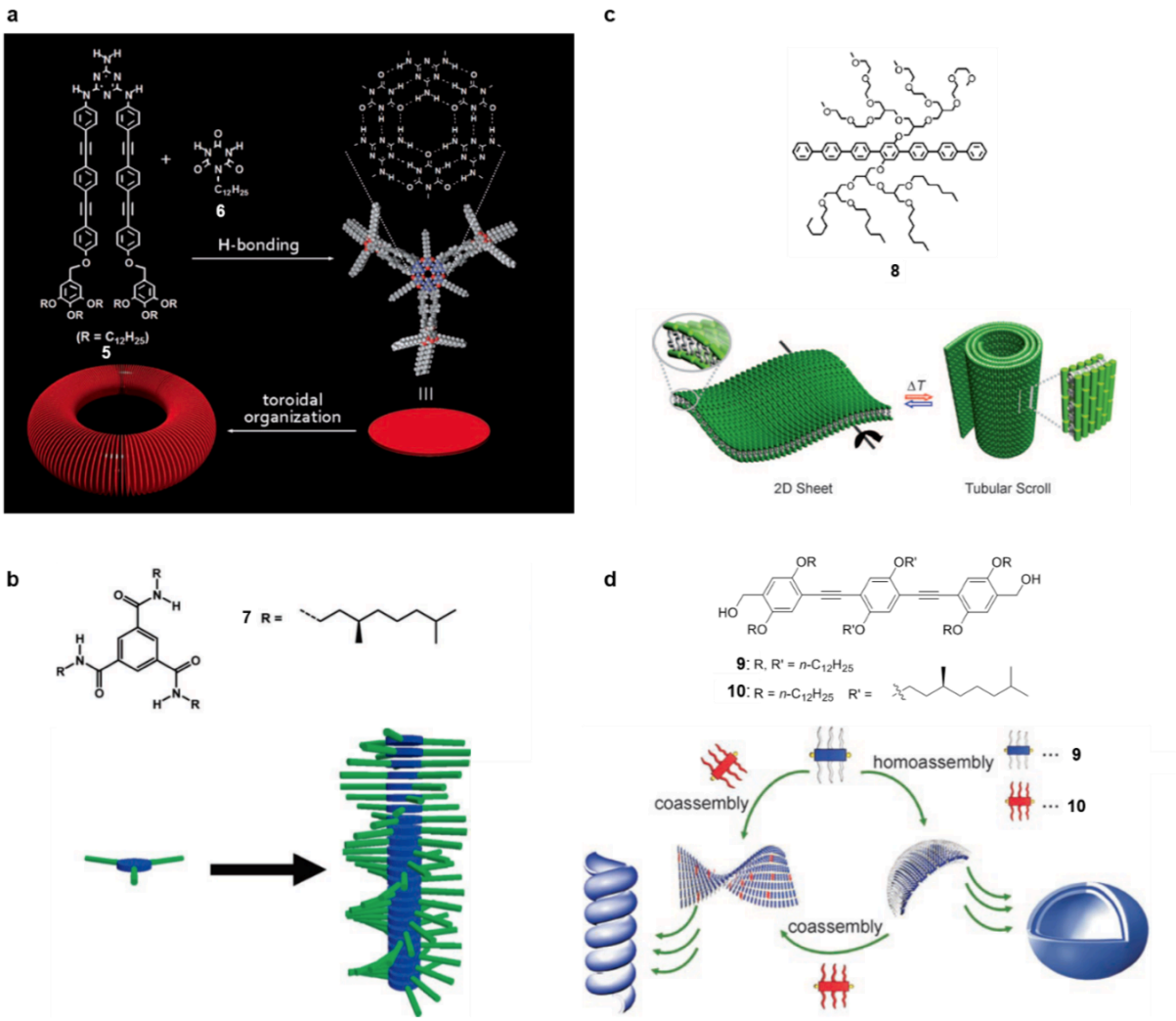

Figure 1-3. (a–d) 0D (a), 1D (b), 2D (c) and 3D (d) nanostructures of self-assembles of synthetic π-conjugated molecules. (Reprinted with permission from ref. 9. Copyright 2008 Wiley-VCH Verlag GmbH & Co. KGaA. Reprinted with permission from ref. 10. Copyright 2008 Wiley-VCH Verlag GmbH & Co. KGaA. Reprinted with permission from ref. 11. Copyright 2009 American Chemical Society. Reprinted with permission from ref. 12. Copyright 2006 Wiley-VCH Verlag GmbH & Co. KGaA)

1-3. Supramolecular Polymer

In the various supramolecular assemblies of organic small molecules, linear assemblies formed by reversible and directional noncovalent interactions are categorized as “supramolecular polymers”, which are highly attractive as stimuli-responsive functional materials.[13] The supramolecular polymers exhibit polymer-like rheological properties in solution and mechanical properties in bulk, and hence afford soft materials such as “supramolecular gel”[14] and “supramolecular liquid crystal”[15]. Importantly, owing to the reversibility of noncovalent bonds, the supramolecular polymers exhibit self-healing and responsiveness to various external stimuli such as temperature, light and others, which enable a construction of smart materials that is rarely attained in the conventional covalent polymer systems.[13a]

The use of multiple hydrogen-bonding interactions with high directionality is regarded as one of the most powerful approaches to create the supramolecular polymers. In 1990, the research group of J.-M. Lehn reported supramolecular polymers composed of triple hydrogen-bonding between difunctional diaminopyridine derivative **11** and difunctional uracil derivative **12** (Figure 1-4a).[16] The equimolar mixture of **11** and **12** showed a liquid crystalline mesophase upon heating in the solid state, whereas the individual compounds became isotropic liquid directly upon heating. To the best of my knowledge, the concept of supramolecular polymer was first established by the authors. After seven years, the research group of E. W. Meijer reported on the self-assembly of difunctional ureidopyrimidinone (UPy) derivative **13** into supramolecular polymers via complementary quadruple hydrogen-bonding interaction (Figure 1-4b).[17] Compound **13** formed a solution with high viscosity in $CHCl_3$ and the degree of viscosity significantly depends on concentration and temperature.

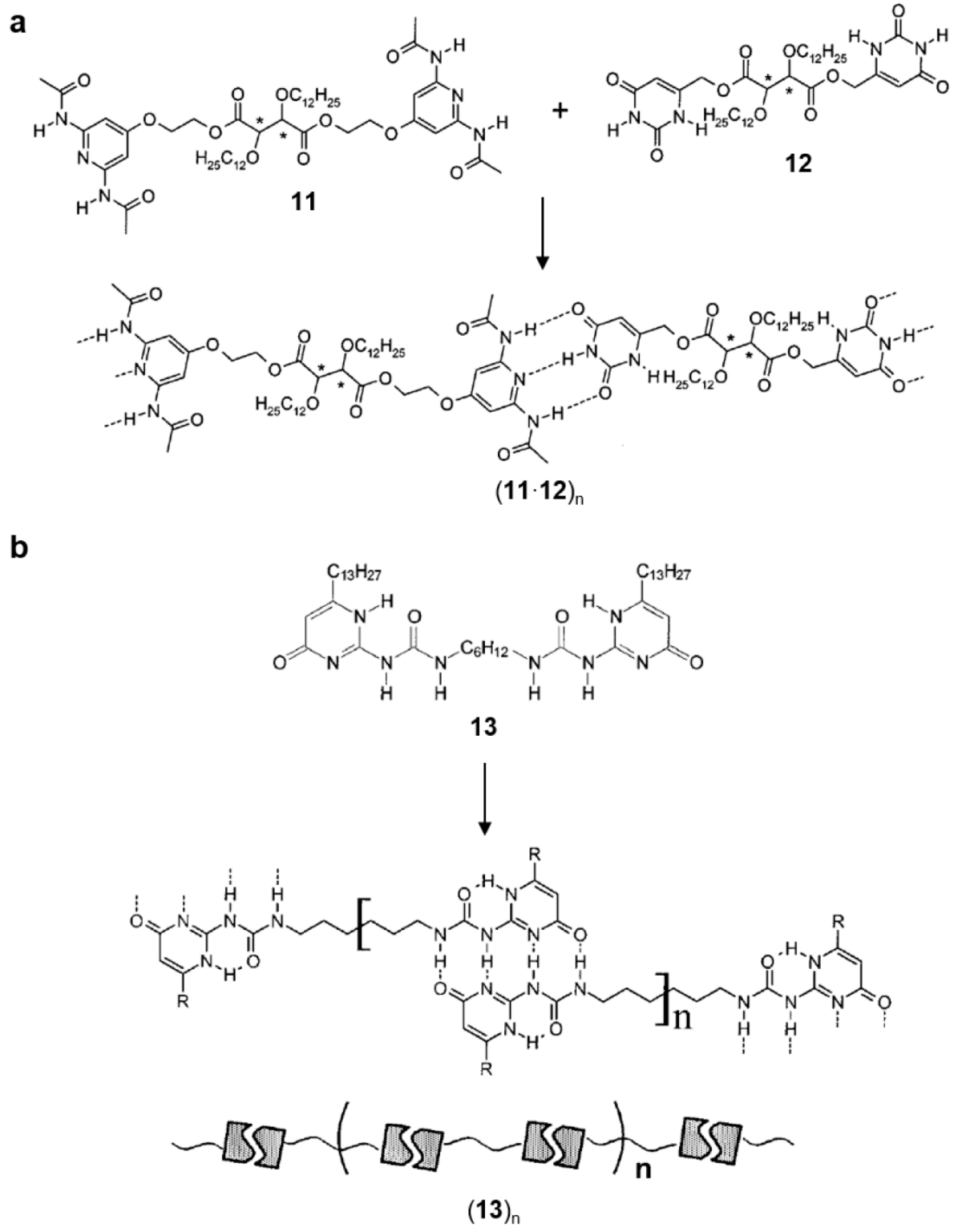

Figure 1-4. Schematic representation of multiple hydrogen-bonding patterns in mixture of compounds **11** and **12** (a) and in pure system of compound **13** (b). (Reprinted with permission from ref. 13a. Copyright 2001 American Chemical Society.)

The above classical supramolecular polymers connected by only multiple hydrogen-bonds generally exist as random coil structures in solution, wherein the degree of polymerization and the interplay between the supramolecular polymer chains affect the macroscopic physical properties (Figure 1-5a,b).[18] These random coil structures do not possess order within 1D supramolecular polymer backbones, *i.e.* internal orders. In sharp contrast, π-conjugated molecules equipped with hydrogen-bonding units self-assemble through π–π stacking between aromatic moieties and hydrogen-bonding into supramolecular polymers with high degrees of internal order.[18] The research group of E. W. Meijer reported a helical supramolecular polymer formed by hierarchical 1D self-assembly of π-conjugated oligo(*p*-phenylene vinylene) (OPV) derivative **14** possessing an ureidotriazine unit showing self-complementary quadruple hydrogen-bonding and chiral side chains (Figure 1-6).[19] This molecule first dimerizes in apolar solvent through complementary hydrogen bonding and subsequently the dimers stack on top of each other by π–π stacking to form helically twisted nanoribbons. Owing to the presence of chiral side chains, the helicity in the resulting supramolecular polymer is biased.

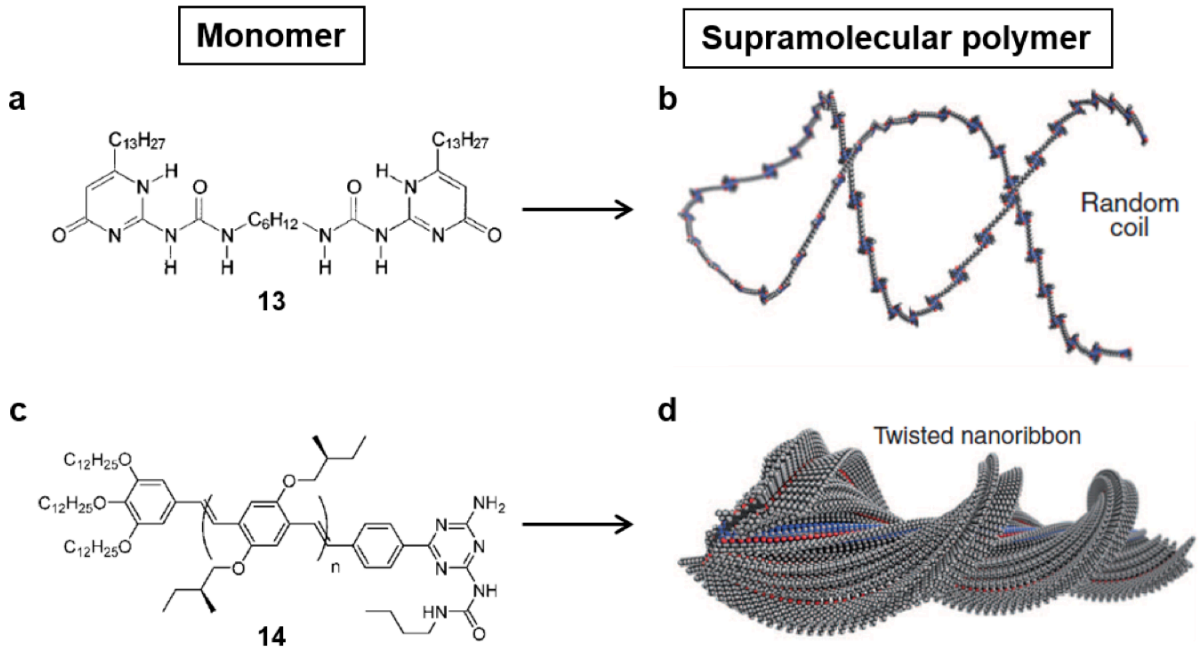

Figure 1-5. Schematic representation of two different monomers **13** (a) and **14** (c) and the corresponding supramolecular polymers without (b) and with high degree of internal order (d). (Reprinted with permission from ref. 18. Copyright 2012 American Association for the Advancement of Science.)

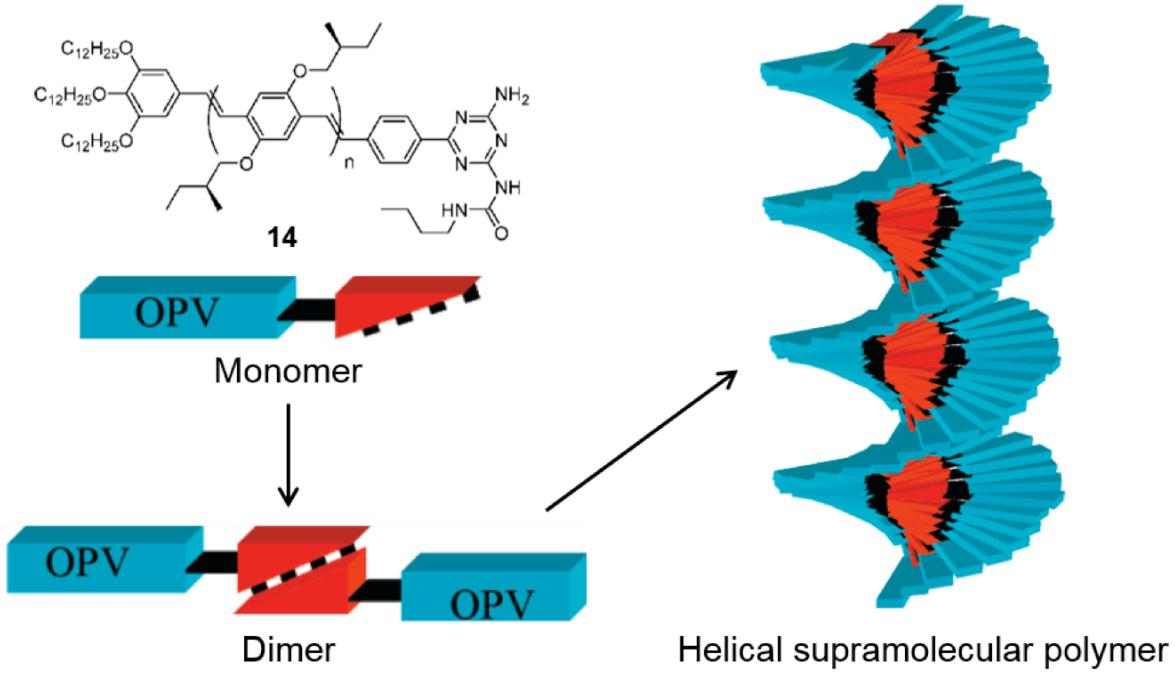

Figure 1-6. Schematic representation of two different monomers **13** (a) and **14** (c) and the corresponding supramolecular polymers without (b) and with the high degree of internal order (d). (Reprinted with permission from ref. 19. Copyright 2001 American Chemical Society.)

The research group of S. Yagai discovered that π-conjugated molecules capped with barbituric acid unit on their one side self-assemble into supramolecular polymers.[20,21] For example, naphthalene derivative **1** with a wedge-shaped aliphatic tail self-assembled in methylcyclohexane (MCH) into 1D rodlike nanostructures through face-to-face (H-type) stacking between naphthalene chromophores, as revealed by atomic force microscopic (AFM) and UV/vis absorption spectroscopic studies (Figure 1-7a,b).[20d] By changing the substituted position on naphthalene from 1,4-position to 2,6-position, the resulting regioisomer **15** underwent a dramatically different self-assembly affording ring-shaped nanostructures via offset (J-type) stacking between naphthalene units (Figure 1-7c,d). X-ray diffraction (XRD) measurements of the two molecules in bulk state implied that both **1** and **15** can form supramolecular columns by the stacking of hydrogen-bonded hexameric supermacrocycles (rosettes). Accordingly, the subtle difference in molecular structure induces the dramatic change in the optical and morphological properties of these regioisomers.

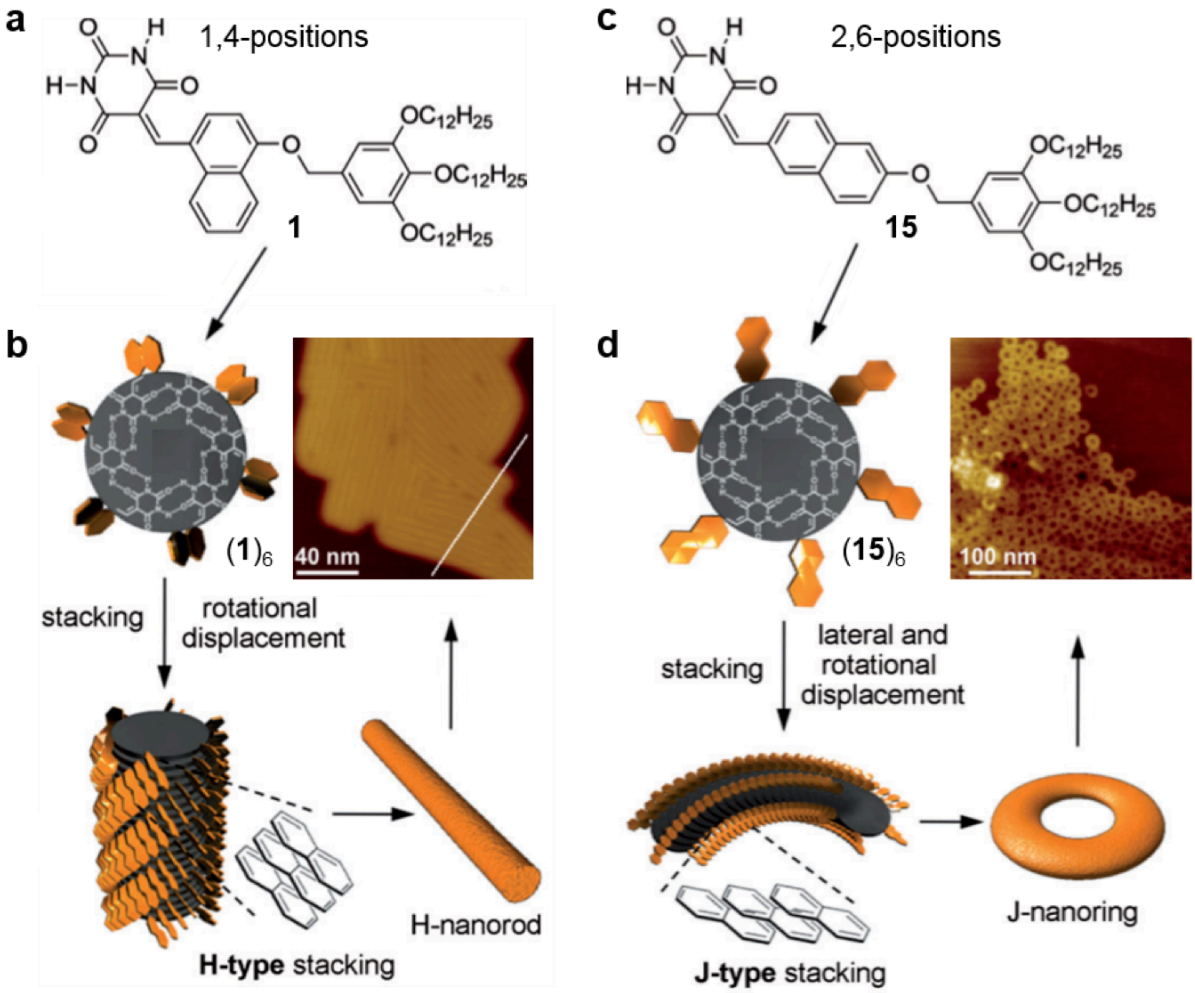

Figure 1-7. (a,b) Molecular structures of barbituric-acid-functionalized naphthalene derivatives **1** and **15**. (c,d) Schematic representation of their hierarchical self-assemblies of rosettes with the corresponding AFM images. (Reprinted with permission from ref. 20d. Copyright 2012 Wiley-VCH.)

In another series of works, the same group reported a precise control over the hierarchy levels of supramolecular polymerization process of V-shaped azobenzene dyad **16**, wherein two amide-group-functionalized alkoxyazobenzenes are dimerized via 3,4,5-(tridodecyloxy)xylylene linkage (Figure 1-8).[22] In MCH, the dyad self-assembles into uniform circular nanostructures (nanoring) that hierarchically assemble into tubular nanostructures (nanotubes), as visualized by AFM and transmission electron microscopy (TEM). The hierarchical assembly of nanorings into nanotubes can be controlled by conditions such as temperature, concentration and even by light stimuli. Under temperatures sufficiently lower than room temperature, the nanotubes further elongate into helical nanofibrils, which ultimately intertwine to form coiled-coil structures possessing one-handed helical sense. UV/vis and CD spectroscopic studies revealed that the dyad undergoes the folding through intramolecular H-type π–π stacking and the chirally folded conformers self-assemble with spontaneous curvature. Such a unique monomer design with foldability is promising to realize unique supramolecular polymerization process as those shown by natural proteins.

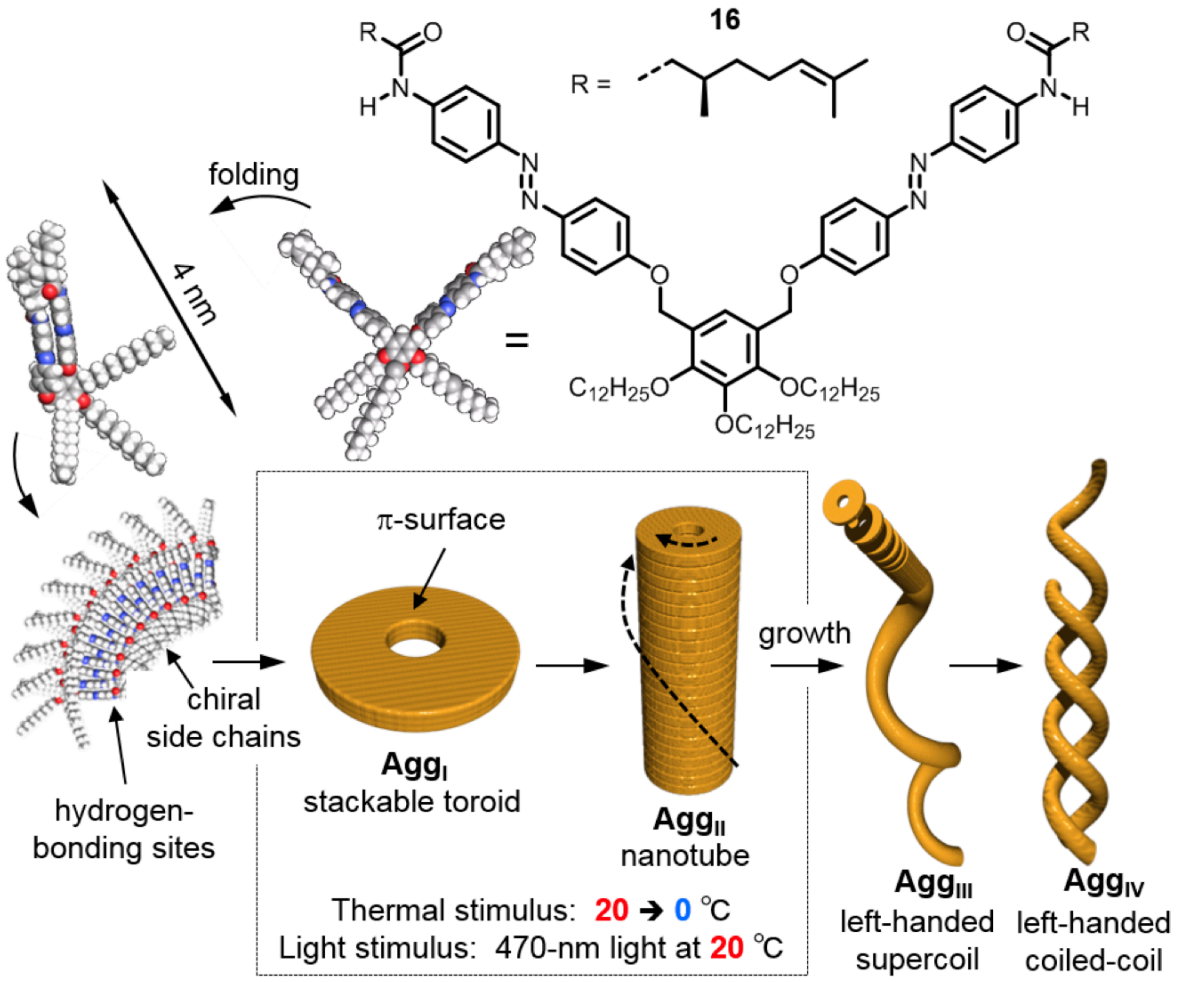

Figure 1-8. Molecular structure of V-shaped azobenzene dyad **16** and its hierarchical self-assembly into nanoring, nanotube, left-handed supercoil and left-handed coiled-coil. (Reprinted with permission from ref. 22a. Copyright 2012 American Chemical Society.)

1-4. Supramolecular Polymerization Processes

To efficiently design aforementioned functional supramolecular polymers, the self-assembly mechanism should be understood in detail from a viewpoint of molecular structure. The development of X-ray diffraction as well as microscopic techniques enables us to study molecular level insight into thermodynamically stable structures of supramolecular polymers. In the last decade, however, not only such thermodynamically stable self-assembled structures but also how these polymers are formed from monomeric components, that is "supramolecular polymerization processes" or "pathways", have attracted much attention.[13b,23,24]

The supramolecular polymerization process can be evaluated by monitoring concentration- and temperature-dependent optical spectra including UV/vis absorption and circular dichroism (CD).[13b,23] Supramolecular polymerization processes of classical supramolecular polymers can be explained by non-cooperative (isodesmic)[25] mechanism (Figure 1-9a). The isodesmic mechanism is the simplest and most common in synthetic molecular assembly. This mechanism is similar to the step-growth polymerization of polyesters.[13b] In the isodesmic equilibrium, each reversible step is governed by a single association constant K_{iso} (Figure 1-9c), and hence this mechanism is also called equal-K model. Reflecting this feature, when the degrees of aggregation (α), calculated from the optical data, are plotted against concentration and temperature, the isodesmic self-assembly displays a sigmoidal transition between molecularly dissolved (monomeric) state and fully aggregated state (Figure 1-9d).[23c]

On the other hand, formation of functional supramolecular polymers is generally governed by cooperative (nucleation-elongation) mechanism[13b,23]. This nucleation-elongation mechanism is characterized by a nonlinear growth of supramolecular polymer chains, in which switching of process from nucleation to elongation occurs at a critical point. At the critical point,

thermodynamically unfavorable species (*i.e.* nucleus) are formed, which is subsequently followed by favorable elongation processes (Figure 1-9b). Hence, the cooperative process is governed by at least two association constants (Figure 1-9c). Unlike the case of the isodesmic process, the degrees of aggregation (α) as a function of temperature (concentration) in the cooperative process display a non-sigmoidal transition from monomeric to fully aggregated state, wherein a sharp change of α is observed around the critical temperature (or concentration) (Figure 1-9d).[23c]

The above two distinct mechanisms are illustrated using energy diagrams shown in Figure 1-10. The isodesmic process is characterized by the successive stack of monomers to a supramolecular polymer chain with a uniform decrease in the Gibbs free energy (Figure 1-10a).[13b] In contrast, the cooperative mechanism is composed of two distinct processes *i.e.* nucleation and elongation processes. Accordingly, a non-uniform change in the Gibbs free energy is observed, wherein the unstable nuclei (like kinetic species) are formed through uphill nucleation process, which is followed by downhill elongation process (Figure 1-10b).[13b] Although the nucleation process is unfavorable due to the presence of other pathways in the equilibrium, the resulting supramolecular polymers have higher degrees of internal order in their main chains in comparison with those formed by isodesmic mechanism (Figure 1-9a). The cooperative supramolecular polymerization is usually observed for monomers possessing multiple directional interactive sites such as hydrogen-bonding and π–π stacking sites (Figure 1-9b).

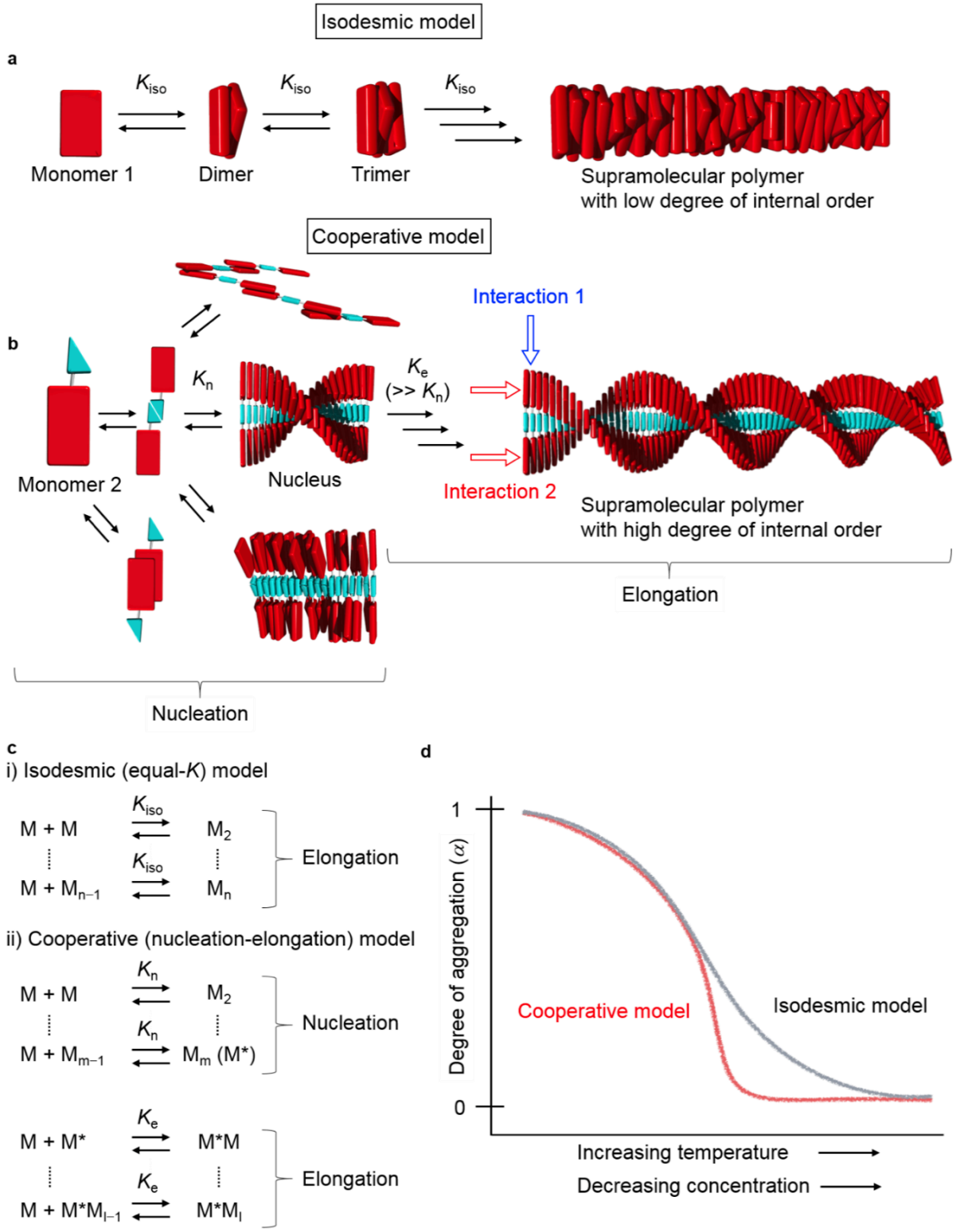

Figure 1-9. (a,b) Graphical illustration of isodesmic (a) and cooperative (b) supramolecular polymerization processes. (c) Schematic representation of the two mechanisms defined by the equilibrium constants (d) Schematic illustration of the degree of aggregation (α) against

temperature and concentration for the two models.

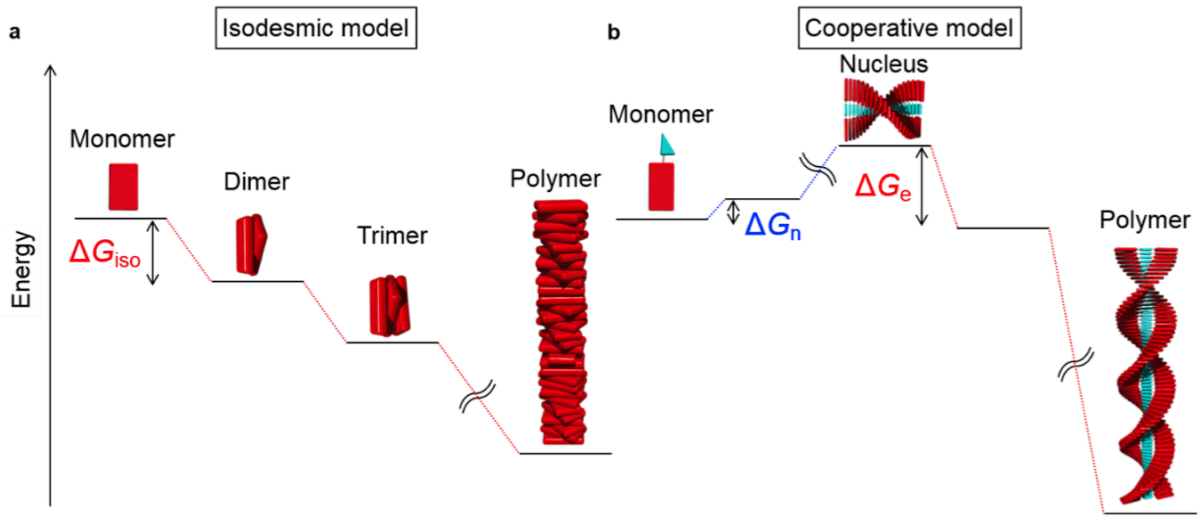

Figure 1-10. Energetic diagrams illustrating isodesmic (a) and cooperative (b) supramolecular polymerization models.

Cooperativity is one of the most important factors in supramolecular assemblies of biological molecules, and cooperative supramolecular polymerization is frequently observed for the organization of protein monomers, for example, in the formation of actin[26] and tobacco mosaic virus.[5] Cooperative supramolecular polymerization achieved by the introduction of multiple interaction sites into π-conjugated synthetic molecules has been revealed by the research group of E. W. Meijer (Figure 1-11).[23a]. Self-assembly of OPV derivative **14** equipped with ureidotriazine self-complementary quadruple hydrogen-bonding unit was studied by temperature-dependent circular dichroism (CD) spectroscopies in apolar solvents. A non-sigmoidal transition of the degree of aggregation as a function of temperature was observed as an evidence of highly cooperative supramolecular polymerization process. This process has been successfully analyzed by applying the theoretical nucleation-elongation model, which has been obtained by modifying Oosawa-Kasai model[27a] developed for analyzing a helical assembly of proteins. Upon cooling the hot monomeric solution, compound **14** first forms non-helically aggregated species composed of 15–20 stacked dimers at 328 K and further cooling

to 325 K results in the growth into helical nuclei with order (Figure 1-11b). Once the nuclei are formed, a favorable elongation into helical supramolecular polymers occurs through the cooperative mechanism.

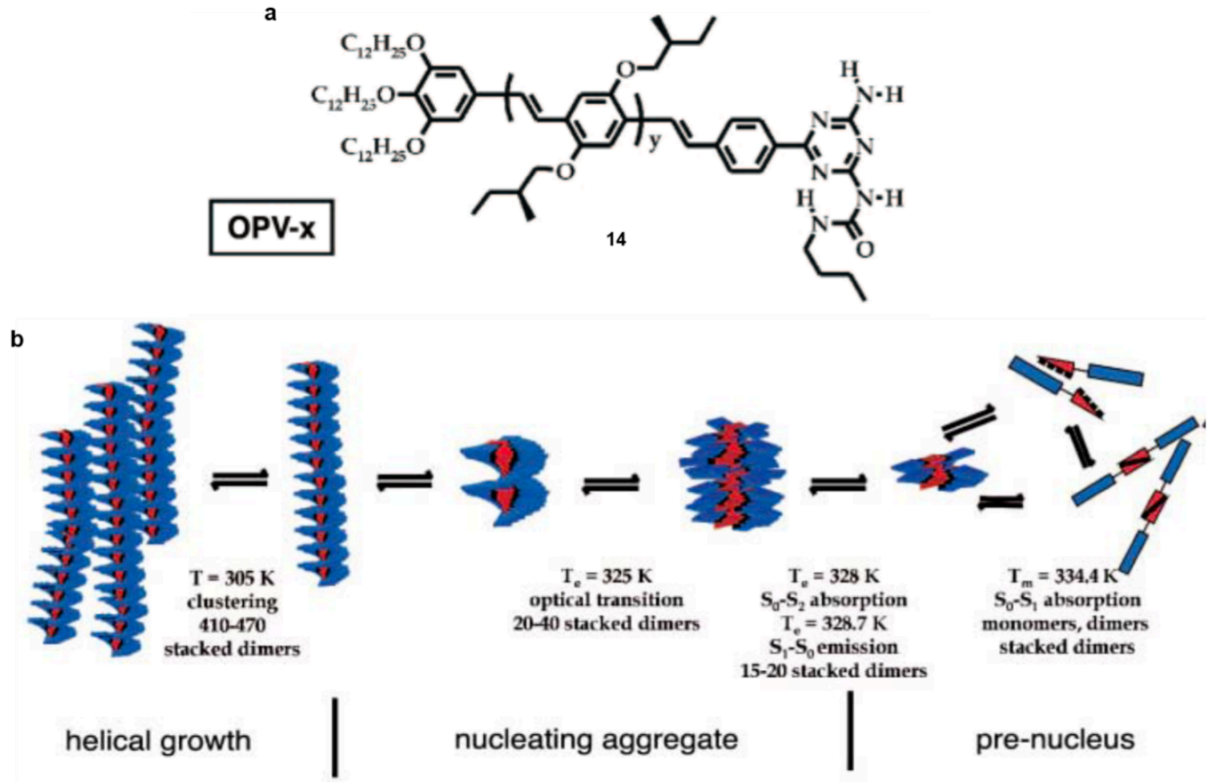

Figure 1-11. (a) Molecular structure of the oligo(*p*-phenylene vinylene) derivative **14** with ureidotriazine self-complementary quadruple hydrogen-bonding unit. (b) Schematic representation of the nucleated cooperative supramolecular polymerization process of **14** in apolar solvents. (Reprinted with permission from ref. 23a. Copyright 2006 American Association for the Advancement of Science.)

Inspired by the aforementioned example of cooperative self-assembly mechanism, chemists attempted to disclose supramolecular polymerization processes of synthetic molecules.[24c] The research group of F. Würthner studied a cooperative slipped (J-type)

aggregation of a hydrogen-bonding perylene bisimide (PBI) derivative **17** (Figure 1-12a).[28] Concentration-dependent UV/vis experiment provided the non-sigmoidal change of the degree of aggregation, which is characteristic of the cooperative nucleation-elongation self-assembly process. The experimental data was analyzed by the K_2–K nucleation-elongation model[24a] wherein the dimerization of monomers is regarded as the nucleation process, providing two association constants of K_2 = 13 M^{-1} for dimerization (nucleation) and $K = 2.3 \times 10^6$ M^{-1} for elongation. Upon increasing concentration, the monomer self-assembles in methylcyclohexane (MCH) into π–π stacked dimers through the nucleation process governed by the K_2, and subsequently the dimers cooperatively grow into helical columns via the elongation process governed by remarkably higher value of K in comparison with that of K_2 due to cooperative hydrogen-bonding and π–π stacking.

The research group of S. Yagai also reported a cooperative supramolecular polymerization of a hydrogen-bonding cyanurate-functionalized PBI derivative **18** that forms supramolecular supermacrocyclic complexes, so-called rosette, by complexing with complementary melamine derivatives **19a–e**, **20** (Figure 1-12b).[29] The 1:1 mixture of **18** and **19b** formed rosettes in chloroform through complementary triple hydrogen-bonding, and the rosettes subsequently self-assemble into columnar structures though the inter-rosette π–π stacking. The cooperative nucleation-elongation process in the hierarchical self-assembly was confirmed by a concentration-dependent UV/vis data, and the theoretical fitting with the K_2–K model[24a] provided the thermodynamic parameters including the values of K_2 (120 M^{-1}) and K (1.2×10^4 M^{-1}).

Cooperative self-assembly processes of π-conjugated molecules without hydrogen-bonding units have been reported. For example, the research group of G. Fernández revealed a cooperative supramolecular polymerization process of oligo(phenylene ethynylene) (OPE)-

functionalized Pd(II)-pyridyl complex **21** in MCH into extended fibrillar assemblies (Figure 1-12c).[30] On the basis of temperature- and concentration-dependent UV/vis data and their theoretical analysis, the authors proposed that the cooperativity in the supramolecular polymerization process is a consequence of interplay of two major interactions, *i.e.* π–π stacking and Pd–Pd metallophilic interactions. As another example, the research group of S. J. George reported a dipole-assisted cooperative supramolecular polymerization of perylene bisimide derivatives **22** and **23** equipped with dipolar carbonate groups as linkers in MCH/1,1,2,2-tetrachloroethane (TCE) (Figure 1-12d).[31] The cooperative nucleation-elongation process in the supramolecular polymerization of **22** and **23** was revealed by a temperature-dependent UV/vis and CD data. On the other hand, the other derivative **24** with ether linker showed the non-cooperative (isodesmic) process due to the absence of dipolar moieties. Furthermore, the authors revealed that the cooperativity was induced by dipole−dipole interaction between monomers along the stacking direction, by means of molecular dynamics (MD) simulations and bulk dielectric measurements as well as extensive spectroscopies.

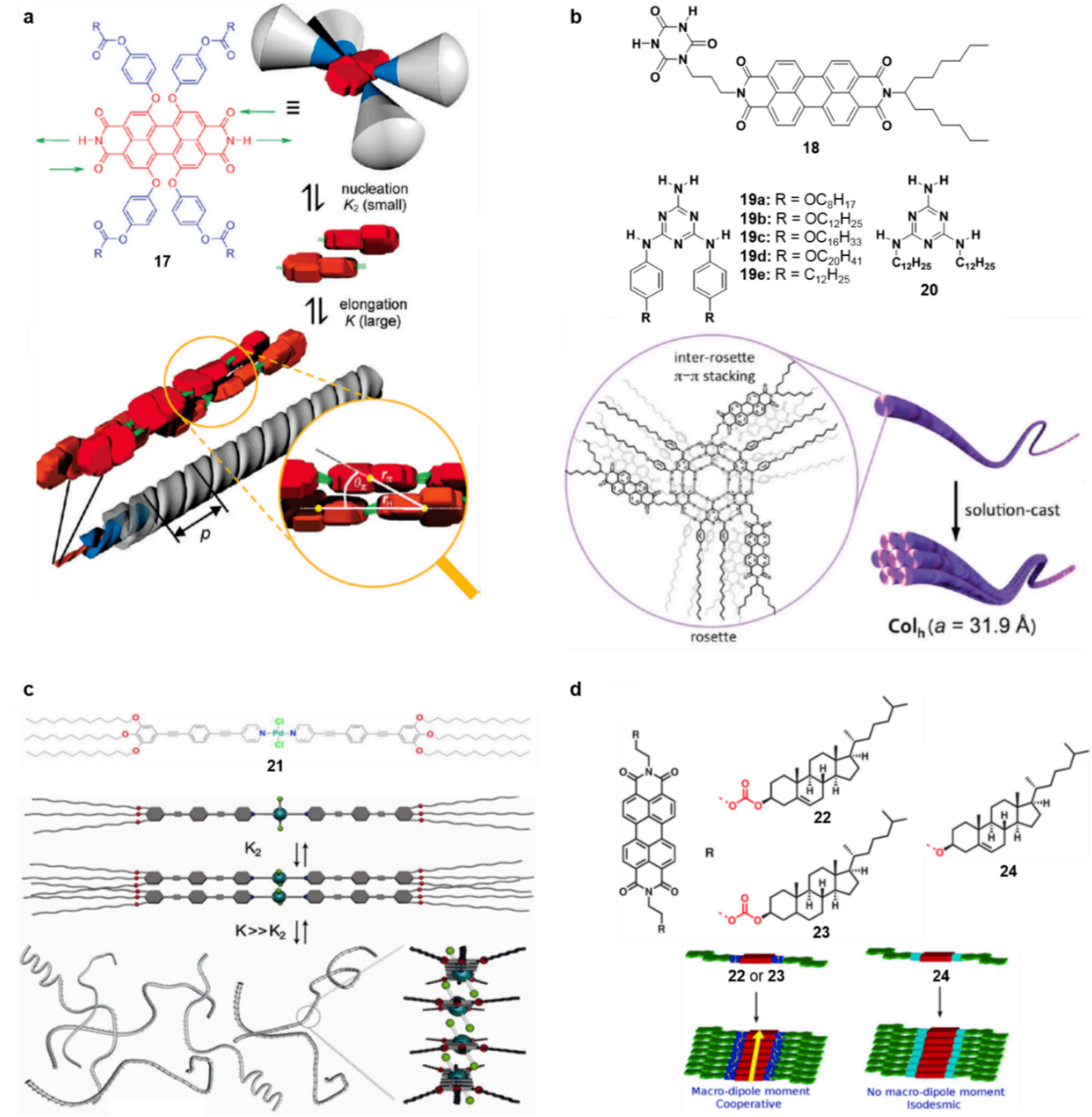

Figure 1-12. (a–d) Schematic representation of four cooperative nucleation-elongation supramolecular polymerizations of synthetic molecules, that is, perylene bisimide (PBI) dye **17** (a), complex of cyanurate-functionalized PBI dye **18** and melamine derivatives **19a–e**, **20** (b), oligo(phenylene ethynylene) (OPE)-functionalized Pd(II)-pyridyl complex **21** (c) and PBI derivatives **22** and **23** equipped with dipolar carbonate groups as linkers (d). PBI derivative **24** equipped with ether linkers in (d) shows isodesmic self-assembly process. (Reprinted with permission from ref. 28. Copyright 2009 American Chemical Society. Reprinted with permission from ref. 29. Copyright 2012 American Chemical Society. Reprinted with permission from ref. 30. Copyright 2013 American Chemical Society. Reprinted with permission from ref. 31. Copyright 2015 American Chemical Society.)

1-5. Pathway complexity

In self-assembly systems of proteins, single protein monomers have multiple supramolecular polymerization pathways because such monomers are able to change in their conformations. For example, prion protein monomers can form not only folded native structures but also misfolded structures that assemble into amyloid fibrils and amorphous aggregates. The emergence and interplay of multiple pathways are known as "pathway complexity".[32]

Recently, the presence of pathway complexity has been found for supramolecular polymerization of synthetic π-conjugated molecules.[33] As a seminal example, the research group of E. W. Meijer studied pathway complexity in a cooperative self-assembly of the chiral OPV derivative **14** via formation of quadruply hydrogen-bonded dimer (Figure 1-13a).[33c] Upon very fast cooling—quenching—of a hot monomeric MCH solution of this molecule to 273 K, this molecule self-assembled under kinetic control into metastable helical aggregates with right-handed (*P*-type) helicity. As evidenced by CD studies, these metastable aggregates transformed over time into thermodynamically stable supramolecular polymers with left-handed (*M*-type) helicity (Figure 1-13b).

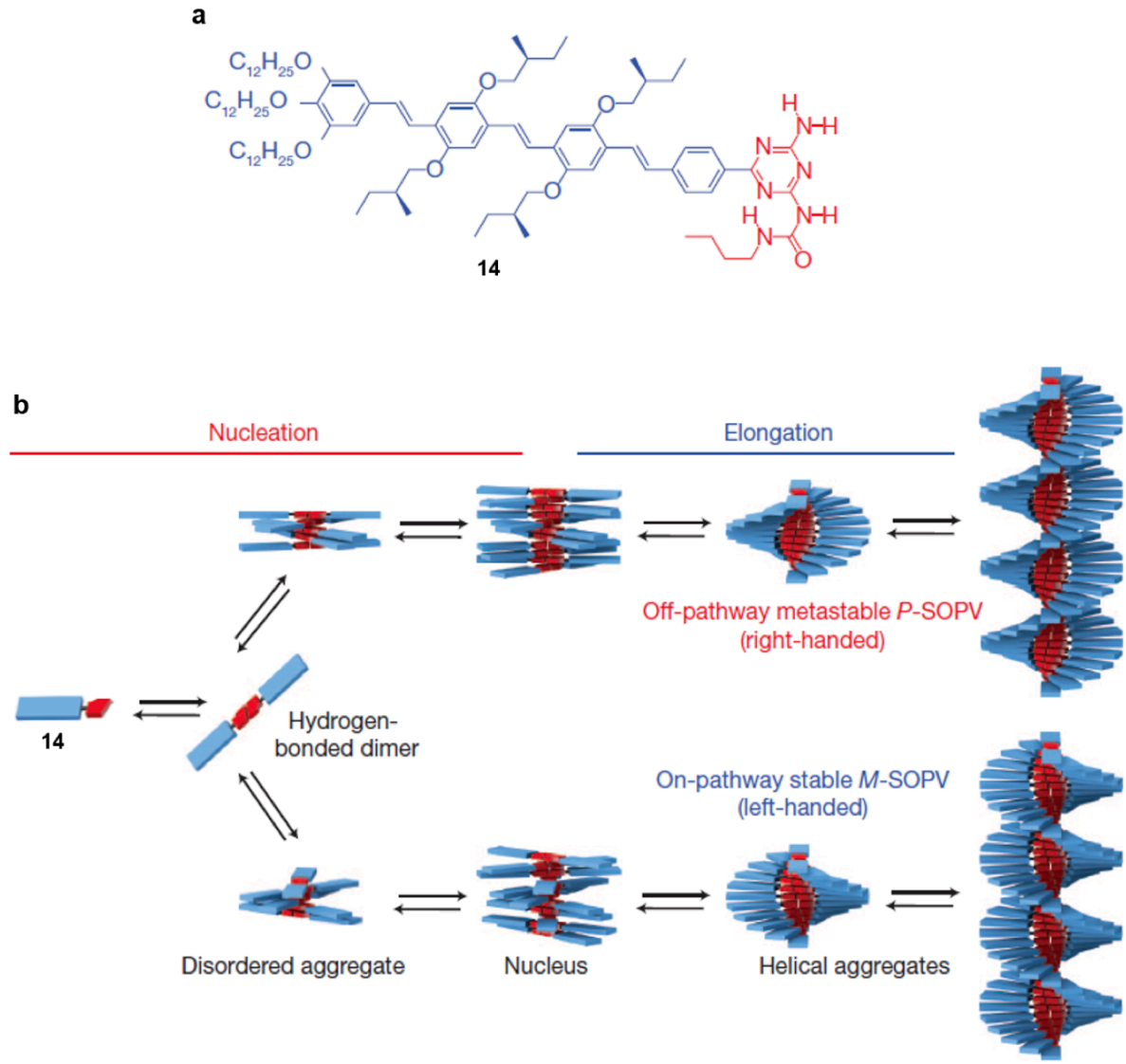

Figure 1-13. (a) Molecular structure of OPV derivative **14**. (b) Schematic representation of cooperative self-assembly pathways of **14**, including the formation of metastable *P*-type helical aggregates and stable *M*-type helical aggregates. (Reprinted with permission from ref. 33c. Copyright 2012 Nature Publishing Group.)

More recently, the research group of K. Sugiyasu realized a living supramolecular polymerization by an elaborate control over pathway complexity between isodesmic and cooperative self-assembly processes of porphyrin derivative **25** with hydrogen-bonding moieties (Figure 1-14a).[33d] When a hot MCH solution of this molecule was cooled, the molecule self-assembled into nanoparticles composed of slipped face-to-face (J-type) stacks of porphyrin chromophores through isodesmic process. The resulting J-type aggregates were stable for several days at room temperature, and then slowly reconstructed via monomeric state into supramolecular polymer fibers composed of face-to-face (H-type) stacks of porphyrin units through cooperative process (Figure 1-14b). Once a relatively small amount of H-type fibers was added into a solution of J-type nanoparticles, a transformation from J- to H-type aggregates was initiated (Figure 1-14c), which is regarded as a supramolecular seeded polymerization. The use of this phenomenon enabled a living supramolecular polymerization of **25**, which led to supramolecular polymers possessing controlled length and narrow polydispersity.

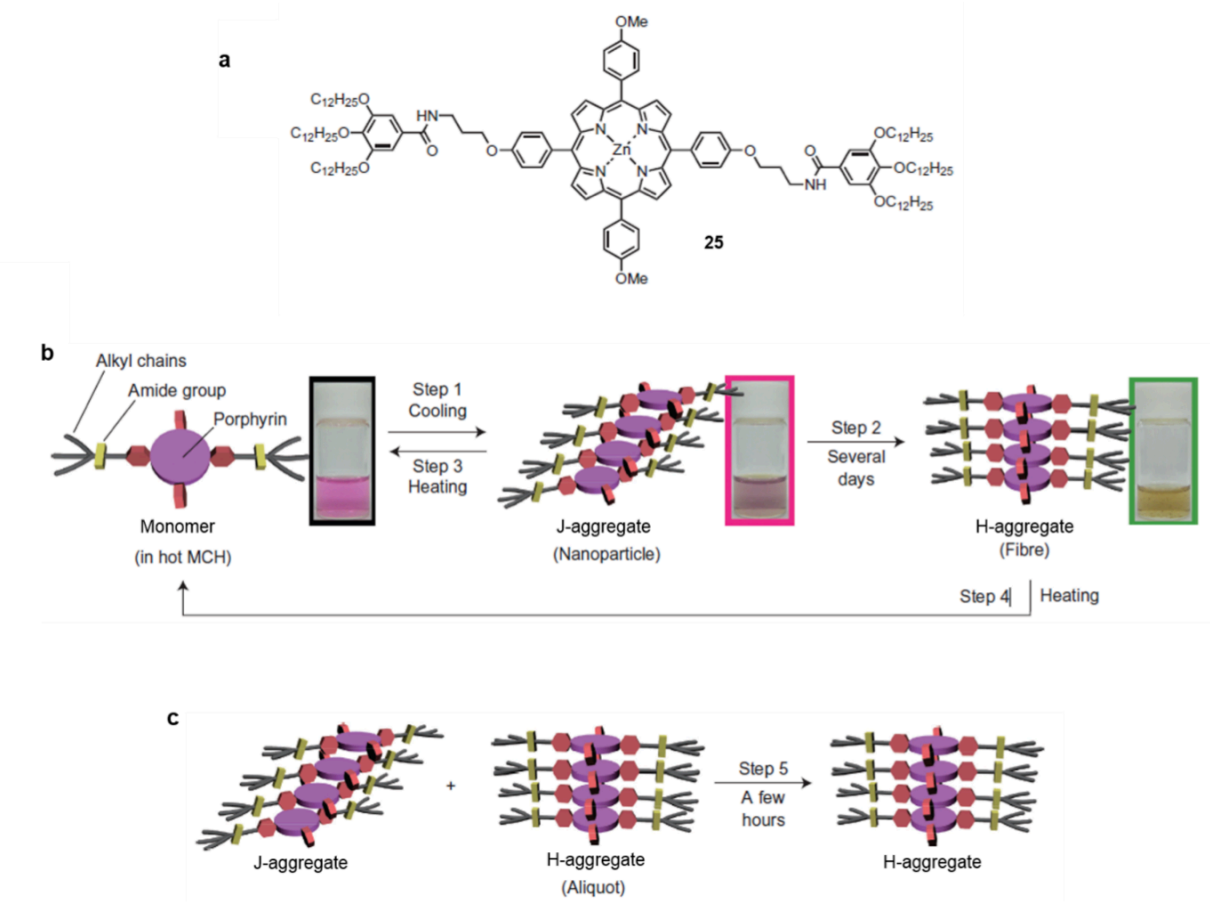

Figure 1-14. (a) Molecular structure of porphyrin derivative **25** with two hydrogen-bonding units. (b) Schematic representation of self-assembly of **25**, which includes the formation of J-type aggregates by cooling of a hot monomeric solution (Step 1), the transformation from J- to H-type aggregates by time course (Step 2) and the disassembly of J- and H-type aggregates into monomers by heating (Step 3 and 4, respectively). (c) Schematic representation of the supramolecular seeded polymerization by mixing J-type aggregates with H-type aggregates (Step 5). (Reprinted with permission from ref. 33d. Copyright 2014 Nature Publishing Group.)

1-6. Aim and Outline of the Thesis

As described above, recent advance on analytical techniques of self-assembly processes has enabled investigation of supramolecular polymerization processes of diverse synthetic molecules including those that have already been reported.[23,29–31] As a result, it was found that many of synthetic molecules self-assemble via cooperative process into supramolecular polymers. Because supramolecular polymerization processes can determine the resulting nanostructures and their functions, a precise control over degrees of cooperativity that can tune the processes would be of great important. Arguably, cooperative supramolecular polymerization processes and pathway complexity can be found for self-assemblies of complex molecules with multiple noncovalent interactive moieties. Although the complexity of molecular structures with respect to the capability to form specific intermolecular interactions seems to be able to guide supramolecular polymerization to higher cooperative process[23], relation between molecular structures and degree of cooperativity in supramolecular polymerization has not been understood yet. Such insight into structure-process relationship enables the design of programmable supramolecular polymerization.

The aim of this thesis is to understand how molecular structures can affect cooperative supramolecular polymerization processes and self-assembled morphologies. To address this issue, I designed and synthesized two type of unique self-assembling building blocks and investigated their supramolecular polymerization processes and self-assembled structures in different scales (Figure 1-15). One series of molecules is π-conjugated molecules that are functionalize with self-complementary double hydrogen-bonding unit (barbituric acid) to form hexameric supermacrocycles as supramolecular monomer units. Another series of molecules is V-shaped covalent dimer of functional π-conjugated chromophores, which are capable of folding via intramolecular stacking.

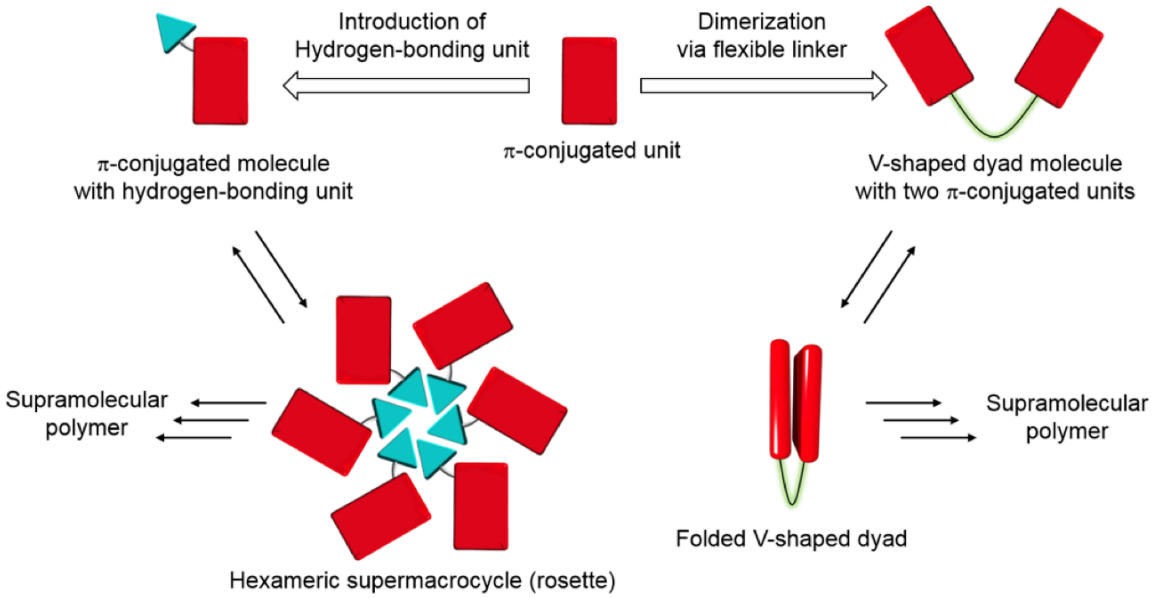

Figure 1-15. Molecular designs in this thesis.

In Chapter 2, I discuss supramolecular polymerization of two different barbituric-acid-functionalized naphthalene derivatives **1** and **2** (Figure 1-16a,b). These molecules aggregate into cyclic hexamers (supermacrocycles or rosettes) through self-complementary multiple hydrogen bonding between barbituric acid moieties.[34] The two molecules have a wedge-shaped aliphatic tail possessing either an ether or ester connection, and thereby they have different degrees of conformational freedom of the wedge unit. The different degrees of conformational freedom of the wedge moieties can affect hierarchical organization of the "supermacrocyclic monomers", which is discussed based on 2D X-ray diffraction (XRD) studies on the orientated supramolecular polymer nanofibers. Such differences in stacking lead to the supramolecular polymers with distinct morphological features (cylindrical or helical fibers). Moreover, the morphological difference is reflected in the macroscopic properties (formation of gel) of concentrated solutions the supramolecular polymers. Notably, the degrees of conformational freedom can affect the kinetics in supramolecular polymerization, whereby the more flexible ether linkage contributes to the delay of supramolecular polymerization under kinetic control

via the formation of off-pathway aggregates. These results represent a good example to show clear relation between *molecular structures* and *supramolecular polymerization processes* governed by kinetics, thermodynamics and pathway complexity.

In Chapter 3, I discuss 'phototriggered supramolecular polymerization' of azobenzene-functionalized molecule **3** (Figure 1-16c) based on a derivative used in Chapter 2. The structurally non-aggregative *cis*-azobenzene isomer is activated under ambient conditions by external light stimuli to initiate supramolecular polymerization.[35] This photo-kinetically controlled supramolecular polymerization provides short supramolecular polymers with narrower polydispersity, which are very different from those obtained by conventional thermal supramolecular polymerization processes.

In Chapter 4, I discuss unprecedented type of synthetic molecular self-assembly based on a photo-cross-linkable V-shaped stilbene dyad **4** (Figure 1-17). In this system, a small amount of photochemical product, generated by UV-irradiation, can guide the total system into completely different supramolecular polymerization processes.[36] The intact dyad self-assembles into right-handed superhelical fibrils via cooperative process. Upon UV-irradiation of the helical fibrils and subsequent thermal reconstruction by heating-cooling treatment, the intact dyad and the photoproduct undergo a co-assembly that furnishes left-handed superhelical fibrils via different cooperative process.

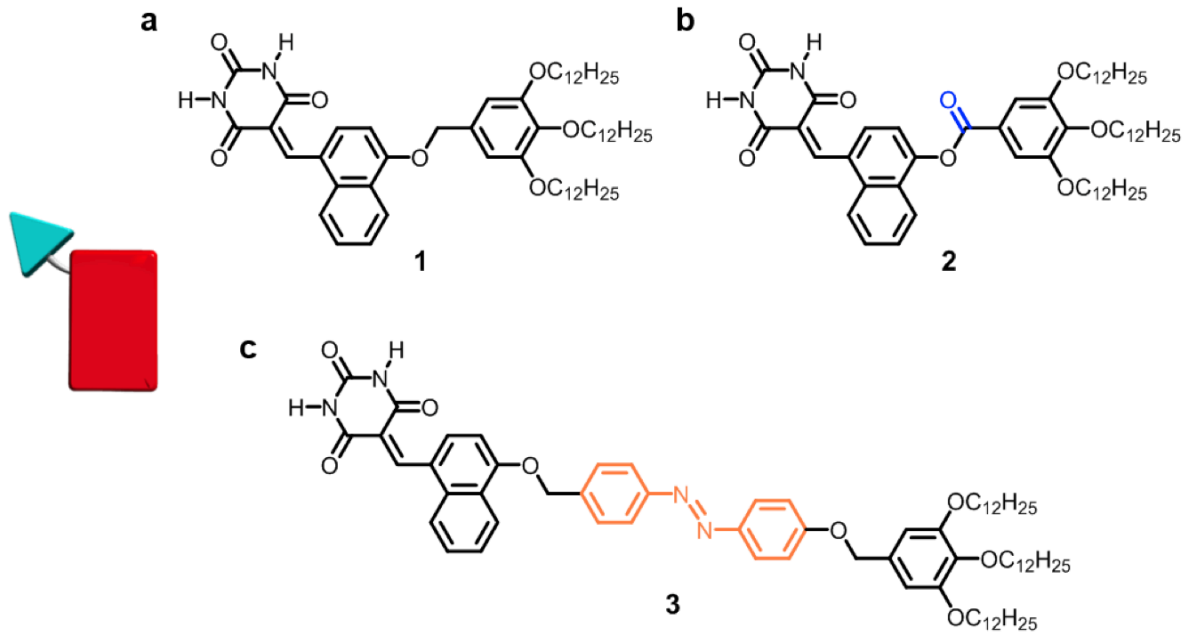

Figure 1-16. Molecular structures of barbituric-acid-functional compounds **1**–**3**.

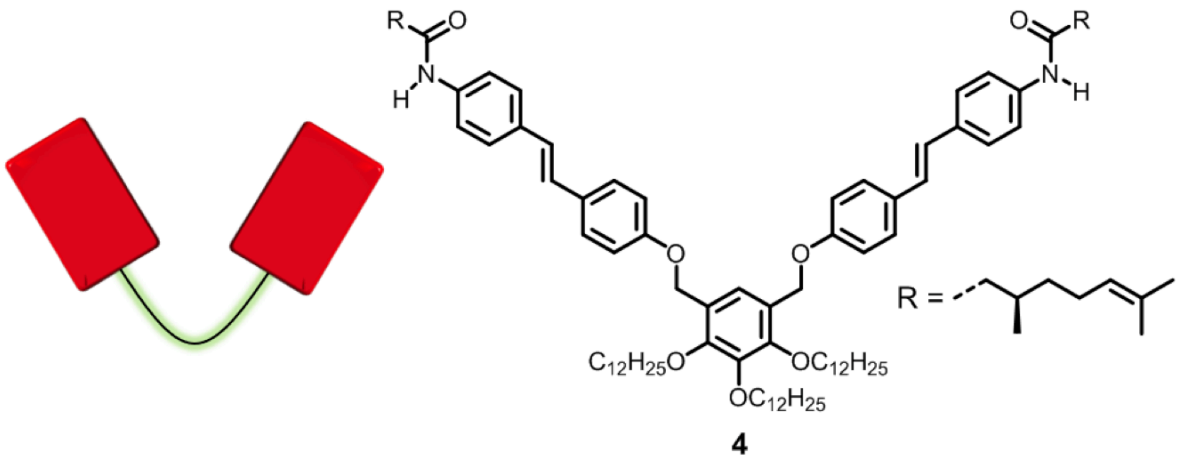

Figure 1-17. Molecular structure of V-shaped stilbene dyad **4**.

1-7. General Methods

General experiments: Column chromatography was performed using 63–210 μm silica gel. All commercially available reagents and solvents were of reagent grade and used without purification. The solvents for the preparation of the assemblies were all spectral grade and used without purification. ^{1}H and ^{13}C NMR, and 2D-COSY NMR spectra were recorded on JEOL JNM-ECA500 NMR spectrometer and chemical shifts are reported in ppm (δ) with the signal of TMS as the internal standard. ESI-MS spectra were measured on an Exactive (Thermo Scientific). UV/vis, fluorescent (FL) and circular dichroism (CD) spectra were recorded on a JASCO V660 spectrophotometer, JASCO FP6600 spectropolarimeter and JASCO J840 spectropolarimeter, respectively. All the spectrometers are equipped with Peltier device temperature-control unit. FT/IR spectra were recorded on JASCO FT/IR-4100 spectrometer with an attenuated total reflectance (ATR) apparatus. Dynamic light scattering (DLS) measurements were performed on a Zetasizer Nano S (Malvern Instruments) device using non-invasive back-scatter technology (NIBS) under 4.0 mW He-Ne laser (633 nm). Differential scanning calorimetry (DSC) was performed on SII DSC6220. Polarized optical microscopic observation was carried out using an Olympus BX51 optical microscopy system with a Linkam temperature-controlled heating stage. The scattering angle was set at 173°. Molecular modeling was performed on MacroModel version 10.4 and the geometry-optimization was carried out using AMBER force field without solvent.

Small angle X-ray scattering (SAXS): SAXS measurements were conducted at the beamline BL-10C at the Photon Factory of the High Energy Accelerator Re-search Organization (KEK) in Tsukuba, Japan. The detector was PILATUS3 2M (DECTRIS) which was located at a distance of ca. 1 m from sample position. The wavelength of X-ray was 0.15 nm. Silver behenate was used as a standard specimen to calibrate SAXS detector. The two-dimensional

scattering data were circularly averaged to convert into the one-dimensional scattering intensity data using the software, SAngler[37]. The scattering intensities were corrected for background scattering and sample absorption. The magnitude of the scattering vector is given by Q = (4π/λ)sinθ/2, where λ is the X-ray wavelength and θ is the scattering angle.

Atomic force microscopy (AFM): AFM images were acquired under ambient conditions using a Multimode 8 Nanoscope V microscope (Bruker Instruments) in peak force tapping (Scanasyst) mode. Silicon cantilevers (SCANASYST-AIR) with a spring constant of 0.4 N/m and frequency of 70 kHz (nominal value, Bruker, Japan) were used. Samples were prepared by spin-coating MCH solutions onto freshly cleaved highly oriented pyrolytic graphite (HOPG).

Transmission electron microscopy (TEM): TEM observation was carried out on JEM-2100F (JEOL) at acceleration voltage at 120 kV. Samples were prepared by spin-coating MCH solutions onto carbon-coated STEM Cu grid (SHR-C075) and dried under vacuum for 24 h. The TEM observations were conducted without staining.

Synchrotron X-ray Diffraction Analysis: Wide-angle X-ray diffraction (WAXD) experiments were performed at BL45XU beamline at SPring-8 (Hyogo Japan) equipped with an R-AXIS IV++ (Rigaku) imaging plate area detector. The scattering vector, $q = 4\pi\sin\theta/\lambda$, and the position of incident X-ray beam on the detector were calibrated using several orders of layer reflections from silver behenate (d = 58.380 Å), where 2θ and λ refer to the scattering angle and wavelength of the X-ray beam (1.0 Å), respectively. The sample-to-detector distances for WAXD measurements were 0.4 m. The obtained diffraction images were integrated along the Debye-Scherrer ring to afford one-dimensional intensity data using the FIT2D software[38]. The lattice parameters were refined using the CellCalc ver. 2.10 software[39].

Vapor pressure osmometry (VPO): The degrees of polymerization of hydrogen-bonded supramolecular assemblies were investigated using KNAUER Vapor Pressure Osmometer K-7000 with EuroOsmo 7000 software. Before performing all the measurements, the reference condition was established by attaching pure solvent on both thermistors and performing AUTOZERO. The individual concentrations of the standards or samples were entered for every single run and more than three osmograms were recorded for a given concentration. A droplet of pure solvent and a droplet of the sample solutions were placed on separate thermistors surrounded by pure solvent vapor. The drop size was kept as constant as possible and equal on both thermistors. The difference in vapor pressures between the two droplets was detected as the difference in temperature at each thermistor. Chloroform was used as solvent for measurements and the temperature for measurements was operated at 20 °C. Benzil was used as the standard for calibration. EuroOsmo software was used to draw the graphs and to calculate the calibration constant and molecular weights. To minimize the error, measurement of each concentration was repeated four times and also the entire experiment also repeated more than three times to confirm the accuracy of the obtained data.

Photoirradiation experiments: Photoirradiation experiments were performed using 365-nm UV light from a LED lamp (17 mW/cm^2). Sample solutions in a quartz cuvette were placed at the distance of 5 cm from the light source.

Calculation of the degree of aggregation (α): Normalized UV/vis (or CD) intensities, which show degree of aggregation (α), were calculated from the intensities of temperature-dependent spectra at appropriate wavelength based on equation (1), in which Int_{agg} and Int_{mon} are the

UV/vis (or CD) intensities of fully aggregated (the lowest temperature) and pure monomeric species (the highest temperature), respectively, and *Int*(*T*) is the UV/vis (or CD) intensity at a given temperature.

$$a(T) = 1 - \frac{Int_{\text{agg}} - Int(T)}{Int_{\text{agg}} - Int_{\text{mon}}} \qquad (1)$$

Isodesmic (equal-*K*) model: If a plot of α *versus T* shows sigmoidal relation, the aggregation can be characterized as isodesmic process[23c,25] , and the plot can be fitted with equation (2):

$$a(T) = \frac{1}{1 + \exp[-0.908\Delta H_{\text{iso}} \frac{T - T_{\text{m}}}{RT_{\text{m}}{}^2}]} \qquad (2)$$

where ΔH_{iso} is the enthalpy release during isodesmic aggregation and T_{m} is the melting temperature for $\alpha = 0.5$.

Degree of polymerization (DP_{n}) for isodesmic model can be described by equation (3):

$$DP_{\text{n}}(T) = \frac{1}{\sqrt{1 - a(T)}} = \frac{1}{2} - \frac{1}{2}\sqrt{4K_{\text{iso}}(T)C_{\text{T}} + 1} \qquad (3)$$

where $K_{\text{iso}}(T)$ is the temperature-dependent equilibrium constant and C_{T} is the total concentration. Thus, $K_{\text{iso}}(T)$ can be obtained by with equation (4).

$$K_{\text{iso}}(T) = \frac{(\frac{2}{\sqrt{1 - a(T)}} - 1)^2 - 1}{4C_{\text{T}}} \qquad (4)$$

Cooperative (nucleation–elongation) model: Cooperative assembly processes were analyzed

by the nucleation–elongation model developed by van der Schoot, Meijer, Schenning and coworkers.[23a,c] If a curve obtained by plotting α *versus* T in temperature-dependent UV/vis (or CD) analysis is non-sigmoidal, the curve can be fitted with a cooperative model, which involves two different regimes expressed by following two equations (5) and (6). The two different regimes are defined as the nucleation and the elongation processes, respectively, which are divided by onset temperature for the elongation (T_e).

In the elongation regime ($T < T_e$), α is given by the following equation (5):

$$a(T) = a_{SAT}[1 - \exp\left[\frac{-\Delta H_e(T - T_e)}{RT_e{}^2}\right]] \qquad (5)$$

where ΔH_e is the enthalpy release in the elongation regime, α_{SAT} is a parameter introduced to ensure that α_n/α_{SAT} does not exceed unity, R is the ideal gas constant. Therefore, the nonlinear least-squares analysis directly provided ΔH_e, T_e and α_{SAT}.

In the nucleation regime ($T > T_e$), α is given by the following equation (6):

$$a(T) = a_{SAT}[K_a{}^{\frac{1}{3}} \exp[\left(\frac{2}{3K_a{}^{\frac{1}{3}}} - 1\right)\Delta H_e\left[\frac{(T - T_e)}{RT_e{}^2}\right]]] \qquad (6)$$

where K_a is the dimensionless activation equilibrium constant at T_e, and can be obtained by nonlinear least-squares analysis. The nucleation step is governed by K_a, a parameter reflecting degree of cooperativity. If $K_a << 1$, the aggregation process can be characterized by a model with high cooperativity. In this case, the critical concentration of monomer is approximately total concentration (C_T) at $\geq T_e$, thereby the elongation constant denoted as K_e is equated to the inverse of C_T.[40] Because K_e is governed by free energy change of the elongation process (ΔG_e),

R and T, $K_e(T_e)$ is given by the following equation (7):

$$K_e(T_e) = \exp\left[\frac{-\Delta G_e}{RT_e}\right] = \frac{1}{C_T} \quad (7)$$

Assuming that K_a is equal to K_n/K_e in the nucleation regime at T_e,[41] the free energy changes of nucleation (ΔG_n) at $>T_e$ is given by the following equation (8):

$$\begin{aligned}\Delta G_n(T_e) &= -RT_e \ln(K_n) = -RT_e \ln(K_a K_e) \\ &= -RT_e \ln\left(\frac{K_a}{C_T}\right) \quad (8)\end{aligned}$$

1-8. References

1. J.-M. Lehn, *Supramolecular Chemistry—Concepts and Perspectives*, VCH, Weinheim, 1995.

2. J. D. Watson, F. H. C. Crick, Nature **1953**, *171*, 737–738.

3. K. Maeda, E. Yashima, Top. Curr. Chem. **2006**, *265*, 47–88.

4. C. B. Anfinsen, *Science* **1973**, *181*, 223–230.

5. (a) A. Klug *Angew. Chem. Int. Ed.* **1983**, *22*, 565–582. (b) A. Klug *Phil.Trans. R. Soc. Lond. B* **1999**, *354*, 531–535.

6. (a) T. Shimizu, M. Masuda, H. Minamikawa, *Chem. Rev.* **2005**, *105*, 1401–1443. (b) L. C. Palmer, S. I. Stupp, **2008**, *41*, 1674–1684 (c) H. J. Kim, T. Kim, M. Lee, *Acc. Chem. Res.* **2011**, *44*, 72–82.

7. (a) F. J. M. Hoeben, P. Jonkheijm, E. W. Meijer, A. P. H. J. Schenning, *Chem. Rev.* **2005**, *105*, 1491–1546. (b) A. P. H. J. Schenning, E. W. Meijer, *Chem. Commun.* **2005**, 3245–3258. (c) S. S. Babu, V. K. Praveen, A. Ajayaghosh, *Chem. Rev.* **2014**, *114*, 1973–2129.

8. (a) A. Ajayaghosh, V. Praveen, *Acc. Chem. Res.* **2007**, *40*, 644–656. (b) F. Würthner, C. R. Saha-Möller, B. Fimmel, S. Ogi, P. Leowanawat, D. Schmidt, *Chem. Rev.* **2016**, *116*, 962–1052.

9. S. Yagai, S. Mahesh, Y. Kikkawa, K. Unoike, T. Karatsu, A. Kitamura, A. Ajayaghosh, *Angew. Chem. Int. Ed.* **2008**, *47*, 4691–4694.

10. M. M. J. Smulders, A. P. H. J. Schenning, E. W. Meijer, *J. Am. Chem. Soc.* **2008**, *130*, 606–611.

11. E. Lee, J.-K. Kim, M. Lee, *Angew. Chem. Int. Ed.* **2009**, *48*, 3657–3660.

12. A. Ajayaghosh, R. Varghese, S. Mahesh, V. K. Praveen, *Angew. Chem. Int. Ed.* **2006**, *45*, 7729–7732.

13. (a) L. Brunsveld, B. J. Folmer, E. W. Meijer, R. P. Sijbesma, *Chem. Rev.* **2001**, *101*, 4071–4098. (b) T. F. A. De Greef, M. M. J. Smulders, M. Wolffs, A. P. H. J. Schenning, R. P. Sijbesma, E. W. Meijer, *Chem. Rev.* **2009**, *109*, 5687–5754. (c) P. Wei, X. Yan, F. Huang, *Chem. Soc. Rev.* **2015**, *44*, 815–832. (d) S. Yagai, *Bull. Chem. Soc. Jpn.* **2015**, *88*, 28–58.

14. P. Terech, R. G. Weiss, *Chem. Rev.* **1997**, *97*, 3133–3159.

15. T. Kato, N. Mizoshita, K. Kishimoto, *Angew. Chem. Int. Ed.* **2005**, *45*, 38–68.

16. C. Fouquey, J.-M. Lehn, A. -M. Levelut, *Adv. Mater*., **1990**, *2*, 254–257.

17. R. P. Sijbesma, F. H. Beijer, L. Brunsveld, B. J. Folmer, J. H. Hirschberg, R. F. Lange, J. K. Lowe, E. W. Meijer, *Science* **1997**, *278*, 1601–1604.

18. T. Aida, E. W. Meijer, S. I. Stupp, *Science* **2012**, *335*, 813–817.

19. A. P. H. J. Schenning, P. Jonkheijm, E. Peeters, E. W. Meijer, *J. Am. Chem. Soc.* **2001**, *123*, 409–416.

20. (a) S. Yagai, S. Kubota, H. Saito, K. Unoike, T. Karatsu, A. Kitamura, A. Ajayaghosh, M. Kanesato, Y. Kikkawa, *J. Am. Chem. Soc.* **2009**, *131*, 5408–5410. (b) S. Yagai, T. Kinoshita, Y. Kikkawa, T. Karatsu, A. Kitamura, Y. Honsho, S. Seki, *Chem.—Eur. J.* **2009**, *15*, 9320–9324. (c) S. Yagai, Y. Goto, T. Karatsu, A. Kitamura, Y. Kikkawa, *Chem. —Eur. J.* **2011**, *17*, 13657–13660. (d) S. Yagai, Y. Goto, X. Lin, T. Karatsu, A. Kitamura, D. Kuzuhara, H. Yamada, Y. Kikkawa, A. Saeki, S. Seki, *Angew. Chem. Int. Ed.* **2012**, *51*, 6643–6647. (e) M. J. Hollamby, K. Aratsu, B. R. Pauw, S. E. Rogers, A. J. Smith, M. Yamauchi, X. Lin, S.

Yagai, *Angew. Chem. Int. Ed.* **2016**, *55*, 9890–9893.

21. S. Yagai, M. Suzuki, X. Lin, M. Gushiken, T. Noguchi, T. Karatsu, A. Kitamura, A. Saeki, S. Seki, Y. Kikkawa, Y. Tani, K. Nakayama, *Chem.—Eur. J.* **2014**, *20*, 16128–16137.

22. (a) S. Yagai, M. Yamauchi, A. Kobayashi, T. Karatsu, A. Kitamura, T. Ohba, Y. Kikkawa, *J. Am. Chem. Soc.* **2012**, *134*, 18205–18208. (b) M. Yamauchi, Y. Chiba, T. Karatsu, A. Kitamura, S. Yagai, *Chem. Lett.* **2013**, *42*, 799–800.

23. (a) P. Jonkheijm, P. van der Schoot, A. P. H. J. Schenning, E. W. Meijer, *Science* **2006**, *313*, 80−83. (b) T. E. Kaiser, V. Stepanenko, F. Würthner, *J. Am. Chem. Soc.* **2009**, *131*, 6719–6732. (c) M. M. J. Smulders, M. M. L. Nieuwenhuizen, T. F. A. de Greef, P. van der Schoot, A. P. H. J. Schenning, E. W. Meijer, *Chem.—Eur. J.* **2010**, *16*, 362–367.

24. (a) D. Zhao, J. S. Moore, *Org. Biomol. Chem.* **2003**, *1*, 3471–3491. (b) Z. Chen, A. Lohr, C. R. Saha-Möller, F. Würthner, *Chem. Soc. Rev.* **2009**, *38*, 564–584. (c) C. Rest, R. Kandanelli, G. Fernández, *Chem. Soc. Rev.* **2015**, *44*, 2543–2572.

25. R. B. Martin, *Chem. Rev.* **1996**, *96*, 3043–3064.

26. E. D. Korn, M. F. Carlier, D. Pantaloni, *Science* **1987**, *238*, 638–644.

27. (a) F. Oosawa, M. Kasai, *J. Mol. Biol.* **1962**, *4*, 10–21. (b) R. F. Goldstein, L. Stryer, *Biophys. J.* **1986**, *50*, 583–599.

28. T. E. Kaiser, V. Stepanenko, F. Würthner, *J. Am. Chem. Soc.* **2009**, *131*, 6719–6732.

29. S. Yagai, M. Usui, T. Seki, H. Murayama, Y. Kikkawa, S. Uemura, T. Karatsu, A. Kitamura, A. Asano, S. Seki, *J. Am. Chem. Soc.* **2012**, *134*, 7983–7994.

30. M. J. Mayoral, C. Rest, V. Stepanenko, J. Schellheimer, R. Q. Albuquerque, G. Fernandez,

J. Am. Chem. Soc. **2013**, *135*, 2148–2151.

31. C. Kulkarni, K. K. Bejagam, S. P. Senanayak, K. S. Narayan, S. Balasubramanian, S. J. George, *J. Am. Chem. Soc.* **2015**, *137*, 3924–3932.

32. (a) I. V. Baskakov, G. Legname, M. A. Baldwin, S. B. Prusiner, F. E. Cohen, *J. Biol. Chem.* **2002**, *277*, 21140–21148. (b) M. Adachi, M. So, K. Sakurai, J. Kardos, Y. Goto, *J. Biol. Chem.* **2015**, *290*, 18134–18145.

33. (a) Y. Tidhar, H. Weissman, S. G. Wolf, A. Gulino and B. Rybtchinski, *Chem.—Eur. J.* **2011**, *17*, 6068–6075. (b) I. D. Tevis, L. C. Palmer, D. J. Herman, I. P. Murray, D. A. Stone and S. I. Stupp, *J. Am. Chem. Soc.* **2011**, *133*, 16486–16494. (c) P. A. Korevaar, S. J. George, A. J. Markvoort, M. M. J. Smulders, P. A. J. Hilbers, A. P. H. J. Schenning, T. F. A. de Greef and E. W. Meijer, *Nature* **2012**, *481*, 492−496. (d) S. Ogi, K. Sugiyasu, S. Manna, S. Samitsu and M. Takeuchi, *Nat. Chem.* **2014**, *6*, 188–195. (e) P. A. Korevaar, T. F. A. de Greef and E. W. Meijer, *Chem. Mater.* **2014**, *26*, 576–586. (f) A. J. Markvoort, H. M. M. ten Eikelder, P. A. J. Hilbers and T. F. A. de Greef, *ACS Cent. Sci.* **2016**, *2*, 232–241. (g) A. Aliprandi, M. Mauro and L. De Cola, *Nat. Chem.* **2016**, *8*, 10–15.

34. M. Yamauchi, B. Adhikari, D. D. Prabhu, X. Lin, T. Karatsu, T. Ohba, N. Shimizu, H. Takagi, R. Haruki, S. Adachi, T. Kajitani, T. Fukushima, S. Yagai, submitted.

35. M. Yamauchi, N. Kanao, B. Adhikari, T. Karatsu, S. Yagai, *Chem. Lett.* **2017**, *46*, 111–114.

36. M. Yamauchi, T. Ohba, T. Karatsu, S. Yagai, *Nat. Commun.* **2015**, *6*, 8936.

37. N. Shimizu, K. Yatabe, Y. Nagatani, S. Saijo, T. Kosuge, N. Igarashi, *AIP Conf. Proc*. **2016**, *1741*, 050017.

38. http://www.esrf.eu/computing/scientific/FIT2D/

39. http://homepage2.nifty.com/~hsc/soft/cellcalc_e.html

40. Van der Schoot, P. Chapter 3 Theory of supramolecular polymerization in *SUPRAMOLECULAR POLYMERS*, A. Ciferri, Ed. (CRC Press, Baton Rouge, LA, 2005).

41. F. García, L. Sánchez, *J. Am. Chem. Soc.* **2012**, *134*, 734–742.

Chapter 2.

Supramolecular Polymers of Noncovalent Supermacrocycles: Effect of High Degrees of Internal Orders on Morphology and Kinetics

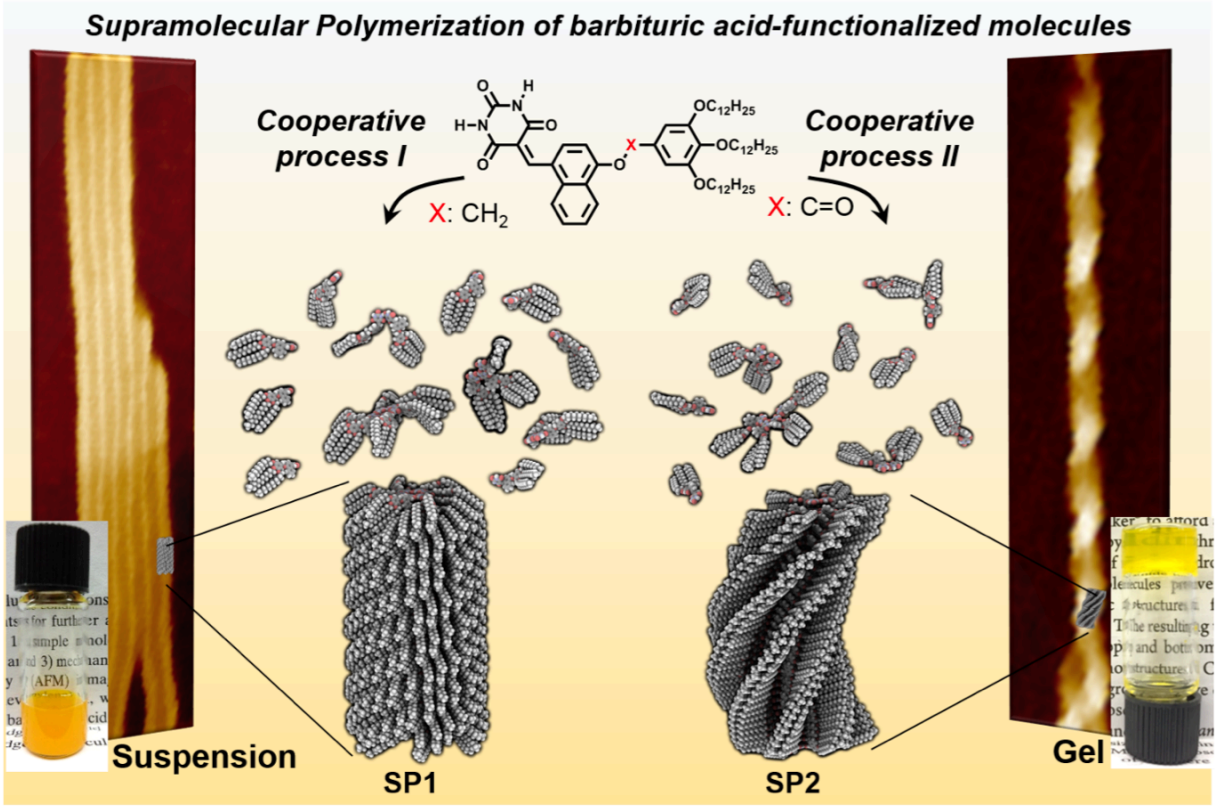

2-1. Abstract

Elaborately designed functional π-conjugated building blocks with additional interactive groups are able to provide supramolecular polymers with the high degrees of internal order, which are expected to exhibit outstanding properties both in function as well as in structure. For constructing such supramolecular polymers, not only intricate synthesis of π-conjugated monomers but also noncovalent synthesis of "supermacrocyclic monomers" formed by relatively simple molecules is an appealing strategy though this process has not been exploited in developing supramolecular polymers. Here, I unravel unique self-assemblies of two barbituric-acid-functionalized naphthalene compounds that noncovalently hexamerize annularly through multiple hydrogen bonds. The two compounds are equipped with a "wedge"-shaped aliphatic unit through ether or ester connection, and this minor difference is amplified through hexamerization to distinctly different features not only in the morphologies of supramolecular polymers but also in their supramolecular polymerization processes. A degree of conformational freedom of the wedge moiety differentiates stacking styles of supermacrocycles while retaining the high degree of internal order as shown by 2D X-ray diffraction of the aligned supramolecular polymers. The different stacking styles provide the supramolecular polymers fearing distinct morphological properties (cylindrical or helical), and these morphological features lead to the contrasting properties in concentrated solution states (suspension, gel, etc.). The degrees of conformational freedom of the wedge unit also can affect kinetics in the supramolecular polymerization, wherein more flexible ether connection retards supramolecular polymerization under the kinetic control through the formation of off-pathway amorphous products. My findings suggest a remarkable merit of noncovalent supermacrocyclization of functional organic molecules, where a minor difference in monomer structures can be transferred to a critical difference in properties of one-dimensional nanofibers.

2-2. Introduction

In nature, one-dimensional self-assembly, *i.e.* supramolecular polymerization, of proteins provides excellent fibrous nanostructures with the high levels of internal order, for example, tobacco mosaic virus (TMV)[1] and microtubules[2]. The intricate high-order nanostructures in biological systems are able to adopt sophisticated conformations via a competition among multiple interactive moieties. The complexity in conformations of the biological molecules potentially affords the complex self-organization with the high degrees of internal order, which is far superior to the synthetic supramolecular systems.[3]

In the synthetic systems, disc-shaped building blocks have been synthesized well as monomer units to exhibit extended supramolecular polymers (SPs) possessing specific photophysical and electronic functions.[4] Recently, the ways to investigate their supramolecular polymerization processes have been established[5] using those for aggregation of protein[6], and furthermore the presence of pathway complexity[7] in polymerization process has been disclosed. Most synthetic molecules self-assemble according to the classical equal-*K* non-cooperative (isodesmic) model[8] that is the simplest mechanism of one-dimensional supramolecular polymerization. However, the introduction of interactive moieties into molecular structures is able to guide a more intricate nucleation-elongation (cooperative) polymerization[5,9], leading to the creation of SPs with the high degrees of internal order[10]. Accordingly, SPs possessing much higher degrees of internal order could be generated by intricate disc-shaped monomers that are constructed noncovalently. By this approach, relatively simple molecules possessing directional interactive moiety can initially form enlarged disc-shaped supermacrocycles[11] possessing intricate geometrical properties, which further stack on top of each other to construct one-dimensional SPs. Although various types of supermacrocycles have been presented so far,[4d,12] the polymerization processes have not been exploited in detail.

Recently, the research group of S. Yagai has extensively investigated supramolecular polymerizations of barbituric-acid-functionalized π-conjugated molecules[13] possessing "wedge"-shaped tridodecyloxyphenyl (TDP) side chain unit[14]. The X-ray diffraction studies suggested that these compounds assemble into columnar structures by stacking of hydrogen-bonded hexameric supermacrocycles (so-called rosettes).[13c,d] Notably, naphthalene compound **1** showed unique absorption spectral feature which implies homogeneous face-to-face (H-type) stacking arrangement of the naphthalene chromophores, though six naphthalene units are involved together in one rosette (Figure 2-1).[13d] Therefore, a high-level internal order is expected for the resulting supramolecular polymer backbones.

By use of the unique supramolecular polymerization property of **1**, I here explore the detailed supramolecular polymerization of rosettes for the first time. The in-depth investigation of **1** unveiled that the degrees of conformational freedom of the wedge moieties play key roles not only in determining internal orders within the SP backbones but also affecting the supramolecular polymerization kinetics. To regulate such a conformational freedom, naphthalene derivative **2**, in which the ether linkage of **1** was substituted for ester linkage, was synthesized newly. Reflecting a decrease in the conformational freedom of the wedge moieties, compound **2** did not exhibit kinetic effect and formed helically undulated SPs possessing distinctive internal order.

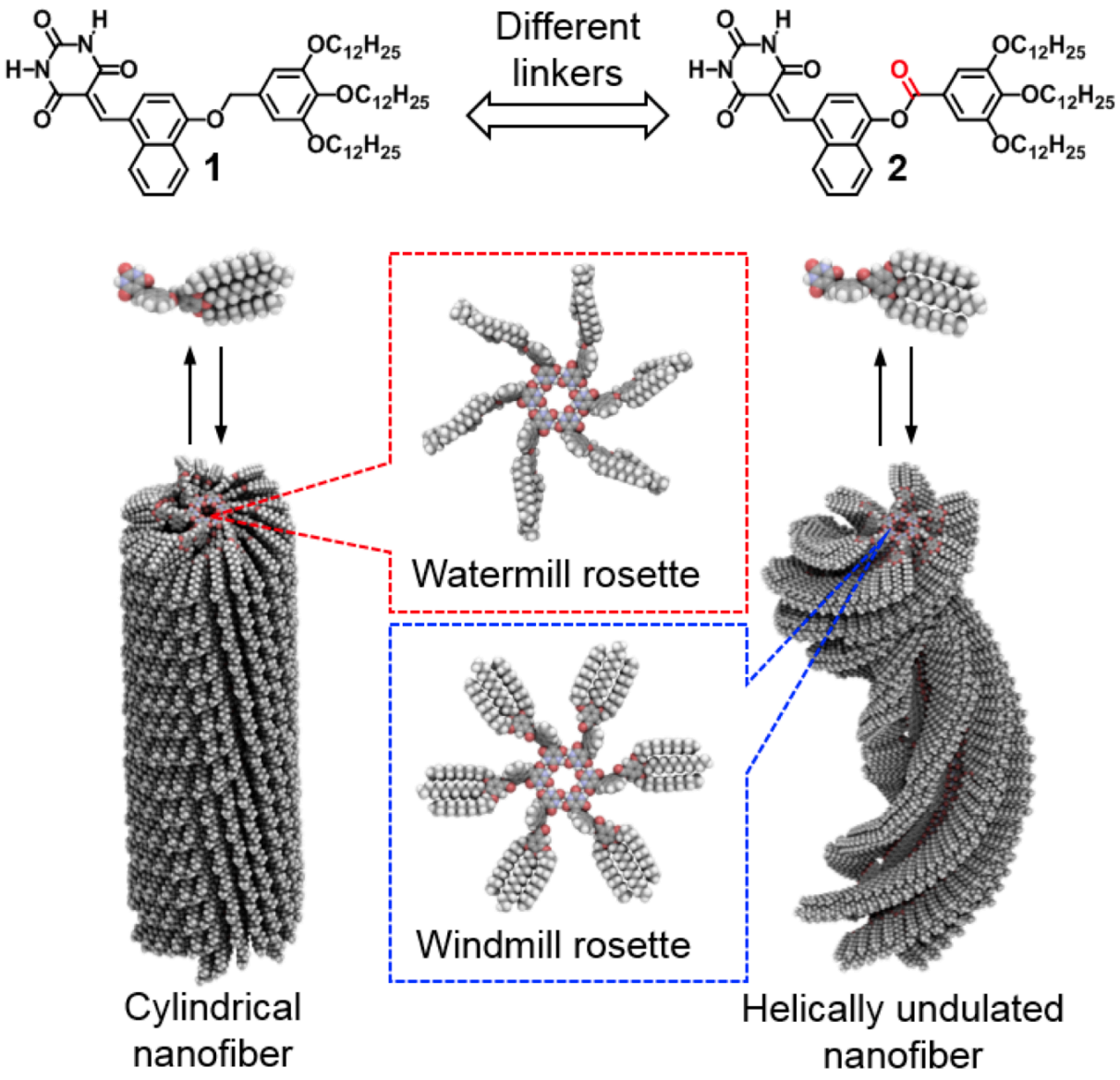

Figure 2-1. Chemical structures of **1** and **2** and schematic illustrations of their supramolecular polymerization via the formation of specific rosettes.

2-3. Formation of Hydrogen-Bonded Hexameric Rosettes in $CHCl_3$

Self-assembly of **1** and **2** was investigated in $CHCl_3$, wherein hydrogen-bonding interaction predominantly occurs while aromatic units are solvated well. Both compounds are effectively soluble in $CHCl_3$ (c_{max} = 450 mM, *i.e.* 420 mg/mL), implying that they do not form open-end polymeric aggregates via hydrogen-bonds[15]. In dynamic light scattering (DLS) analysis of the concentrated solutions ($CHCl_3$, c = 450 mM), both compounds showed only the presence of small products possessing an average hydrodynamic diameter (D_H) of 6 nm (Figure 2-2a,b),[16] which is consistent with the diameter of hexameric rosettes (ca. 6.5 nm, Figure 2-2c,d). In vapor pressure osmometry (VPO) studies[17], **1** exhibited an increase in the average aggregation number (N) upon raising concentration, resulting in 6 at 450 mM (Figure 2-2e). For **2**, the VPO measurement at 450 mM revealed N = ca. 4, which is different from the case of **1** (N = 6); this difference is presumably due to increase of viscosity at higher concentrations (Figure 2-2f).

^{1}H NMR spectra were measured at 293 K for $CDCl_3$ solutions of **1** and **2** upon varying concentrations in the range of 0.1 to 450 mM (Figure 2-3a,b,d,e). At c = 0.1 mM, both compounds exhibited sharp NMR signals for all protons, wherein the signals corresponding to two barbituric acid NH protons (H_{syn} and H_{anti}) were detected in the range of δ = 7.7–7.9 ppm. When raising the concentration, these signals underwent downfield shift by intermolecular hydrogen bonds. These protons resulted in δ = 10.5 ppm (H_{syn}), 10.0 ppm (H_{anti}) for **1** and δ = 10.2 ppm (H_{syn}), 9.6 ppm (H_{anti}) for **2** (Figure 2-3b,e) at c = 450 mM. The intermolecular hydrogen-bonding was corroborated by the observation of nuclear Overhauser effect[12b] between two protons H_{syn} and H_{anti} only at higher concentration regime (Figure 2-4). Definite signal broadening, which attributes to the formation of polymeric spices, was not observed for all protons, even in the submolar concentrations, indicating the formation of well-defined hydrogen-bonded small aggregates.

In order to analyze the above concentration-dependent NMR data in detail, the chemical shifts of the two NH protons (H_{syn} and H_{anti}) were plotted against concentration (Figure 2-3c,f). Both compounds showed a sigmoidal change in the degree of aggregation (α) upon raising concentration. The sigmoidal transition could be fitted with an isodesmic (equal-K) model[8,18] and isodesmic equilibrium constant (K_{iso}) was estimated to be of 13 M^{-1} for **1** and 14 M^{-1} for **2**. The theoretical fitting with the dimer model[18] as well as nucleation–elongation (cooperative) model[5b] resulted in failure. Assuming the hexamerization of **1** and **2** into rosettes via isodesmic process, the apparent equilibrium constant for rosette formation ($K_{rosette} = K_{iso}^5$; Scheme 2-1)[19] was calculated to be 3.7×10^5 M^{-5} for **1** and 5.4×10^5 M^{-5} for **2** (Figure 2-3c,f). Variable temperature ^1H NMR studies for solutions at c = 10 mM indicated that thermal assembly/disassembly also follows isodesmic process with the almost same values of K_{iso} (12 M^{-1} for **1** and 11 M^{-1} for **2**, Figure 2-5).[5c] Combined with the DLS and VPO results, the results of the NMR studies demonstrate that both **1** and **2** favorably form hydrogen-bonded hexameric rosettes.

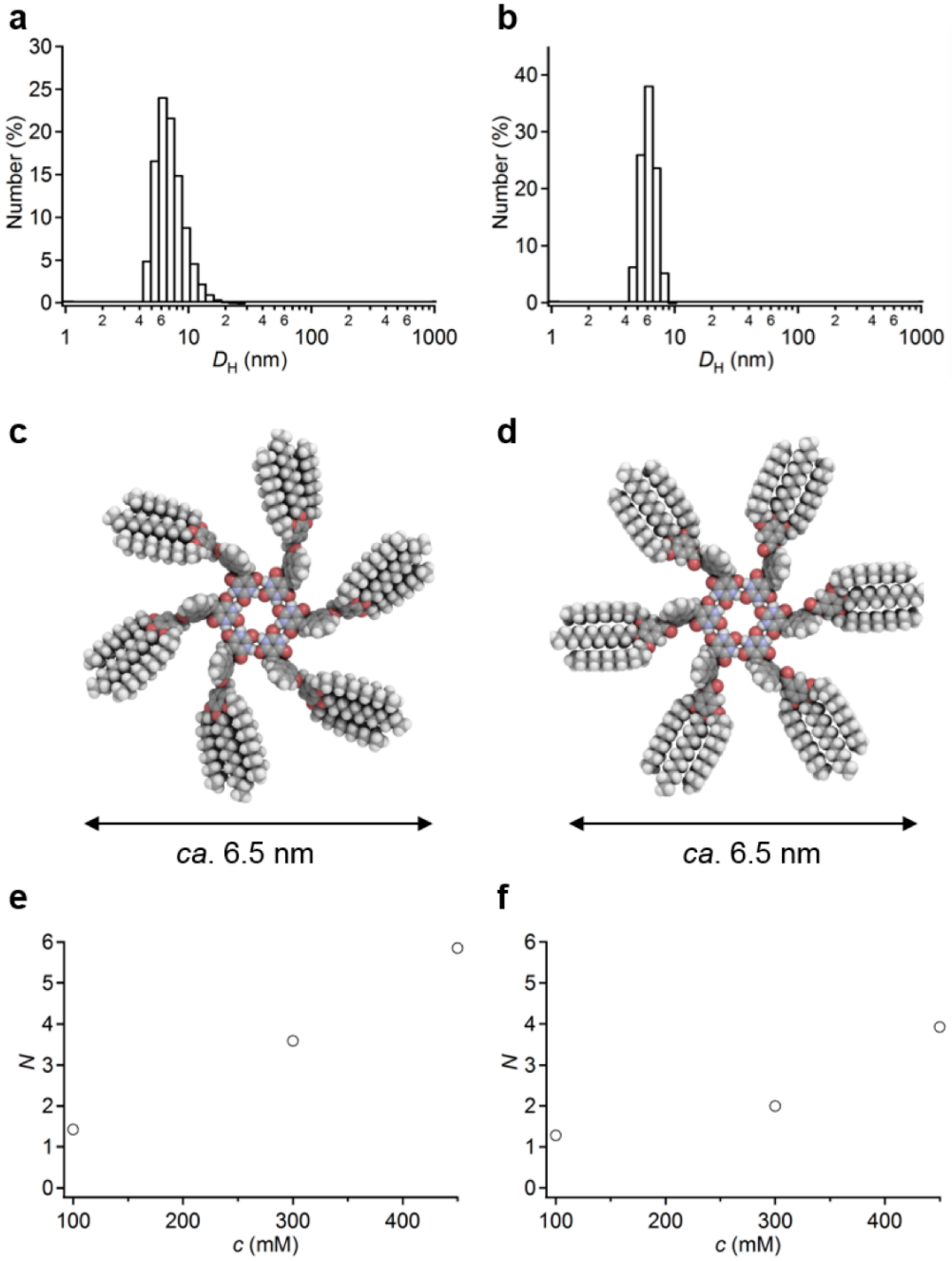

Figure 2-2. (a,b) Dynamic light scattering (DLS) of assemblies of **1** (a) and **2** (d) in $CHCl_3$ (c = 450 mM, T = 293 K). (c,d) Geometry optimized hydrogen-bonded hexameric rosettes of **1** (c) and **2** (d), calculated by force field calculations (MacroModel 10.4, AMBER force field without solvent). (e,f) VPO-derived plots of the aggregation number $N = c_{subs}/c_{collig}$, wherein c_{collig} is the colligative concentration measured by VPO, as a function of the monomer concentration of **1** (e) and **2** (f).

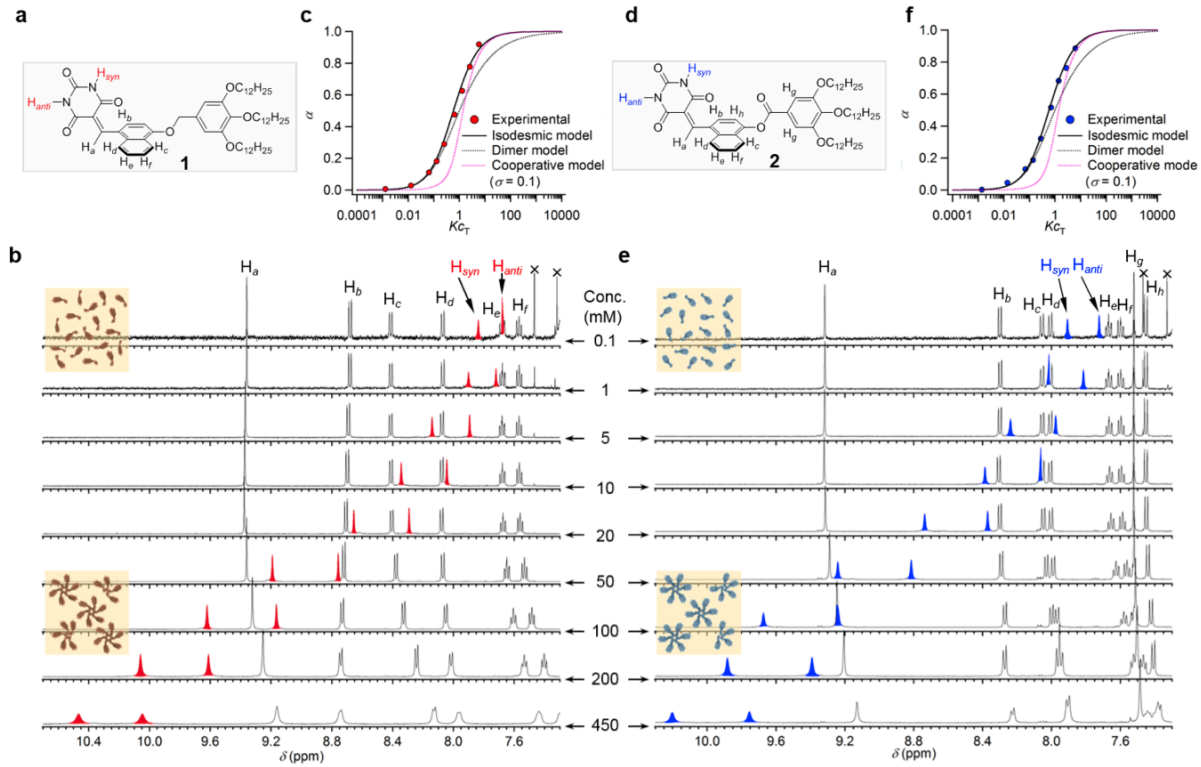

Figure 2-3. (a,d) Chemical structures of **1** and **2** with assignment of the corresponding ^{1}H NMR signals. (b,e) Variable-concentration ^{1}H NMR spectra of $CDCl_3$ solutions of **1** (b) and **2** (e) in the range of c = 0.1 to 450 mM at 293 K. (c,f) Plots of degree of aggregation (α), calculated from the chemical shifts (δ) of barbituric acid NH protons (H_{syn} and H_{anti}) of **1** (c) and **2** (f), against the concentration, with simulated curves based on theoretical models.

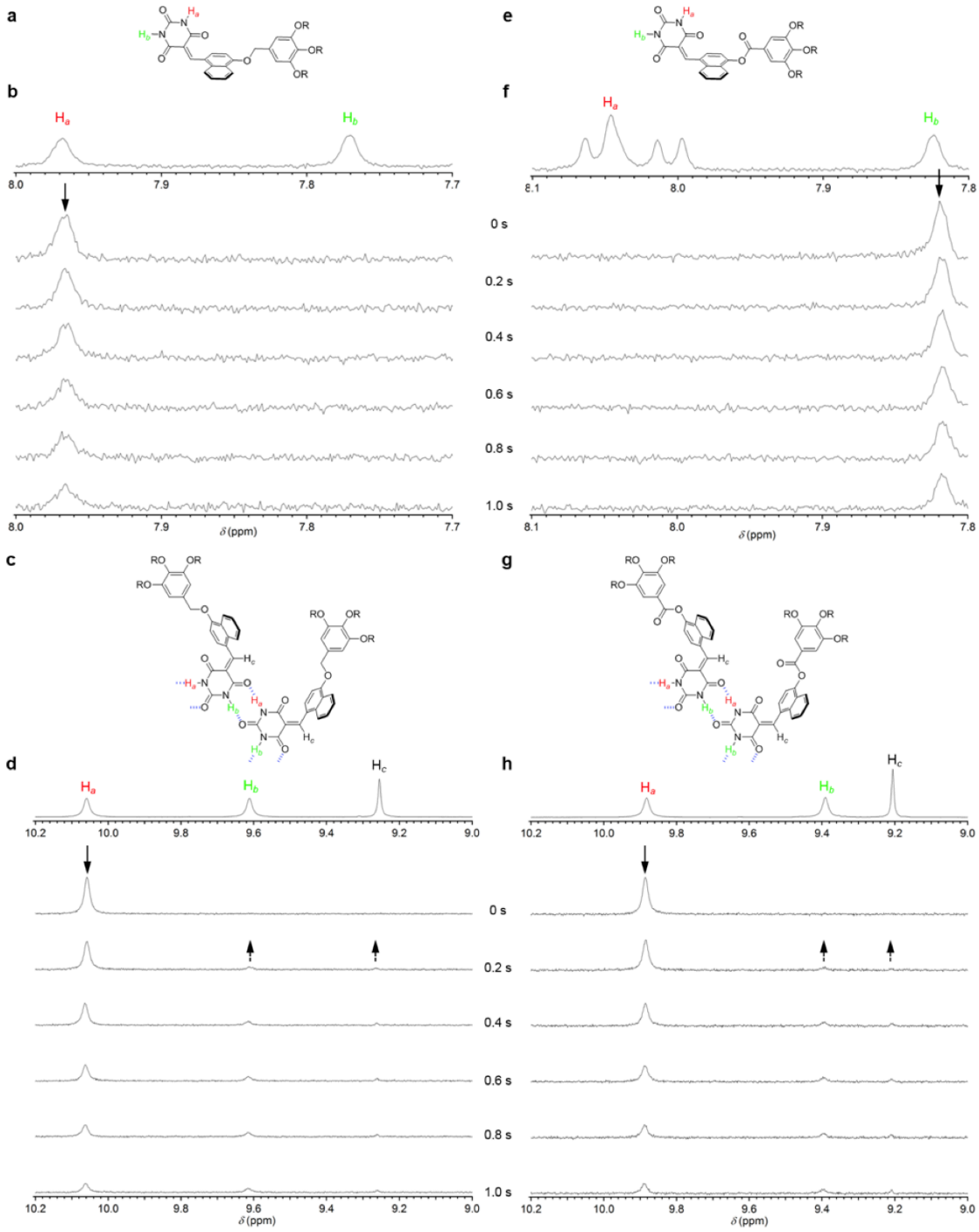

Figure 2-4. (a,c,e,g) Chemical structures of **1** (a,c) and **2** (e,g) with assignment of the corresponding NOE signals. (b,d,f,h) 1D NOE spectra of **1** (b,d) and **2** (f,h) in $CDCl_3$ at $T = 293$ K at different mixing times (0–1.0 s) irradiating the signals at 7.96 ppm (b), 10.06 ppm (d), 7.82 ppm (f) and 9.89 ppm (h). Concentrations in (b,f) and (d,h) are 2 and 200 mM, respectively.

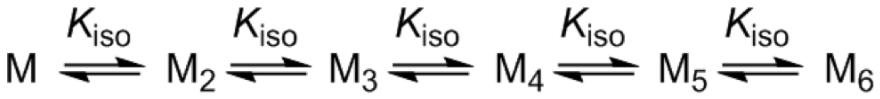

Scheme 2-1. Formation of rosette $\mathbf{M}_6$ by isodesmic assembly of monomer **M** with K_{iso}.

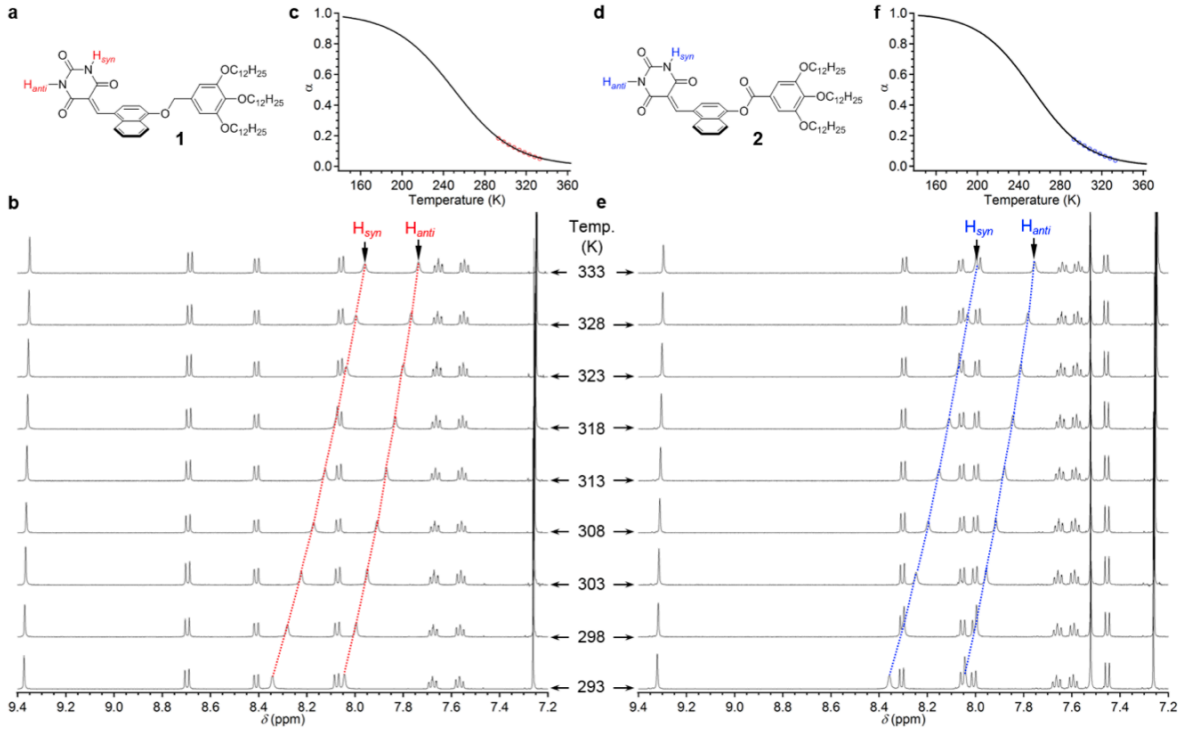

Figure 2-5. (a,d) Chemical structures of **1** (a) and **2** (b) with assignments of the corresponding ^{1}H NMR signals of barbituric acid NH (H_{anti} and H_{syn}). (b,e) Variable temperature ^{1}H NMR spectra of **1** (b) and **2** (e) in $CDCl_3$ at c = 10 mM upon heating from 293 to 333 K. (c,f) Plots of degree of aggregation (α), calculated from the chemical shifts of NH protons of **1** (c) and **2** (f), against temperature The black curves correspond to simulations based on isodesmic theoretical model.[5c]

2-4. Aggregation studies in Methylcyclohexane

Extended aggregation of both **1** and **2** was explored in methylcyclohexane (MCH), an apolar solvent that facilitates not only hydrogen-bonding but also π–π stacking interactions by means of UV-vis absorption and fluorescence (FL) spectroscopies. At 323 K, the ether compound **1** (c = 50 μM) exhibited two vibronic absorption maxima (λ_{max} = 425, 444 nm) attributable to π–π* transitions of monomeric barbiturate naphthalene chromophore (Figure 2-6a). Upon cooling to 293 K, the spectra exhibited hypso- and hypochromic changes, resulting in a single absorption band (λ_{max} = 406 nm) at 293 K. This spectral change suggests an electronic interaction between naphthalene units stacked by face-to-face (H-type).[13d,20] The emergence of a weak band around 480 nm is an indication of a rotational displacement on naphthalene stacking that allows the partial radiative transition to lower excited state.[21]

The ester compound **2** (c = 50 μM) at 323 K showed a vibronically less structured absorption band (λ_{max} = 403 nm, Figure 2-6c). Upon cooling to 293 K, a new absorption band appeared around 460 nm with a hypochromic change of the major band (λ_{max} = 409 nm). Although the spectral change of **2** is less specific compared to that of **1** presumably due to inhomogeneously π–π stacked naphthalene units, the emergence of the red-shifted absorption band (460 nm) suggests the presence of an offset (J-type) π–π stacking arrangement.[20]

Reflecting the different absorption features, **1** and **2** show distinct emission properties upon supramolecular aggregation. At 323 K, these compounds are nearly nonemissive probably because of nonradiative deactivation via the bond twist in the excited state (Figure 2-6b,d and Figure 2-7).[22,23] Upon cooling the hot solution of **1** to 293 K, the aggregation did not enhance the emission as it displayed a negligible weak emission at λ_{em} = ~580 nm (λ_{ex} = 410 nm) (Figure 2-6b), which supports the H-type fashion. In contrast, **2** displayed aggregation-induced enhanced emission upon cooling to 293 K, as shown by a significant emission band at λ_{em} =

539 nm (λ_{ex} = 438 nm) (quantum yield Φ = 0.02[24], Figure 2-6d). The excitation spectrum measured at λ_{em} = 539 nm suggested the presence of emissive aggregate having a red-shifted absorption band around 450 nm (Figure 2-8). This finding is consistent with the involvement of naphthalene units stacked with J-type nature.[20]

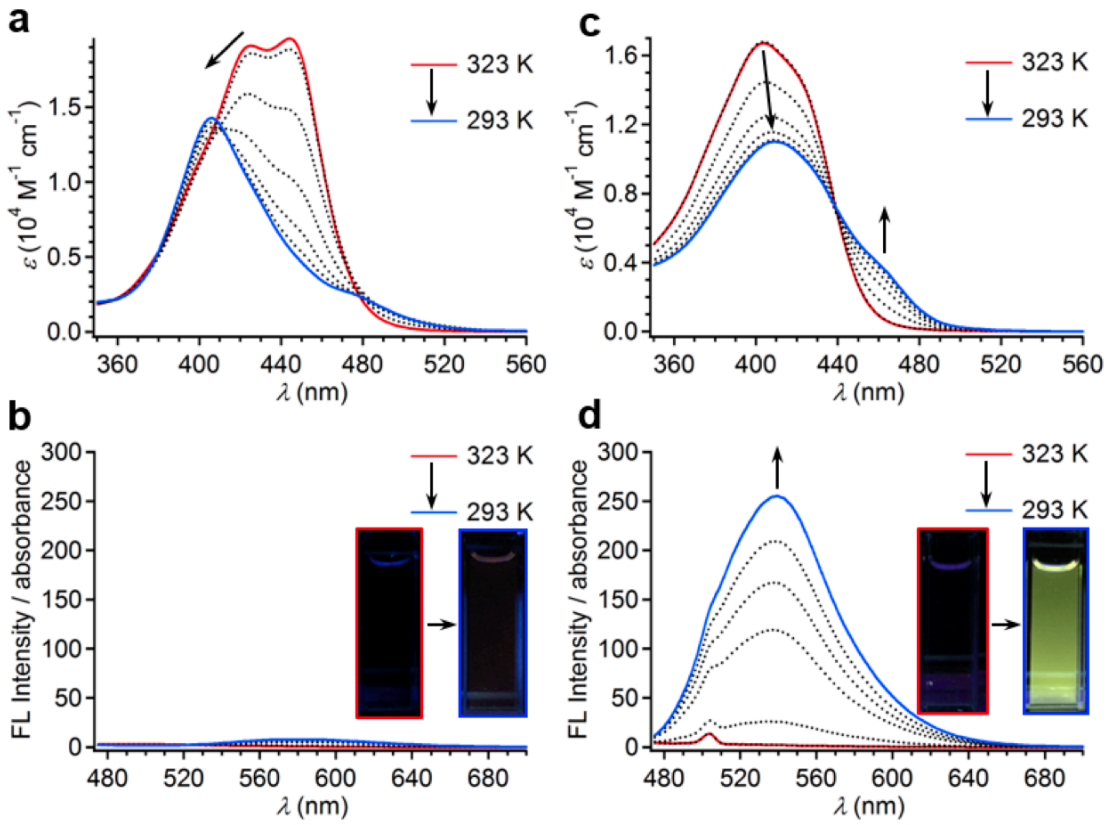

Figure 2-6. Variable temperature UV/vis absorption (a,c) and FL (b,d) spectra of **1** (a,b) and **2** (c,d) in MCH (c = 50 μM). These spectra are displayed at interval of 5 K. FL spectra were corrected by absorption for clarity. Weak signals around 505 nm in (d) is derived from a scattering light. Insets in (b,d) indicate photographs of MCH solutions of **1** and **2** at 323 K and 293 K illuminated with 365nm UV-light.

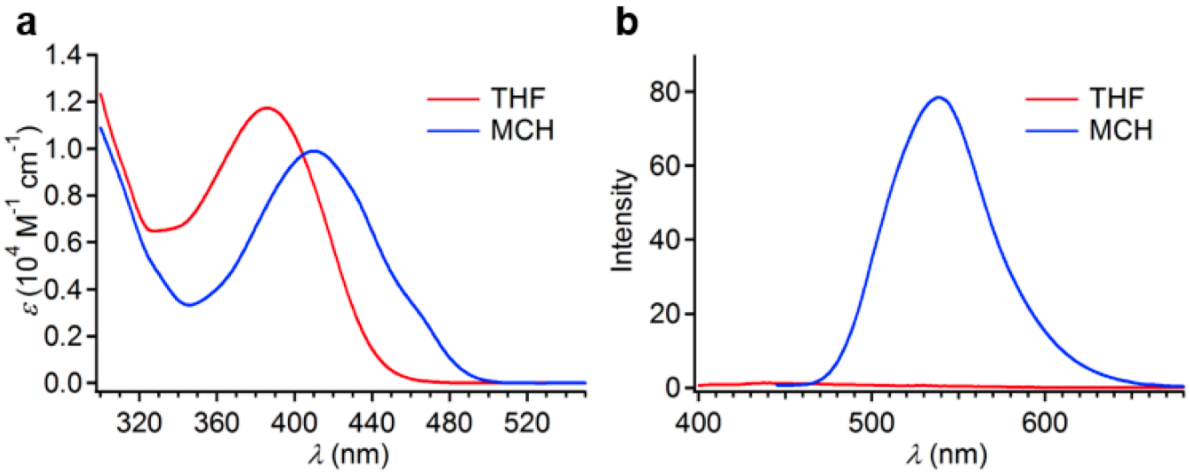

Figure 2-7. Solvent-dependent UV/vis (a) and FL (b) spectra of **2** (c = 50 μM) in THF (red spectra) and MCH (blue spectra) at 293 K.

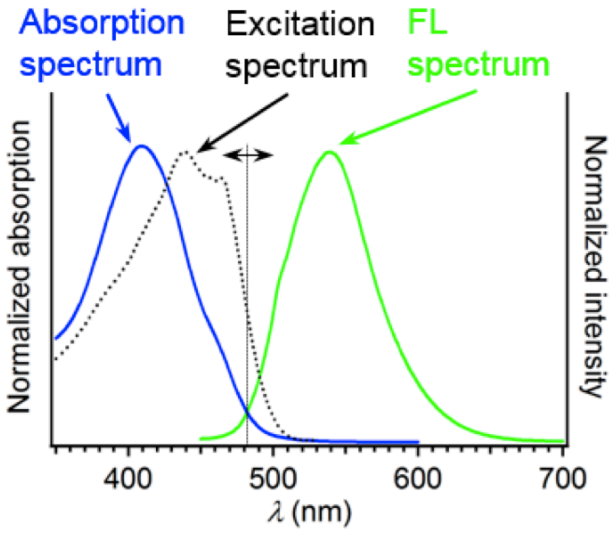

Figure 2-8. Normalized absorption, excitation (monitored at λ_{em} = 539 nm) and FL (λ_{ex} = 435 nm) spectra of **2** (c = 50 μM) in MCH at 293 K.

2-5. Morphologies of Supramolecular Polymers of 1 and 2

The aforementioned spectroscopic studies have suggested the involvement of hydrogen-bonding between barbituric acid moieties and π–π stacking interaction between naphthalene units in the supramolecular aggregation processes of **1** and **2**. In order to further pursuit these processes, morphologies of the resultant polymeric aggregates were investigated. For the direct detection of the aggregates in solution, small-angle X-ray scattering (SAXS) and DLS experiments of **1** and **2** in MCH were carried out. The SAXS profile of the 50 μM solutions of the two compounds has a broad peak (*d*-spacing of 5.30 nm for **1**, *d*-spacing of 5.40 nm for **2**; Figure 2-9a,b). According to the results of AFM studies shown below, these peaks are presumably derived from aggregates formed via the stacking of rosettes. The DLS measurements indicated that the above solutions (c = 50 μM) contain extended aggregates possessing D_H of 1000 nm (Figure 2-9c,d).

Transmission electron microscopic (TEM) and atomic force microscopic (AFM) imaging of these aggregates of **1** and **2** revealed different morphologies, spin-coated from corresponding solutions onto appropriate substrates. For **1**, cylindrical supramolecular polymers (referred to as $\mathbf{SP_1}$) with thickness (t) of ca. 5.5 nm (AFM) and width (w) of ca. 6 nm (TEM) were visualized (Figure 2-10). These dimensions of $\mathbf{SP_1}$ perfectly agree with one-dimensionally stacked rosettes with rotational displacement (Figure 2-10h). Most $\mathbf{SP_1}$ fibers were observed as closely aligned state possessing the top-to-top distance (d) between the fibers of ca. 6.4 nm as measured by AFM (Figure 2-10f,g), which suggests that they tend to organize into higher order structures. For **2**, on the other hand, supramolecular polymers (referred to as $\mathbf{SP_2}$) that are helically twisted with both right (*P*-type) and left (*M*-type) handedness were visualized by AFM and TEM (Figure 2-11). The width of the helical twisting (w_1) and of the primary columnar structure (w_2) were estimated from the TEM images to be ca. 10 nm and ca.

6 nm, respectively (Figure 2-11c). Because w_2 is consistent with the diameter of rosette (6.5 nm), **SP$_2$** is composed of one-dimensionally stacked rosettes of **2** with helical undulation (Figure 2-11h). AFM analysis demonstrated that the helical undulation is well-defined to give the pitch of ca. 23 nm (Figure 2-11f,g). The helical undulation of **SP$_2$** would be derived from local translational offset stacking of the rosettes, which is in line with the aforementioned finding on the involvement of stacked naphthalene units with J-type fashion (Figure 2-6c,d).

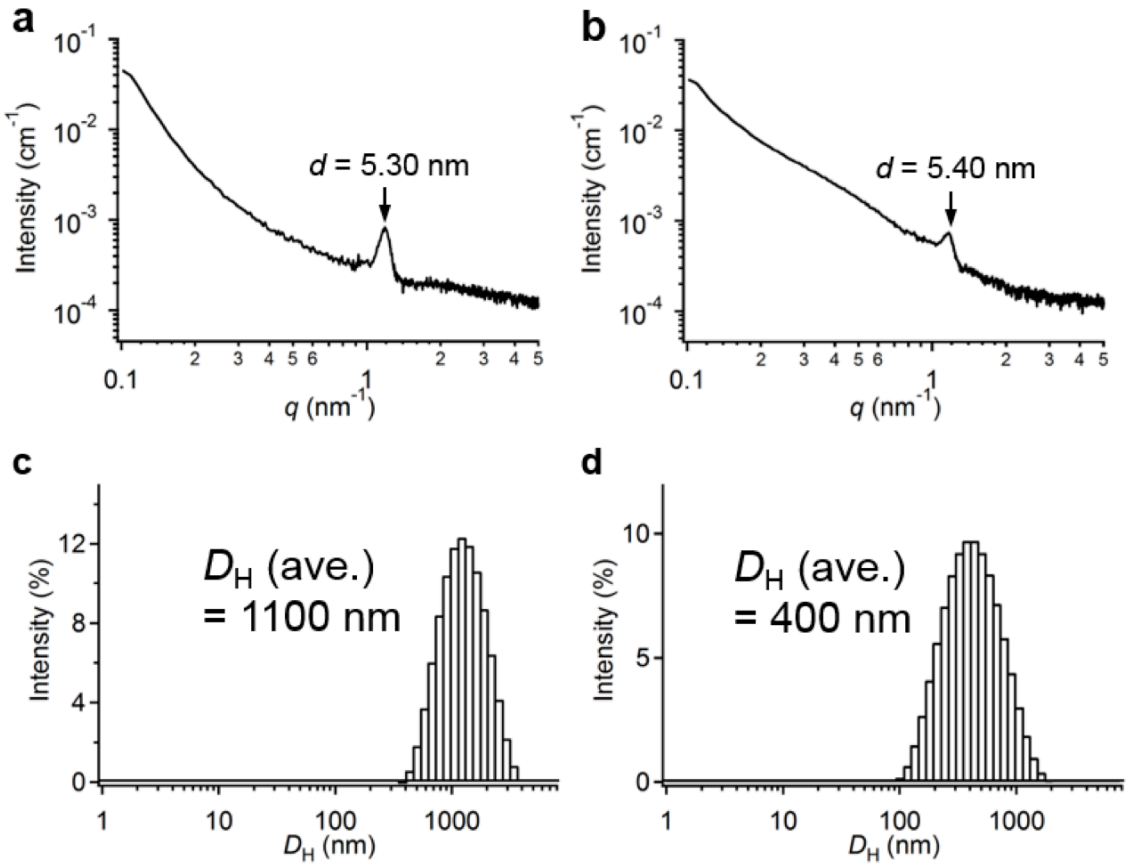

Figure 2-9. (a,b) SAXS profiles for aggregates of **1** (a) and **2** (b) in MCH (c = 50 μM, T = 293 K). (c,d) DLS results for aggregates of **1** (c) and **2** (d) in MCH (c = 50 μM, T = 293 K).

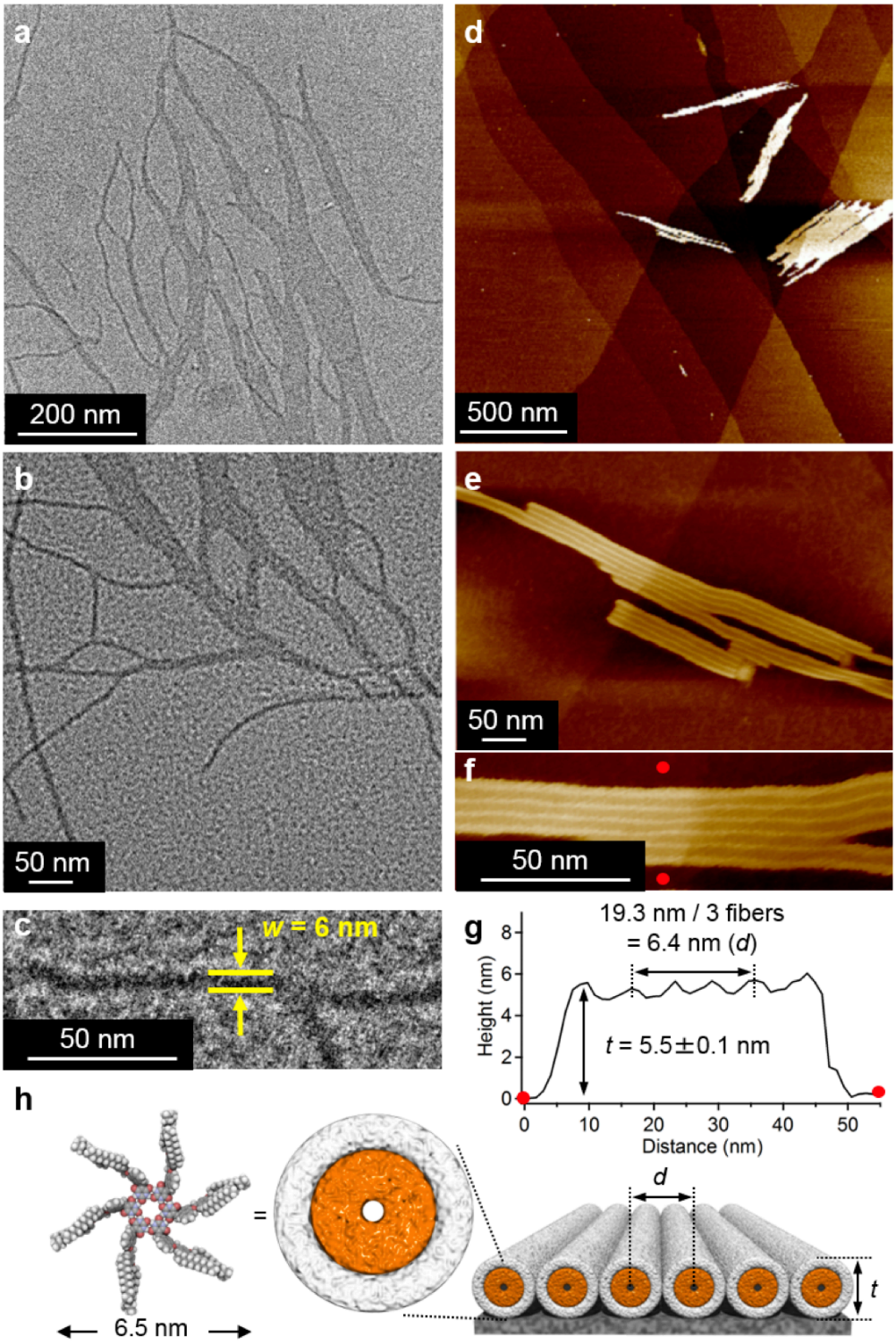

Figure 2-10. (a–f) TEM images (a–c) and AFM height images (d–f) of $\mathbf{SP_1}$, spin-coated from MCH solutions ($c = 50$ μM, $T = 293$ K) onto carbon-coated copper grid (TEM) or HOPG (AFM). (g) AFM cross-sectional analysis of $\mathbf{SP_1}$ between red dots in (f). (h) Cartoon illustration of aligned $\mathbf{SP_1}$ fibers on substrate.

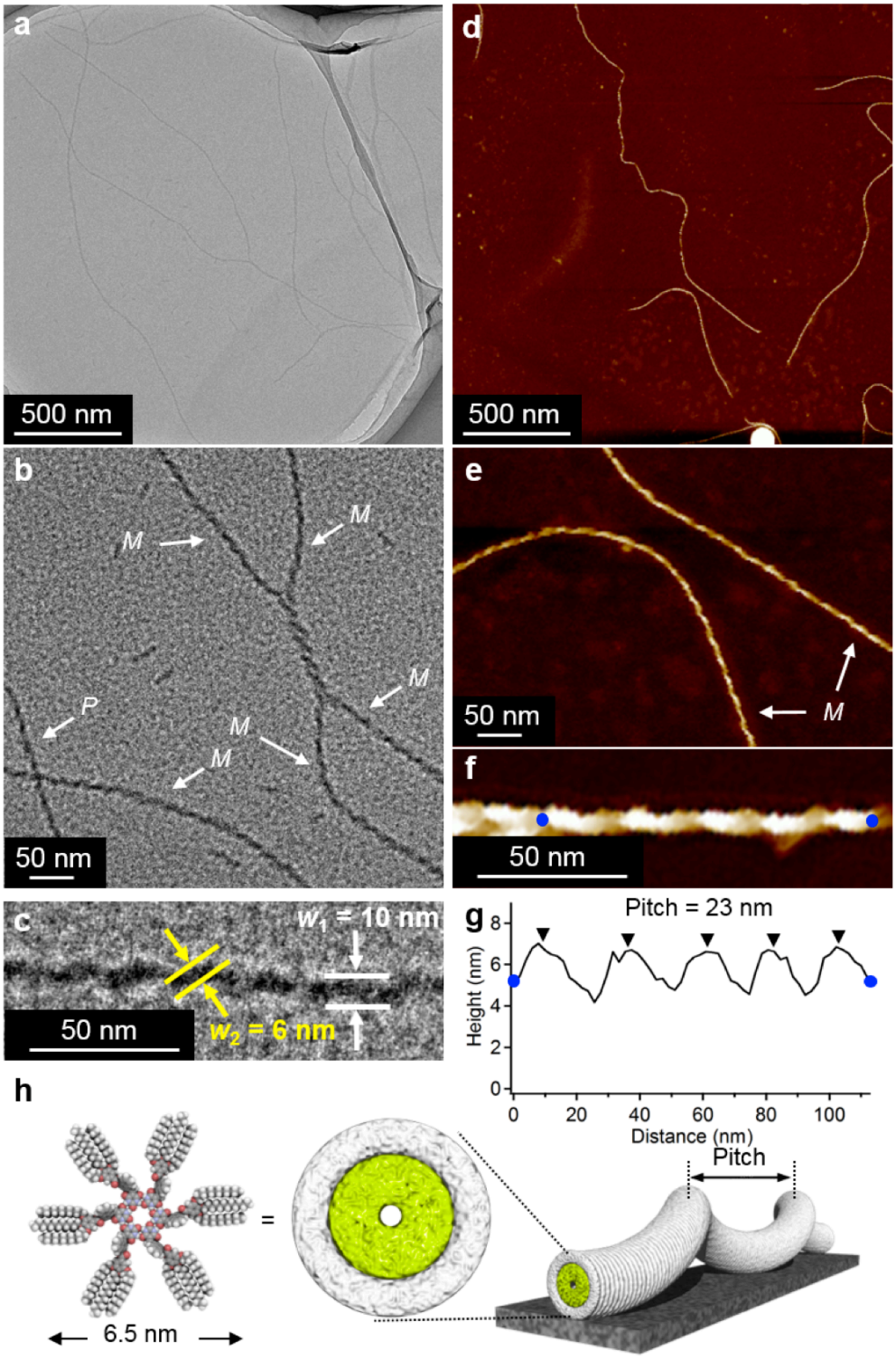

Figure 2-11. (a–f) TEM images (a–c) and AFM height images (d–f) of **SP_2**, spin-coated from MCH solutions (c = 50 μM, T = 293 K) onto carbon-coated copper grid (TEM) or HOPG (AFM). (g) AFM cross-sectional analysis of **SP_2** between blue dots in (f). (h) Cartoon illustration of **SP_2** on substrate.

2-6. XRD Analysis of Supramolecular Polymers of 1 and 2

The distinct nanostructures of $\mathbf{SP_1}$ and $\mathbf{SP_2}$ provide the different macroscopic properties of their MCH solutions at higher concentrations (c > 1 mM). For **1**, an unstable MCH suspension was attained by cooling its hot solution to 293 K (Figure 2-12a), which finally precipitated within ca. 1 h. The X-ray diffraction (XRD) measurement of the suspension (c = 5 mM, T = 293 K) enclosed in a glass capillary showed a sharp and intense peak (d-spacing = 5.19 nm), which was accompanied by other weak peaks (d-spacing = 3.00, 2.59, 1.95, and 1.72 nm) (Figure 2-12b). These peaks could be assigned to diffractions from the (100), (110), (200), (210) and (300) planes, respectively, of a two-dimensional (2D) hexagonal columnar packing structure with a lattice parameter a = 5.98 nm. AFM imaging of the dried suspension displayed densely packed cylindrical $\mathbf{SP_1}$ fibers (Figure 2-12c).

In sharp contrast, a transparent MCH gel was obtained from **2** within ca. 10 min upon cooling its hot solution to 293 K (Figure 2-13d). The XRD profile of the gel (c = 5 mM, T = 293 K) showed only two broad peaks (d-spacing = 9.64 nm, 5.52 nm) (Figure 2-12e). These peaks are in line with the width of the helical twisting (w_1 in Figure 2-11c) and the primary columnar structure (w_2 in Figure 2-11c) as analyzed in the TEM image of $\mathbf{SP_2}$ fibers, respectively. On the basis of these results, the two peaks may correspond to the helical structure in $\mathbf{SP_2}$ fibers. AFM images of the dried gel *i.e.* xerogel displayed entangled network of helical fibers, which is contrastive with highly bundled $\mathbf{SP_1}$ fibers (Figure 2-12c).

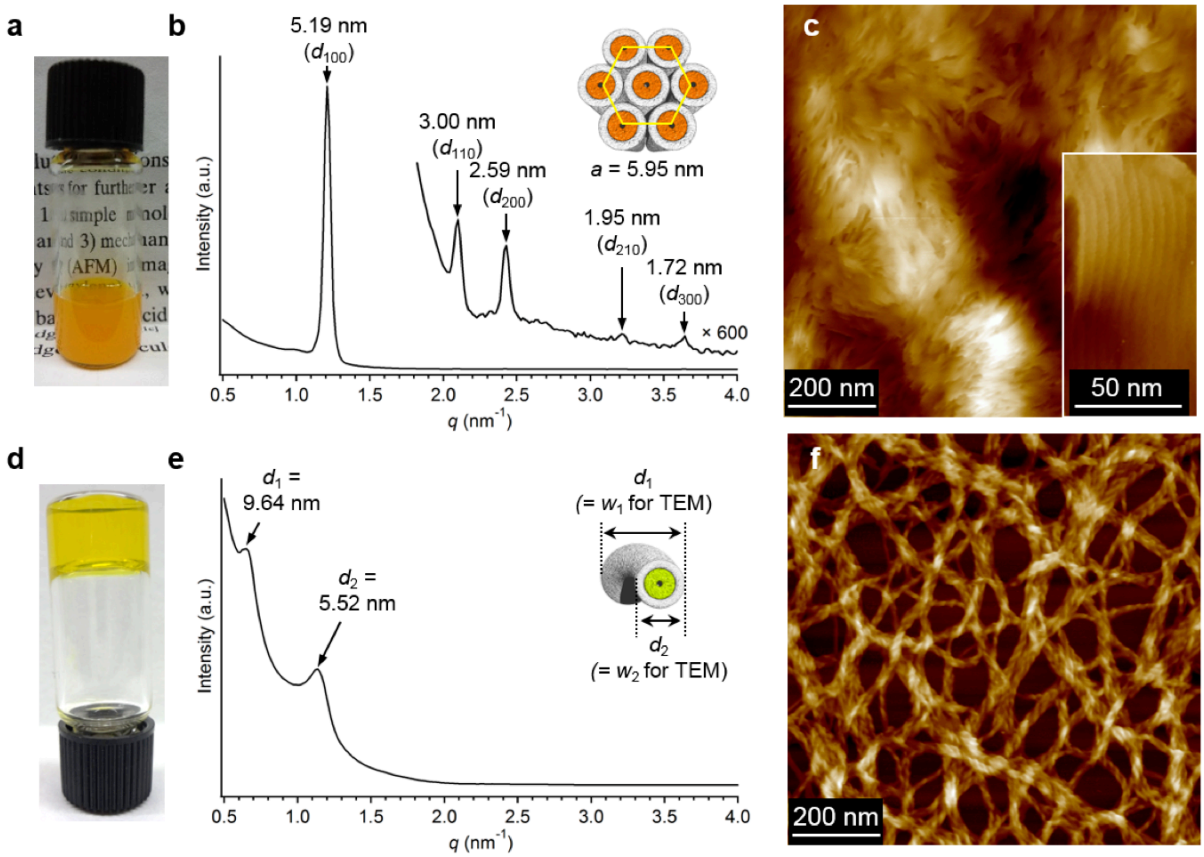

Figure 2-12. (a,d) Photographs of a MCH suspension of **SP$_1$** (a) and a MCH gel of **SP$_2$** (d). (b,e) XRD patterns of the suspension of **SP$_1$** (b) and the gel of **SP$_2$** (e) in MCH (c = 5 mM, T = 293 K) with schematic representation of these **SP** fibers in this state. (c,f) AFM height images of concentrated **SP$_1$** (c) and **SP$_2$** (f) spin-coated from their MCH suspension (**1**, c = 1 mM) or gel (**2**, c = 1 mM) onto HOPG. Inset in (c) indicates a magnified AFM image.

2-7. Analysis of Internal order in Supramolecular Polymers

To understand how a subtle difference in the monomer structures can be amplified to notable differences in properties of one-dimensional nanofibers, the molecular packing structures of **SP$_1$** and **SP$_2$** were analyzed by using two-dimensional X-ray diffraction (2D XRD) measurement of oriented samples. Upon heating, powders of **1** and **2** became fluidal as a result of formation of liquid crystalline mesophases (T = 135–139 °C for **1**[12d], 55–148 °C for **2**) as measured by polarized optical microscopy (POM) and differential scanning calorimetry (DSC) (Figure 2-13). Mechanical shearing of the mesophases on sapphire substrates resulted in a thin film oriented anisotropically along the sheared direction (Figure 2-14 and Figure 2-15a).

The sheared **SP$_1$** film of **1** showed XRD peaks possessing several *d*-spacings (4.80, 2.43, 1.81, 1.38, 1.10, 1.05, 0.96 and 0.92 nm) and other small peaks (Figure 2-15b,c). These eight peaks could be assigned to diffractions from (100), (200), (210), (220), (320), (410), (500) and (330) planes, respectively, corresponding to 2D hexagonal columnar packing structure with a = 5.52 nm. This attribution is based on the XRD analysis of powder sample of **1** (Figure 2-16). The 2D XRD image exhibited diffraction arcs assignable to the 2D intercolumnar ordering on the equatorial direction, which is indicative of the successful alignment of **SP$_1$** (Figure 2-15b,d). On the meridional direction, a diffracted arc possessing *d*-spacing of 0.37 nm was detected (Figure 2-15d), which corresponds to the cofacial distance between one-dimensionally stacked rosettes (Figure 2-17c). Furthermore, two sets of four-split diffraction spots having *d*-spacing of 0.78 and 1.05 nm were detected in the non-equatorial and non-meridional directions, respectively (Figure 2-15d). Azimuthal plots at each diffraction indicated that these diffractions are tilted by 62° and 51°, respectively, relative to the meridional direction (Figure 2-18). The emergence of such tilted diffraction spots is typical of the helical intracolumnar order.[25] The observation of two helical periodicities indicates the a bilayered helical wrapping in columns by TDP benzene rings (*d*-spacing = 1.05 nm) and naphthalene units (*d*-spacing = 0.78 nm) as

shown in Figure 2-17a–d. Taking into account the C_6 symmetrical structure of the rosette, a full turn helical pitch in **SP$_1$** could be estimated to be ca. 10 nm.[26,27]

Moreover, two sets of four-split diffraction arcs possessing *d*-spacing of 0.35 and 0.45 nm were detected with an almost same tilting angle of 24° relative to the meridional direction (Figure 2-15d). The two arcs are ascribable to a cofacial distance between helically arranged TDP and naphthalene moieties, respectively (Figure 2-17c).[25b] This result suggests that these two aromatic units adopt a coplanar placement to construct a watermill-shaped rosette of **1** (Figure 2-1). A rotational displacement of the watermill-rosettes prevents naphthalene units from perfect face-to-face (H-type) stacking, which is in line with the emergence of the red-shifted UV/vis absorption bands as minor components (Figure 2-6a). A good correlation between the spectroscopic and the structural information is a direct result of the high degree of internal order in **SP$_1$** fibers.

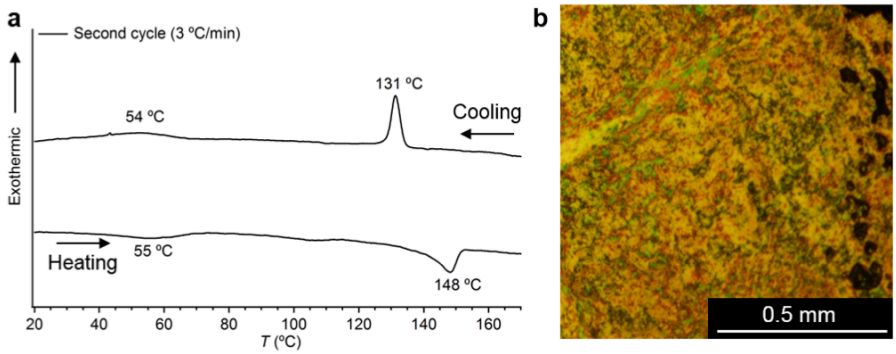

Figure 2-13. (a) DSC profile of **2** during the second heating and cooling scans at 3 °C/min. (b) POM image of mesophase of **2** at 140 °C in the heating process.

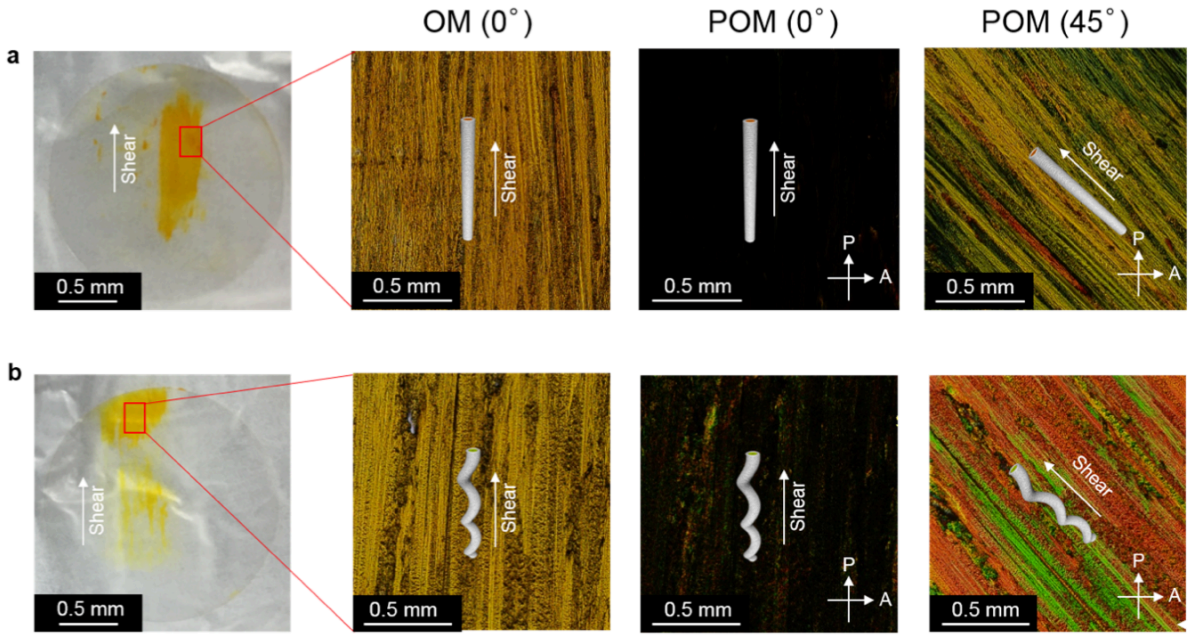

Figure 2-14. Photographs, optical micrographs (OMs) and polarized optical micrographs (POMs) of a film sample composed of 1D orientated **SP** fibers of **1** (a) and **2** (b) on sapphire substrates. The directions of polarizer (P) and analyzer (A) are shown by arrows.

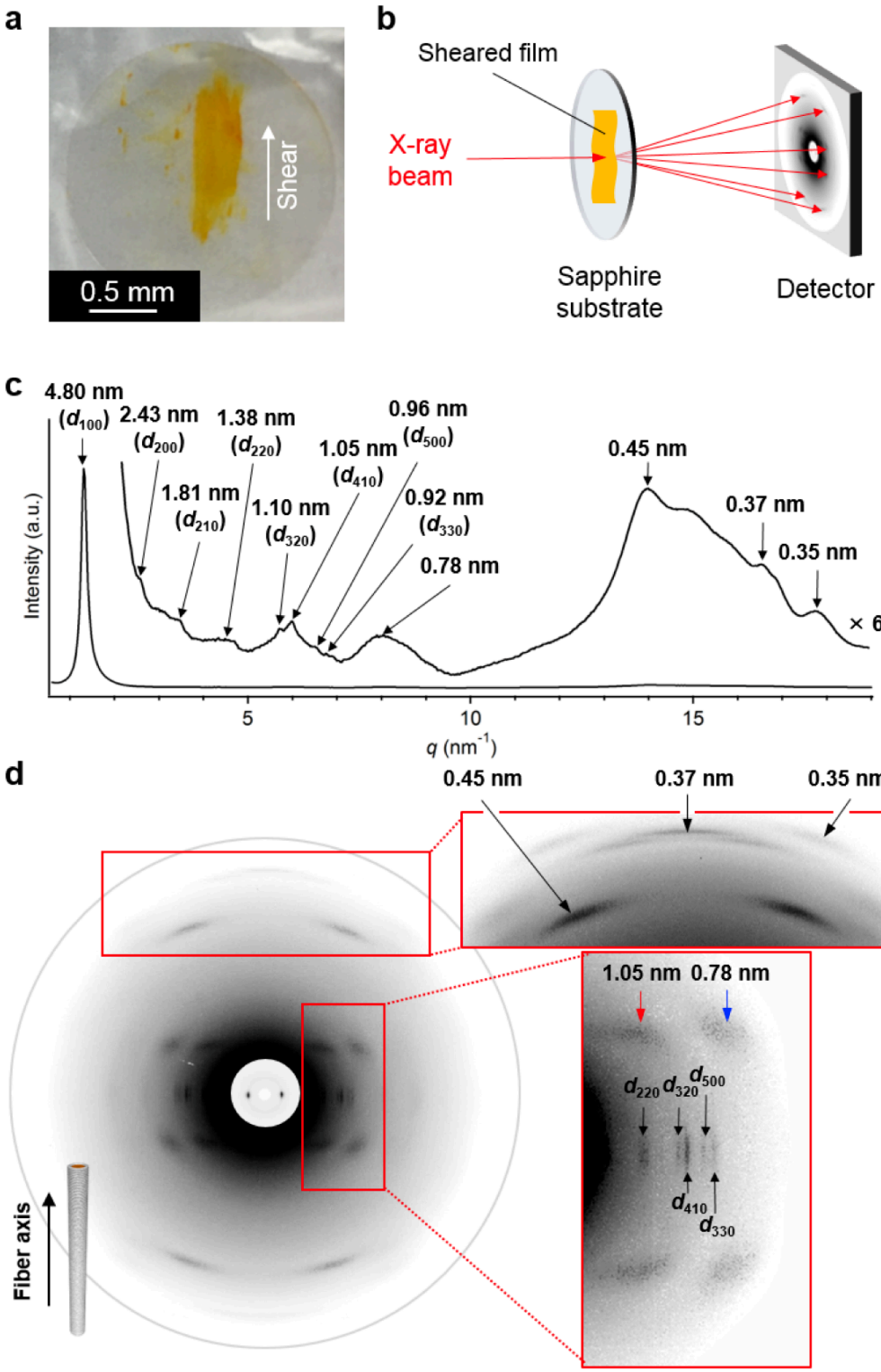

Figure 2-15. (a) Photograph of the macroscopic sheared film of **1** on sapphire. (b) Schematic representation of the experimental setup for the through-view 2D XRD measurement. (c) XRD pattern of sheared $\mathbf{SP_1}$ film, measured at 293 K. (d) 2D XRD images, measured at 293 K, of sheared $\mathbf{SP_1}$ film with magnified images.

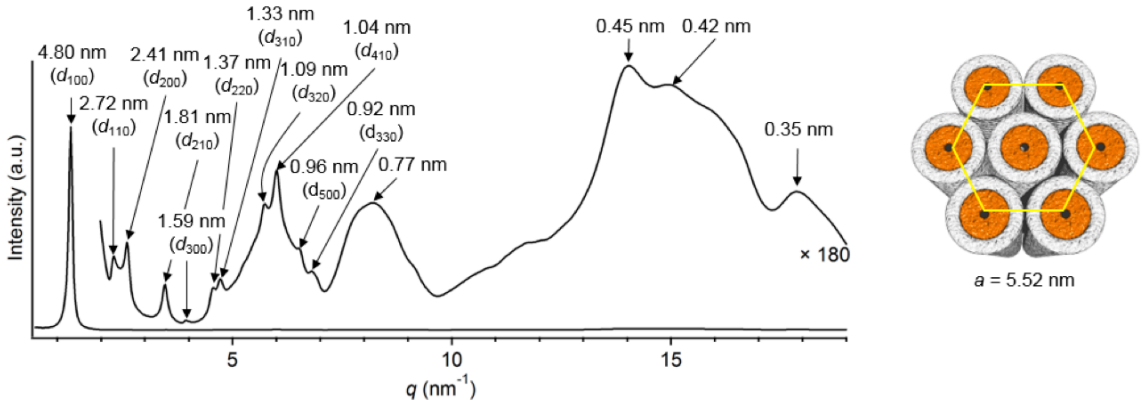

Figure 2-16. XRD patterns of a bulk sample of **1** at 293 K. Insets represent the corresponding hexagonal packing structure.

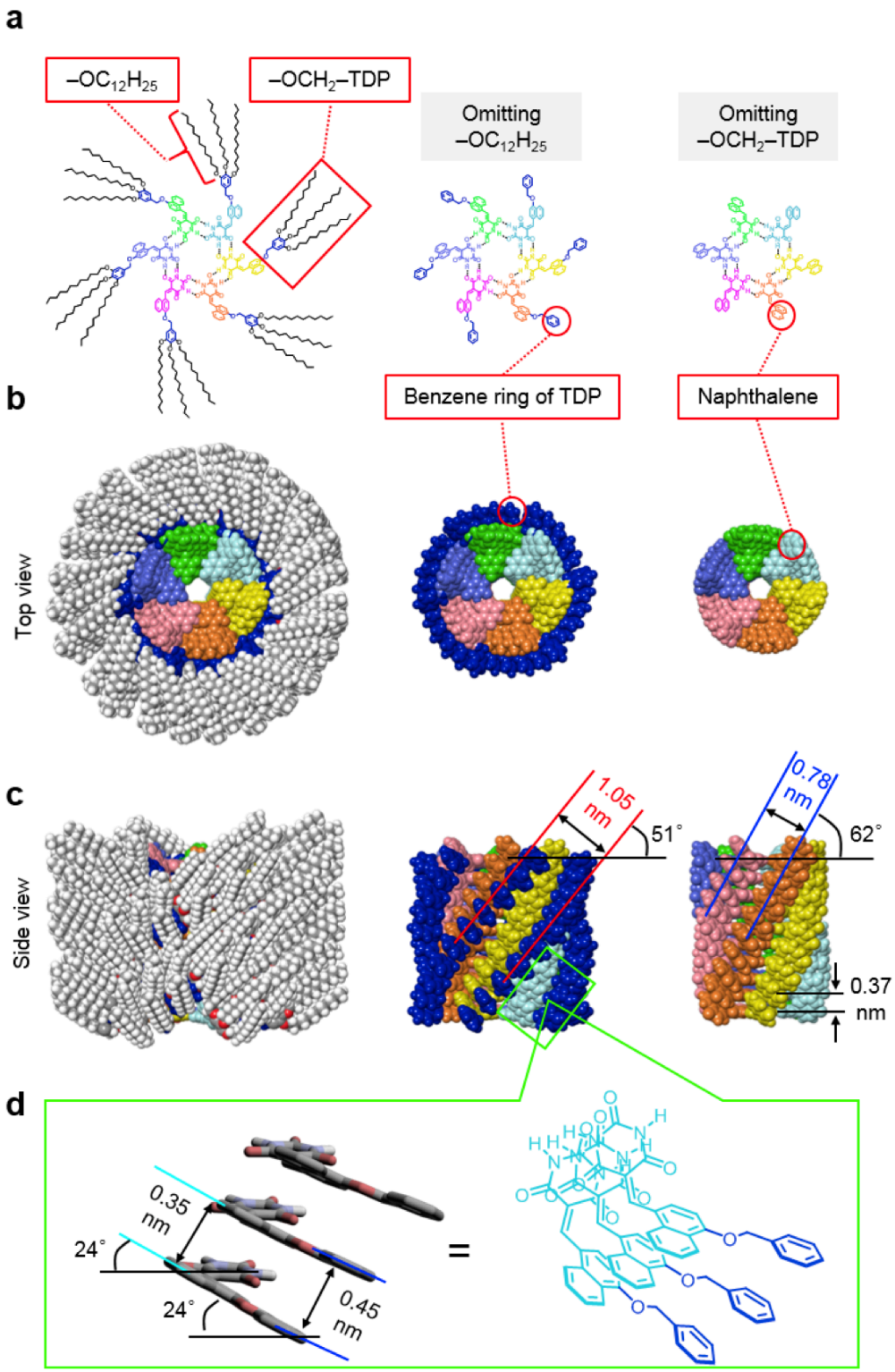

Figure 2-17. (a–d) Schematic illustration of chemical structure of hexameric rosettes of **1** (a) and stacking arrangements of **1** in $\mathbf{SP_1}$ (b–d). (b) indicates top views using space-filling models. (c) indicates side views using space-filling models. (d) Schematic representation of the intramolecular arrangement of **1** in $\mathbf{SP_1}$. In this figure, right-handed helical structures are described.

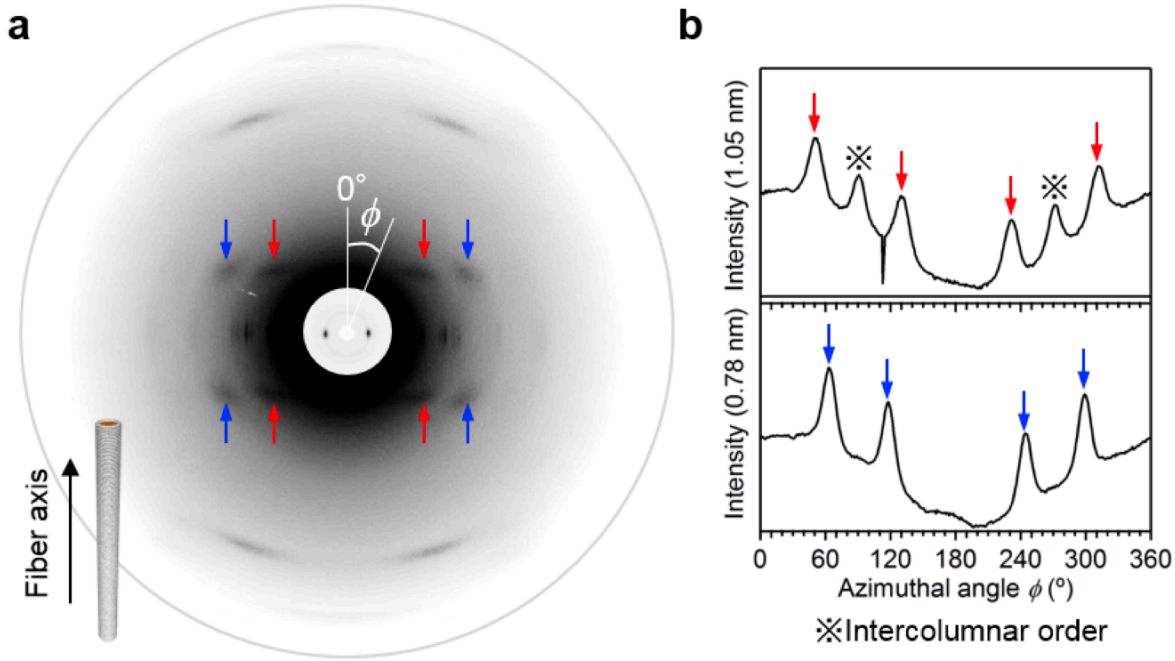

Figure 2-18. (a) 2D XRD images of sheared $\mathbf{SP_1}$ films of **1**. (b) Azimuthal plots for the 2D XRD intensities of the sheared films at given *d*-spacings as a function of azimuthal angle (ϕ).

The sheared film of **2** showed several XRD peaks (*d*-spacing = 4.80, 1.50, 1.03, 0.75, 0.57, 0.41, 0.38 nm) as shown in Figure 2-19a–c. The first intense peak (4.80 nm) could be assigned to the diameter of $\mathbf{SP_2}$ fibers formed by offset stacking of rosettes of **2**, whereas the others broad peaks (1.50 to 0.57 nm) might suggest the presence of periodicities corresponding to a helical structure (Figure 2-19c). The 2D XRD image showed the presence of a helical intracolumnar order (Figure 2-19d and Figure 2-20). The helical pitch was calculated to be ca. 11 nm[27], which is nearly half of that of helically undulated $\mathbf{SP_2}$ (23 nm) observed by TEM and AFM (Figure 2-11g). This finding demonstrates that the internal helical order (primary order) in $\mathbf{SP_2}$ is not comparable to the visualized helical nanostructure (secondary order). In wider angle region, a diffraction arc (*d*-spacing = 0.41 nm, tilting angle = 27° relative to the meridional direction) was detected (Figure 2-19d and Figure 2-21). This diffraction is assignable to a cofacial distance between helically arranged naphthalene moieties (Figure 2-20d). Moreover, another diffraction arc corresponding to a cofacial distance between arranged TDP moieties was detected with *d*-spacing of 0.46 nm, but in the meridional direction in contrast to the case of **1** (Figure 2-19d). This is an important difference in the packing structure of **1** (Figure 2-16d). Accordingly, the TDP moieties in $\mathbf{SP_2}$ adopt the coplanar orientation relative to the rosette plane—this rosette closely resembles a windmill (Figure 2-20d and see Figure 2-1).

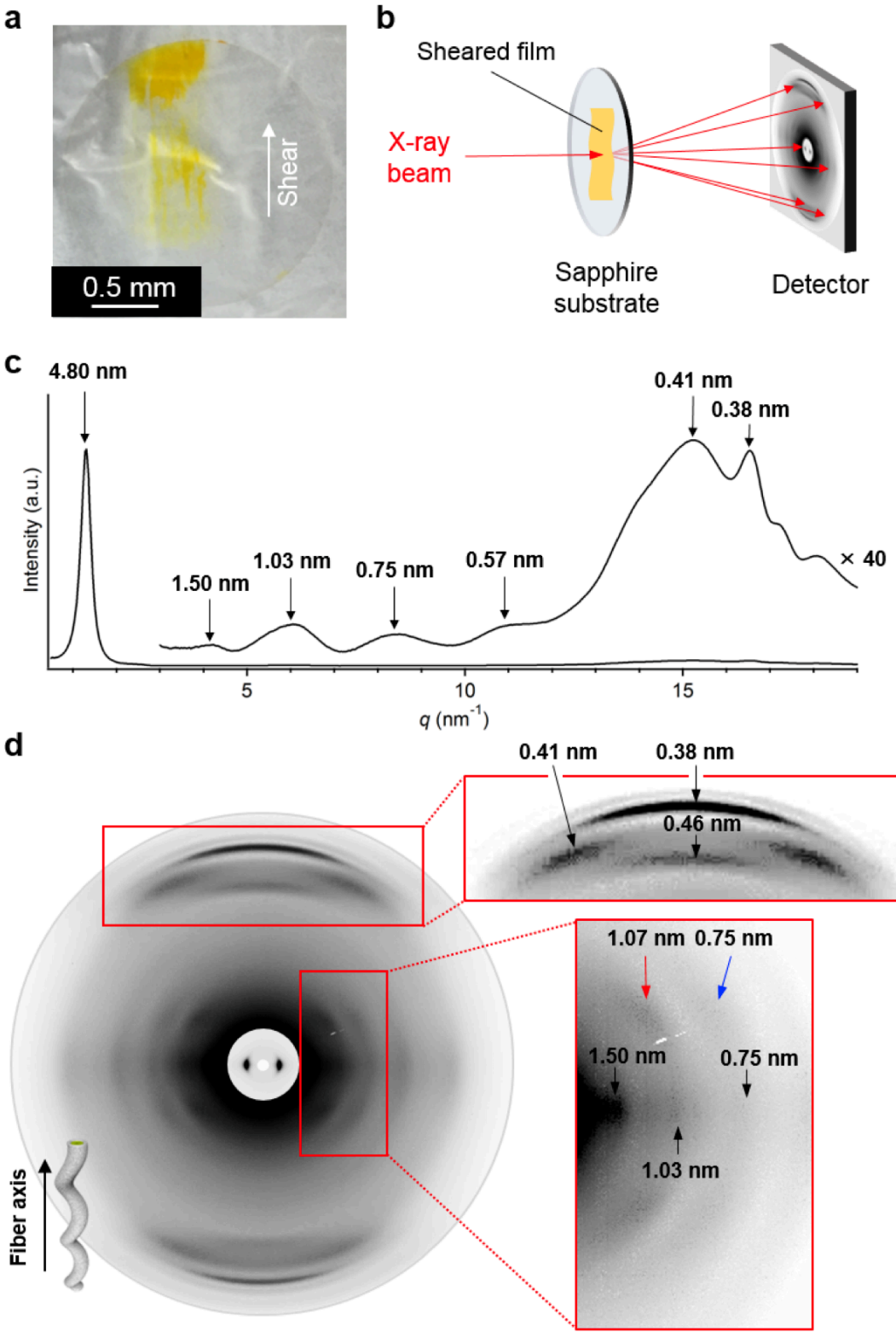

Figure 2-19. (a) Photograph of the macroscopic sheared film of **2** on sapphire. (b) Schematic representation of the experimental setup for the through-view 2D XRD measurement. (c) XRD pattern of sheared $\mathbf{SP_2}$ film, measured at 293 K. (d) 2D XRD images, measured at 293 K, of sheared $\mathbf{SP_2}$ film with magnified images.

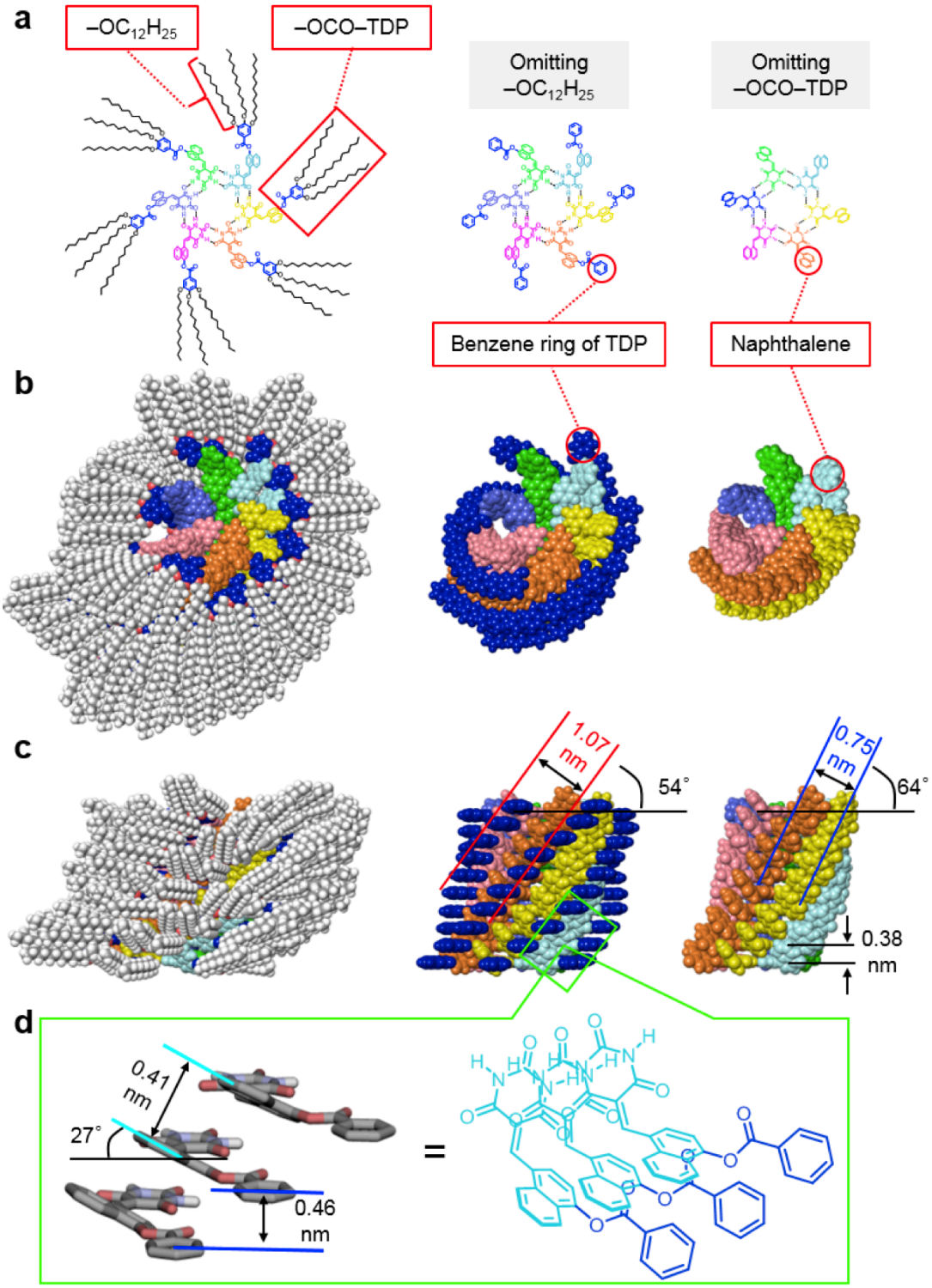

Figure 2-20. (a–d) Schematic illustration of chemical structure of hexameric rosettes of **2** (a) and stacking arrangements of **2** in $\mathbf{SP_2}$ (b–d). (b) indicates top views using space-filling models. (c) indicates side views using space-filling models. (d) Schematic representation of the intramolecular arrangement of **2** in $\mathbf{SP_2}$. In this figure, right-handed helical structures are described.

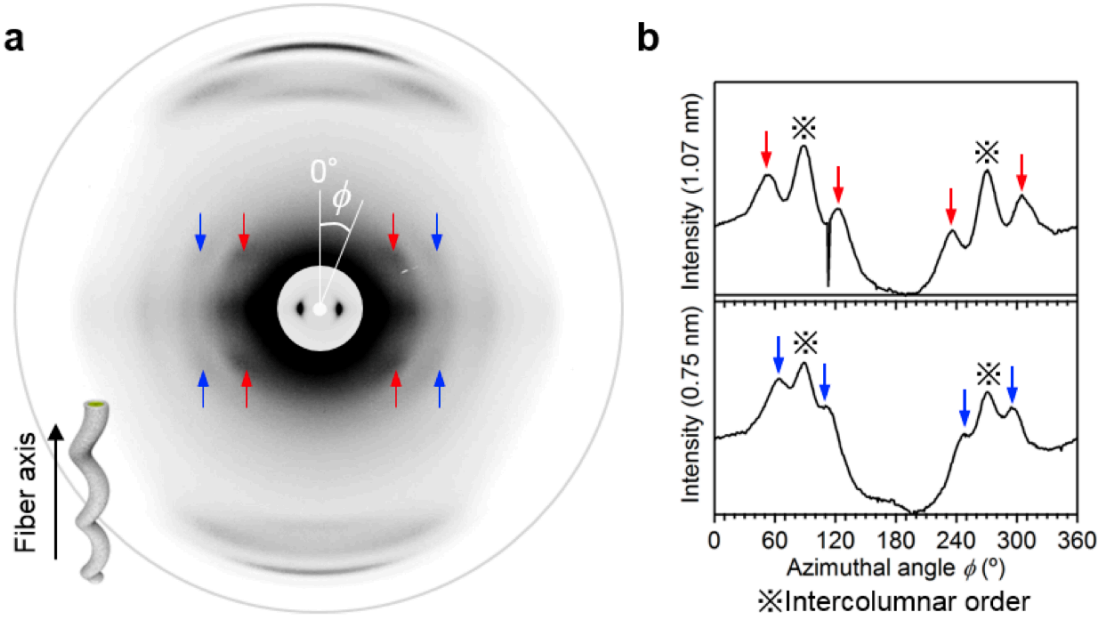

Figure 2-21. (a) 2D XRD images of sheared films of **2**. (b) Azimuthal plots for the 2D XRD intensities of sheared films of **2** at given *d*-spacings as a function of azimuthal angle (ϕ).

2-8. Supramolecular Polymerization Processes

Taking into consideration the involvement of hexameric macrocyclization and the subsequent stacking of the resulting rosettes into **SP** with the high degrees of internal order, supramolecular polymerizations of **1** and **2** are expected to undergo a cooperative process.[5] Thus, supramolecular polymerization processes of the two compounds were investigated by monitoring the change in absorption intensities upon cooling their hot MCH solutions (c = 50 μM, T = 353 K) at a slow cooling-rate of 0.1 K min^{-1} (Figure 2-23a,b). As displayed by degree of aggregation (α)[28] against temperature (353–293 K), a non-sigmoidal change of fully monomeric to aggregated state was found for both compounds with the almost same elongation temperature T_e' (ca. 319 K for **1**, ca. 318 K for **2**). Although these changes are characteristic of the nucleated cooperative (nucleation–elongation) supramolecular polymerization mechanism,[5a,5c] the subsequent heating processes of the cooled solutions (293 K) at a rate of 0.1 K min^{-1} showed the disassembly processes whose trajectories shifted toward higher temperature region. Indeed, when the solutions of both compounds were maintained at T_e' after cooling (353 K $\rightarrow$ T_e'), the spectrum displayed a time-course transition to show increase in α ($\Delta\alpha$ = 0.31 for **1**, 0.16 for **2**; see Figure 2-24). This finding indicates that the supramolecular polymerization processes attained by cooling is controlled kinetically. Hence, the subsequent heating (depolymerization) processes exhibited thermal hystereses (Figure 2-23a,b).[29,30] The apparently larger hysteresis detected in **1** indicates that its supramolecular polymerization process is controlled more kinetically in comparison with that of **2**.

When the non-sigmoidal curves, which is characteristic of the cooperative mechanism, in the heating processes of **1** and **2** were compared, the cooperativity of **1** was found to be apparently lower than that of **2** (Figure 2-22a,b). This finding is counterintuitive, because the higher level of cooperativity in the supramolecular polymerization of **1** compared to **2** was

expected from more noticeable kinetic control of the former compared with the latter. Moreover, the heating curve of **1** was remarkably shifted to higher temperature region relative to that of **2**, which is indicative of superior thermal stability of $\mathbf{SP_1}$ compared to $\mathbf{SP_2}$ (Figure 2-22a,b). Thus, it can be assumed that secondary interaction such as bundling of **SP** fibers, which is more noticeable in $\mathbf{SP_1}$ than in $\mathbf{SP_2}$ (Figure 2-10 and Figure 2-11), affect the depolymerization process of **1**. Reflecting this assumption, a heating curve with higher degree of cooperativity was attained at the lower concentration of **1** (20 μM), and the degree of the thermal hysteresis considerably decreased (Figure 2-24a,b). Assuming that the heating processes of **1** and **2** (c = 20 μM) were monitored under thermodynamic control, the experimentally obtained curves were analyzed with the cooperative theoretical models developed by the research group of E. W. Meijer (Figure 2-24a,b and see the General Methods in Chapter 1-7 for details).[5a] Based on these analyses, I could calculate the enthalpy difference in the elongation process (ΔH_e). A well-defined difference in ΔH_e was noticed between **1** (−98.0 kJ mol^{-1}) and **2** (−47.4 kJ mol^{-1}), demonstrating stronger cohesive force of **1** than of **2**.

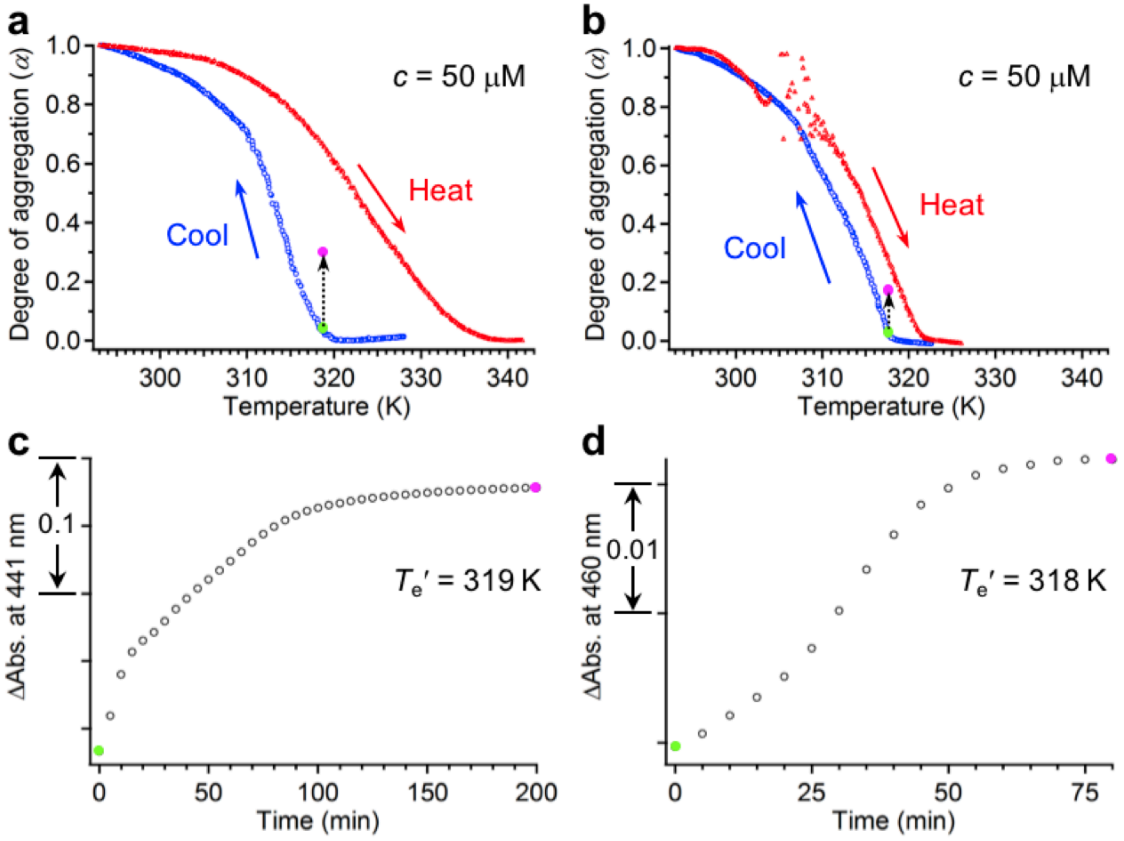

Figure 2-22. (a–d) Temperature-dependent degree of aggregation (α) of **1** (a) and **2** (b) in MCH at c = 50 μM against the temperature in the cooling (blue curves) and heating (red curves) processes at a rate of 0.1 K min^{-1}. Monitoring wavelengths of **1** and **2** are 441 and 460 nm, respectively.

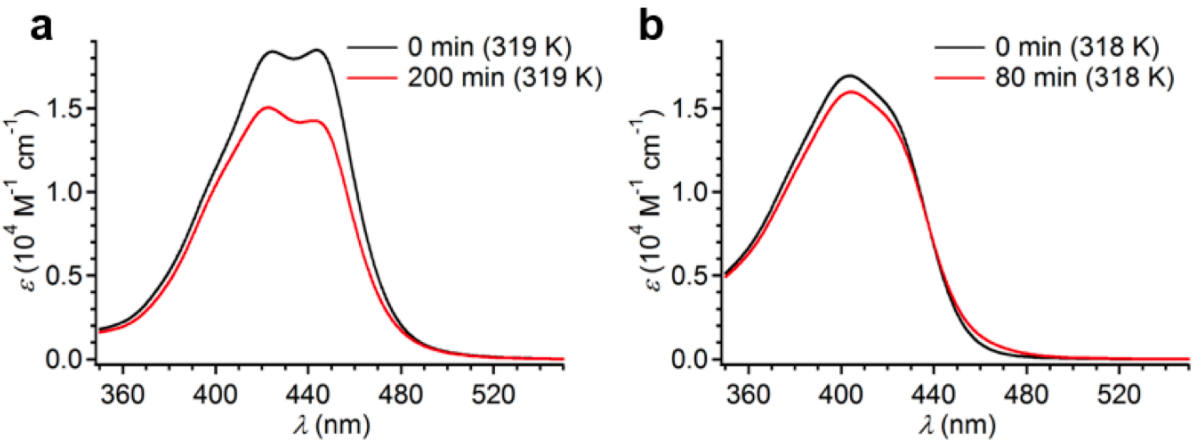

Figure 2-23. Time change of UV/vis absorption spectra of **1** (a) and **2** (b) in MCH (c = 50 μM) upon standing the solution at given T_e' (319 K for **1**, 318 K for **2**) after cooling to the T_e' at heating-rate of 0.1 K min^{-1}.

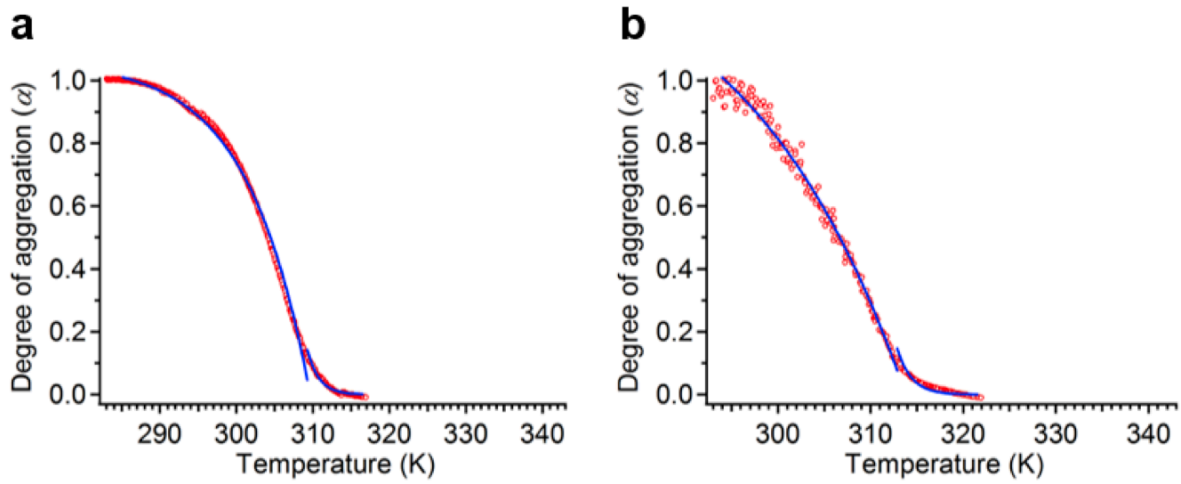

Figure 2-24. Degree of aggregation (α) of **1** (a) and **2** (b) (c = 20 μM) at the given wavelength (441 nm for **1**, 460 nm for **2**) as a function of the temperature in heating (red curves) processes at a rate of 0.1 K min^{-1}. Solid blue curves indicate fitting traces based on a cooperative theoretical model.

2-9. Pathway Complexity in Supramolecular Polymers

To further study different kinetics of the supramolecular polymerization of **1** and **2**, a quenching experiment of their hot monomeric solutions was conducted.[7c,29] When a 3 mL hot MCH solution (c = 50 μM, T = 353 K) was quenched by using ice-bath, the solution temperature rapidly went down to 293 K in 10 s. The time course UV/vis spectral measurements revealed that only compound **1** with ether linkage shows the presence of remarkable kinetic trap, though the measurement temperature was sufficiently lower than the T_e' (319 K).[29] The UV/vis spectrum of **1** measured just after quenching (t = 1 min) exhibited λ_{max} at 425 nm with two shoulders at ca. 450 nm and ca. 500 nm (Figure 2-25a). Because the absorption of quenched solution is not consistent with that of monomer solution (c = 3 μM) measured at 293 K (Figure 2-25b), **1** may be kinetically trapped to provide π–π stacked aggregates. The less hypsochromically shifted absorption bands indicate the presence of aggregates possessing more slipped stacking between the naphthalene chromophores compared with those in $\mathbf{SP_1}$. When excitation at 413 nm, which is an isosbestic point detected for the following time course UV/vis spectral change (Figure 2-25a), a weak but non-trivial emission was observed at 578 nm (Figure 2-25c). The excitation spectrum with λ_{max} = 434 nm was close to the absorption spectrum with λ_{max} = 425 nm, indicating that the emission derives from the kinetically trapped aggregates (Figure 2-25d). AFM analysis showed the formation of ill-defined aggregates by quenching (referred to as $\mathbf{Agg_1}$, Figure 2-26a–c). These aggregates were slowly transformed into $\mathbf{SP_1}$ over 40 min as observed by time-dependent absorption and emission as well as DLS measurements (Figure 2-25a,c,e,f). The AFM analysis at t = 10 min already showed the presence of a minor amount of short nanofiber and at t = 40 min agglomerated $\mathbf{SP_1}$ fibers were observed (Figure 2-26d–i). In comparison to $\mathbf{SP_1}$ formed by very slow cooling at a rate of 0.1 K min^{-1} (Figure 2-27), apparently shorter $\mathbf{SP_1}$ fibers are formed by quenching which is presumably due to higher frequency of the nucleation. A noteworthy point here is that the half-life period ($t_{0.5}$) of the

kinetically formed aggregates became longer by elevating the total concentration of **1** (Figure 2-28). The finding indicates that the trapped aggregates are off-pathway intermediates.[7d,31] Moreover, the $t_{0.5}$ value of the kinetically formed species became longer with lowering temperature (Figure 2-29). This temperature-dependence is contrast to a perylene bisimide self-assembly system reported by the research group of F. Würthner, where the supramolecular polymerization of sleeping monomers, trapped through intramolecular hydrogen bonds, can be facilitated by decreasing temperature.[28] In the present system, not only supramolecular polymers $\mathbf{SP_1}$ but also off-pathway aggregate $\mathbf{Agg_1}$ are stabilized together by decreasing temperature. At 281 K, the UV/vis spectral change become adequately slow to disclose the sigmoidal transition, which is feature of an autocatalytic mechanism including nucleation and elongation processes (Figure 2-29d).[32]

In sharp contrast, the ester compound **2** showed no arguable kinetic effect in the quenching experiments even by changing conditions such as concentration and temperature (Figure 2-30 and Figure 2-31). The quenched solution (c = 50 μM, T = 293 K) at t = 1 min already showed the absorption and emission spectra of $\mathbf{SP_2}$ (Figure 2-30a,c) though morphologies of aggregates are immature as shown by AFM (Figure 2-31a,b). At t = 10 min, a large amount of $\mathbf{SP_2}$ was confirmed by DLS and AFM (Figure 2-30d and Figure 2-31c,d). These results suggest that kinetic trap of compound **2** is too shallow to be detected spectroscopically under applied experimental conditions and accordingly the monomers can immediately supramolecularly polymerize into thermodynamically stable $\mathbf{SP_2}$.

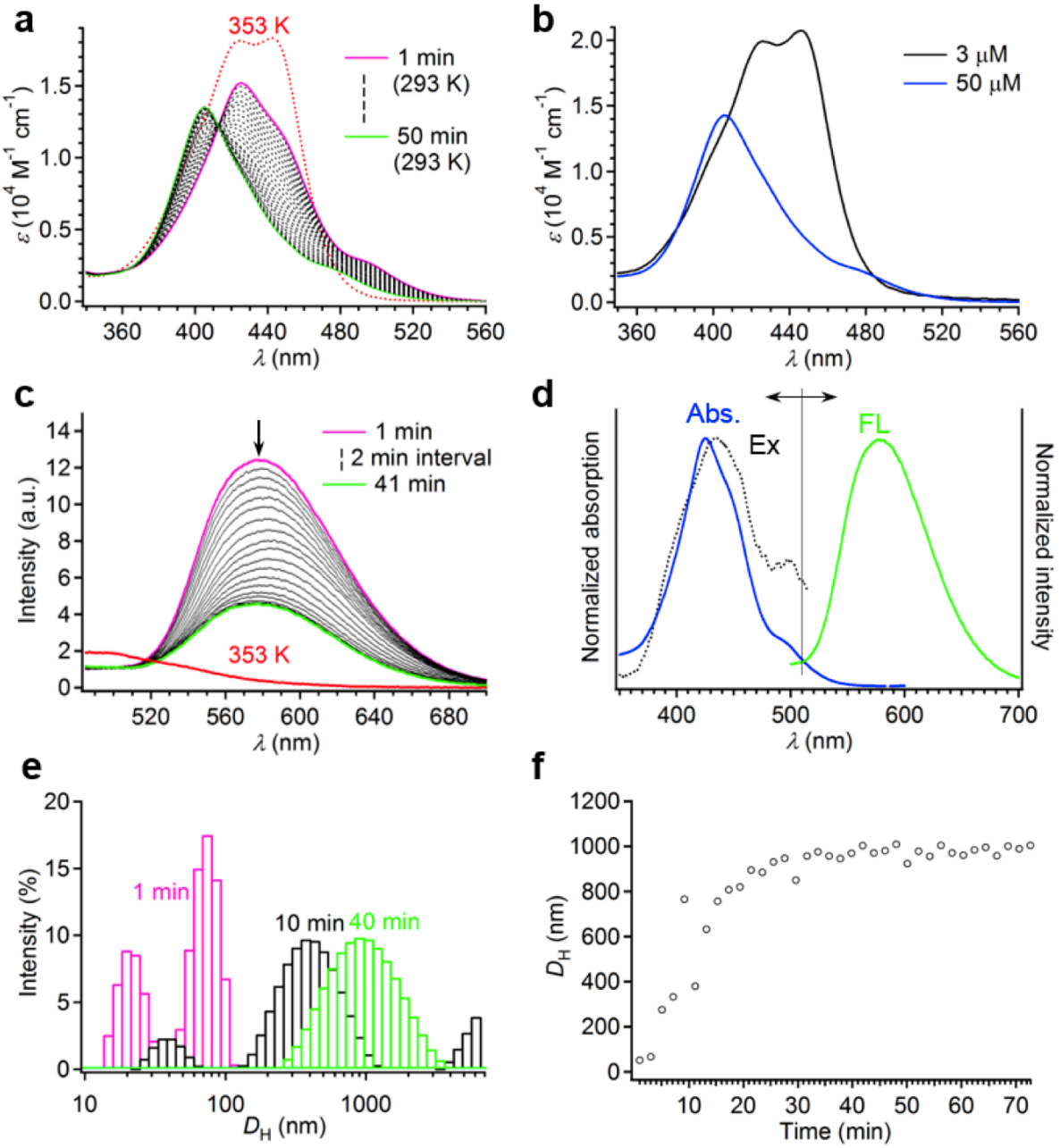

Figure 2-25. (a) Time change of UV/vis absorption spectra of **1** in MCH (c = 50 μM, T = 293 K) detected after quenching from 353 to 293 K. (b) UV/vis spectra of **1** in MCH at 293K at two different concentrations (c = 3 and 50 μM). (c) Time change of FL spectra of quenched MCH solution of **1** (c = 50 μM) at 293 K. (d) Normalized absorption, excitation (λ_{em} = 578 nm) and FL (λ_{ex} = 413 nm) spectra of quenched MCH solution of **1** (c = 50 μM) at 293 K. (e) DLS-derived size distribution of the quenched species of **1** (c = 50 μM) in MCH at t = 1, 10 and 40 min. (f) Plot of the DLS-derived average hydrodynamic diameter (D_H) of the quenched species of **1** (c = 50 μM) in MCH against the time.

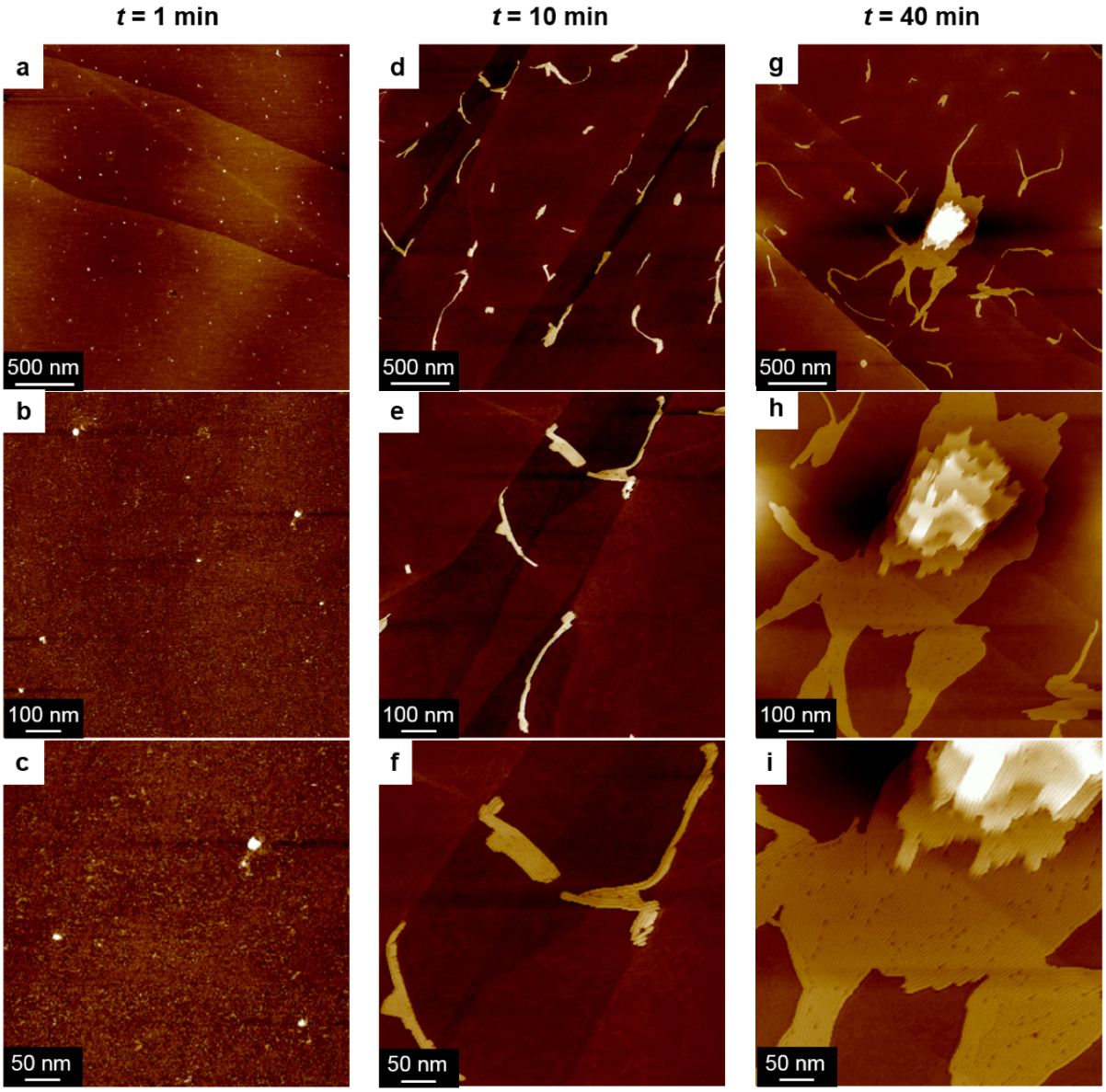

Figure 2-26. (a–i) AFM height images of time-dependent morphologies formed by quenching the hot MCH solution of **1** (c = 50 μM, T = 353 K). Samples were prepared by spin-coating the quenched solutions at 293 K after t = 1 (a–c), 10 (d–f), 40 min (g–i), onto HOPG.

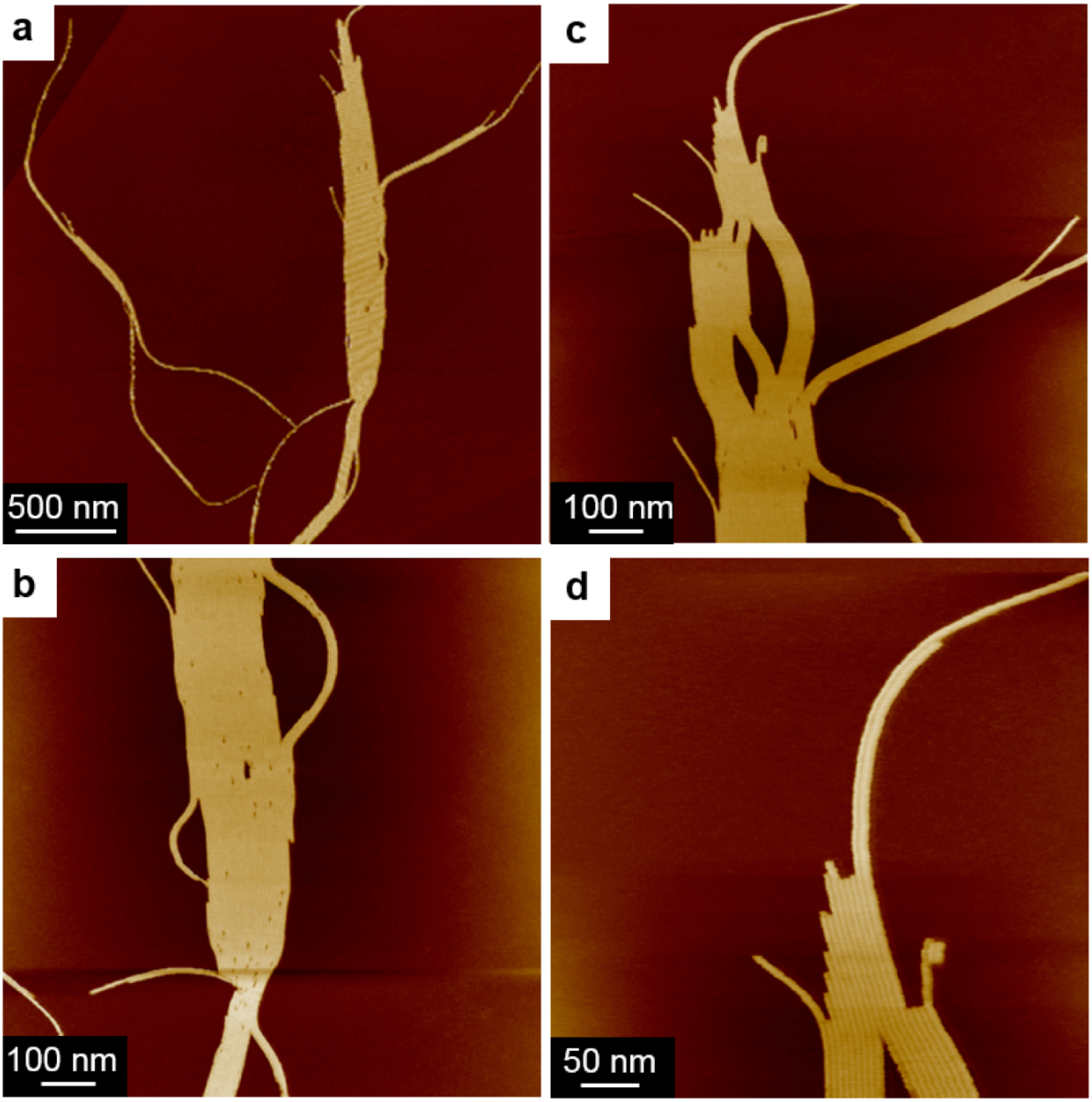

Figure 2-27. (a–d) AFM height images of $\mathbf{SP_1}$ formed by very slow-cooling a hot MCH solution of **1** (c = 50 μM, T = 353 K) at a rate of 0.1 K min^{-1}. Samples were prepared by spin-coating the MCH solutions onto HOPG.

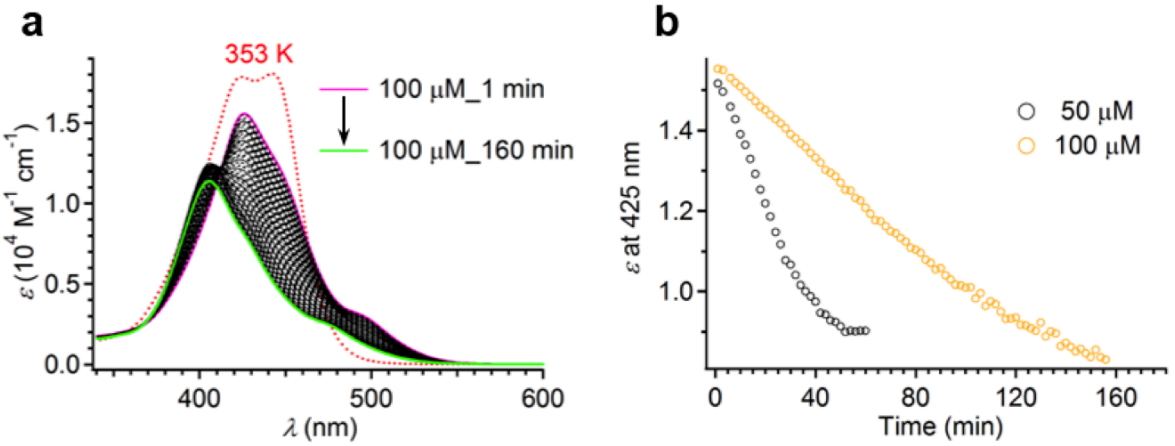

Figure 2-28. (a) Time change of UV/vis spectra of **1** in MCH (c = 100 μM, T = 293 K) detected after quenching from 353 to 293 K. (b) Time course changes in ε values of quenched **1** in MCH at c = 50 and 100 μM.

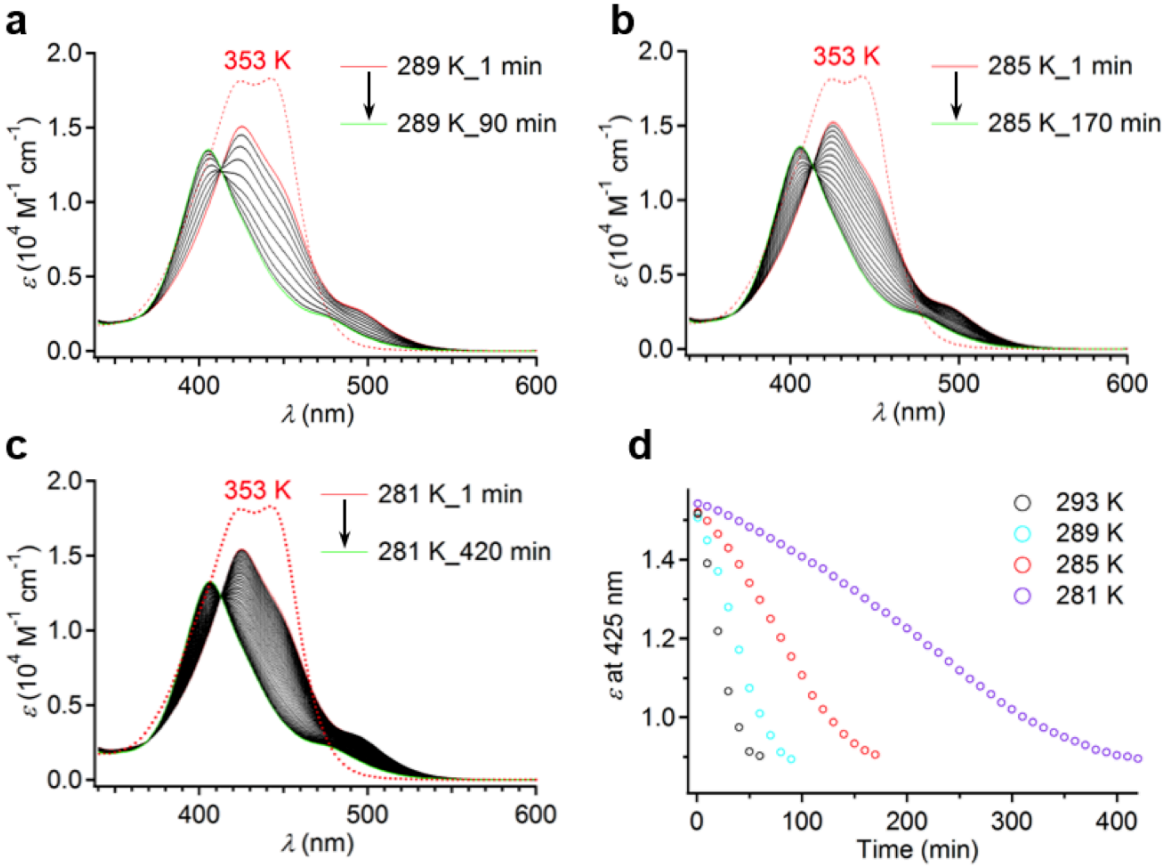

Figure 2-29. (a–c) Time change of UV/vis spectra of **1** in MCH (c = 50 μM) detected after quenching from 353 to 293 K at different keeping temperatures (T = 289, 285, 281 K). (d) Plots of time changes in ε values of quenched MCH solution of **1** (c = 50 μM) at the different keeping temperatures.

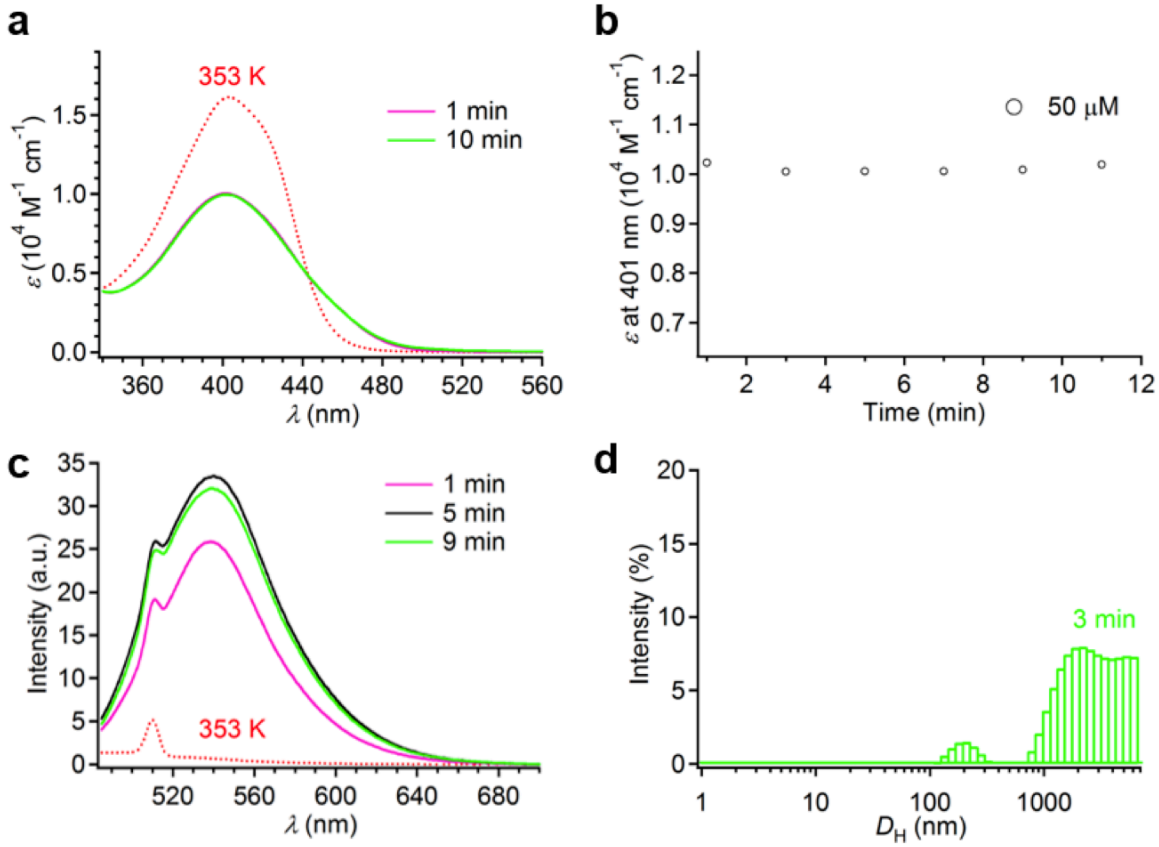

Figure 2-30. (a,b) Time changes of UV/vis (a) and FL (c) spectra of MCH solution of **2** (c = 50 μM, T = 293 K) detected after quenching from 353 to 293 K. (b) Plots of ε at 401 nm as a function of time. (d) DLS-derived size distribution of aggregates in quenched MCH solutions at t = 3 min (c = 50 μM) of **2** at 293 K.

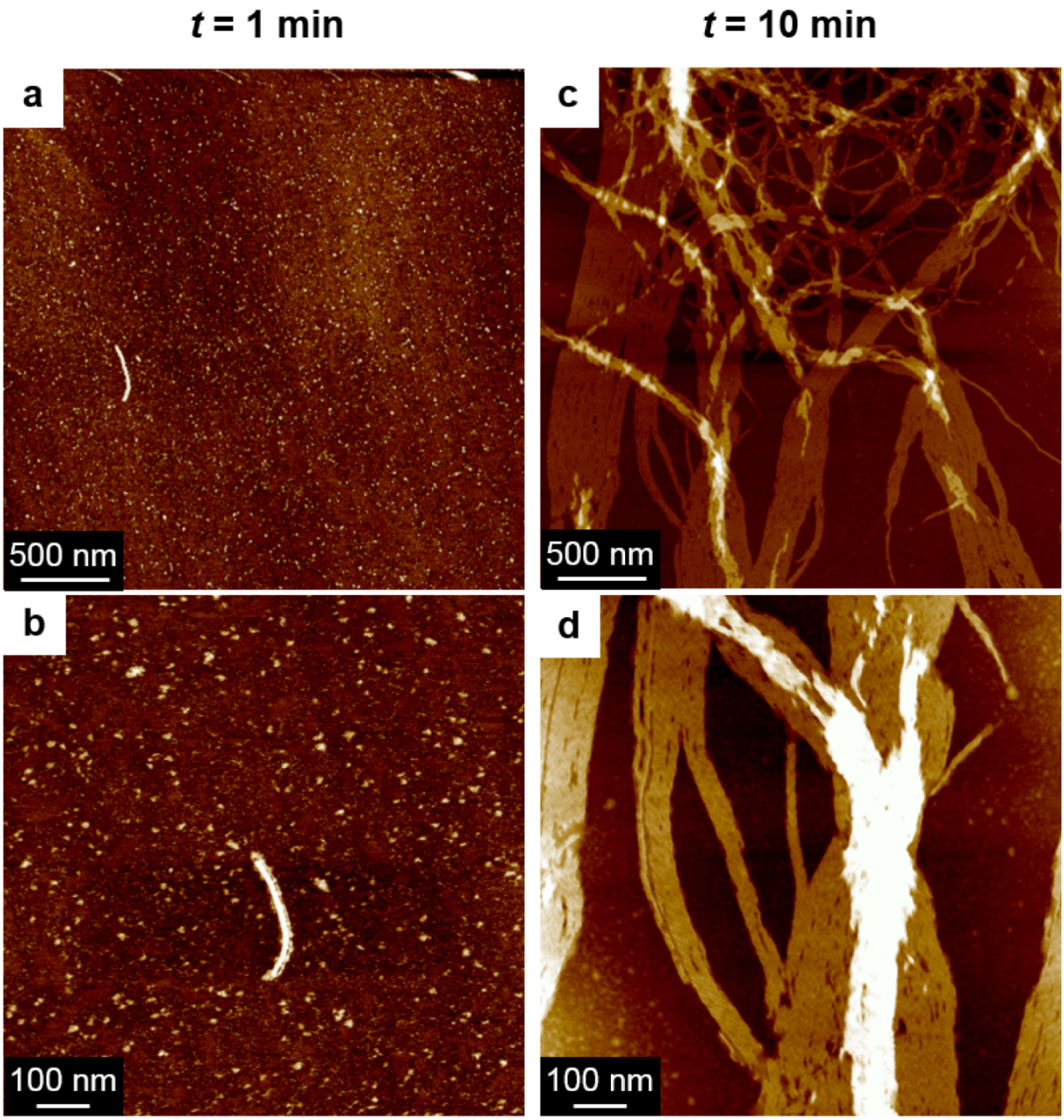

Figure 2-31. (a–d) AFM height images of quenched aggregates of **2** at t = 1 (a,b) and 10 min (c,d). Samples were prepared by spin-coating the quenched MCH solutions (t = 1 and 10 min, c = 50 μM) at 293 K onto HOPG.

2-10. Discussion

In this section, relation between molecular structures and supramolecular polymerization processes of **1** and **2** is discussed. On the basis of scanning tunneling microscopic (STM) analysis and various crystal structures of barbituric acid molecules reported so far,[15,33] **1** and **2** may form polydisperse open-ended oligomers (so-called tapes) via multiple hydrogen bonding. However, the DLS, VPO and NMR measurements in $CHCl_3$ have concluded that both compounds preferentially form hexameric rosettes.

In apolar MCH, in which π–π interaction as well as hydrogen-bonding arises effectively, these rosettes cannot exist as discrete species at ambient condition and thereby stack immediately into supramolecular polymers as shown by the spectroscopic and microscopic analyses. On the basis of these findings, the formation of hydrogen-bonded tapes during the supramolecular polymerization can be disregarded, and would not be a major factor for the pathway complexity observed only for **1**. Furthermore, one should take into account the formation of diverse geometrical rosette isomers, interconversion of which gives rise to breakage of hydrogen-bonds (Figure 2-32)[34]. The high levels of internal order in the $\mathbf{SP_1}$ and $\mathbf{SP_2}$ as shown by 2D XRD analysis suggest that component molecules are packed in the supramolecular polymers with specific rosette isomers. If the formation of diverse rosette isomers comes into play in the supramolecular polymerization processes, one should have observed the pathway complexity for both **1** and **2**. Thus, the fact that the pathway complexity was detected only for **1** indicates that the origin of kinetic effect should be considered apart from the formation of competing hydrogen-bonded species.

The 2D XRD results showed that the packing structures of the two compounds in the **SP** differ chiefly in the conformation of the TDP moieties (Figure 2-17d and Figure 2-20d). For **1**, the TDP plane is coplanar to the naphthalene plane and orient orthogonally to the rosette

planes while in the case of **2** this TDP unit is twisted against the naphthalene unit and thereby arranges in the direction parallel to the rosette planes (Figure 2-17d and Figure 2-20d). When the molecular structures of **1** and **2** were geometrically optimized by molecular mechanics calculation, it was found that these molecules have a global minimum geometry when the TDP planes are twisted relative to the naphthalene planes (Figure 2-33a,b). Thus, for **1**, a large conformational alteration of the TDP moieties should occur to attain the high levels of internal order upon aggregation. In contrast, the molecular conformation of **2** is very similar to that found in $\mathbf{SP_2}$ because a coplanar structure of the TDP–naphthalene moieties is not allowed as a result of the steric repulsion of carbonyl oxygen of the ester linkage and the protons on the naphthalene ring (Figure 2-33c,d). Furthermore, the entropic penalty of **1** for this geometrical restriction is expected to be large, considering the conformational freedom of the TDP moieties.

A different entropic contribution in the aggregation processes of **1** and **2** was revealed by cooling studies at several concentrations (Figure 2-34). Upon lowering concentration, the T_e' value became lower for both compounds. The plots of natural logarithm of the concentrations against reciprocal T_e' (namely van't Hoff plot[35]) exhibited a linear relationship for both compounds (Figure 2-34c,d), from which the standard enthalpy difference (ΔH°) and the entropy difference (ΔS°) in aggregation were estimated to be $\Delta H° = -80.7$ kJ mol^{-1} and $\Delta S° = -0.173$ kJ mol^{-1} K^{-1} for **1**, and $\Delta H° = -69.3$ kJ mol^{-1} and $\Delta S° = -0.138$ kJ mol^{-1} K^{-1} for **2** (Table 2-1). The larger value of $\Delta S°$ for **1** indicates the larger entropic penalty upon supramolecular polymerization. Therefore, a higher energetic barrier to on-pathway aggregation is expected for **1**, which promotes the generation of off-pathway ill-defined aggregates ($\mathbf{Agg_1}$) via the inhomogeneous stacking of rosettes without watermill conformation (Figure 2-34e), as revealed by the less blue-shifted UV/vis absorption band of the kinetically formed species (Figure 2-25a). Once $\mathbf{SP_1}$ cylindrical nanofiber forms and accumulates, they can be further stabilized through interchain interactions such as bundling. In contrast, the

conformational rigidity of the ester-wedge-linked **2** does not allow the formation of off-pathway intermediate in the supramolecular polymerization process, and then the resulting **SP$_2$** nanofiber is less susceptible to interchain associations reflecting its helical morphology (Figure 2-34f).

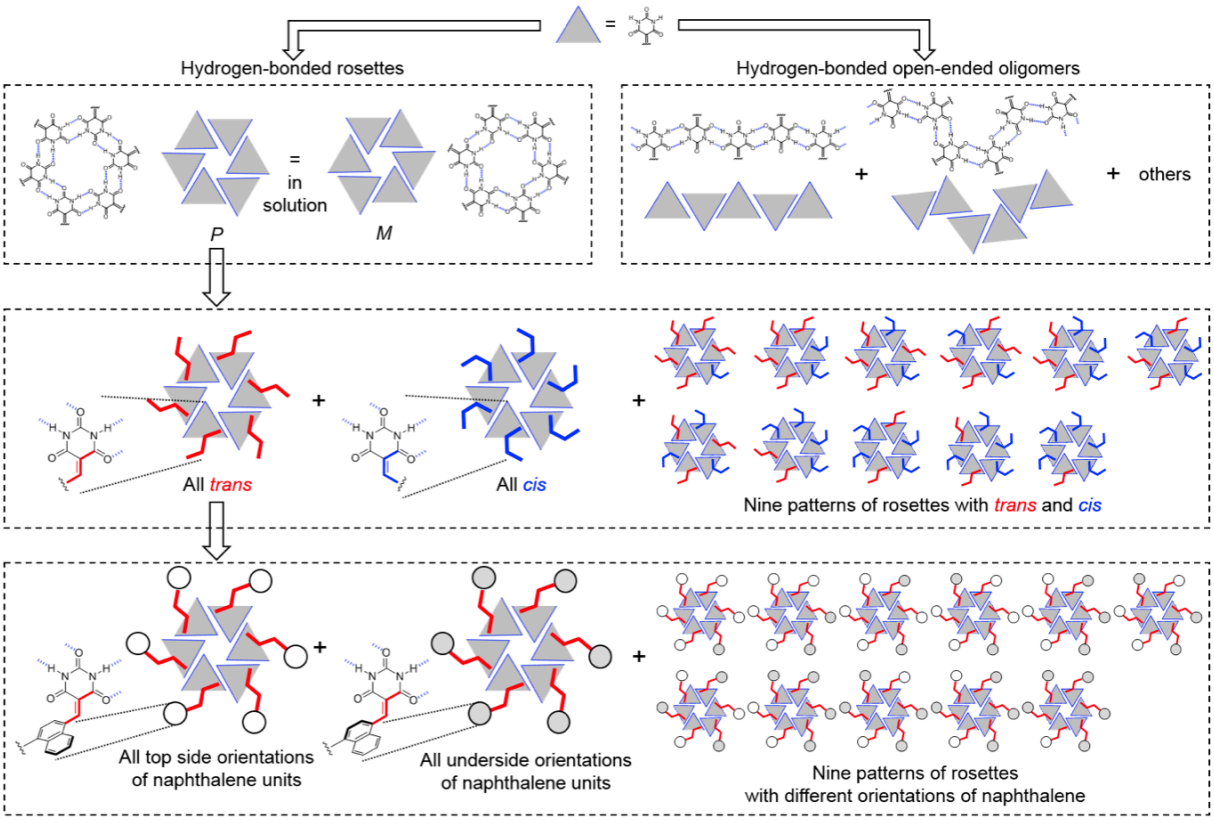

Figure 2-32. Schematic illustration of possible geometries of hydrogen-bonded rosettes.

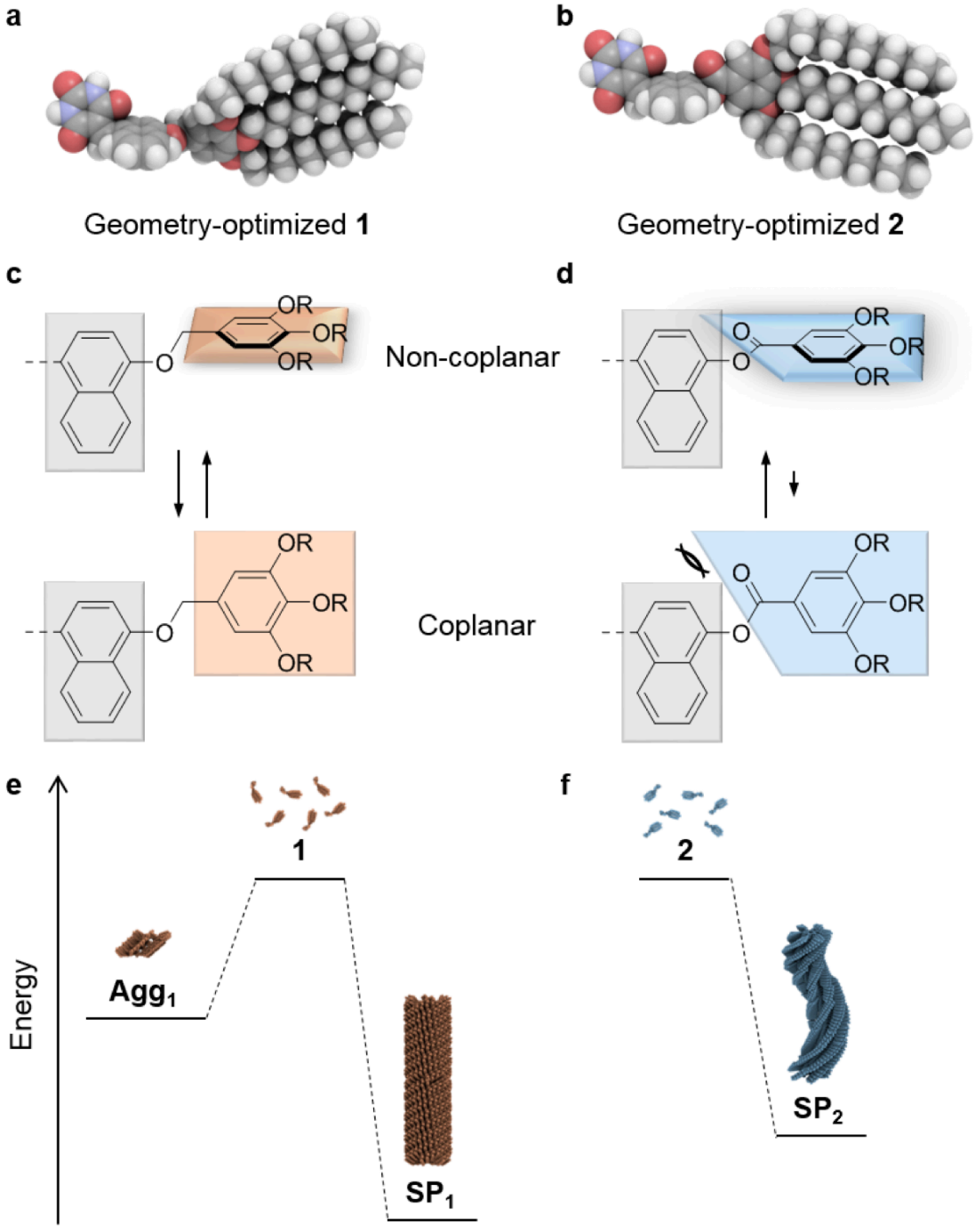

Figure 2-33. (a,b) Geometry optimized molecular structures of monomers of **1** (a) and **2** (b). (c,d) Possible geometries of TDP units of **1** (c) and **2** (d) relative to naphthalene units. (e,f) Energy diagrams for supramolecular aggregations of **1** (e) and **2** (f).

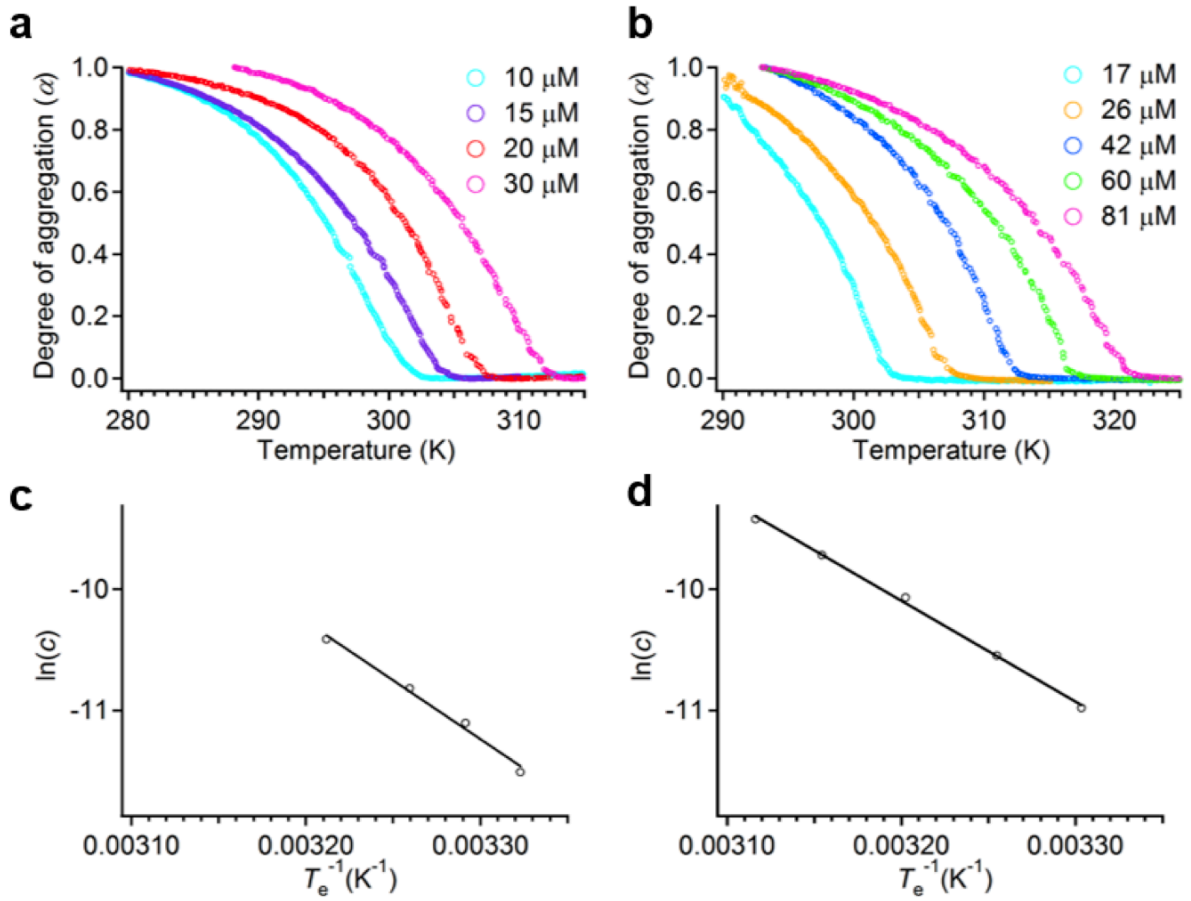

Figure 2-34. (a,b) Degree of aggregation (α) of **1** (a) and **2** (b) in MCH at different concentrations against the temperature in the cooling processes at a rate of 1.0 K min^{-1}. (c,d) van't Hoff plots of natural logarithm of the concentration (c) of **1** (c) and **2** (d) in MCH ag the reciprocal against critical temperature (T_e), which are attained from cooling data. These plots indicate linear relationship.

	$\Delta H°$ (kJ mol^{-1})	$\Delta S°$ (J mol^{-1}K^{-1})	$\Delta G°$ (kJ mol^{-1}) at 298 K	K_e (M^{-1}) at 298 K
1	−80.7	−173.0	−29.2	1.3×10^5
2	−69.3	−137.8	−28.2	8.8×10^4

Table 2-1. Thermodynamic parameters attained from the analysis of van't Hoff plots of **1** and **2** in Figure 2-34.

2-11. Conclusion

Details of two supramolecular polymers that are hierarchically organized from hydrogen-bonding naphthalene molecules via the formation of hexameric supermacrocycles (rosettes) have been revealed. The spectroscopic and probe microscopic studies showed that a tiny structural difference in their monomer structure, *i.e.*, whether the naphthalene unit and aliphatic wedge moiety are connected through an ether or ester group, leads to significant differences in stacking arrangements of the aromatic unit (H-type versus J-type), as well as morphologies of one-dimensional nanofibers (cylindrical versus helical). Although both monomeric building blocks were found to be packed in the supramolecular polymers possessing high levels of internal order, as shown by the X-ray diffraction studies, conformations of the aliphatic wedges differ significantly between the two molecules due to difference in the degree of their conformational freedom. Thus, the ether compound **1** undergoes a larger conformational alteration upon aggregation, whereas in the case of the ester compound **2** the monomer structure is almost maintained upon aggregation. This difference was clearly reflected in pathway complexity observed in quenching experiments, which has been prominently observed only for the ether compound. The findings exhibit a prominent merit of supramolecular macrocyclization of functional molecules, that is, a subtle difference in monomer structures can be transferred to a critical difference of internal molecular ordering of the one-dimensional fibers. Because supramolecular polymers are supposed to be used in concentrated solution state and the bulk state, physical properties, derived from these condensed materials like polymers, might be important, which could be engineered by a subtle tuning the internal order, as mentioned in this study by the different gelation properties as well as mesomorphic temperatures.

2-12. Synthesis and Characterization

Compound **2** was prepared according to Synthetic scheme 2-1.

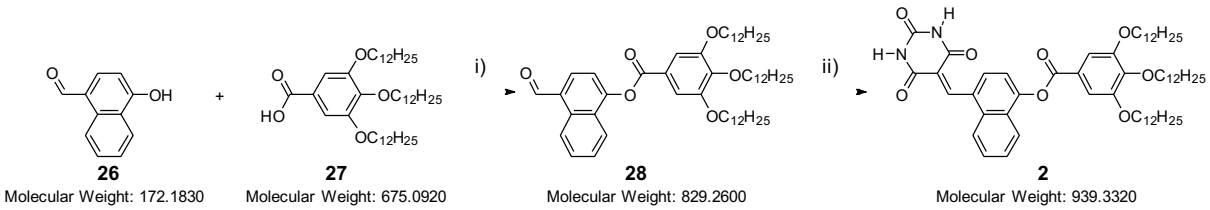

Synthetic scheme 2-1. Synthetic scheme of **2**. i) DCC, DMAP, CH_2Cl_2, room temperature; ii) barbituric acid, EtOH, reflux.

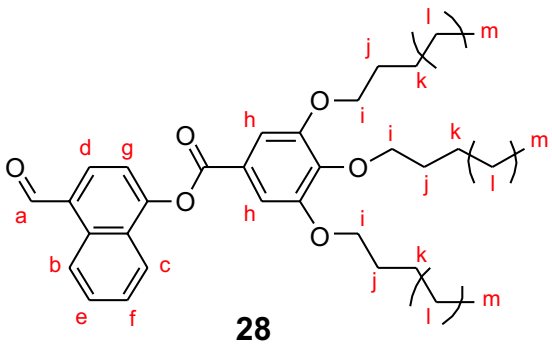

Synthesis of compound 28: Compound **26** (235 mg, 1.37 mmol), compound **27** (935 mg, 1.37 mmol) and *N,N*-dimethyl-4-aminopyridine (DMAP, 16 mg, 0.13 mmol) were dissolved in dry CH_2Cl_2 (10 mL). A solution of *N,N'*-dicyclohexylcarbodiimide (DCC, 282 mg, 1.37 mmol) in dry CH_2Cl_2 (5 mL) was added dropwise at 0 °C, and the mixture was stirred for 24 h at room temperature under N_2 atmosphere. After the resulting white precipitates were filtered off, the filtrate was diluted with $CHCl_3$ and washed with water and brine. The organic layer separated was dried over Na_2SO_4 and then evaporated to dryness under a reduced pressure. The resulting solid was purified by column chromatography over silica gel ($CHCl_3$) to give pure compound **28** as a white solid (866 mg, 76% yield).

^{1}H NMR (500 MHz, $CDCl_3$, 298 K): δ (ppm) 10.39 (1H, s, Ar-CH_aO), 9.34 (1H, d, J = 8.6 Hz, Ar-H_b), 8.06 (2H, d, J = 7.9 Hz, Ar-$H_{c,d}$), 7.74 (1H, ddd, J = 8.6, 7.0, 0.9 Hz, Ar-H_e), 7.62 (1H, ddd, J = 8.6, 7.0, 0.9 Hz, Ar-H_f), 7.53 (1H, d, J = 7.7 Hz, Ar-H_g), 7.53 (2H, s, Ar-H_h), 4.12–4.06 (6H, m, Ar-OCH_i), 1.88–1.76 (6H, m, CH_j), 1.54–1.47 (6H, m, CH_k), 1.39–1.25 (48H, m, CH_l), 0.90–0.86 (9H, m, CH_m).

^{13}C NMR (125 MHz, $CDCl_3$, 298 K): δ (ppm) 192.73, 164.56, 153.31, 152.34, 143.69, 137.19, 132.21, 129.79, 129.60, 127.64, 127.50, 125.37, 123.12, 121.98, 117.79, 108.88, 73.81, 69.48, 32.08, 32.05, 30.50, 29.87, 29.83, 29.81, 29.79, 29.77, 29.71, 29.53, 29.49, 29.42, 26.22, 26.20, 22.82, 14.25.

HRMS (ESI): *m/z* calculated for $C_{54}H_{84}O_6Na$ 851.6160 $[M+Na]^+$, found 851.6177.

Synthesis of compound 2: A mixture of compound **28** (500 mg, 0.603 mmol) and barbituric acid (270 mg, 2.11 mmol) in EtOH (20 mL) was stirred for 12 h under reflux. The reaction mixture was cooled to room temperature and the resulting precipitates were collected by filtration and washed with hot ethanol repeatedly to give pure compound **2** as orange solid (525 mg, 93%).

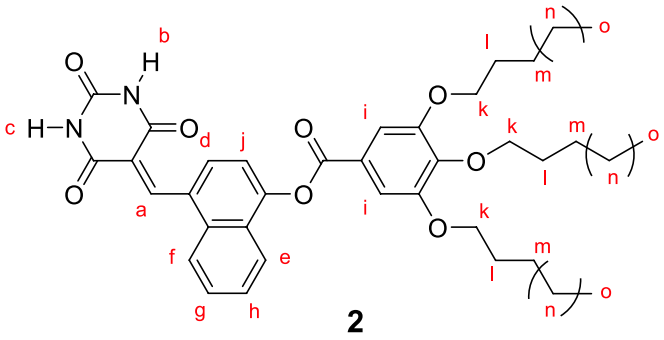

2

^{1}H NMR (500 MHz, $CDCl_3$, 298 K): δ (ppm) 9.30 (1H, s, C=CH_a), 9.12 (1H, s, NH_b), 8.68 (1H, s, NH_c), 8.30 (1H, d, J = 8.1 Hz, Ar-H_d), 8.03 (1H, d, J = 8.4 Hz, Ar-H_e), 7.99 (1H, d, J = 8.5 Hz, Ar-H_f), 7.63 (1H, t, J = 7.6 Hz, Ar-H_g), 7.56 (1H, t, J = 7.6 Hz, Ar-H_h), 7.52 (2H, s, Ar-H_i), 7.44 (1H, d, J = 8.1 Hz, Ar-H_j), 4.11–4.05 (6H, m, Ar-OCH_k), 1.87–1.76 (6H, m, CH_l), 1.54–1.46 (6H, m, CH_m), 1.37–1.25 (48H, m, CH_n), 0.90–0.86 (9H, m, CH_o).

^{13}C NMR (125 MHz, $CDCl_3$, 298 K): δ (ppm) 164.70, 162.90, 160.29, 157.44, 153.27, 151.27, 149.41, 143.59, 133.75, 131.78, 128.48, 127.22, 127.18, 127.06, 124.38, 123.25, 122.67, 118.07, 117.75, 108.87, 73.80, 69.46, 32.08, 32.05, 32.03, 30.50, 29.89, 29.87, 29.83, 29.79, 29.77, 29.72, 29.62, 29.59, 29.54, 29.49, 29.43, 29.29, 29.23, 26.23, 26.20, 22.84, 22.81, 14.25.

HRMS (ESI): *m/z* calculated for $C_{58}H_{86}O_8N_2Na$ 961.6282 $[M+Na]^+$, found 961.6307.

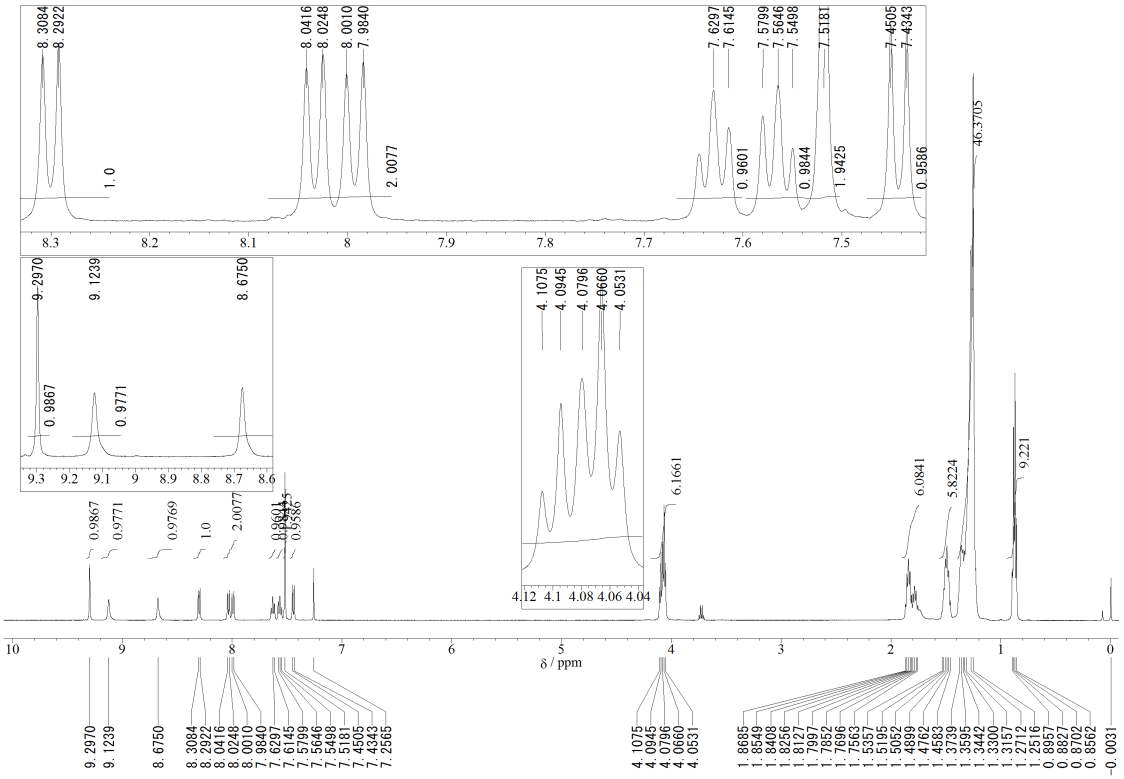

Chart 2-1. ^{1}H NMR spectrum of compound **2** in $CDCl_3$ at 298 K.

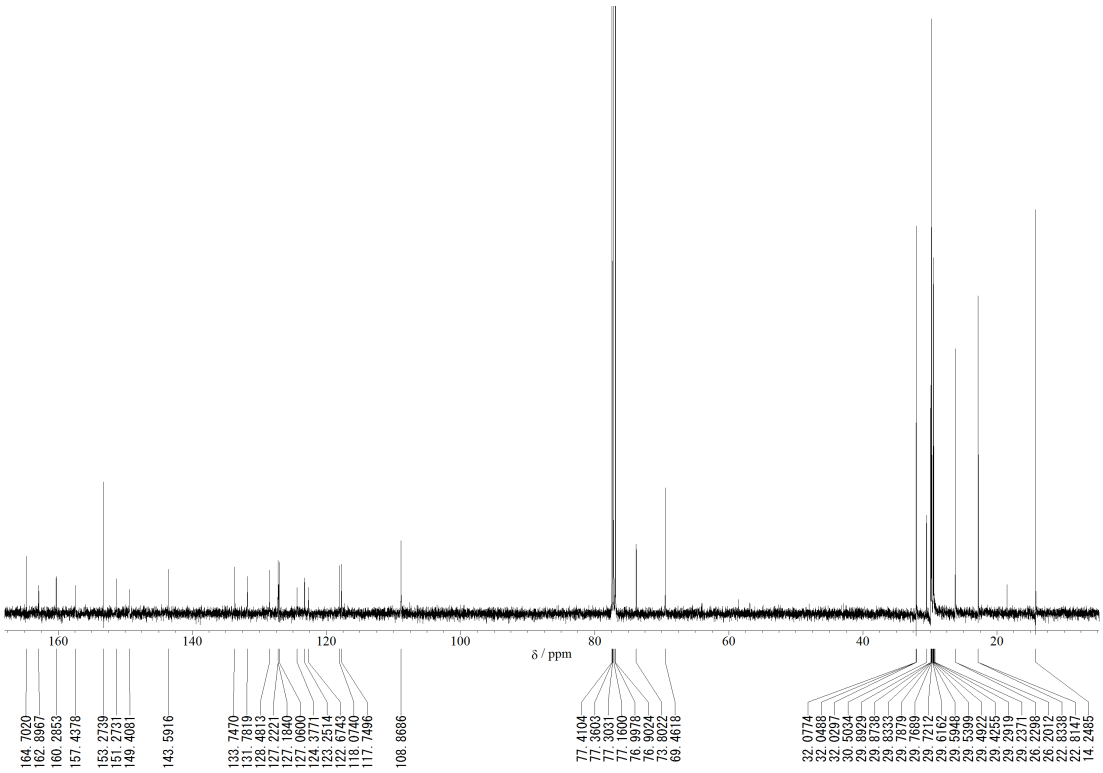

Chart 2-2. ^{13}C NMR spectrum of compound **2** in $CDCl_3$ at 298 K.

2-13. References and Notes

1. A. Klug, *Angew. Chem. Int. Ed*. **1983**, *22*, 565–582.
2. H. Mohri, *Nature* **1968**, *217*, 1053–1054.
3. I. V. Baskakov, G. Legname, M. A. Baldwin, S. B. Prusiner and F. E. Cohen, *J. Biol. Chem.* **2002**, *277*, 21140–21148.
4. (a) F. J. M. Hoeben, P. Jonkheijm, E. W. Meijer and A. P. H. J. Schenning, *Chem. Rev.* **2005**, *105*, 1491–1546. (b) Z. Chen, A. Lohr, C. R. Saha-Möller and F. Würthner, *Chem. Soc. Rev.* **2009**, *38*, 564–84. (c) S. S. Babu, V. K. Praveen and A. Ajayaghosh, *Chem. Rev.* **2014**, *114*, 1973–2129. (d) S. Yagai, *Bull. Chem. Soc. Jpn.* **2015**, *88*, 28–58. (e) C. Rest, R. Kandanelli and G. Fernández, *Chem. Soc. Rev.* **2015**, *44*, 2543–2572. (f) L. Herkert, A. Sampedro and G. Fernández, *CrystEngComm* **2016**, *18*, 8813–8822.
5. (a) P. Jonkheijm, P. van der Schoot, A. P. H. J. Schenning and E. W. Meijer, *Science* **2006**, *313*, 80−83. (b) T. E. Kaiser, V. Stepanenko and F. Würthner, *J. Am. Chem. Soc.* **2009**, *131*, 6719–6732. (c) M. M. J. Smulders, M. M. L. Nieuwenhuizen, T. F. A. de Greef, P. van der Schoot, A. P. H. J. Schenning and E. W. Meijer, *Chem.—Eur. J.* **2010**, *16*, 362–367.
6. (a) F. Oosawa and M. Kasai, *J. Mol. Biol.* **1962**, *4*, 10–21. (b) R. F. Goldstein and L. Stryer, *Biophys. J.* **1986**, *50*, 583–599.
7. (a) Y. Tidhar, H. Weissman, S. G. Wolf, A. Gulino and B. Rybtchinski, *Chem.—Eur. J.* **2011**, *17*, 6068–6075. (b) I. D. Tevis, L. C. Palmer, D. J. Herman, I. P. Murray, D. A. Stone and S. I. Stupp, *J. Am. Chem. Soc.* **2011**, *133*, 16486–16494. (c) P. A. Korevaar, S. J. George, A. J. Markvoort, M. M. J. Smulders, P. A. J. Hilbers, A. P. H. J. Schenning, T. F. A. de Greef and E. W. Meijer, *Nature* **2012**, *481*, 492−496. (d) S. Ogi, K. Sugiyasu, S. Manna, S. Samitsu and M. Takeuchi, *Nat. Chem.* **2014**, *6*, 188–

195. (e) P. A. Korevaar, T. F. A. de Greef and E. W. Meijer, *Chem. Mater.* **2014**, *26*, 576–586. (f) A. J. Markvoort, H. M. M. ten Eikelder, P. A. J. Hilbers and T. F. A. de Greef, *ACS Cent. Sci.* **2016**, *2*, 232–241. (g) A. Aliprandi, M. Mauro and L. De Cola, *Nat. Chem.* **2016**, *8*, 10–15.

8. R. B. Martin, *Chem. Rev.* **1996**, *96*, 3043–3064.
9. (a) D. Zhao and J. S. Moore, *Org. Biomol. Chem.* **2003**, *1*, 3471–3491. (b) T. F. A. de Greef, M. M. J. Smulders, M. Wolffs, A. P. H. J. Schenning, R. P. Sijbesma and E. W. Meijer, *Chem. Rev.* **2009**, *109*, 5687–5754.
10. T. Aida, E. W. Meijer and S. I. Stupp, *Science* **2012**, *335*, 813–817.
11. M. Mascal, N. M. Hext, R. Warmuth, M. H. Moore and J. P. Turkenburg, *Angew. Chem. Int. Ed.* **1996**, *35*, 2204–2206.
12. (a) N. Kimizuka, T. Kawasaki, K. Hirata and T. Kunitake, *J. Am. Chem. Soc.* **1995**, *117*, 6360–6361. (b) H. Fenniri, P. Mathivanan, K. L. Vidale, D. M. Sherman, K. Hallenga, K. V. Wood and J. G. Stowell, *J. Am. Chem. Soc.* **2001**, *123*, 3854–3855. (c) P. Jonkheijm, A. Miura, M. Zdanowska, F. J. M. Hoeben, S. De Feyter, A. P. H. J. Schenning, F. C. De Schryver and E. W. Meijer, *Angew. Chem. Int. Ed.* **2004**, *43*, 74–78. (d) S. Yagai, T. Nakajima, K. Kishikawa, S. Kohmoto, T. Karatsu and A. Kitamura, *J. Am. Chem. Soc.* **2005**, *127*, 11134–11139. (e) T. Seki, X. Lin and S. Yagai, *Asian J. Org. Chem.* **2013**, *2*, 708–724.
13. (a) S. Yagai, S. Kubota, H. Saito, K. Unoike, T. Karatsu, A. Kitamura, A. Ajayaghosh, M. Kanesato and Y. Kikkawa, *J. Am. Chem. Soc.* **2009**, *131*, 5408–5410. (b) S. Yagai, T. Kinoshita, Y. Kikkawa, T. Karatsu, A. Kitamura, Y. Honsho and S. Seki, *Chem.—Eur. J.* **2009**, *15*, 9320–9324. (c) S. Yagai, Y. Goto, T. Karatsu, A. Kitamura and Y. Kikkawa, *Chem. —Eur. J.* **2011**, *17*, 13657–13660. (d) S. Yagai, Y. Goto, X. Lin, T. Karatsu, A. Kitamura, D. Kuzuhara, H. Yamada, Y. Kikkawa, A. Saeki and S. Seki,

Angew. Chem. Int. Ed. **2012**, *51*, 6643–6647. (e) M. J. Hollamby, K. Aratsu, B. R. Pauw, S. E. Rogers, A. J. Smith, M. Yamauchi, X. Lin and S. Yagai, *Angew. Chem. Int. Ed.* **2016**, *55*, 9890–9893.

14. B. M. Rosen, C. J. Wilson, D. A. Wilson, M. Peterca, M. R. Imam and V. Percec, *Chem. Rev.* **2009**, *109*, 6275–6540.
15. S. Yagai, Y. Nakano, S. Seki, A. Asano, T. Okubo, T. Isoshima, T. Karatsu, A. Kitamura and Y. Kikkawa, *Angew. Chem. Int. Ed.* **2010**, *49*, 9990–9994.
16. S. Yagai, S. Mahesh, Y. Kikkawa, K. Unoike, T. Karatsu, A. Kitamura and A. Ajayaghosh, *Angew. Chem. Int. Ed.* **2008**, *47*, 4691–4694.
17. (a) C. T. Seto, J. P. Mathias and G. M. Whitesides, *J. Am. Chem. Soc.* **1993**, *115*, 1321–1329. (b) I. Higler, L. Grave, E. Breuning, W. Verboom, F. de Jong, T. M. Fyles and D. N. Reinhoudt, *Eur. J. Org. Chem.* **2000**, *31*, 1727–1734. (c) S. Yagai, K. Iwai, T. Karatsu and A. Kitamura, *Angew. Chem. Int. Ed.* **2012**, *51*, 9679–9683.
18. Z. Chen, A. Lohr, C. R. Saha-Möller and F. Würthner, *Chem. Soc. Rev.* **2009**, *38*, 564–584.
19. C. Montoro-García, J. Camacho-García, A. M. López-Pérez, N. Bilbao, S. Romero-Pérez, M. J. Mayoral and D. González-Rodríguez, *Angew. Chem. Int. Ed.* **2015**, *54*, 6780–6784.
20. M. Kasha, H. R. Rawls and M. A. El-Bayoumi, *Pure Appl. Chem.* **1965**, *11*, 371–392.
21. (a) U. Rösch, S. Yao, R. Wortmann and F. Würthner, *Angew. Chem. Int. Ed.* **2006**, *45*, 7026–7030. (b) A. Rödle, B. Ritschel, C. Mück-Lichtenfeld, V. Stepanenko and G. Fernández, *Chem.—Eur. J.* **2016**, *22*, 15772–15777.
22. S. Yagai, K. Iwai, T. Karatsu and A. Kitamura, *Angew. Chem. Int. Ed.* **2012**, *51*, 9679–9683.
23. Even at 293 K, **1** and **2** are weakly emissive in THF (Figure 2-7).[13d]

24. This quantum yield is relative to the fluorescence of a previously reported compound; for details, see ref. 13d.

25. (a) M. Peterca, V. Percec, M. R. Imam, P. Leowanawat, K. Morimitsu and P. A. Heiney, *J. Am. Chem. Soc.* **2008**, *130*, 14840–14852. (b) W. Jin, Y. Yamamoto, T. Fukushima, N. Ishii, J. Kim, K. Kato, M. Takata and T. Aida, *J. Am. Chem. Soc.* **2008**, *130*, 9434–9440. (c) M. H. C. J. van Houtem, R. Martín-Rapún, J. A. J. M. Vekemans, E. W. Meijer, *Chem. —Eur. J.* **2010**, *16*, 2258–2271.

26. W. Cochran, F. H. Crick and V. Vand, *Acta Crystallogr.* **1952**, *5*, 581–586.

27. The pitch (*P*) of the sextuple-helix columns was estimated based on the following equation: $P/6 = d/\cos\phi$, where *d* and ϕ are the *d*-spacing (**1**: 1.05 nm; **2**: 1.07 nm) and the tilt angle (**1**: 51°; **2**: 54°), respectively.

28. The values of α were calculated by normalization of the absorption change at a specific wavelength (**1**: 441 nm; **2**: 460 nm).

29. S. Ogi, V. Stepanenko, K. Sugiyasu, M. Takeuchi and F. Würthner, *J. Am. Chem. Soc.* **2015**, *137*, 3300–3307.

30. M. Shigeno, Y. Kushida and M. Yamaguchi, *Chem. —Eur. J.* **2013**, *19*, 10226–10234.

31. R. L. Baldwin, *Fold. Des.* **1996**, *1*, R1–R8.

32. (a) P. A. Bachmann, P. L. Luisi and J. Lang, *Nature* **1992**, *357*, 57−59. (b) T. S. Balaban, J. Leitich, A. R. Holzwarth and K. Schaffner, *J. Phys. Chem. B* **2000**, *104*, 1362–1372. (c) A. Lohr and F. Würthner, *Angew. Chem., Int. Ed.* **2008**, *47*, 1232−1236. (d) J. M. A. Carnall, C. A. Waudby, A. M. Belenguer, M. C. A. Stuart, J. J.-P. Peyralans and S. Otto, *Science* **2010**, *327*, 1502−1506.

33. (a) J. C. MacDonald and G. M. Whitesides, *Chem. Rev.* **1994**, *94*, 2383–2420. (b) C. C. Chu, G. Raffy, D. Ray, A. Del Guerzo, B. Kauffmann, G. Wantz, L. Hirsch and D. M. Bassani, *J. Am. Chem. Soc.* **2010**, *132*, 12717–12723.

34. S. Yagai, M. Suzuki, X. Lin, M. Gushiken, T. Noguchi, T. Karatsu, A. Kitamura, A. Saeki, S. Seki, Y. Kikkawa, Y. Tani and K. Nakayama, *Chem. —Eur. J.* **2014**, *20*, 16128–16137.

35. M. M. J. Smulders, A. P. H. J. Schenning and E. W. Meijer, *J. Am. Chem. Soc.* **2008**, *130*, 606–611.

Chapter 3.

Phototriggered Supramolecular Polymerizations from Supermacrocycles of Barbiturated Naphthalene-Azobenzene Dyad

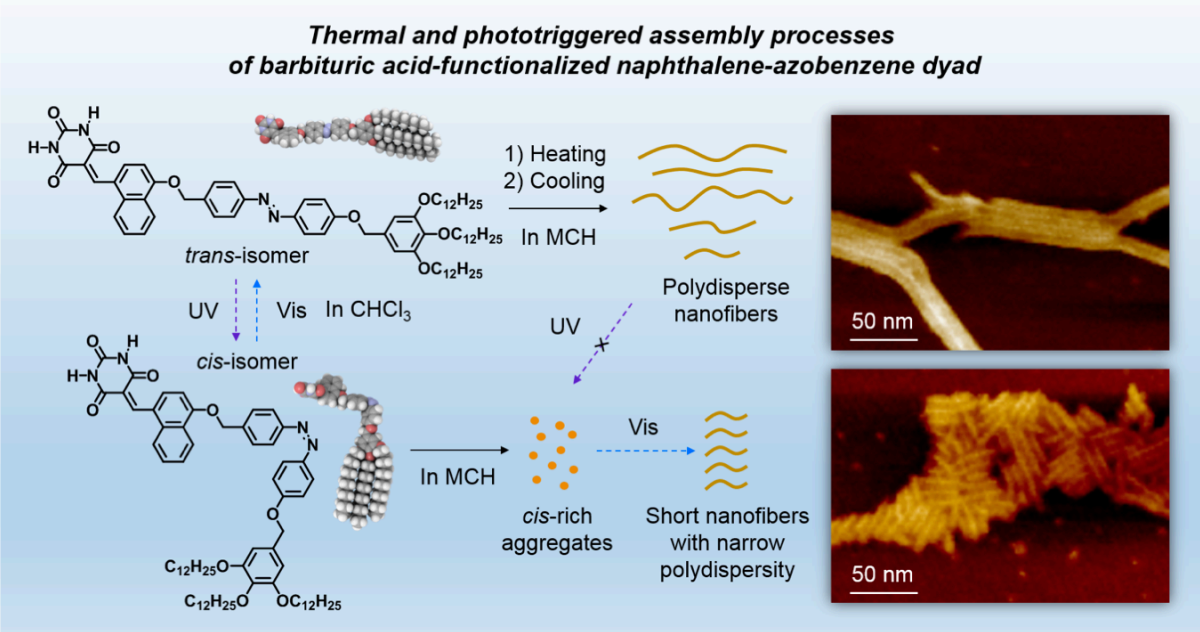

3-1. Abstract

Supramolecular polymerization of an azobenzene-functionalized barbiturated naphthalene was investigated in apolar solvent. The supramolecular polymer length can be controlled by modification of aggregation conditions with respect to kinetics. Phototriggered supramolecular polymerization is realized by using *cis*-to-*trans* photoisomerization induced with visible light irradiation and results in the emergence of shorter nanofibers with narrower polydispersity in comparison with those formed by thermal process.

3-2. Introduction

One-dimensionally extended aggregates, namely supramolecular polymers, constructed by intricate control over aggregation processes are expected to exhibit outstanding structural and physical properties.[1,2] Most supramolecular polymerization processes under a thermodynamic control can be discussed in depth using either isodesmic (non-cooperative)[3] or nucleation-elongation (cooperative)[4] models. In recent reports, pathway-complexity in self-aggregation of synthetic molecules has been actively investigated, and the formation of kinetically formed species that transform into thermodynamically favorable aggregates has been disclosed.[2] However, a methodology to create such kinetic species is a challenging task in the research field of supramolecular assembly, because most examples of such kinetically controlled systems would be discovered accidentally.

In an important paper reported by the research group of E. W. Meijer, a fast-cooling of hot monomeric solutions (quenching) was applied to the self-assembly system of a π-conjugated molecule to realize kinetic behavior of the supramolecular polymer.[2c] In order to attain kinetic system under more convenient way, in this present study a novel concept of "phototriggered supramolecular polymerization" was explored. With the concept, the research group of S. Yagai has realized a photocontrol of formation of self-complementary hydrogen-bonded supermacrocycles (rosettes).[5] In this strategy, geometrically unstackable *cis*-azobenzene isomers[6] can be activated under ambient conditions with light irradiation so as to initiate the supramolecular complexation controlled kinetically by *cis*-to-*trans* isomerization. By utilizing similar strategy in supramolecular polymer system based on azobenzene, a photo-kinetically controlled supramolecular polymerization would be attained.

Recently, the research group of S. Yagai investigated supramolecular polymerizations

of a series of barbituric-acid-functionalized π-conjugated molecules.[7,8] From powder X-ray diffraction[7c,d] and scanning tunneling microscopic (STM)[8] measurements, the group obtained insight into the unique supramolecular polymerization of these barbituric acid derivatives that form columnar structures via the formation of hydrogen-bonded hexameric supermacrocycles (rosettes) and their stacking. As a particular example, barbituric-acid-functionalized naphthalene compound **1** possessing "wedge"-shaped tridodecyloxyphenyl (TDP) unit[9] supramolecularly polymerized into well-ordered cylindrical nanofibers via homogeneous face-to-face (H-type) stacking between the naphthalene chromophores (Figure 3-1a).[7d] Incorporation of azobenzene unit into this self-assembly system would lead to abovementioned phototriggered supramolecular polymerization. In this chapter, supramolecular polymerization process of newly synthesized *trans*-azobenzene derivative **3** and the phototriggered supramolecular polymerization using *cis*-to-*trans* isomerization (Figure 3-1b) is reported. The polymerization of **3** kinetically initiated by rapid *cis*-to-*trans* photoisomerization affords short nanofibers with narrower polydispersity in comparison with those formed through conventional thermal treatment that is cooling of a hot solution.

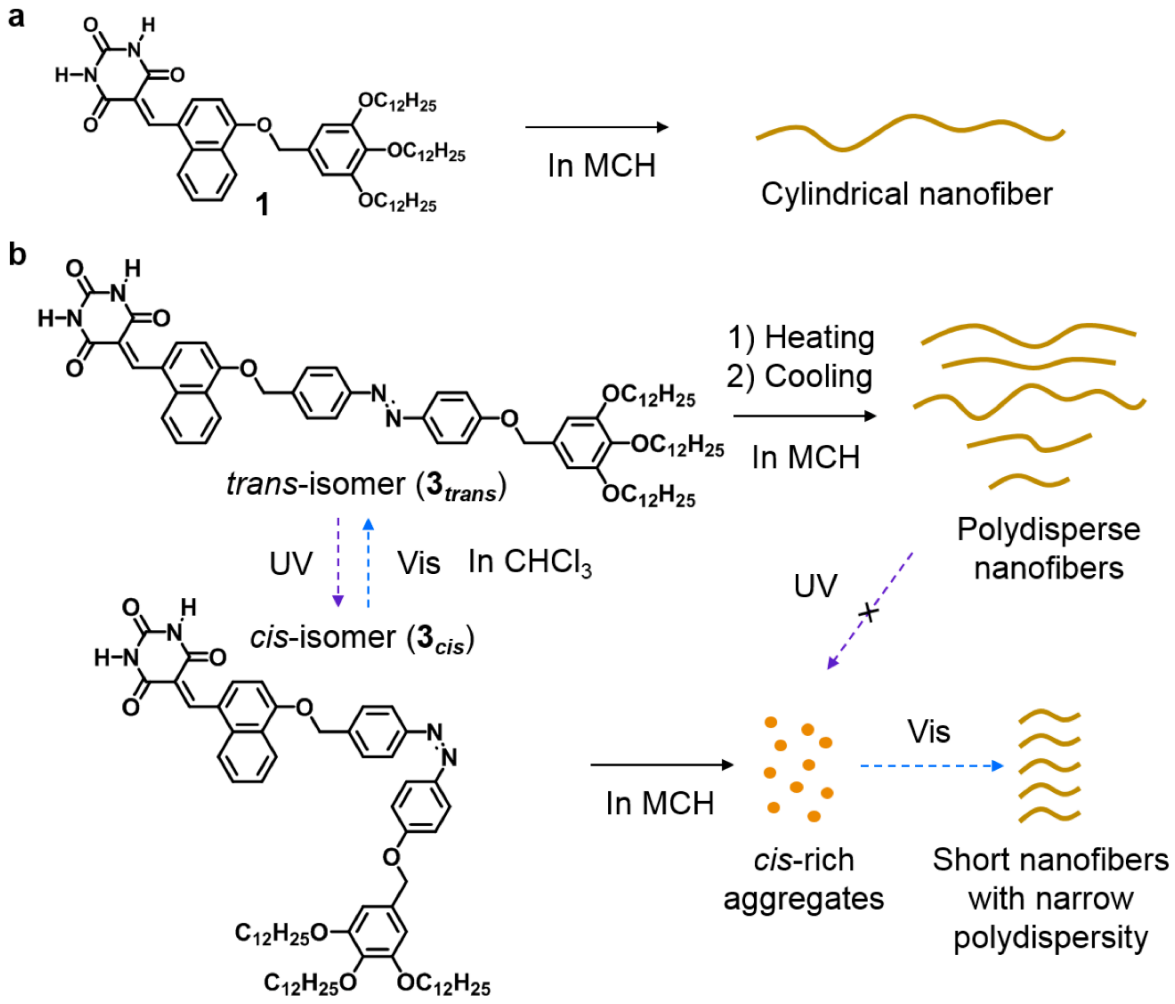

Figure 3-1. Chemical structures of **1** (a), $\mathbf{3}_{trans}$ and $\mathbf{3}_{cis}$ (b) and schematic illustration of their thermal- and photo-induced supramolecular polymerizations.

3-3. Aggregation behavior of 3 in Methylcyclohexane

Compound **3** possessing *trans*-azobenzene chromophore (**3**$_{trans}$) was designed and synthesized according to Synthetic scheme 3-1 (see Synthesis and Characterization). Supramolecular polymers of **3**$_{trans}$ were obtained by cooling the hot monomeric methylcyclohexane (MCH) solution ([**3**$_{trans}$] = 100 μM) from 368 K to 293 K. In UV-vis spectrum at 368 K, **3**$_{trans}$ exhibited two separated absorption bands, one with single maximum (λ_{max} = 347 nm) and the other one with two vibronic maxima (λ_{max} = 421, 439 nm) (Figure 3-2). These bands are associated with the π–π* transitions of the azobenzene and barbituric-acid-conjugated naphthalene chromophores, respectively.[7d] When lowering the temperature to 293 K, the azobenzene absorption band showed hypsochromic shift (λ_{max} = 347 nm → 337 nm), which is indicative of the face-to-face (H-type) stacking between the chromophores.[10] On the other hand, the naphthalene absorption band changed into non-vibronic band to exhibit a single maximum (λ_{max} = 432 nm). Notably, a broad absorption band around 500 nm was emerged (Figure 3-2). The naphthalene derivative **1** previously reported without azobenzene chromophore showed a more prominent hypsochromic shift (λ_{max} = 425, 444 nm → 405 nm) as a result of the formation of H-type supramolecular assemblies.[7d] Accordingly, the addition of azobenzene chromophore disturbs the homogeneous H-type stacking between the naphthalene chromophores.

To obtain insight into the supramolecular polymerization process of **3**$_{trans}$, the temperature-dependent polymerization and depolymerization behaviors were further explored by monitoring change in the UV/vis absorption at 490 nm upon cooling and heating processes (rate: 1.0 K min^{-1}). In order to disturb secondary interactions such as bundling of supramolecular polymers, diluted solutions at lower concentrations (10–40 μM) were used. When the change of the normalized UV/vis absorption intensity, which exhibits

degree of aggregation (α), was plotted versus temperature, a non-sigmoidal curve was obtained with an elongation temperature T_e' (*e.g.,* T_e' = 326.5 K at [$\mathbf{3}_{trans}$] = 10 μM) (Figure 3-3a). Such transition is characteristic for cooperative nucleation-elongation process.[4,11] The T_e' of $\mathbf{3}_{trans}$ is notably higher ($\Delta T_e'$ = 25.0 K) than that of naphthalene derivative **1** (T_e' = 301.5 K at [**1**] = 10 μM), which is due to the presence of additional π–π interactive azobenzene moiety. It should be noted that the heating curves exhibited the depolymerization processes possessing trajectories shifted toward higher temperature region in comparison with the cooling curves corresponding to polymerization processes, and have higher elongation temperatures T_e during heating (*e.g.,* 335.5 K at [$\mathbf{3}_{trans}$] = 10 μM). These thermal hystereses indicate that the polymerization during cooling may be kinetically controlled.[12] When raising concentration from 10 → 20 → 30 → 40 μM, T_e' and T_e increase together, whereas these shapes of curves are almost superimposable (Figure 3-3a). The van't Hoff plot of natural logarithm of the concentration against reciprocal T_e obtained from the heating data exhibited a linear relationship. From this plot, the standard enthalpy difference (ΔH°) and the entropy difference (ΔS°) for the growth process were calculated to be −78.8 kJ mol^{-1} and −0.139 kJ mol^{-1} K^{-1}, respectively (Figure 3-3b). Based on these values, the Gibbs free energy (ΔG° = −37.3 kJ mol^{-1}) and the binding constant (K_e = 3.5 × 10^6 M^{-1}) estimated at 298 K were further calculated. The ΔH° value calculated from the van't Hoff analysis is well in line with the elongation enthalpy difference (ΔH_e = −75.8 ± 2.4 kJ mol^{-1} at the range of 10–40 μM) calculated by model fitting of the experimental curves with a theoretical cooperative model applied by the research group of E. W. Meijer (Figure 3-4 and Table 3-1, and see the General Methods in Chapter 1-7 for details).[11] Notably, analysis the cooling data revealed significant difference between the ΔH° (van't Hoff plot; −64.3 kJ mol^{-1}) and the ΔH_e (model fitting; *e.g.,* −105.2 kJ mol^{-1} at c = 10 μM, −82.7 kJ mol^{-1} at c = 30 μM) as shown in Figure 3-5 and Table 3-2. The discrepancy further supports the kinetic

effect in the cooling process, which also shows concentration-dependence probably because of bundling of supramolecular polymers.

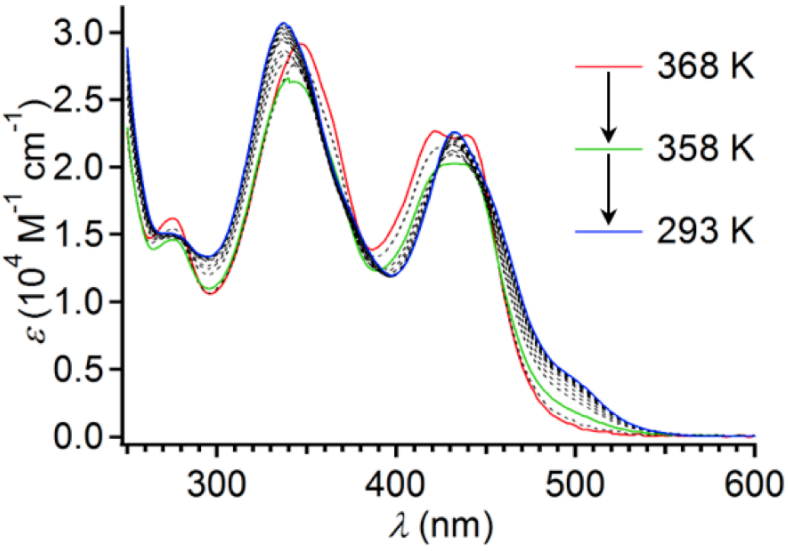

Figure 3-2. Change of UV/vis spectra of $\mathbf{3}_{trans}$ in MCH (c = 50 μM) upon cooling from 368 K to 293 K. These spectra are shown at interval of 5 K.

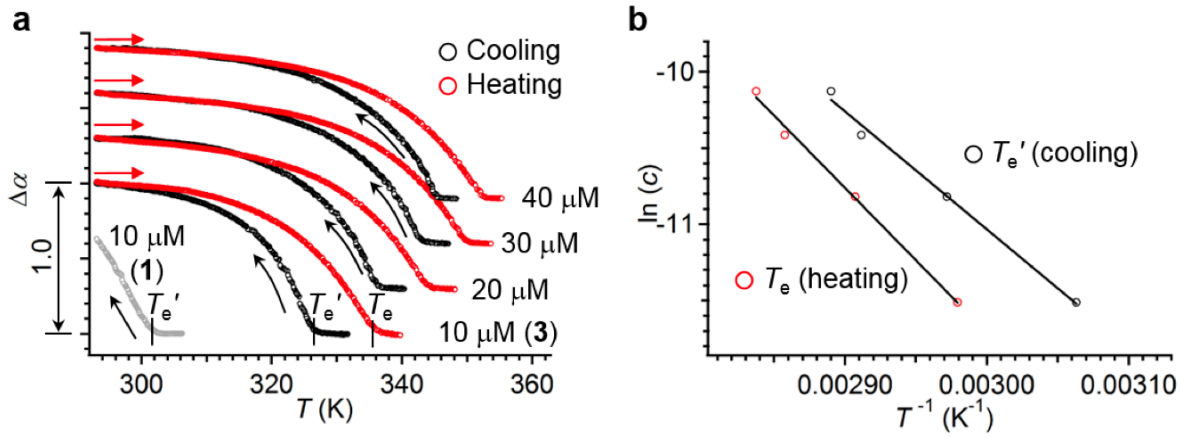

Figure 3-3. (a) Temperature-dependent degree of aggregation (α) calculated from changes in normalized absorption intensity at 490 nm in the cooling and heating processes (rate: 1.0 K min^{-1}) at given concentrations (10 μM for **1**, 10, 20, 30, 40 μM for $\mathbf{3}_{trans}$). In (a), the curves of $\mathbf{3}_{trans}$ are displayed with an offset ($\Delta\alpha = 0.3$) for clarity. (b) van't Hoff plots of natural logarithm of the concentration (c) of $\mathbf{3}_{trans}$ against the reciprocal elongation temperatures, T_e' and T_e, which are estimated from cooling (polymerization) and heating data (depolymerization), respectively. The plots are a linear relationship.

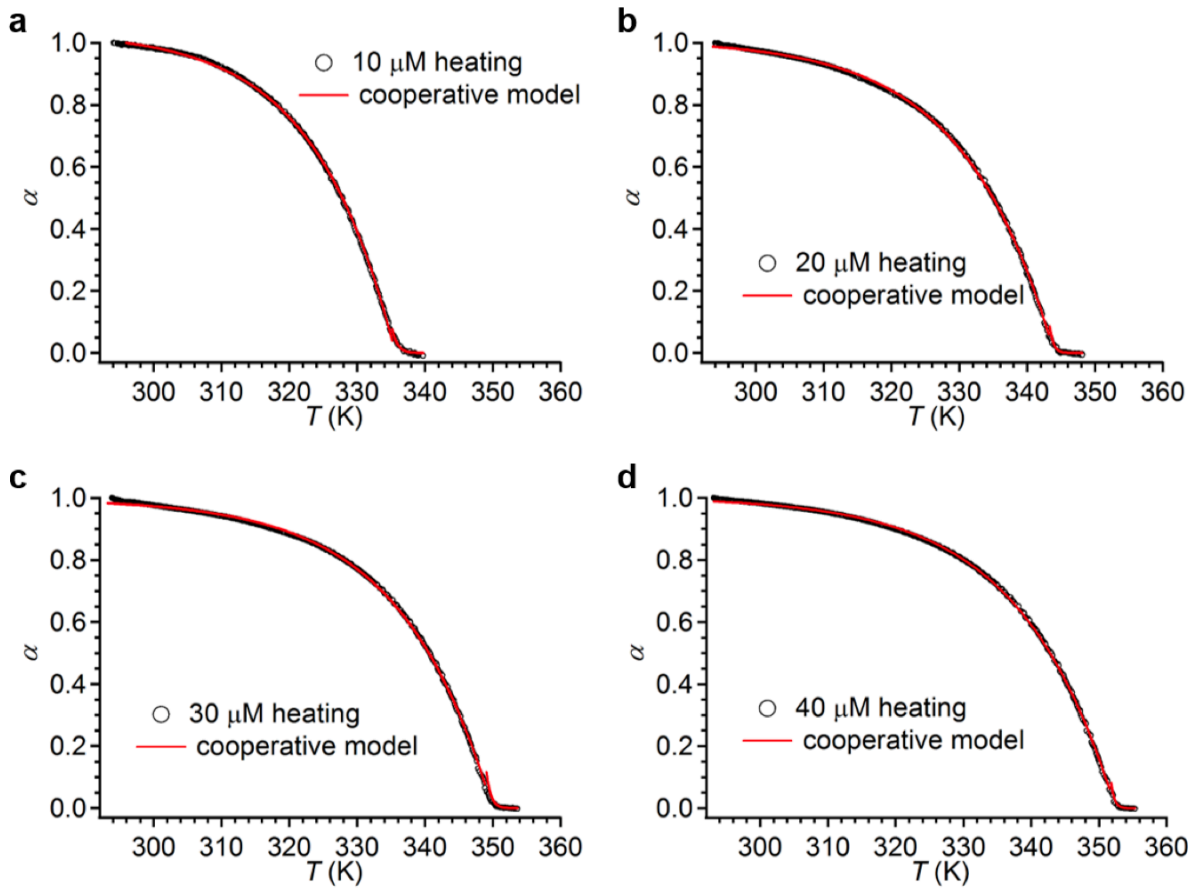

Figure 3-4. (a–d) Temperature-dependent degree of aggregation (α) estimated from changes in absorption of $\mathbf{3}_{trans}$ at 490 nm in MCH at given concentrations (10–40 μM) upon heating (rate: 1.0 K min^{-1}). Solid red curves show fitting traces with a theoretical cooperative model developed by the research group of E. W. Meijer.

$[\mathbf{3}_{trans}]$ (μM)	T_e (K)	ΔH_e (kJ mol^{-1})	K_a
10	335.6	−79.1 ± 0.2	7.2×10^{-5}
20	344.0	−74.7 ± 0.2	2.0×10^{-5}
30	350.0	−75.5 ± 0.2	2.9×10^{-5}
40	352.4	−73.7 ± 0.2	1.2×10^{-5}

Table 3-1. Thermodynamic parameters (T_e, ΔH_e and K_a) calculated from the fitting analysis of the cooperative supramolecular polymerization of $\mathbf{3}_{trans}$ (heating data) at different concentrations.

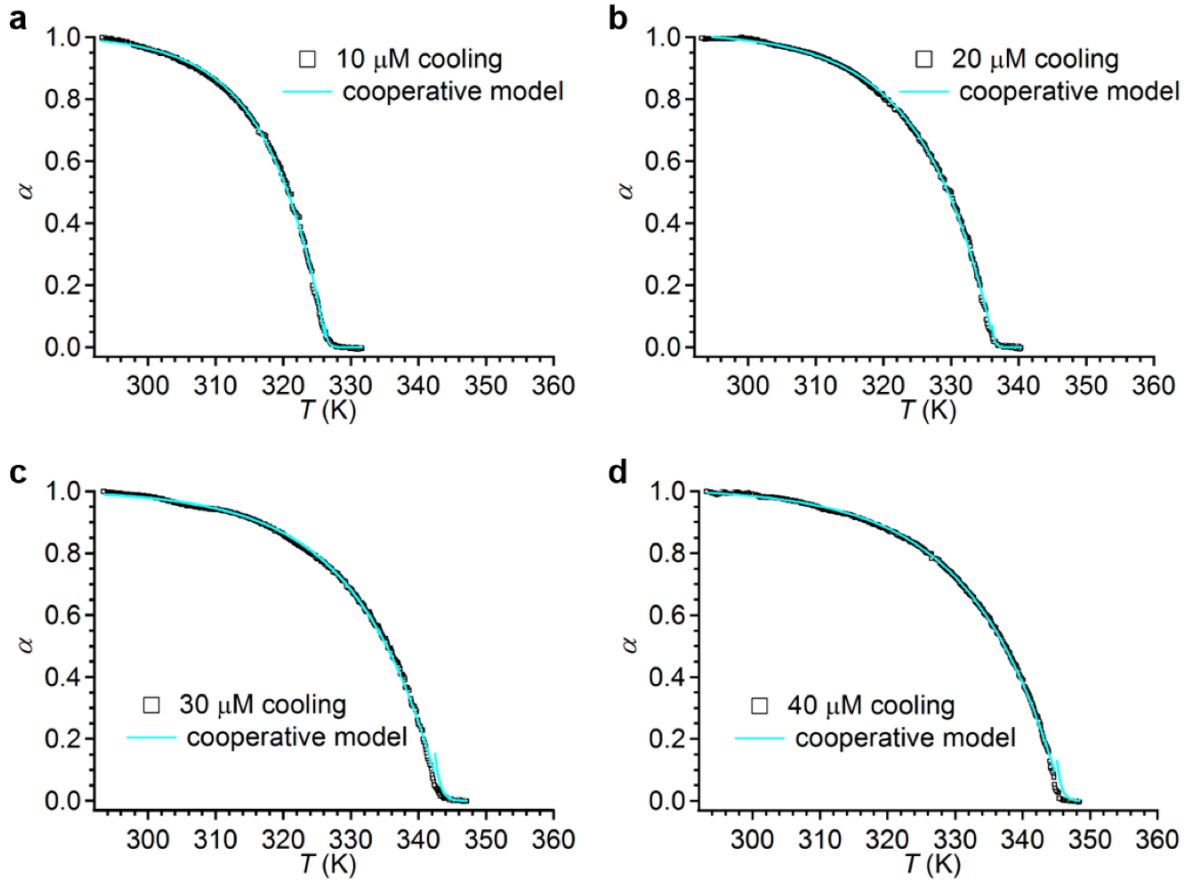

Figure 3-5. (a–d) Temperature-dependent degree of aggregation (α) estimated from absorption changes of $\mathbf{3}_{trans}$ at 490 nm in MCH at given concentrations (10–40 μM) upon cooling (rate: 1.0 K min^{-1}). Solid cyan curves show fitting traces with a theoretical cooperative model developed by the research group of E. W. Meijer.

$[\mathbf{3}_{trans}]$ (μM)	T_e (K)	ΔH_e (kJ mol^{-1})	K_a
10	326.5	−105.2 ± 0.5	3.4×10^{-5}
20	336.5	−92.2 ± 0.3	1.0×10^{-5}
30	343.5	−82.7 ± 0.3	6.2×10^{-5}
40	346.0	−78.1 ± 0.2	3.4×10^{-5}

Table 3-2. Thermodynamic parameters (T_e, ΔH_e and K_a) calculated from the fitting analysis of the cooperative supramolecular polymerization of $\mathbf{3}_{trans}$ (cooling data) at different concentrations.

3-4. Nanostructures of Supramolecular Polymers of 3

In order to gain insight into the kinetically controllable supramolecular polymerization of $\mathbf{3}_{trans}$, I explored how structural properties of the supramolecular polymers change through the slow cooling and very fast cooling processes (*i.e.*, quenching) that may induce more kinetic effect.[2c] When quenching a hot monomeric solution of $\mathbf{3}_{trans}$ ([$\mathbf{3}_{trans}$] = 100 μM) at 373 K by using ice-water bath, the temperature suddenly decreased to ~293 K within 10 sec. The resultant supramolecular polymers ($\mathbf{SP}_{fast}$) as well as supramolecular polymers obtained by slow cooling at a rate of 1.0 K min^{-1} ($\mathbf{SP}_{slow}$) in MCH were spin-coated at high-speed (3000 rpm) onto highly oriented pyrolytic graphite (HOPG), and their morphologies were visualized by atomic force microscopy (AFM). Figure 3-6 displays cylindrical nanofibers observed for both $\mathbf{SP}_{slow}$ and $\mathbf{SP}_{fast}$. These nanofibers are adjoiningly aligned with an average top-to-top distance of ca. 8.2 nm, which is in line with the formation of hexameric rosettes of $\mathbf{3}_{trans}$ as a hydrogen-bonded intermediate supramolecule (Figure 3-6). A notable difference between $\mathbf{SP}_{slow}$ and $\mathbf{SP}_{fast}$ nanofibers is their lengths. Namely, the lengths of main $\mathbf{SP}_{slow}$ nanofibers exceed 1000 nm while those of $\mathbf{SP}_{fast}$ nanofibers are in the range of 50–400 nm.

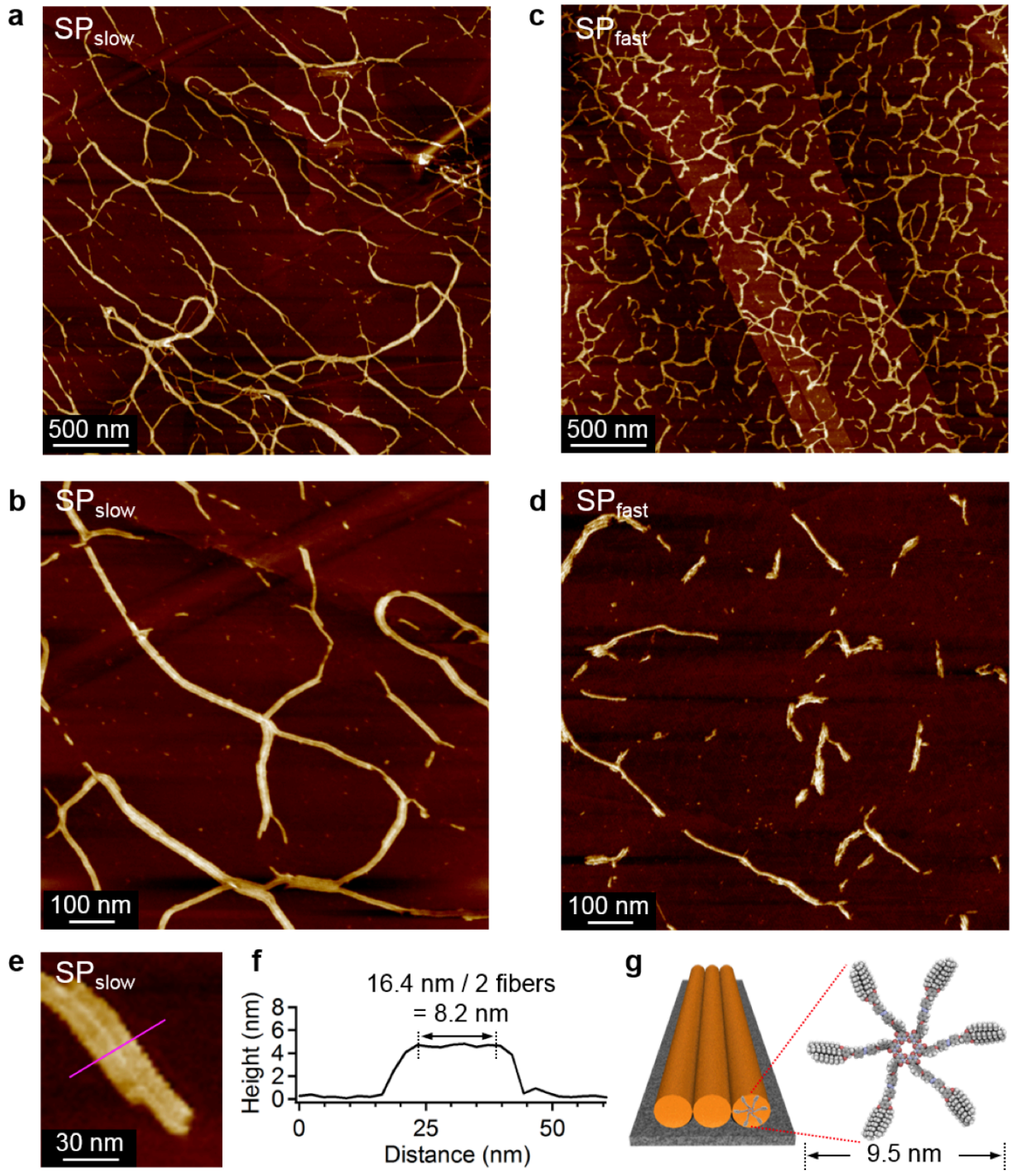

Figure 3-6. (a–e) AFM height images of $\mathbf{SP}_{\mathbf{slow}}$ (a,b,e) and $\mathbf{SP}_{\mathbf{fast}}$ (c,d) spin-coated from their corresponding MCH solutions of $\mathbf{3}_{trans}$ ([$\mathbf{3}_{trans}$] = 100 μM, T = 293 K) onto HOPG. (f) AFM cross-sectional analysis along the pink line in (e). (g) Schematic illustration of cylindrical supramolecular polymers composed of stacked hexameric rosettes of $\mathbf{3}_{trans}$.

3-5. Phototriggered Supramolecular Polymerization

In this section, the supramolecular polymerization of **3** triggered by photoisomerization is described. Upon UV-irradiation of the MCH solution of $\mathbf{SP}_{\mathbf{slow}}$ ([**3**] = 100 μM, T = 293 K) with 365 nm light for 2 min, a minor decrease of the *trans*-azobenzene absorption band (λ_{max} = 337 nm) was observed, which is indicative of the photoisomerization from $\mathbf{3}_{trans}$ to $\mathbf{3}_{cis}$. The $\mathbf{3}_{trans}$:$\mathbf{3}_{cis}$ ratio at the photostationary state (PSS) under UV-irradiation was calculated to be 79:21 (Figure 3-7). The low photoisomerization efficiency is probably due to densely aggregated state via π–π stacking between rosettes in the supramolecular polymer fibers. As anticipated, the UV-irradiated $\mathbf{SP}_{\mathbf{slow}}$ did not exhibit meaningful morphological change (Figure 3-8).

In sharp contrast, UV-irradiation of monomeric $\mathbf{3}_{trans}$ in $CHCl_3$ ([$\mathbf{3}_{trans}$] = 2 mM) caused much higher photoisomerization efficiency to provide $\mathbf{3}_{trans}$:$\mathbf{3}_{cis}$ ratio of 10:90, which was calculated by ^{1}H NMR studies (Figure 3-9). Adding 0.1 mL of this $\mathbf{3}_{cis}$-rich $CHCl_3$ solution into 1.9 mL of pure MCH solvent afforded 2.0 mL of $\mathbf{3}_{cis}$-rich aggregate solution (MCH:$CHCl_3$ = 19:1, [$\mathbf{3}_{trans}$+$\mathbf{3}_{cis}$] = 100 μM). The UV/vis spectrum of this solution at 293 K exhibited the significantly decreased absorption band corresponding to *trans*-azobenzene unit (Figure 3-10a). When this $\mathbf{3}_{cis}$-rich solution was exposed to irradiation with 470 nm visible light, a gradual recovery of $\mathbf{3}_{trans}$ was observed by UV/vis absorption measurements, which approximately completed after 10 sec (Figure 3-10a,b). The $\mathbf{3}_{trans}$:$\mathbf{3}_{cis}$ ratio at this PSS under visible irradiation was calculated to be 98:2.

The phototriggered supramolecular polymerization of $\mathbf{3}_{trans}$ was visualized by AFM. When spin-coating the $\mathbf{3}_{cis}$-rich solution just after mixing, only ill-defined aggregates were observed (Figure 3-11a,b). Upon visible light irradiation of the *cis*-rich solution up to the PSS state, well-defined cylindrical supramolecular polymers were formed (Figure 3-11c,d). These photogenerated supramolecular polymers ($\mathbf{SP}_{\mathbf{vis}}$) are apparently shorter than $\mathbf{SP}_{\mathbf{fast}}$ (Figure 3-

6c,d). Analysis of the lengths for one hundred $\mathbf{SP_{vis}}$ nanofibers and forty $\mathbf{SP_{slow}}$ nanofibers suggested a narrower polydispersity index (PDI = L_w/L_n = 1.26) of $\mathbf{SP_{vis}}$ than that of $\mathbf{SP_{fast}}$ (PDI = 1.50) (Figure 3-11e).[13] Distinct size distributions of these supramolecular polymers were also supported by dynamic light scattering (DLS) analysis, in which the average hydrodynamic diameters (D_H) for $\mathbf{SP_{vis}}$ and $\mathbf{SP_{fast}}$ were detected to be 50 nm and 200 nm, respectively (Figure 3-11f). The shorter length of $\mathbf{SP_{vis}}$ attained by photoisomerization is most likely due to different formation mechanism of "aggregative" $\mathbf{3}_{trans}$. Considering the *cis*-to-*trans* photoisomerization pathway, the emergence of aggregative $\mathbf{3}_{trans}$ can occur very extremely under an ambient temperature (ca. 293 K) largely below T_e' (368 K). Such a special condition is able to realize a more supercooled state compared with that prepared by thermal quenching method. In this state wherein a degree of solute diffusion is not enough to elongate the nucleus created in the initial region, additional nucleation of monomers occurs, which results in the formation of a larger number of supramolecular polymers with relatively smaller lengths in comparison with those generated by quenching.

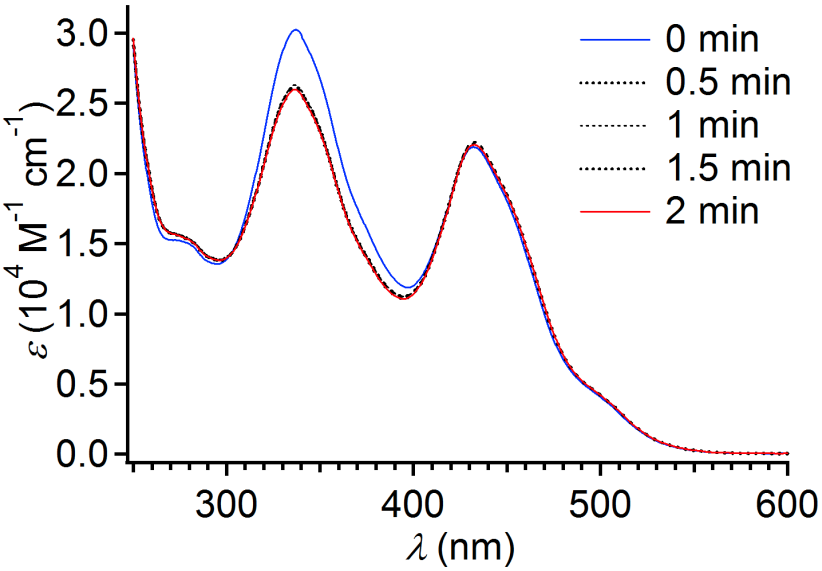

Figure 3-7. Change in UV/vis absorption spectra of $\mathbf{3}_{trans}$ in MCH ([$\mathbf{3}_{trans}$] = 100 μM, T = 293 K) upon UV-irradiation with 365 nm light.

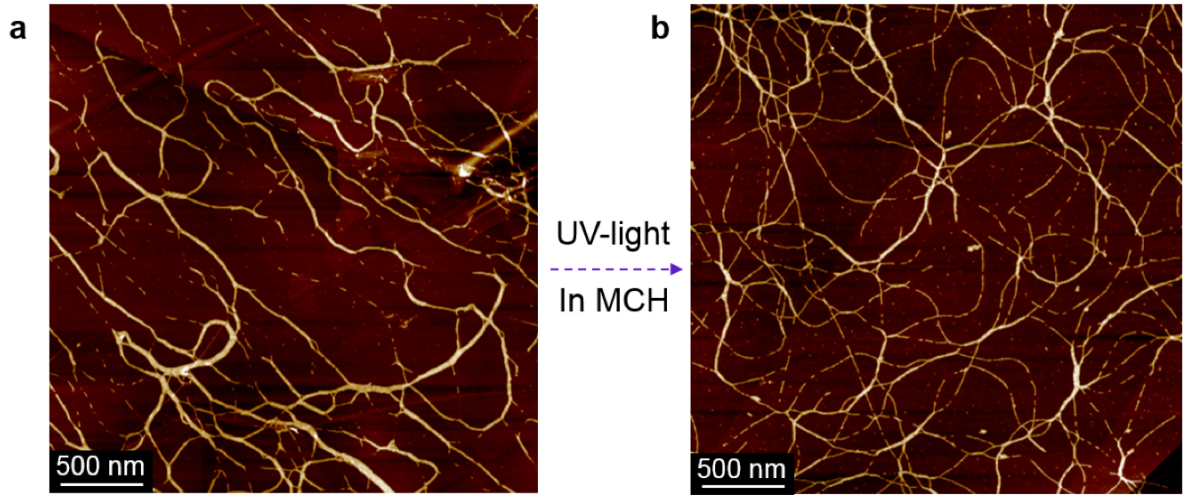

Figure 3-8. (a,b) AFM height images of $\mathbf{SP}_{slow}$ (a) and the UV-irradiated $\mathbf{SP}_{slow}$ (b) with 365 nm light for 2 min. Samples were prepared by spin-coating the corresponding MCH solutions of **3** ([**3**]= 100 μM) onto HOPG.

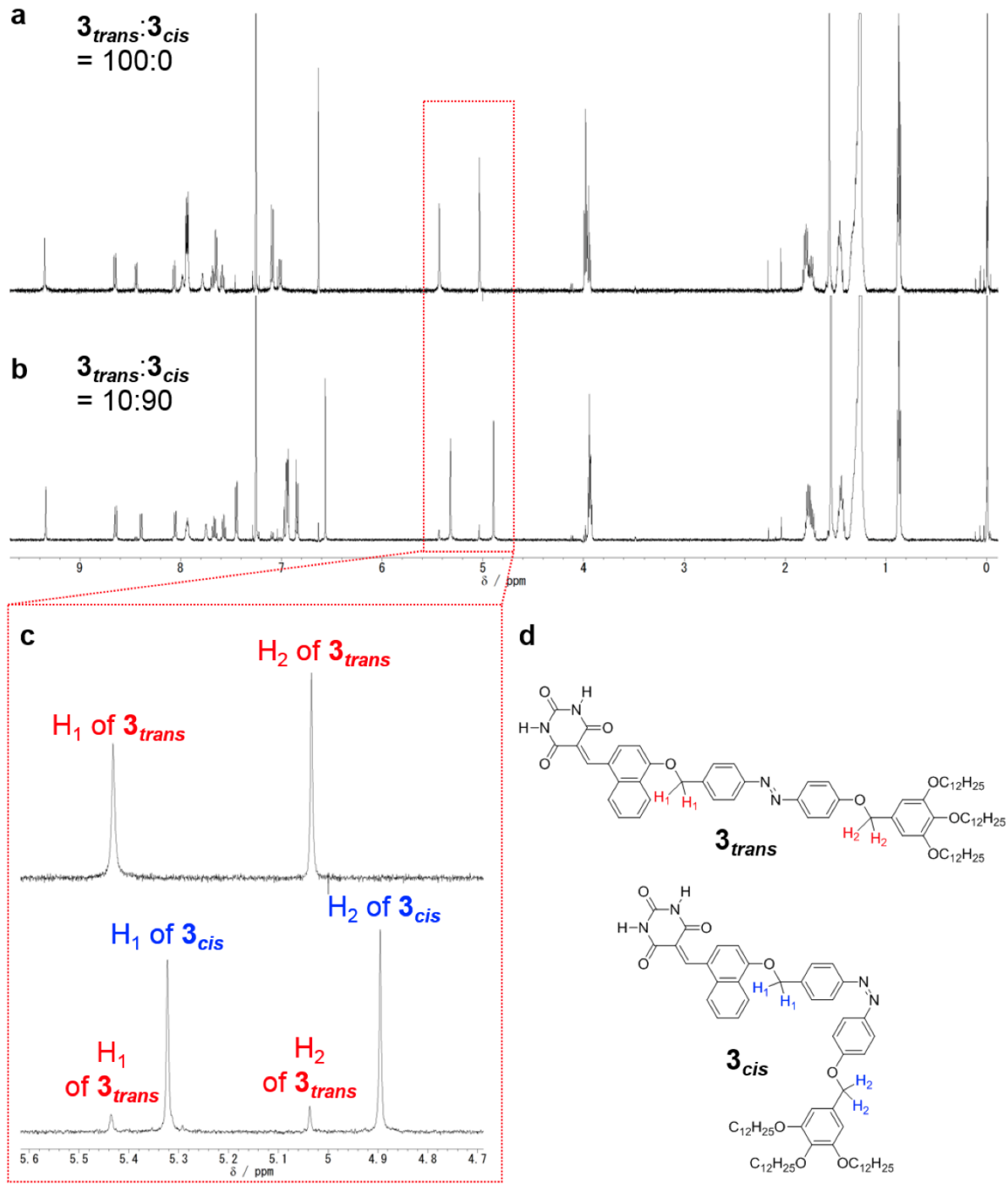

Figure 3-9. ^{1}H NMR spectra of **3** ([**3**] = 2 mM) at 293 K in $CDCl_3$ before (a) and after irradiation of UV-light (365 nm) for 20 min to reach a PSS (b). (c) The zoom ^{1}H NMR spectra in the region of 5.6–4.7 ppm where the integration of the benzylic proton signals (H_1 and H_2) of $\mathbf{3}_{trans}$ (red) and $\mathbf{3}_{cis}$ (blue) suggests that the UV irradiation leads to 90% photoisomerization ($\mathbf{3}_{trans}$:$\mathbf{3}_{cis}$ = 10:90). (d) Chemical structures of $\mathbf{3}_{trans}$ and $\mathbf{3}_{cis}$ with assignment of the corresponding ^{1}H NMR signals of benzylic hydrogens (H_1 and H_2) in (c).

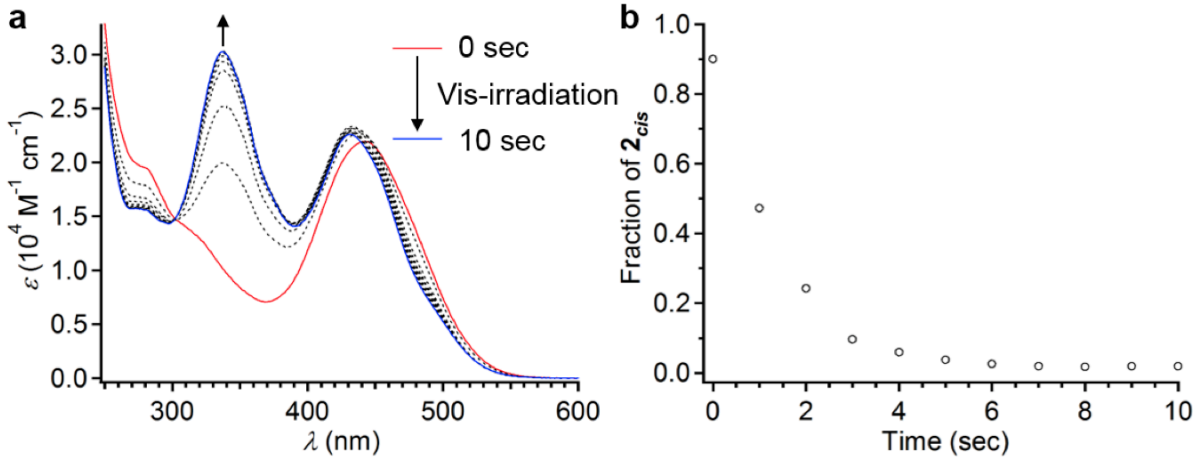

Figure 3-10. (a) Change of the UV/vis absorption spectra in MCH upon exposure to visible light irradiation of $\mathbf{3}_{cis}$-rich ($\mathbf{3}_{trans}$:$\mathbf{3}_{cis}$ = 10:90, [$\mathbf{3}_{trans}$+$\mathbf{3}_{cis}$] = 100 μM) solution (MCH:$CHCl_3$ = 19:1). (b) Plot of fraction of $\mathbf{3}_{cis}$ against visible light irradiation time.

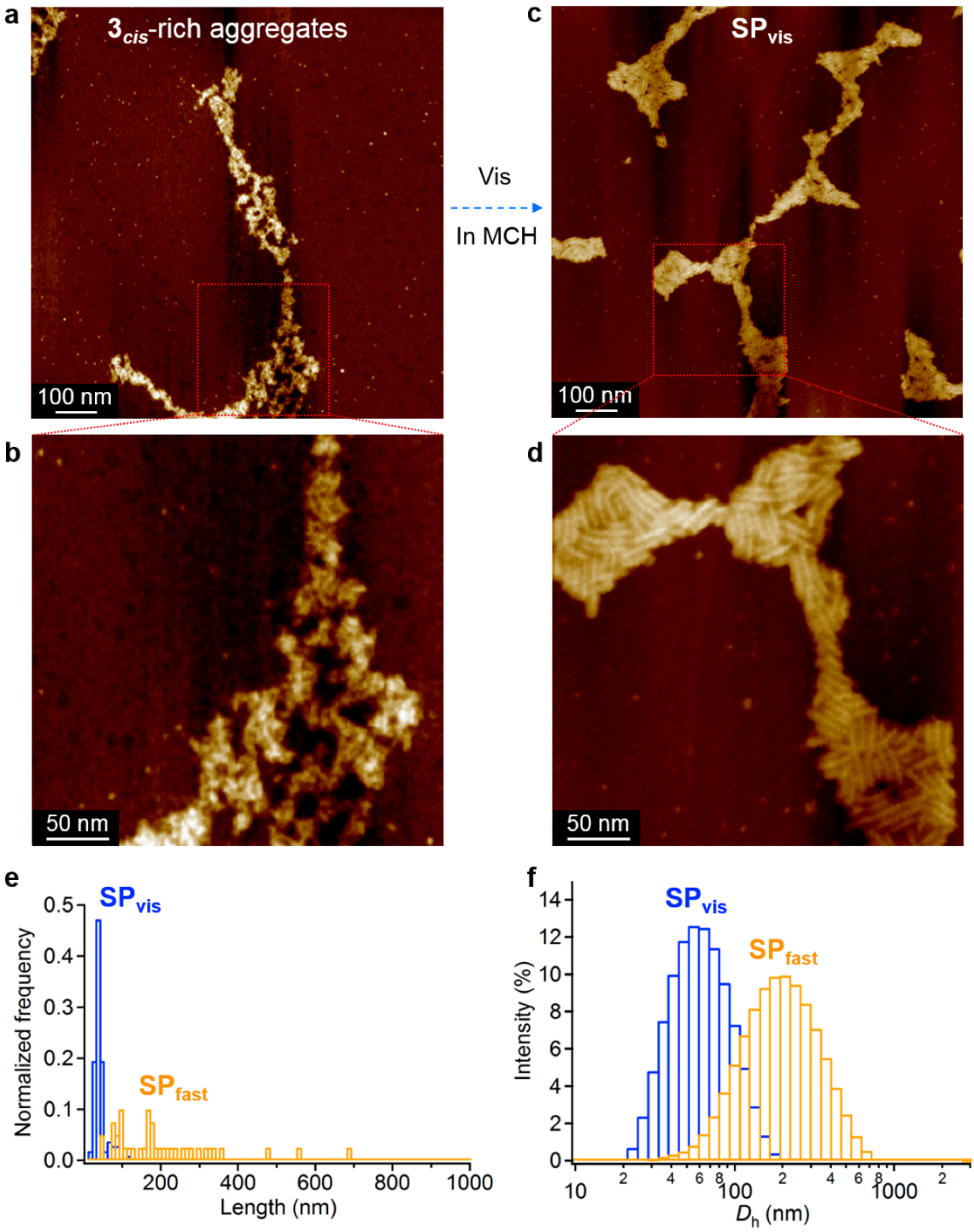

Figure 3-11. (a–d) AFM height images of $\mathbf{3}_{cis}$-rich ill-defined aggregates ($\mathbf{3}_{trans}$:$\mathbf{3}_{cis}$ = 10:90, a,b) and $\mathbf{SP}_{vis}$ nanofibers ($\mathbf{3}_{trans}$:$\mathbf{3}_{cis}$ = 98:2, c,d) that was attained by exposure of the $\mathbf{3}_{cis}$-rich solution to 470 nm visible light for 10 sec. Samples were obtained by spin-coating the corresponding MCH solutions at 293 K onto HOPG. (e) Histogram for the length distributions of $\mathbf{SP}_{vis}$ and $\mathbf{SP}_{fast}$ from AFM images. (f) DLS results of $\mathbf{SP}_{vis}$ and $\mathbf{SP}_{fast}$ in solution at 293 K.

3-6. Conclusion

In conclusion, I have revealed supramolecular polymerization of $\mathbf{3}_{trans}$ under kinetic control obtained by fast temperature decrease (so called "quenching") or photoisomerization under an ambient temperature enough below the nucleation temperature. The latter supramolecular polymerization triggered by photoisomerization demonstrated the more kinetic aggregation process as a result of well-defined difference in the size distributions of aggregated fibers. The resultant kinetically trapped short supramolecular polymers can be utilized as "seeds" for precise supramolecular polymerization such as living polymerization,[14] which is ongoing in the laboratory of S. Yagai. More notably, this strategy can be applied to realize exciting supramolecular assemblies and organic materials that cannot be attained by conventional temperature-controlled processes.

3-7. Synthesis and Characterization

Compound **3** was synthesized according to Synthetic scheme 3-1.

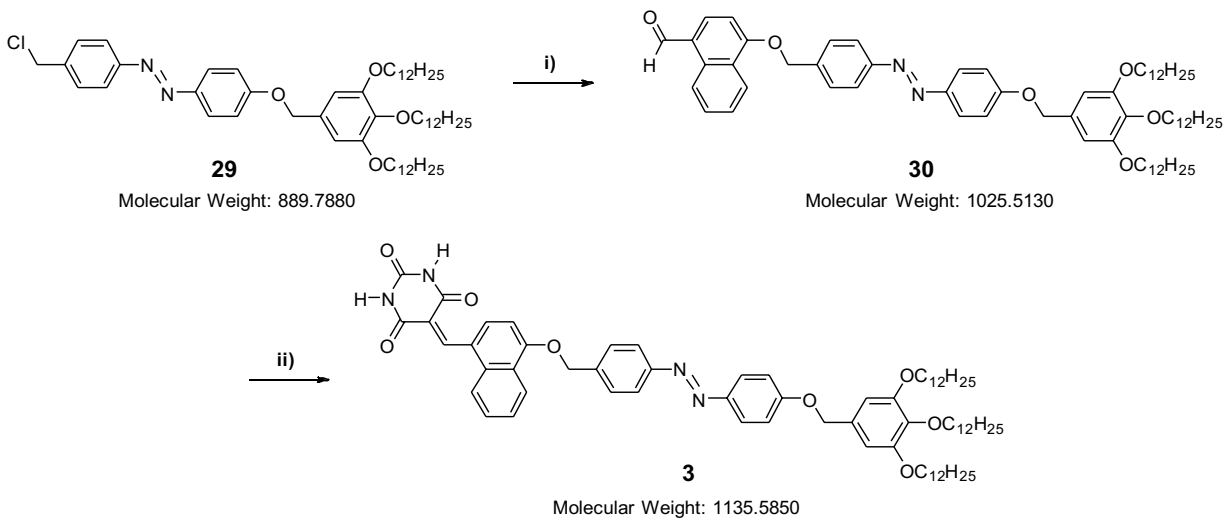

Synthetic scheme 3-1. Synthetic scheme of **3**. i) 4-hidroxy-1-naphtaldehyde, K_2CO_3, dry DMF, 70 °C; ii) barbituric acid, ethanol, reflux.

Synthesis of compound 30: 4-Hidroxy-1-naphtaldehyde (139 mg, 0.804 mmol) was dissolved in a suspension of K_2CO_3 (1.124 g, 8.13 mmol) in DMF (50 mL) at 70 °C under N_2 atmosphere, and the mixture was stirred until the solution turned green. Compound **29** (706 mg, 0.793 mmol) was added and the mixture was stirred for 22.5 h at 70 °C. The reaction mixture was poured into water and extracted with $CHCl_3$, washed with H_2O and then brine. The organic layer was dried over Na_2SO_4, concentrated in vacuo and evaporated to dryness. The residue was purified by column chromatography on silica gel (hexane/AcOEt = 4:1) to give pure compound **30** as orange solid (334 mg, 41% yield).

^{1}H NMR (500 MHz, $CDCl_3$): δ (ppm) 10.19 (1H, s, Ar-C*H*O), 9.33 (1H, d, J = 8.5 Hz, Ar-*H*), 8.42 (1H, d, J = 8.4 Hz, Ar-*H*), 7.94 (4H, d, J = 8.6 Hz, Ar-*H*), 7.86 (1H, d, J = 8.0 Hz, Ar-*H*), 7.72–7.69 (1H, m, Ar-*H*), 7.63–7.57 (3H, m, Ar-*H*), 7.10 (2H, d, J = 9 Hz, Ar-*H*), 6.94 (1H, d, J = 8.2 Hz, Ar-*H*), 6.65 (2H, s, Ar-*H*), 5.36 (2H, s, Ar-OC*H*-Ar), 5.03 (2H, s, Ar-OC*H*-Ar),

4.01–3.98 (6H, m, Ar-OC*H*-CH_2), 1.84–1.75 (6H, m, C*H*), 1.49–1.28 (54H, m, C*H*), 0.92–0.89 (9H, m, C*H*).

^{13}C NMR (125 MHz, $CDCl_3$): δ (ppm) 192.23, 161.54, 159.66, 153.49, 152.75, 147.20, 139.49, 138.25, 138.20, 132.07, 131.37, 129.71, 128.04, 126.62, 125.73, 125.38, 125.06, 125.03, 124.98, 123.07, 122.59, 115.28, 115.21, 106.29, 104.34, 104.29, 77.45, 77.20, 76.94, 73.65, 73.58, 73.49, 70.92, 70.82, 70.72, 70.26, 70.21, 70.16, 69.37, 69.29, 69.21, 32.09, 30.53, 29.92, 29.87, 29.82, 29.58, 29.54, 26.28, 26.28, 22.86, 14.29.

HRMS (ESI): *m/z* calculated for $C_{67}H_{97}N_2O_6$ = 1025.7347 $[M+H]^+$, found 1025.7356.

Synthesis of compound 3: Compound **30** (144 mg, 0.141 mmol) was dissolved in ethanol (45 mL), and stirred until the solution turned clear at 85 °C. To this solution, barbituric acid (186 mg, 1.45 mmol) was added and the mixture was stirred for 5 h at 85 °C under reflux. The reaction mixture was cooled to room temperature and the resulting precipitates were collected by filtration and washed with hot ethanol repeatedly to give pure compound **3** as red-brown solid (133 mg, 83% yield).

^{1}H NMR (500 MHz, $CDCl_3$): δ (ppm) 9.36 (1H, s, C=C*H*), 8.66 (1H, d, *J* = 8.5 Hz, Ar-*H*), 8.44 (1H, d, *J* = 8.5 Hz, Ar-*H*), 8.23 (1H, s, N*H*), 8.07 (1H, d, *J* = 8.5 Hz, Ar-*H*), 7.99 (1H, s, N*H*), 7.99–7.92 (4H, m, Ar-*H*), 7.70–7.57 (4H, m, Ar-*H*), 7.09 (2H, d, *J* = 9.0 Hz, Ar-*H*), 7.01 (1H, d, *J* = 8.5 Hz, Ar-*H*), 6.63 (2H, s, Ar-*H*), 5.43 (2H, s, Ar-OC*H*-Ar), 5.03 (2H, s, Ar-OC*H*-Ar), 3.99–3.94 (6H, m, Ar-OC*H*-CH_2), 1.82–1.72 (6H, m, C*H*), 1.47–1.25 (54H, m, C*H*), 0.89–0.86 (9H, m, C*H*).

^{13}C NMR (125 MHz, $CDCl_3$): δ (ppm) 163.77, 161.47, 160.23, 156.79, 153.45, 152.66, 149.71, 147.15, 138.18, 135.98, 134.62, 131.31, 128.98, 128.17, 126.13, 125.32, 124.96, 123.63,

123.28, 123.02, 121.72, 115.18, 114.53, 106.25, 104.77, 73.57, 70.80, 70.31, 69.26, 32.06, 30.49, 29.90, 29.85, 29.80, 29.58, 29.54, 29.51, 26.28, 26.25, 22.83, 14.26.

HRMS (ESI): *m/z* calculated for $C_{71}H_{99}N_4O_8$ = 1135.7457 $[M+H]^+$, found 1135.7429.

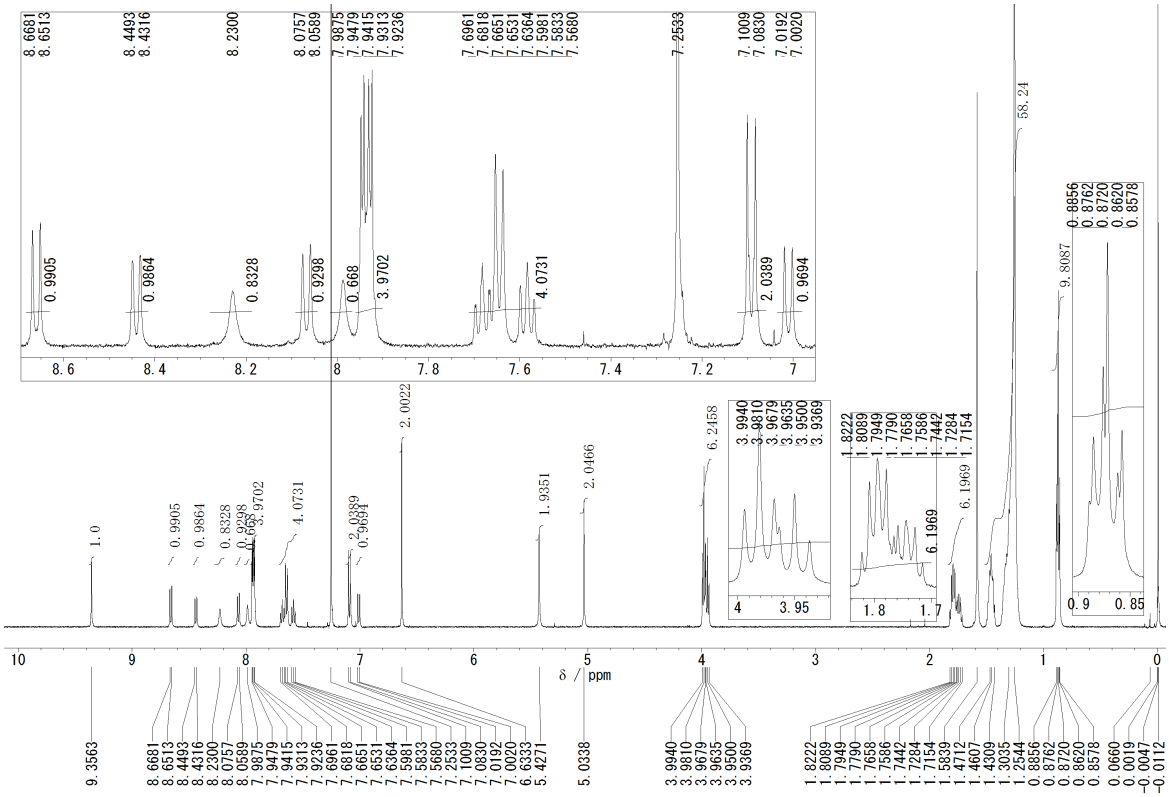

Chart 3-1. ^{1}H NMR spectrum of compound **3** in $CDCl_3$ at 298 K.

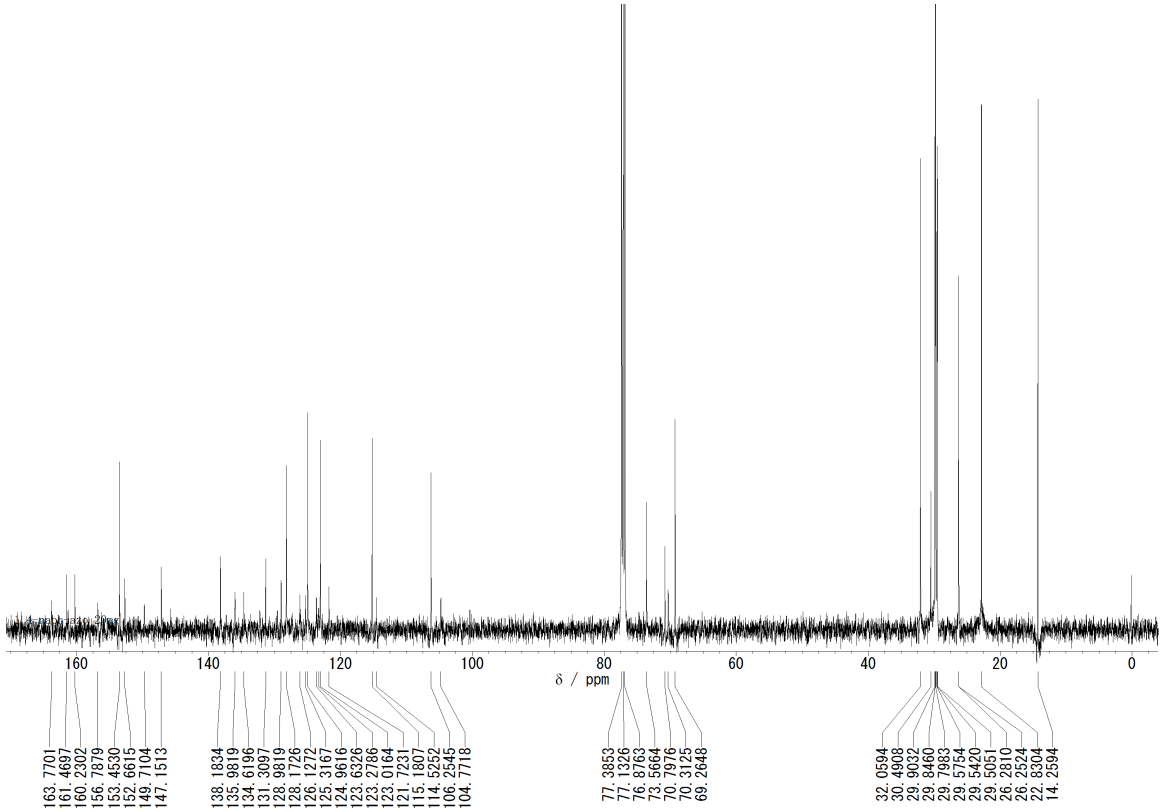

Chart 3-2. ^{13}C NMR spectrum of compound **3** in $CDCl_3$ at 298 K.

3-8. References and Notes

1. a) T. F. A. De Greef, M. M. J. Smulders, M. Wolffs, A. P. H. J. Schenning, R. P. Sijbesma, E. W. Meijer, *Chem. Rev.* **2009**, *109*, 5687–5754. b) T. Aida, E. W. Meijer, S. I. Stupp, *Science* **2012**, *335*, 813–817. c) R. D. Mukhopadhyay, A. Ajayaghosh, *Science* **2015**, *349*, 241–242.
2. a) Y. Tidhar, H. Weissman, S. G. Wolf, A. Gulino, B. Rybtchinski, *Chem.—Eur. J.* **2011**, *17*, 6068–6075. b) I. D. Tevis, L. C. Palmer, D. J. Herman, I. P. Murray, D. A. Stone, S. I. Stupp, *J. Am. Chem. Soc.* **2011**, *133*, 16486–16494. c) P. A. Korevaar, S. J. George, A. J. Markvoort, M. M. J. Smulders, P. A. J. Hilbers, A. P. H. J. Schenning, T. F. A. De Greef, E. W. Meijer, *Nature* **2012**, *481*, 492–496. d) S. Ogi, K. Sugiyasu, S. Manna, S. Samitsu, M. Takeuchi, *Nat. Chem.* **2014**, *6*, 188–195. e) A. Aliprandi, M. Mauro, L. De Cola, *Nat. Chem.* **2016**, *8*, 10–15.
3. R. B. Martin, *Chem. Rev.* **1996**, *96*, 3043–3064.
4. D. Zhao, J. S. Moore, *Org. Biomol. Chem.* **2003**, *1*, 3471–3491.
5. a) S. Yagai, T. Nakajima, T. Karatsu, K. Saitow, A. Kitamura, *J. Am. Chem. Soc.* **2004**, *126*, 11500–11508. b) S. Yagai, T. Karatsu, A. Kitamura, *Chem.—Eur. J.* **2005**, *11*, 4054–4063.
6. a) K. Murata, M. Aoki, T. Suzuki, T. Harada, H. Kawabata, T. Komori, F. Ohseto, K. Ueda, S. Shinkai, *J. Am. Chem. Soc.* **1994**, *116*, 6664–6676. b) T. Kawasaki, M. Tokuhiro, N. Kimizuka, T. Kunitake, *J. Am. Chem. Soc.* **2001**, *123*, 6792–6800. c) S. Yagai, T. Karatsu, A. Kitamura, *Chem. Commun.* **2003**, 1844. d) S. Yagai, T. Nakajima, K. Kishikawa, S. Kohmoto, T. Karatsu, A. Kitamura, *J. Am. Chem. Soc.* **2005**, *127*, 11134–11139. e) S. Yagai, T. Iwashima, K. Kishikawa, S. Nakahara, T. Karatsu, A. Kitamura, *Chem.—Eur. J.* **2006**, *12*, 3984–3994. f) S. Yagai, A. Kitamura, *Chem. Soc. Rev.* **2008**, *37*, 1520–1529.

7. a) S. Yagai, S. Kubota, H. Saito, K. Unoike, T. Karatsu, A. Kitamura, A. Ajayaghosh, M. Kanesato, Y. Kikkawa, *J. Am. Chem. Soc.* **2009**, *131*, 5408–5410. b) S. Yagai, T. Kinoshita, Y. Kikkawa, T. Karatsu, A. Kitamura, Y. Honsho, S. Seki, *Chem.—Eur. J.* **2009**, *15*, 9320–9324. c) S. Yagai, Y. Goto, T. Karatsu, A. Kitamura, Y. Kikkawa, *Chem.—Eur. J.* **2011**, *17*, 13657–13660. d) S. Yagai, Y. Goto, X. Lin, T. Karatsu, A. Kitamura, D. Kuzuhara, H. Yamada, Y. Kikkawa, A. Saeki, S. Seki, *Angew. Chem. Int. Ed.* **2012**, *51*, 6643–6647. e) S. Yagai, *Bull. Chem. Soc. Jpn.* **2015**, *88*, 28–58. f) M. J. Hollamby, K. Aratsu, B. R. Pauw, S. E. Rogers, A. J. Smith, M. Yamauchi, X. Lin, S. Yagai, *Angew. Chem. Int. Ed.* **2016**, *55*, 9890–9893. g) K. Aratsu, D. D. Prabhu, H. Iwawaki, X. Lin, M. Yamauchi, T. Karatsu, S. Yagai, *Chem. Commun.* **2016**, *52*, 8211–8214.
8. a) S. Yagai, M. Suzuki, X. Lin, M. Gushiken, T. Noguchi, T. Karatsu, A. Kitamura, A. Saeki, S. Seki, Y. Kikkawa, Y. Tani, K. Nakayama, *Chem.—Eur. J.* **2014**, *20*, 16128–16137. b) H. Ouchi, X. Lin, T. Kizaki, D. D. Prabhu, F. Silly, T. Kajitani, T. Fukushima, K. Nakayama, S. Yagai, *Chem. Commun.* **2016**, *52*, 7874–7877.
9. B. M. Rosen, C. J. Wilson, D. A. Wilson, M. Peterca, M. R. Imam, V. Percec, *Chem. Rev*. **2009**, *109*, 6275–6540.
10. M. Kasha, H. R. Rawls, M. Ashraf El-Bayoumi, *Pure Appl. Chem.* **1965**, *11*, 371–392.
11. P. Jonkheijm, P. van der Schoot, A. P. H. J. Schenning, E.W. Meijer, *Science* **2006**, *313*, 80–83.
12. S. Ogi, V. Stepanenko, K. Sugiyasu, M. Takeuchi, F. Würthner, *J. Am. Chem. Soc.* **2015**, *137*, 3300–3307.
13. A Polydispersity index (PDI) is defined as L_w/L_n, where L_w = weight-average length, L_n = number-average length. For **Agg$_{vis}$**, L_w = 37.4, L_n = 29.76. For **Agg$_{fast}$**, L_w = 289.1, L_n = 192.5.

14. M. Endo, T. Fukui, S. H. Jung, S. Yagai, M. Takeuchi, K. Sugiyasu, *J. Am. Chem. Soc.* **2016**, *138*, 14347–14353.

Chapter 4.

Photoresponsive Helical Supramolecular Polymers Exhibiting Morphology Transition upon Thermal Reconstruction

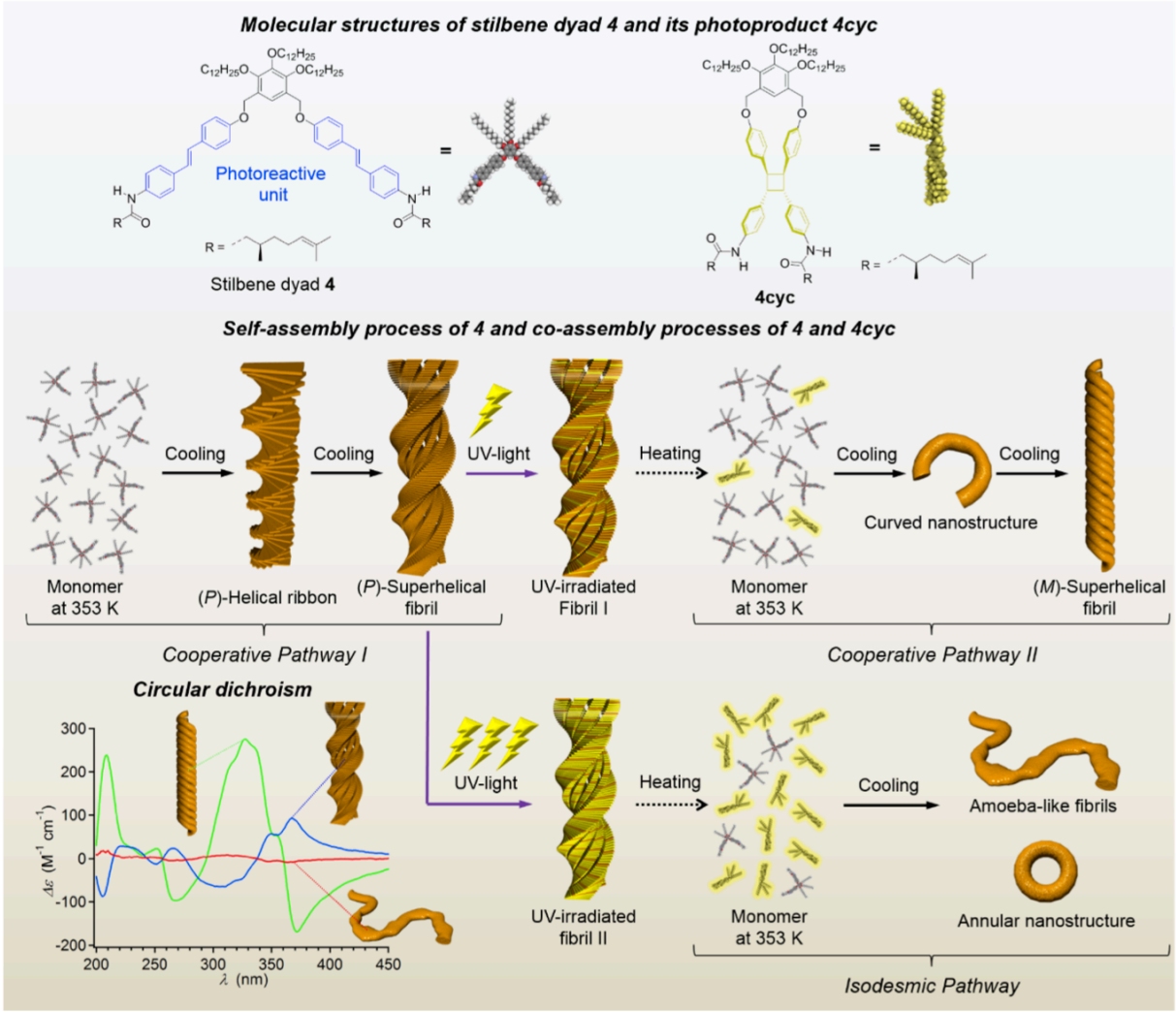

4-1. Abstract

Functionalization of photochromic molecules, based on a specific supramolecular design, has provided a variety of smart molecular assemblies that are able to switch their supramolecular structures or functions by external light stimuli. However, for the interconversion of the system between two assembled states, most of these studies rely on well-defined changes in structures of photochromic molecules, and such photoreactions with large changes in molecular shape often result in the low photoreactivity within the assembled nanostructures. In the following sections, an unexampled supramolecular polymerization of photo-cross-linkable chromophoric dyad molecule is reported, where a small amount of photochemical product generated by UV-irradiation guides the original system into completely different supramolecular polymerization processes. Circular dichroism (CD) and atomic force microscopy (AFM) studies revealed that the intact molecules supramolecularly polymerize into right-handed (*P*-type) superhelical fibrils in dilute apolar solutions. Upon irradiation of the helical fibrils with UV light, the photoreaction afforded a sole cross-linked photoproduct. When *P*-type helical fibrils with small quantity of the photoproduct are reconstructed thermally, a co-polymerization of the intact dyad and its photoproduct is realized to form left-handed (*M*-type) superhelical fibrils. This new molecular design principle will facilitate access to novel paradigms for smart supramolecular assembles.

4-2. Introduction

Naturally occurring photoreactions of π-conjugated moieties enable a critical effect in their complex dynamic organization. For instance, DNA bases in the duplex undergo a photodimerization reaction between base pairs such as guanine and adenine by UV-irradiation, and such a DNA damage, even occurring in a small extent, would lead to malfunctions in duplication and transfer of genetic informations.[1] Although the photoreactions are unfavorable event for biological system, their application to synthetic supramolecular systems can lead to the emergence of intricate stimuli-responsive properties.[2]

Significant progress in the research field of synthetic supramolecular assemblies in this decade has enabled the construction of well-defined supramolecular ensembles with intricate hierarchical structures.[3] Not only sophisticated supramolecular design that can lead the system to thermodynamically organized nanostructures, but also methodologies that can switch the system toward different nanostructures with external stimuli are of important toward further progress of this research field.[4] A widely explored strategy to design stimuli-responsive supramolecular assembly is utilization of photochromic molecules such as azobenzene and diarylethene[5] as building components, by which photochromic reaction of these molecules could lead the system to new equilibrium and switch the aggregates from certain structures to other structures,[6] or to the monomeric state.[7] Most photoresponsive researches thus have focused on large changes in structures of photochromic molecules to switch two states. However, such photochromic reactions with large changes of molecular shapes often give rise to the suppression of photoreactivity within assembled nanostructures.[8] What follows is an unexampled photoresponsive supramolecular polymerization system, wherein a photoproduct generated in an assembled nanostructure fully changes the supramolecular polymerization mechanism of the intact molecules via thermal reconstruction process, guiding the system to

individual assembled nanostructures.

Recently, the research group of S. Yagai has reported a unique supramolecular assembly system shown by a V-shaped azobenzene dyad with chiral side chains, where the two aromatic units are connected by xylylene linker.[9] This dyad showed a remarkable hierarchical supramolecular assembly process in apolar methylcyclohexane (MCH). The circular dichroism (CD) study suggested that the dyad takes a chiral folded conformation via intramolecular π–π stacking between two azobenzene units. The folded dyads further assemble through homogeneous curvature into uniform ring-shaped nanostructures at 293 K. Upon cooling the solution to 273 K, the ring-shaped nanostructures further stack on top of each other to afford tubular nanostructures that further grow into chiral helical fibrils. In another paper, the same group found that an analogous dyad possessing two oligo(*p*-phenylene vinylene) does not give an uniform nanostructure and assembles into irregular fibrils and a small amount of ring-shaped nanostructures.[10] An obvious degradation of the ability to construct uniform nanostructures is attributable to a very strong intramolecular π–π stacking between oligo(*p*-phenylene vinylene) units, which decreases the degrees of conformational freedom of the folded dyad structure needed for further organization.

The above results demonstrate that the conformational property of the folded V-shaped molecule is a key factor for construction of well-defined nanostructures. If the structural property can be tuned by light stimulus, the emergence of different assembled structures would be expected. With this expectation, stilbene V-shaped dyad **4**, in which the two stilbene units are cross-linkable via intramolecular [2+2] photocycloaddition between vinylene group of stilbene units in the folded state, was designed and synthesized (Figure 4-1a).[11] The synthesis and characterization are described in Chapter 4-9. The photocyclization could decrease the degrees of conformational freedom of the folded dyad (Figure 4-1b), which may result in

different assembled structure. The chiral **4** can self-assemble into helical supramolecular polymers with right-handed (*P*-type) helicity, while the cross-linked photoproducts do not form well-defined nanoaggregates. Interestingly, upon co-assembling these intact dyads and their photoproducts by the help of thermal treatments, different co-assembly pathways emerged even in a minor content of the photoproduct, guiding completely different nanoaggregates including supramolecular co-polymers with left-handed (*M*-type) helicity (Figure 4-1c). This study thus could be regarded as an extraordinary example of an integrated self-sorting system guided by external stimuli[12].

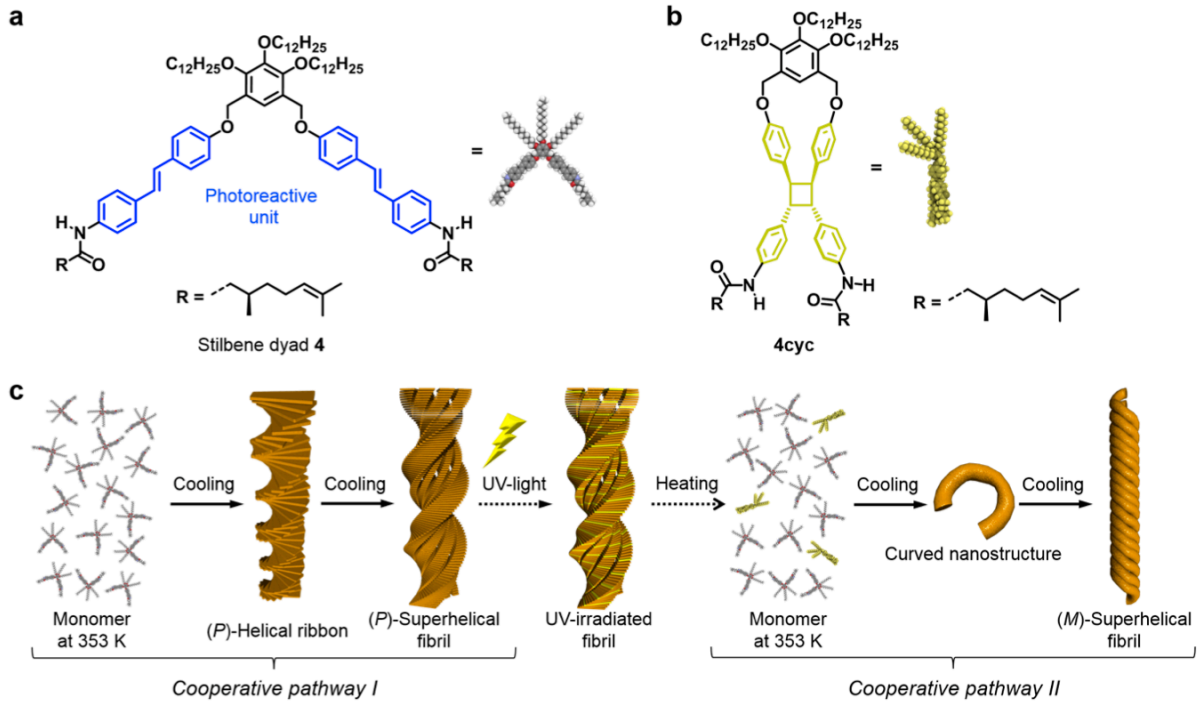

Figure 4-1. (a,b) Chemical structures of the V-shaped stilbene dyad **4** (a) and its [2+2] photocycloaddition product **4cyc** (b). (c) Schematic representation of proposed supramolecular polymerization process of **4** and co-polymerization process of **4** and **4cyc**.

4-3. Cooperative Self-Assembly of Stilbene Dyad 4 in Methylcyclohexane

Supramolecular polymers of stilbene dyad **4** were obtained upon cooling its hot MCH solution ([**4**] = 100 μM) from 353 K to 293 K at a cooling-rate of 1 K min^{-1}. When the temperature went below 333 K, the absorption band at λ_{max} = 323 nm, which is derived from the π–π* electronic transition of *trans*-stilbene chromophores, started to shift hypsochromically, and reached 304 nm at 293 K with the growth of an absorption shoulder around 358 nm (Figure 4-2a). This change is attributed to an electronic interaction of transition dipoles between face-to-face (H-type) stacked stilbene chromophores.[13] In the CD spectroscopic study, the sharp emergence of CD signal was observed and the spectra showed bisignate cotton effect with two positive maxima (341 nm and 360 nm) and one negative maximum (287 nm) at 323 K (Figure 4-2b). The zero-crossing point in the signal is 304 nm that is close to the absorption maximum (312 nm) at 323 K (Figure 4-2). This bisignate CD signal indicates the chiral exciton coupling of the stilbene units stacked in a clockwise (*P*-type) twisted arrangemet.[14] Upon further decreasing the temperature of the solution to 293 K, CD signals became stronger and complicated, giving two positive maxima (348 nm and 365 nm) and a negative maximum (309 nm) (Figure 4-2b). The transition in CD spectra implies unique supramolecular polymerization process of **4** into chiral aggregates (referred to as $\mathbf{4}_{\mathbf{agg}}$).

Because the supramolecular polymerization process of **4** was thermally reversible, the change in the CD intensity (at 365 nm) in the cooling process was monitored to study the aggregation mechanism. When the increase of the normalized CD intensity, which shows the degree of aggregation (α), was plotted as a fraction of temperature, a non-sigmoidal transition was described with a precipitous increase of the α at ~328 K (Figure 4-3c). The feature of the curve is typical of a cooperative (nucleation–elongation) supramolecular polymerization process with the elongation-starting temperature (T_e = 327.7 K), which shows a critical point

between (unfavorable) nucleation and (favorable) elongation steps.[15] This curve was well fitted with a nucleation–elongation theoretical model developed by the research group of E. W. Meijer (Figure 4-3 and see the General Methods in Chapter 1-7 for details).[16] The curve fitting afforded several thermodynamic parameters including the enthalpy difference in the elongation process (ΔH_e = −78.1 kJ mol^{-1}) and the degrees of cooperativity defined by dimensionless constant (K_a = 2.6 × 10^{-5}). The negative value of enthalpy indicates that the cooperative supramolecular polymerization of **4** is enthalpically driven by multiple non-covalent interactions such as hydrogen-bonding and π–π stacking. Such a sufficiently low K_a value (K_a << 1) is suggestive of the high degree of cooperativity in the polymerization process of monomer **4** to **4**$_{agg}$.[29,35] It should be noted that the cooperative curve of **4** was sustained upon decreasing the concentration to 40 μM, while the value of T_e was decreased to 318 K (Figure 4-3 and Table 4-1).

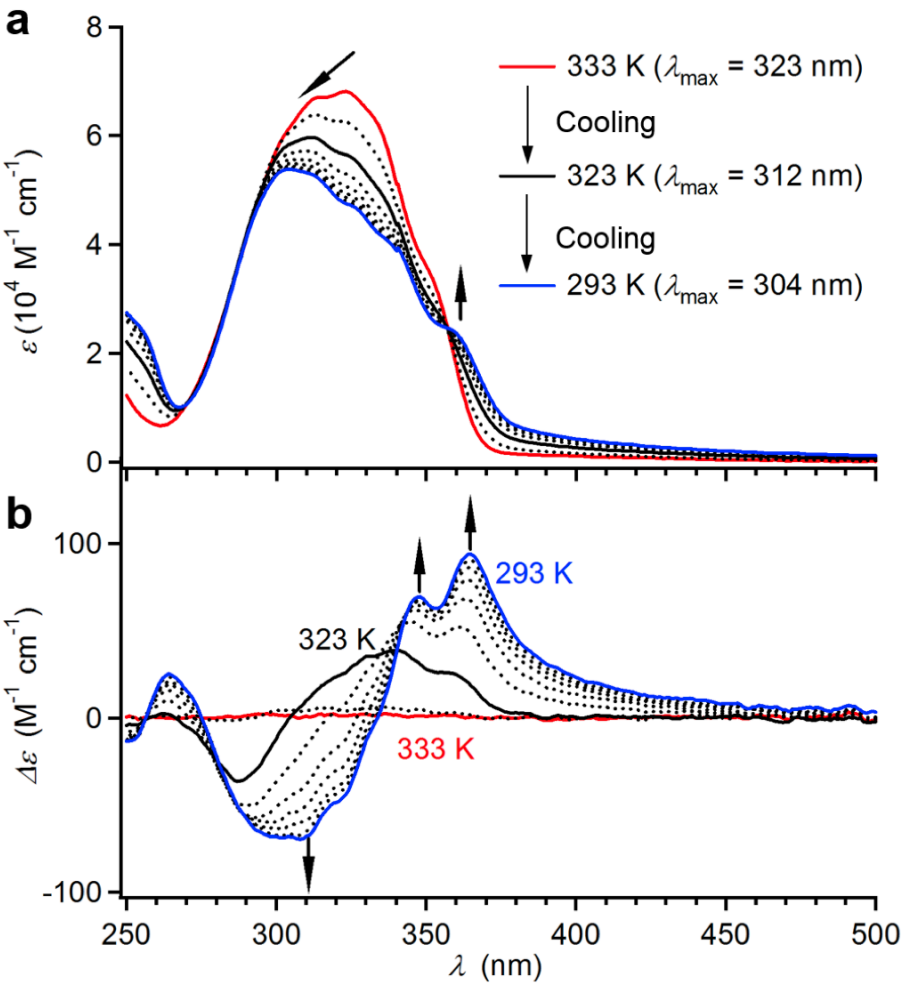

Figure 4-2. (a,b) Temperature-dependent absorption (a) and CD spectra (b) of the MCH solution of **4** ([**4**] = 100 μM) upon cooling the hot solution at a cooling-rate of 1 K min^{-1} (T = 353 K to 293 K), where the spectra are shown at an interval of 5 K. Because spectral change was not observed in the range of 353–333K, only the spectra between 333 K (red spectrum) and 293 K (blue spectrum) are shown for clarity.

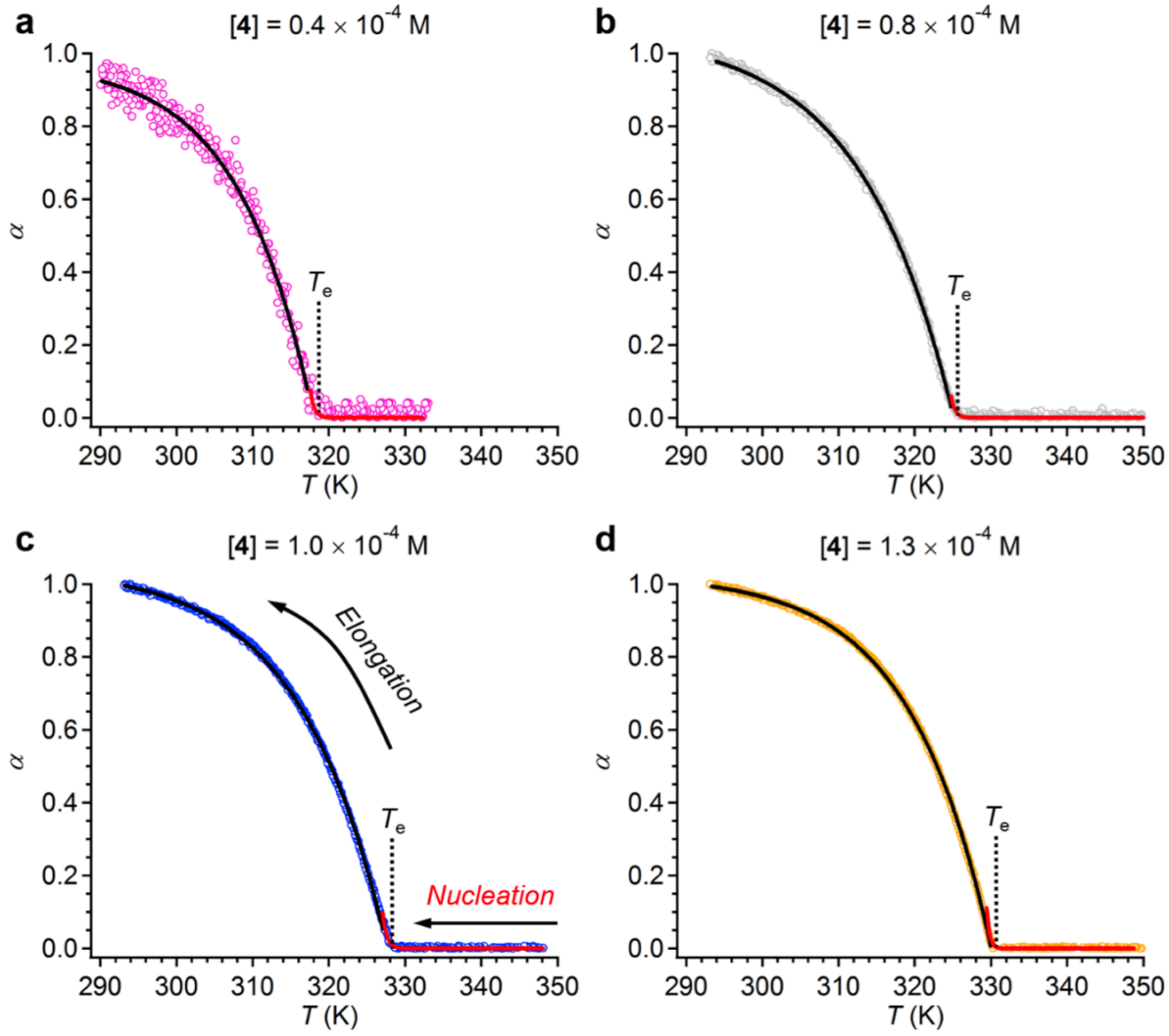

Figure 4-3. (a–d) Temperature-dependent normalized CD intensity (α) monitored at 365 nm, obtained by monitoring the CD intensity of MCH solutions of **4** at four different concentrations upon cooling hot monomeric solutions to 293 K (cooling rate: 1 K min^{-1}). The red and black lines indicate the simulated curves based on the cooperative theoretical model in the nucleation and elongation processes, respectively.

[**4**] (M)	T_e (K)	ΔH_e (kJ mol^{-1})	K_a
1.3×10^{-4}	330.0	-84.6 ± 0.2	1.1×10^{-5}
1.0×10^{-4}	327.7	-78.1 ± 0.4	2.6×10^{-5}
0.8×10^{-4}	325.1	-72.4 ± 0.4	2.2×10^{-5}
0.4×10^{-4}	318.0	-86.7 ± 2.2	4.4×10^{-5}

Table 4-1. Thermodynamic parameters T_e, ΔH_e and K_a for the cooperative supramolecular polymerization of **4** in MCH, estimated from temperature-dependent CD spectra measured at varying concentrations.

4-4. Nanostructures of Right-Handed Helical Aggregates of 4

Atomic force microscopic (AFM) and transmission electron microscopic (TEM) studies demonstrated that the cooperative supramolecular polymerization of **4** results in a formation of well-organized superhelical nanoarchitecture with one-hand helicity ($\mathbf{4}_{\mathbf{agg}}$). In order to visualize nanostructures constructed in the two regimes of the above cooperative polymerization model, the MCH solutions of **4** ([**4**] = 100 μM) at 323 K (just below T_e) and 293 K ($<< T_e$) were spin-coated onto HOPG, respectively. The AFM imaging of the sample obtained from 323-K solution revealed that **4** forms well-defined ribbonlike nanostructures possessing exclusively right-handed (*P*-type) helicity ((*P*)-helical ribbons, Figure 4-4). The (*P*)-helical ribbon is in line with a local helical stacking determined from the CD results that indicated a *P*-type twisting between the stilbene chromophores upon stacking (Figure 4-2b). In the AFM cross-sectional analysis, the (*P*)-helical ribbons show the average thickness of 3.7 ± 0.3 nm (Figure 4-4d), which is consistent with the molecular length of folded **4** (ca. 4 nm, Figure 4-5). The helical pitch and angle (θ) relative to the fiber axis of ribbons are approximately 8 nm and 41°, respectively (Figure 4-4c,e). Based on the thickness of the molecular modeled folded conformer of **4** and a typical π–π stacking distance of 0.35 nm (Figure 4-5), the helical structure is assumed to be composed of approximately 11 stacked molecules of the folded **4** per one pitch (Figure 4-4f).

Upon further cooling to 293 K, higher-order helical fibrils were formed with the average thickness of 45 ± 3 nm as visualized by AFM and TEM (Figure 4-6). The higher-order fibrils also featured right-handed superhelicity ((*P*)-superhelical fibrils), and helical pitches were approximately 300 nm (Figure 4-6e), and helical angles (θ) were approximately 24° (Figure 4-6f). Although the above AFM analysis demonstrated the hierarchical elongation to two individual helical nanostructures, the curve obtained from temperature-dependent CD data

exhibits a single process in the elongation regime (Figure 4-3c). This finding was supported by a temperature-dependent UV absorption measurement as shown in Figure 4-7, which also showed a typical cooperative transition composed of a single elongation process. These results suggest that the final product (*P*)-superhelical fibrils are be formed by bundling the helical ribbons in the elongation end regime (~293 K), and thereby the bundling should not affect the cooling curves.

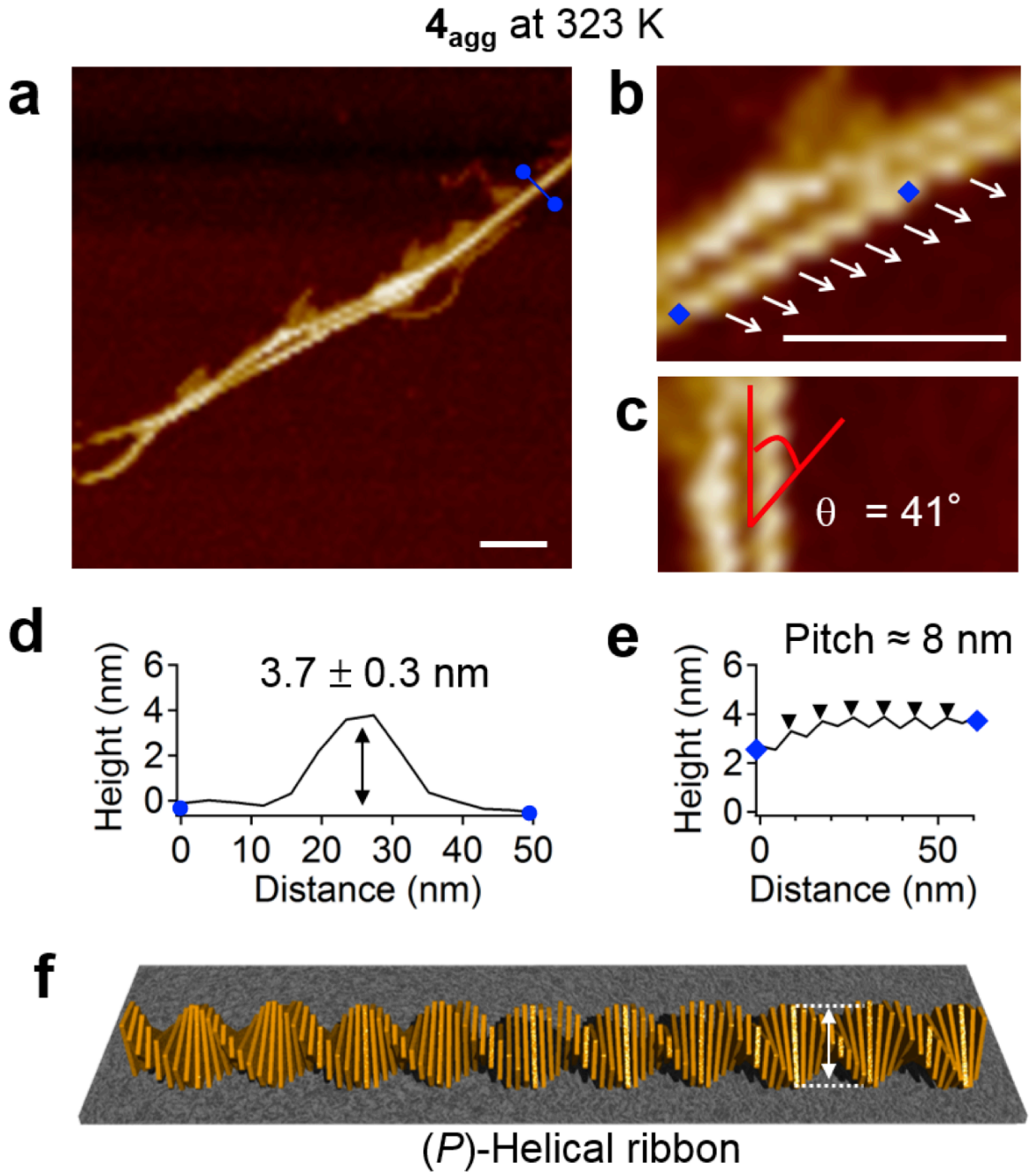

Figure 4-4. (a–c) AFM height image (a) and it magnified images (b,c) of (*P*)-helical ribbons spin-coated from MCH solutions of **4** ([**4**] = 100 μM) at 323 K onto HOPG. (d,e) AFM cross-sectional analyses between the blue dots in images (a) and (b). Scale bar, 50 nm. (f) Schematic illustration of the (*P*)-superhelical ribbon on substrate.

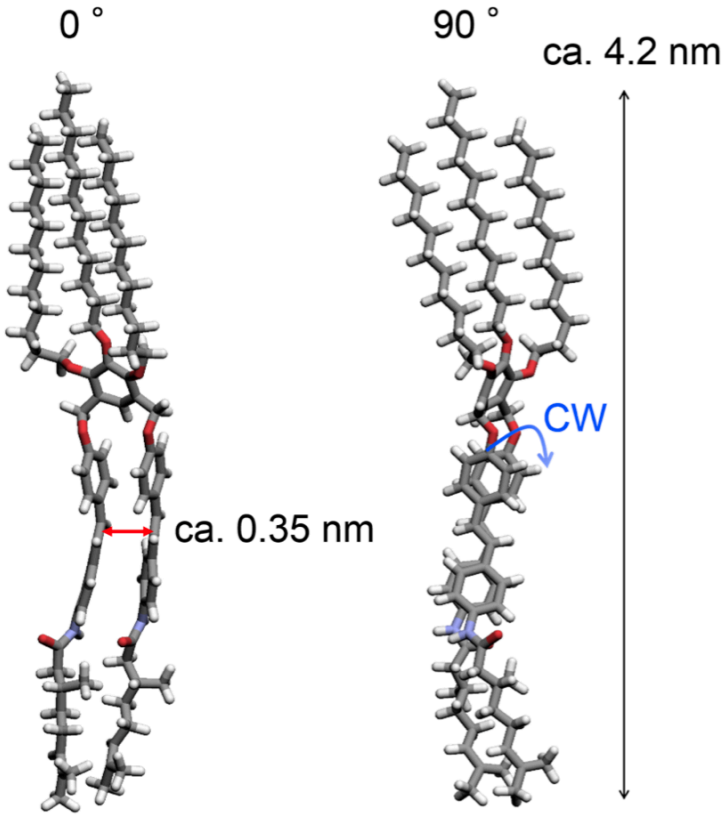

Figure 4-5. Optimized geometry for the folded conformation of **4** with minimized energy, where two stilbene chromophores are stacked in a clockwise (*P*-type) rotational displacement. A typical distance of ca. 0.35 nm between the C=C bonds of stilbene moieties was observed.

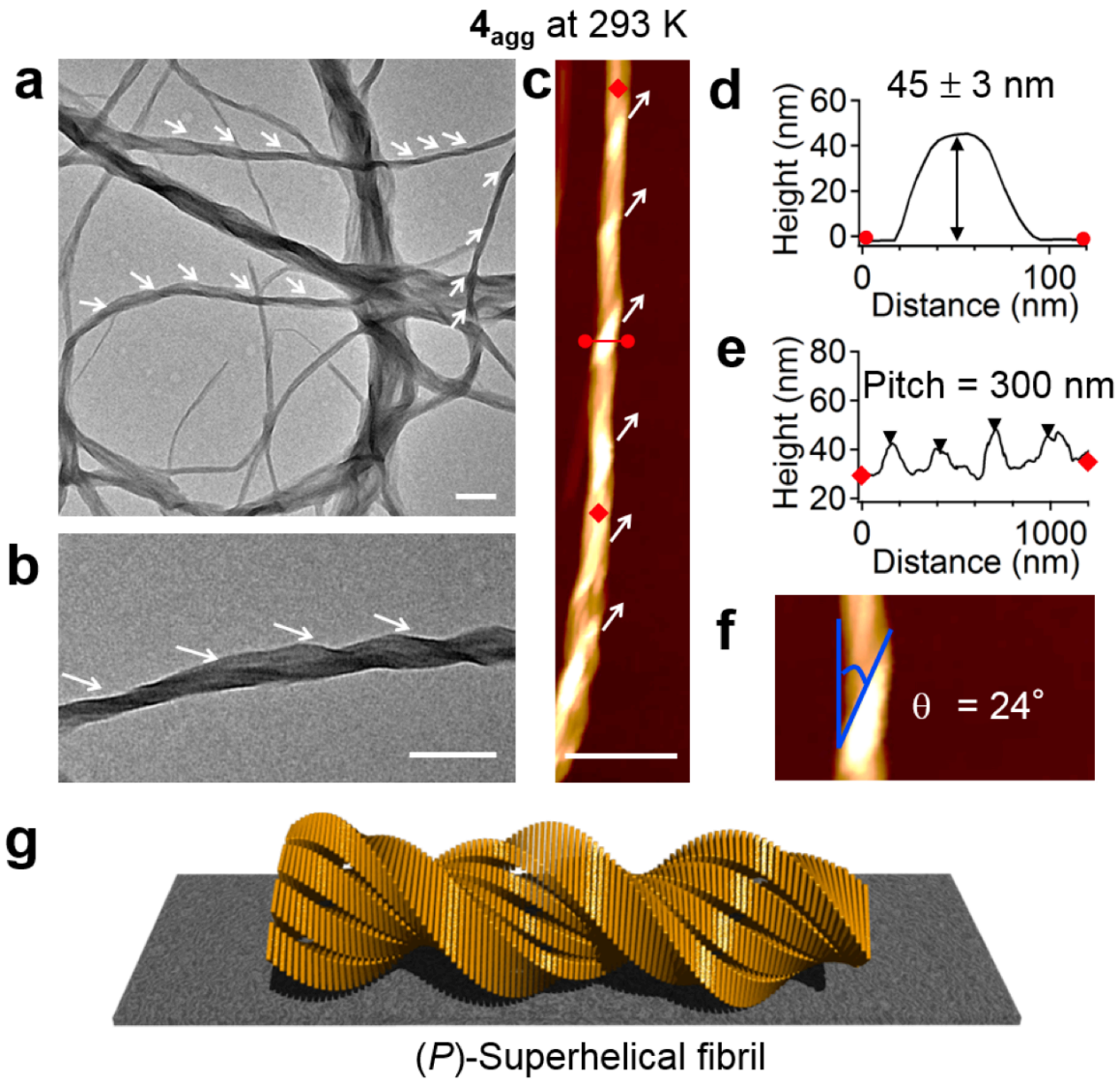

Figure 4-6. (a,b) TEM images and (c,f) AFM height images of (*P*)-superhelical fibrils of $\mathbf{4}_{agg}$ observed at 293 K. Scale bar, 300 nm. (d,e) AFM cross-sectional analyses between the red dots in image (c). Samples were prepared by spin-coating MCH solutions of **4** ([**4**] = 100 μM) at 293 K onto HOPG (for AFM) or carbon-coated copper grid (for TEM). (g) Schematic illustration of the (*P*)-superhelical fibril on substrate.

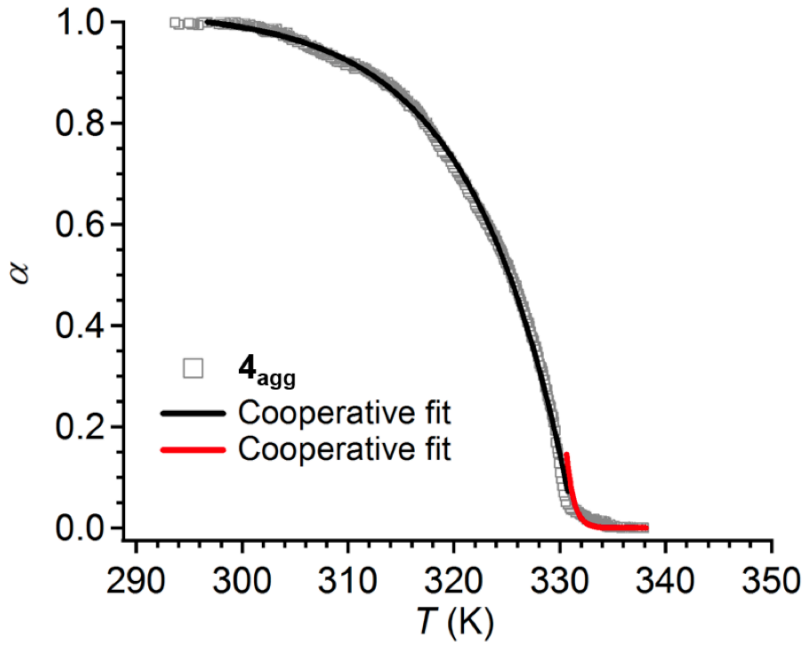

Figure 4-7. Temperature-dependent normalized UV intensity (α) at 365 nm, obtained by monitoring the UV intensity of MCH solutions of **4** ([**4**] = 100 μM) upon cooling a hot monomeric solution to 293 K (cooling rate: 1 K min^{-1}). The red and black lines show the simulated curves based on the cooperative theoretical model in the nucleation and elongation processes, respectively.

4-5. [2+2] Photocycloadditions within Helical Aggregates

If **4** takes a folded conformation, as shown in Figure 4-5, in the supramolecular polymers, the configuration of two stilbene chromophores is suitable for the intramolecular [2+2] photocycloaddition.[17] The molecular modeling for folded-**4** exhibited that the 0.35 nm distance between two vinylene units of two stilbene chromophores, which is very suitable distance for the [2+2] photocycloaddition (Figure 4-5).

When the (*P*)-superhelical fibrils of **4** dispersed in MCH were irradiated with 365-nm UV light, the absorption band of the *trans*-stilbene chromophore decreased, which was compensated by the growth of broad absorption bands in the wavelength region shorter than 255 nm (Figure 4-8a).[18] A 90-min irradiation bleached 80% of the initial absorption intensity. CD measurements exhibited a monotonic decrease in the bisignate signals by UV-irradiation due to the bleaching of the stilbene chromophores (Figure 4-8b). Upon spin-coating the UV-irradiated solution onto HOPG, thin and fragile fibrils were observed by AFM (Figure 4-9), suggesting the dissolution of the photoproduct.

Fourier transform infrared (FT-IR) measurements of the thin films dried from the MCH solutions before ($\mathbf{4}_{\mathbf{agg}}$) and after 90-min UV-irradiation showed a decrease in the C=C−H out-of-plane bending bands (960, 989 and 1002 cm^{-1}) and C=C stretching band (1590 cm^{-1}), which are all related to the vinylene unit of stilbene chromophores (Figure 4-5a,b).[19] Intermolecular photoreaction of **4** can be excluded by the detection of only monomeric species (*m*/*z* = 1382) as measured by electrospray ionization mass (ESI-MS) of the UV-irradiated species: neither dimeric nor oligomeric species have been detected (Figure 4-10c). These results support the emergence of an intramolecular photoreaction and indirectly corroborate a supramolecular polymerization mechanism of **4** via intramolecular folding.

^{1}H NMR analysis of the resulting photoproduct in $CDCl_3$ unveiled the generation of a

sole intramolecular [2+2] cycloaddition product (**4cyc**) and provided insight into its conformational structure. The ^{1}H NMR spectrum of **4cyc** isolated from the sufficiently UV-irradiated solution of $\mathbf{4}_{\mathbf{agg}}$ showed a single set of signals, where all signals in the aromatic region undergo high-field shifts in comparison with those of the intact **4** (Figure 4-11a–e). The two doublets detected in the aliphatic region (H_f' and H_g') are ascribable to a cyclobutane ring.[20] Taking into account the chemical shifts (δ = 4.20 and 4.39 ppm, respectively) and the coupling constants (J = 5.9 Hz) of these doublets, **4cyc** has a stereoselectively constructed cyclobutane ring possessing two couples of *cis*-configurated phenyl groups, and another photoisomer with the cyclobutane ring possessing all-*trans*-configurated four phenyl groups (**4cyc′**) can be excluded (Figure 4-11a). The stereoselective photoreaction demonstrates that **4** takes a particular chiral conformation in the supramolecular polymers (Figure 4-11a, left). As a supportive evidence of this result, a complex ^{1}H NMR spectra that show the formation of several photoproducts including isomerized products in addition to **4cyc** was obtained in an UV-irradiation experiment of monomeric **4** dissolved in $CDCl_3$ (Figure 4-11f).

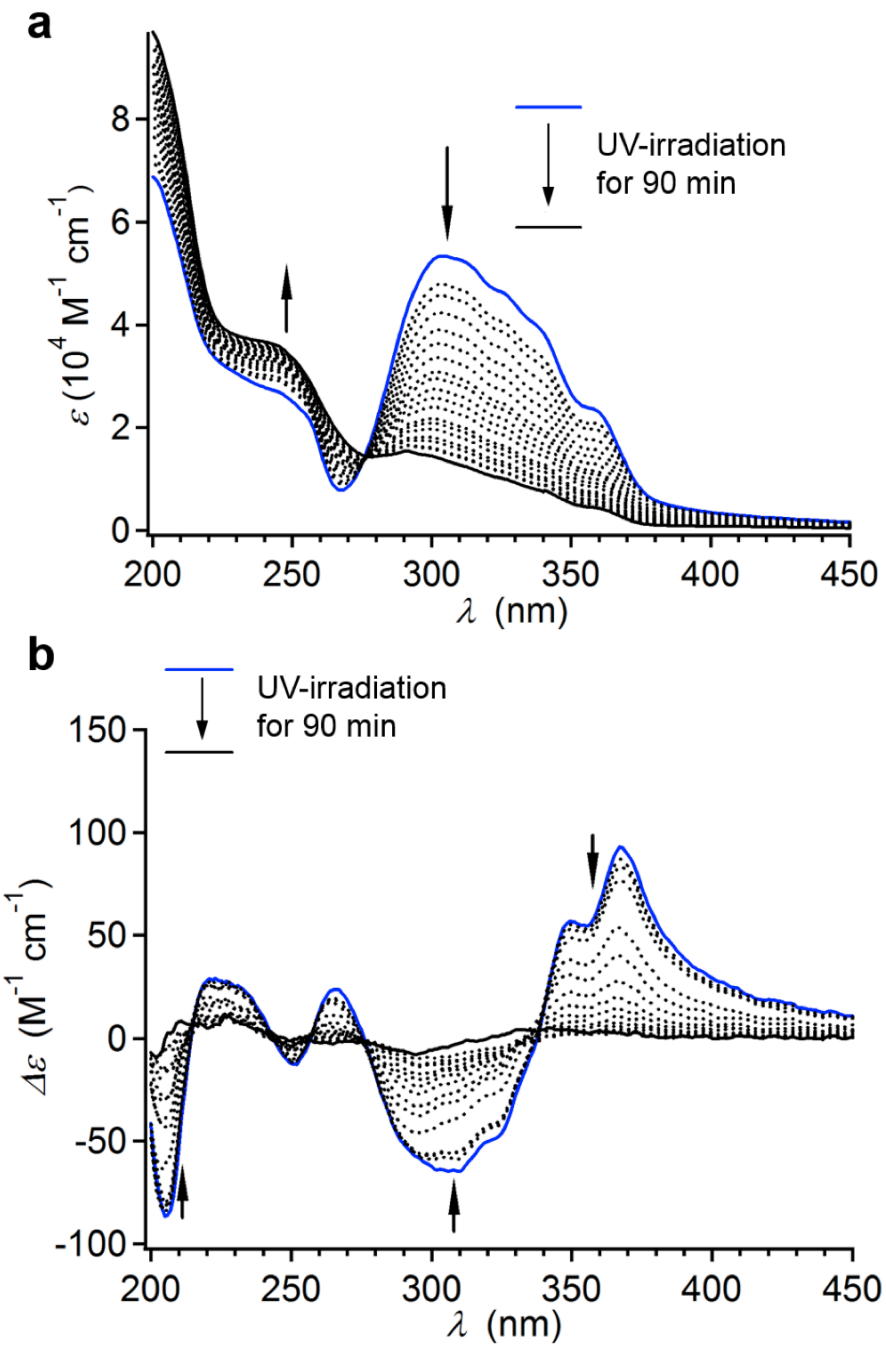

Figure 4-8. (a,b) UV absorption (a) and CD spectra (b) of **4** ([**4**] = 100 μM) in MCH at 293 K upon 365-nm UV-irradiation for 90 min.

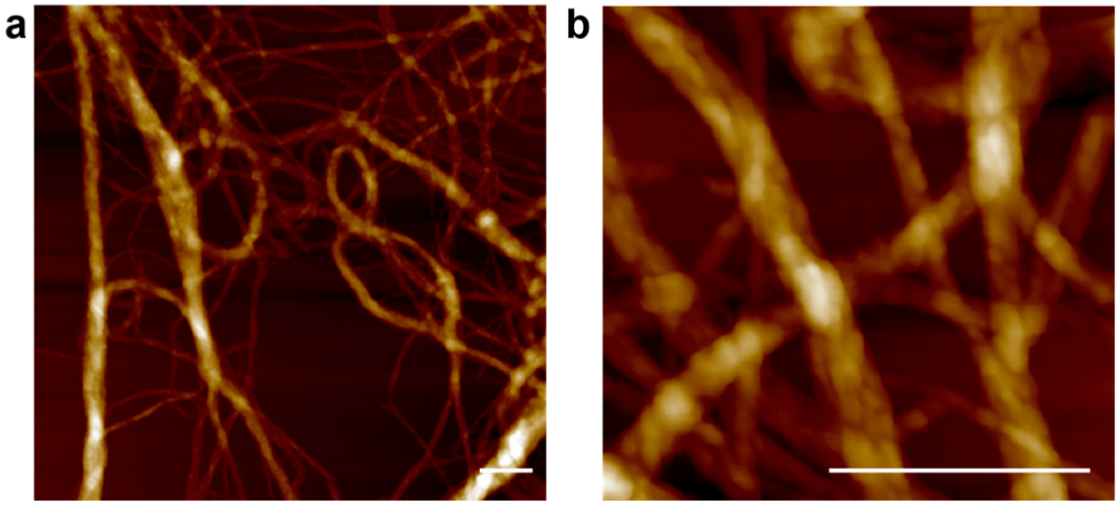

Figure 4-9. (a,b) AFM height images of **(4:4cyc$_{f=0.8}$)$_{agg}$**, spin-coated from MCH solution ([**4**+**4cyc**] = 100 μM) at 293 K onto HOPG. Scale bar, 500 nm.

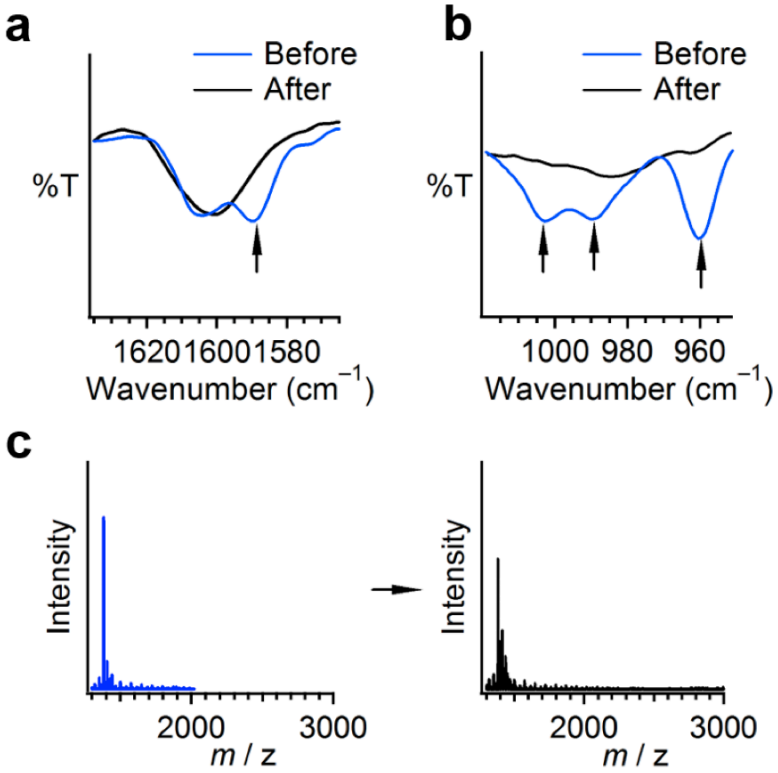

Figure 4-10. (a,b) FT/IR spectra of **4**$_{agg}$ (blue) and UV-irradiated **4**$_{agg}$ (black). Thin film samples for IR spectroscopy were prepared by drying MCH solutions (before and after UV-irradiation for 90 min) onto substrates. (c) ESI-MS spectra of **4** before (blue) and after (black) UV-irradiation for 90 min.

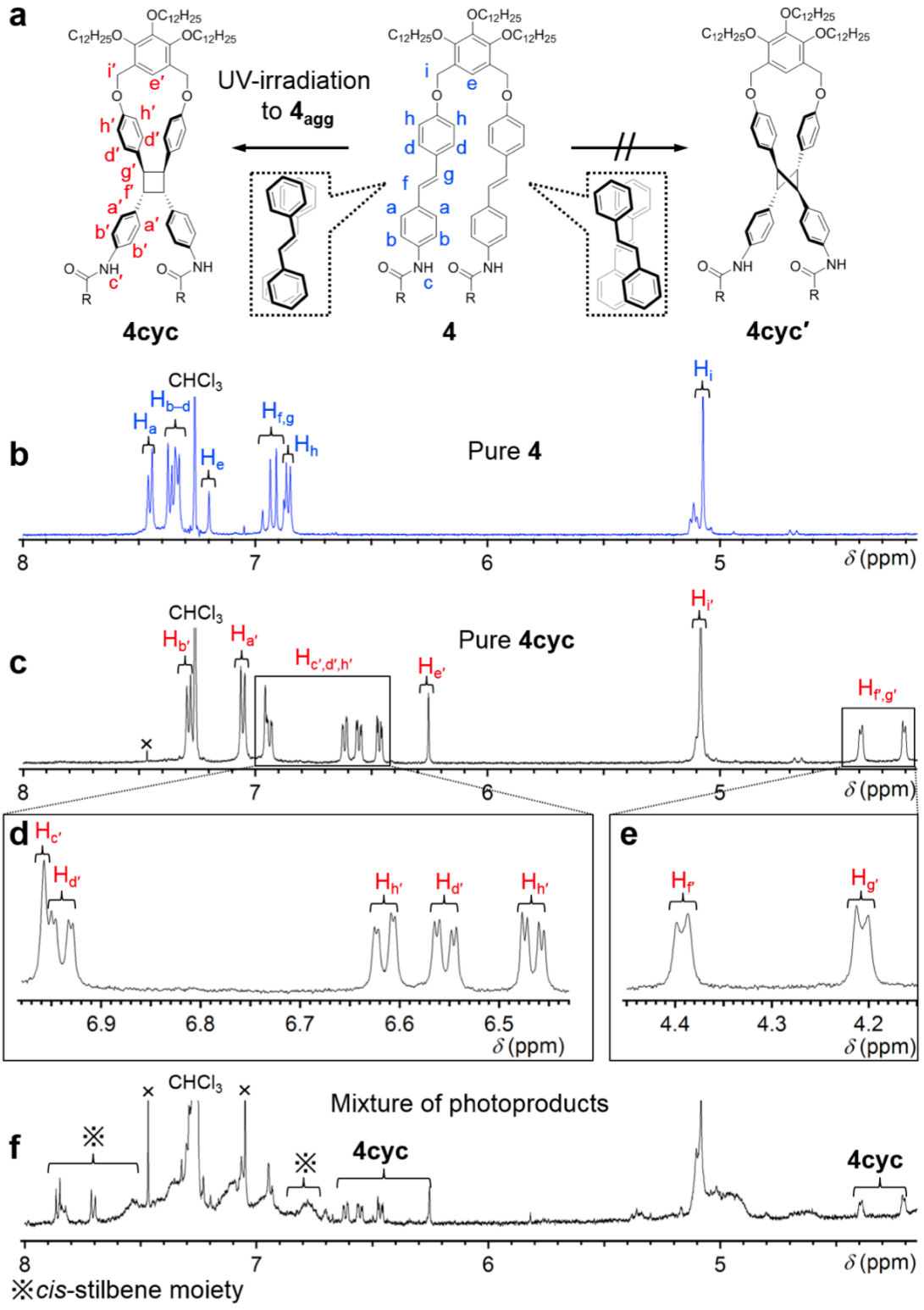

Figure 4-11. (a) Possible intramolecular photo-cross-linked products of **4** with assignment of the corresponding ^{1}H NMR signals. (b) ^{1}H NMR spectrum of **4** in $CDCl_3$. (c–e) ^{1}H NMR spectra of **4cyc** in $CDCl_3$ after UV-irradiation in MCH. (f) ^{1}H NMR spectrum of a mixture of photoproducts in $CDCl_3$ after UV-irradiation in $CHCl_3$.

4-6. Reconstruction of Photoirradiated Aggregates

Photoproduct **4cyc** can dramatically alter the supramolecular polymerization process of **4** via thermal reconstruction, leading to the formation of helical nanofibrils with the chiral sense opposite to that of $\mathbf{4}_{agg}$. In order to address the effect of the content of **4cyc** on the supramolecular polymerization of **4**, the yields of the photocycloaddition were modulated by altering the UV-irradiation time for $\mathbf{4}_{agg}$ ([**4**] = 100 μM) (Figure 4-12a). After UV-irradiation, the solutions were heated to ~353 K to disassemble into monomer state and subsequently cooled to 293 K (cooling rate: 1 K min^{-1}). Hence, UV-irradiated $\mathbf{4}_{agg}$ involving distinct molar fractions of **4cyc** [denoted as $\mathbf{(4:4cyc}_{f=0.1–0.8}\mathbf{)}_{agg}$ were obtained, where subscript *f* shows the molar fraction of **4cyc**], and thermally reconstructed supramolecular coassemblies of **4** and **4cyc** [denoted as $\mathbf{(4:4cyc}_{f=0.1–0.8}\mathbf{)}_{recon}$] with distinct molar fractions of **4cyc** (*f* = 0.1, 0.25, 0.6, 0.8).

In Figures 4-12b and 4-12c, CD spectra of $\mathbf{(4:4cyc}_{f=0.1–0.8}\mathbf{)}_{agg}$ and $\mathbf{(4:4cyc}_{f=0.1–0.8}\mathbf{)}_{recon}$ are compared. The reconstructed coaggregates with minor amount of **4cyc**, *i.e.*, $\mathbf{(4:4cyc}_{f=0.1}\mathbf{)}_{recon}$ and $\mathbf{(4:4cyc}_{f=0.25}\mathbf{)}_{recon}$, showed CD signals with two large positive peaks (209, 327 nm) and two negative peaks (268 and 371 nm) (Figure 4-12c), which are significantly different from the CD signals derived from $\mathbf{(4:4cyc}_{f}\mathbf{)}_{agg}$. The positive and negative CD signs in the longer wavelength region indicate the counterclockwise (*M*-type) helicity in the stacked stilbene chromophores. The CD signals of $\mathbf{(4:4cyc}_{f=0.1}\mathbf{)}_{recon}$ and $\mathbf{(4:4cyc}_{f=0.25}\mathbf{)}_{recon}$ are not well-defined mirror images of those of $\mathbf{4}_{agg}$, and the CD intensities of the reconstructed coaggregates are remarkably high compared to those of the (*P*)-superhelical fibrils of **4** (Figure 4-12c). For instance, the anisotropy factor ($|g| = \Delta\varepsilon/\varepsilon$) of **4** in $\mathbf{4}_{agg}$ is 0.0046 (estimated from CD intensity at 364 nm), which increased to 0.012 (estimated from CD intensity at 372 nm) in $\mathbf{(4:4cyc}_{f=0.1}\mathbf{)}_{recon}$. This remarkable **4cyc**-induced CD enhancement suggests that the supramolecular polymerization of **4** could be sensitively affected by **4cyc**. Further increase in the fraction of **4cyc** to 0.6 and 0.8

[**(4:4cyc$_{f=0.6}$)$_{recon}$** and **(4:4cyc$_{f=0.8}$)$_{recon}$**] resulted in decrease of CD intensity (Figure 4-12c), which demonstrates that the newly observed CD signals of **(4:4cyc$_{f}$)$_{recon}$** do not originate from the self-assembly of sole **4cyc**.

In order to shed light into how supramolecular polymerization process of **4** is affected by **4cyc**, an increase in the CD activity at 370 nm upon the thermal reconstruction (cooling) process was monitored (Figure 4-13a). The **4cyc**-rich reconstructed coaggregates **(4:4cyc$_{f=0.6}$)$_{recon}$** and **(4:4cyc$_{f=0.8}$)$_{recon}$** exhibited cooling curves that are apparently sigmoidal. These sigmoidal curves could be fitted with isodesmic (equal K) model, in which the entire polymerization process is defined by a single equilibrium constant (K_{iso}) (Figure 4-13b,c).[21] The theoretical fitting provided thermodynamic parameters containing enthalpy difference (ΔH_{iso}) and K_{iso} in the isodesmic process, and the melting temperature T_m at which $\alpha = 0.5$ (Table 4-2). The K_{iso} values of **(4:4cyc$_{f=0.6}$)$_{recon}$** and **(4:4cyc$_{f=0.8}$)$_{recon}$** at 298 K are 8.6×10^4 and 8.3×10^4 M^{-1}, respectively. Notably, as already described before, the cooperative supramolecular polymerization of pure **4** (to provide **4$_{agg}$**) was maintained upon decreasing its concentration up to 40 μM [the same concentration of **4** in **(4:4cyc$_{f=0.6}$)$_{recon}$**], which reveals the occurrence of coaggregation via the thermal reconstruction process.

On the other hand, for the **4cyc**-poor reconstructed coaggregates **(4:4cyc$_{f=0.1}$)$_{recon}$** and **(4:4cyc$_{f=0.25}$)$_{recon}$**, cooperative curves in the cooling process was again obtained (Figure 4-13d,e). Notably, these curves are apparently different from those of **4$_{agg}$**, and consist of more gradual nucleation process (see magnified inset in Figure 4-13a) followed by steeper growth of elongation process (Figure 4-13a). These findings suggest that these coaggregates are formed via lower-cooperative processes but with larger enthalpy releases in the elongation regime. Indeed, the theoretical fitting of these experimentally obtained curves to the cooperative model[35] afforded thermodynamic parameters T_e, ΔH_e and K_a (Table 4-3). The value of K_a, which indicates the degrees of cooperativity, increased from 2.6×10^{-5} for **4$_{agg}$** to 5.9×10^{-4} for

(4:4cyc$_{f=0.1}$)$_{recon}$. Furthermore, coaggregates **(4:4cyc$_{f=0.1}$)$_{recon}$** showed more negative enthalpy release ($\Delta H_e = -187.8$ kJ mol^{-1}) compared with that of **4$_{agg}$** ($\Delta H_e = -78.1$ kJ mol^{-1}), which is indicative of stronger adhesion force of nucleus in the coaggregation system despite a decrease in concentration of stilbene chromophores in the whole system. Thus, the analysis demonstrates that the presence of a minor amount of photoproduct **4cyc** enables **4** to polymerize into completely distinctive coaggregates.[22]

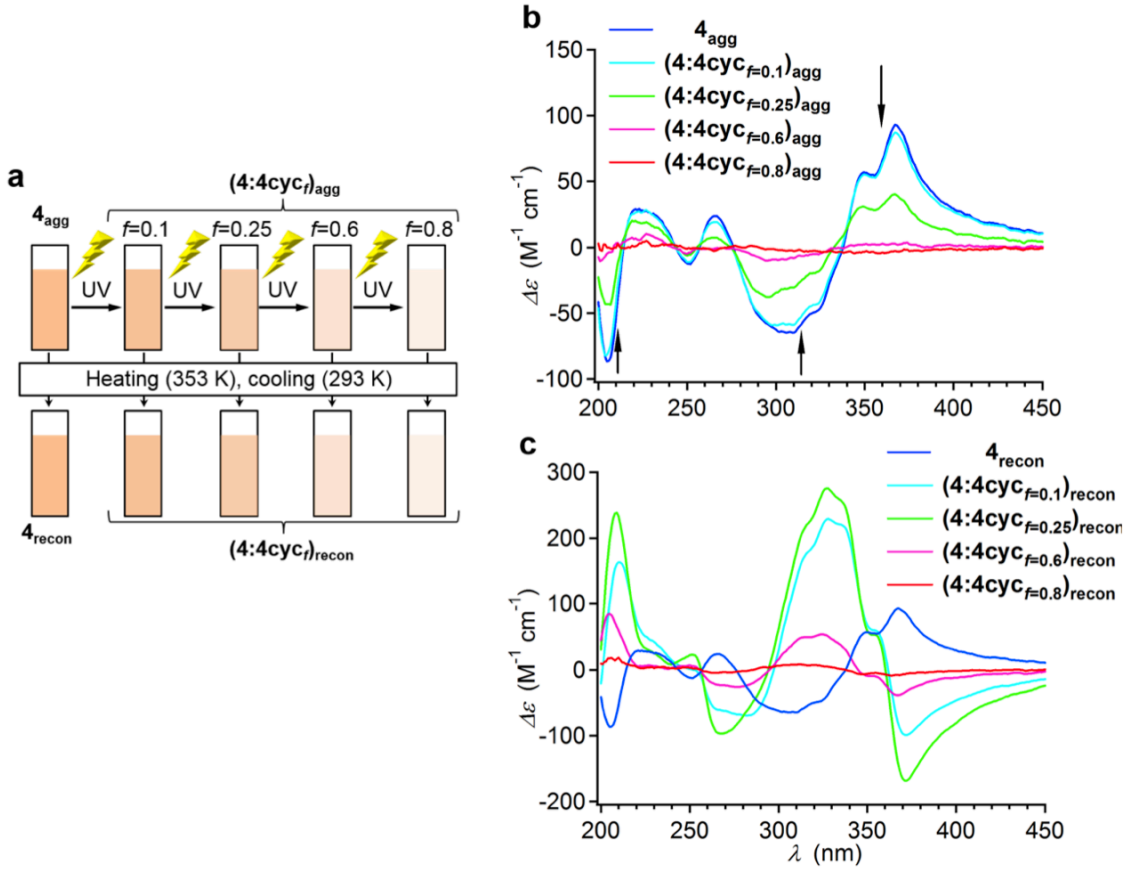

Figure 4-12. (a) Schematic conversion procedure from **4$_{agg}$** to **(4:4cyc$_f$)$_{recon}$**. (b,c) CD spectra of the mixtures of **4** and **4cyc** in MCH ([**4**+**4cyc**] = 100 μM) at 293 K (b) before [**(4:4cyc$_f$)$_{agg}$**] and (c) after thermal annealing [**(4:4cyc$_f$)$_{recon}$**].

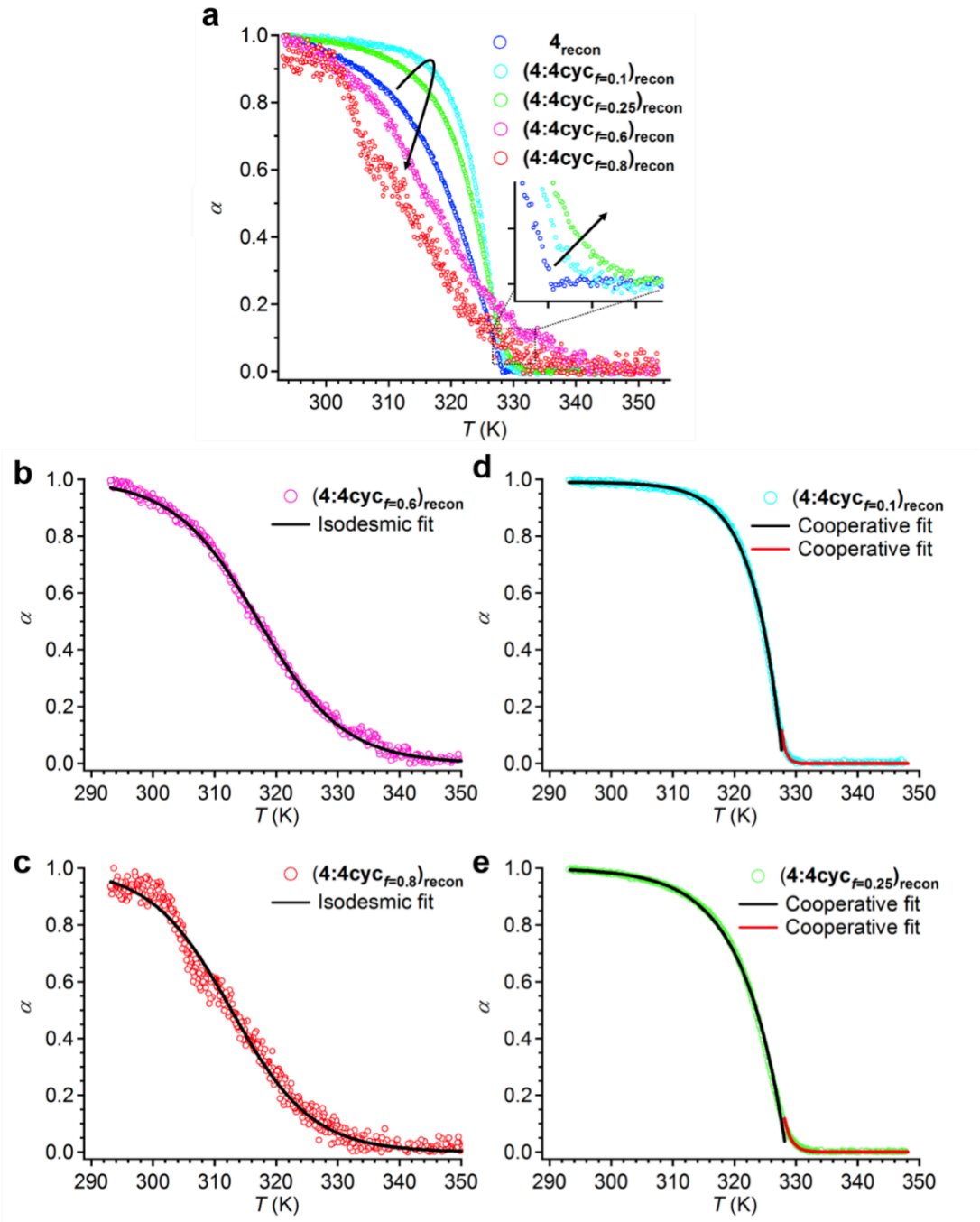

Figure 4-13. (a) Temperature-dependent normalized CD intensity at 370 nm (α) in the thermal reconstruction (cooling) processes of **(4:4cyc$_f$)$_{recon}$** from 353 to 293 K (cooling-rate: 1 K·min^{-1}). The arched arrow shows the change in the cooling curves of **4** upon increasing the fraction of photoproduct **4cyc**. The inset indicates magnified plots in the regime between nucleation and elongation (around T_e), and the straight arrow shows the change in the cooling curves of **4** upon increasing the fraction of **4cyc**. (b,c) Isodesmic theoretical model fitting of the experimental cooling curves of **(4:4cyc$_{f=0.6}$)$_{recon}$** and **(4:4cyc$_{f=0.8}$)$_{recon}$**. (c,d) Cooperative theoretical model fitting of the experimental cooling curves of **(4:4cyc$_{f=0.1}$)$_{recon}$** and **(4:4cyc$_{f=0.25}$)$_{recon}$**.

	fraction of **4cyc**	T_m (K)	ΔH_{iso} (kJ mol^{-1})	K_{iso} (M^{-1})[a]
(**4**:**4cyc**$_{f=0.6}$)$_{recon}$	0.6	317.2	−133.7 ± 0.6	4.9×10^5
(**4**:**4cyc**$_{f=0.8}$)$_{recon}$	0.8	312.7	−136.8 ± 1.4	1.9×10^5

Table 4-2. Thermodynamic parameters for the isodesmic assembly process of **4** in the presence of major amounts of **4cyc** in MCH, determined by fitting the temperature-dependent CD data.

	fraction of **4cyc**	T_e (K)	ΔH_e (kJ mol^{-1})	K_a
4$_{agg}$	0	327.7	−78.1 ± 0.4	2.6×10^{-5}
(**4**:**4cyc**$_{f=0.1}$)$_{recon}$	0.1	327.9	−187.8 ± 0.8	5.9×10^{-4}
(**4**:**4cyc**$_{f=0.25}$)$_{recon}$	0.25	328.4	−128.9 ± 0.6	7.9×10^{-4}

Table 4-3. Thermodynamic parameters for the cooperative assembly process of **4** in the presence of minor amounts of **4cyc** in MCH, determined by fitting the temperature-dependent CD data.

4-7. Nanostructures of Reconstructed Coaggregates

AFM analysis revealed that the reconstructed coaggregates consisting of **4** and **4cyc** have morphologies that are different from $\mathbf{4}_{agg}$. AFM images of the coaggregates $\mathbf{(4:4cyc}_{f=0.8}\mathbf{)}_{recon}$ ([**4**] = 20 μM; [**4cyc**] = 80 μM), reconstructed through the isodesmic mechanism, suggested ameba-like irregular structures with an average width of ca. 20 nm and the average thickness of ca. 2.1 nm as shown by AFM cross-sectional analysis (Figure 4-14a–d). No helical fibrils were observed for these coaggregates while pure **4** at 20 μM afforded elongated nanofibrils (Figure 4-15). These findings demonstrate that the small amount of **4** are integrated into the ameba-like fibrils, and no self-sorting takes place between **4** and **4cyc** through the reconstruction process.[23] The formation of the ill-defined morphologies in this **4cyc**-rich coaggregated system shows that the photocycloaddition of **4** results in a deterioration in its aggregation ability, probably because of a decrease in conformational flexibility of the folded monomer structure. The similar behavior was observed for the previously reported self-assembly of oligo(*p*-phenylene vinylene) dyad,[10] which predominantly yielded irregular fibrils because the conformational flexibility of the folded monomer was decreased by strong intramolecular π–π interaction.

When the molar fraction of **4cyc** decreased to 0.6 [$\mathbf{(4:4cyc}_{f=0.6}\mathbf{)}_{recon}$], a minor amount of annular nanostructures started to emerge in addition to ameba-like fibrils (Figure 4-14e–h). These annular nanostructures have the average thickness of 1.5 ± 0.2 nm and the average outside diameter of 25 ± 2 nm. Such closed nanostructures were not observed for the supramolecular polymerization of individual components either **4** (Figure 4-4 and Figure 4-6) or **4cyc** (Figure 4-16). More interestingly, further decreasing the fraction of **4cyc** to 0.25 [$\mathbf{(4:4cyc}_{f=0.25}\mathbf{)}_{recon}$] and 0.1 [$\mathbf{(4:4cyc}_{f=0.1}\mathbf{)}_{recon}$] guided the production of left-handed (*M*-type) superhelical fibrils (Figure 4-17). The helical angle (θ) was 40° (Figure 4-17d). Combining the

results of the CD studies (Figure 4-12b,c), **4cyc** completely alter the supramolecular polymerization mechanism of **4**, providing superhelical structures with the handedness opposite to those of $\mathbf{4}_{\mathbf{agg}}$.

To elucidate the observed difference in the two cooperative polymerization processes of $\mathbf{4}_{\mathbf{agg}}$ and $\mathbf{(4:4cyc}_{f=0.1}\mathbf{)}_{\mathbf{recon}}$, morphologies of "nuclei" $\mathbf{4}_{\mathbf{nuc}}$ and $\mathbf{(4:4cyc}_{f=0.1}\mathbf{)}_{\mathbf{nuc}}$ were further investigated, which are closely related to the formation of their (co)aggregates. Therefore, AFM observation was conducted for the samples prepared by spin-coating MCH solutions heated around 328 K (T_e) onto HOPG. The AFM images of $\mathbf{4}_{\mathbf{nuc}}$ showed many ill-defined particles with a minor amount of extended helical supramolecular polymer fibrils (Figure 4-18a). In sharp contrast, AFM imaging of $\mathbf{(4:4cyc}_{f=0.1}\mathbf{)}_{\mathbf{nuc}}$ suggested a formation of agglomerates of a plenty of curved nanostructures including annulus with diameters of ca. 25 nm (Figure 4-18b). This finding demonstrates that the formation of curved species is involved in the nucleation for elongation to the (*M*)-superhelical fibrils. On the basis of these results, cooperative supramolecular polymerization mechanisms shown in Figure 4-18c for $\mathbf{4}_{\mathbf{agg}}$ and Figure 4-18d for $\mathbf{(4:4cyc}_{f=0.1}\mathbf{)}_{\mathbf{recon}}$, respectively can be proposed.

In the pure system of **4**, their monomers supramolecularly polymerizes through intramolecular folding into the helical nuclei ($\mathbf{4}_{\mathbf{nuc}}$, Figure 4-18c left). The observed bisignate CD signal of $\mathbf{4}_{\mathbf{nuc}}$ at 323 K (see black curve in Figure 4-2b) that is slightly below elongation temperature (T_e = 328 K) could be attributed to the *P*-type helical stacks between stilbene chromophores, in which folded **4** also takes a *P*-twisted conformation. Below T_e, these helical nuclei $\mathbf{4}_{\mathbf{nuc}}$ elongates precipitously to form (*P*)-helical ribbons at 323 K, which are further bundled to give higher-order (*P*)-superhelical fibrils at 293 K, thus enhancing CD activity (Figure 4-18c, right). In the presence of small amounts of **4cyc**, **4** is supposed to undergo the same folding process. However, extended helical supramolecular polymerization would be interfered by covalently-folded **4cyc**, which cannot form well-organized supramolecular

polymer alone but can facilitate the strong curvature upon coaggregation. Accordingly, in these **4cyc**-involved systems, curved nuclei $\mathbf{(4{:}4cyc_{\mathit{f}=0.1})_{nuc}}$ would be formed (Figure 4-18d, left): this coaggregation system is analogous to the self-aggregation of V-shaped azobenzene dyad into annular nanostructures reported by the research group of S. Yagai.[9] Because of nonhelical stacking of the coaggregates, the resultant nuclei can possess π–π interactive surfaces, and thereby they can further bundle upon extension via π–π interaction (Figure 4-18d, right). FT-IR measurements indicated that the (*P*)- and (*M*)-superhelical supramolecular polymers were formed by the help of hydrogen-bonding between amide groups (Figure 4-19). Because of the unique polymerization process of $\mathbf{(4{:}4cyc_{\mathit{f}=0.1–0.25})_{recon}}$, which is entirely different from that of $\mathbf{4_{agg}}$, the molecular chirality of **4** is transferred to the higher-order structures through a distinctive mechanism, resulting in the formation of the (*M*)-superhelical fibrils that display intricate CD signals derived from a multiple exciton coupling.

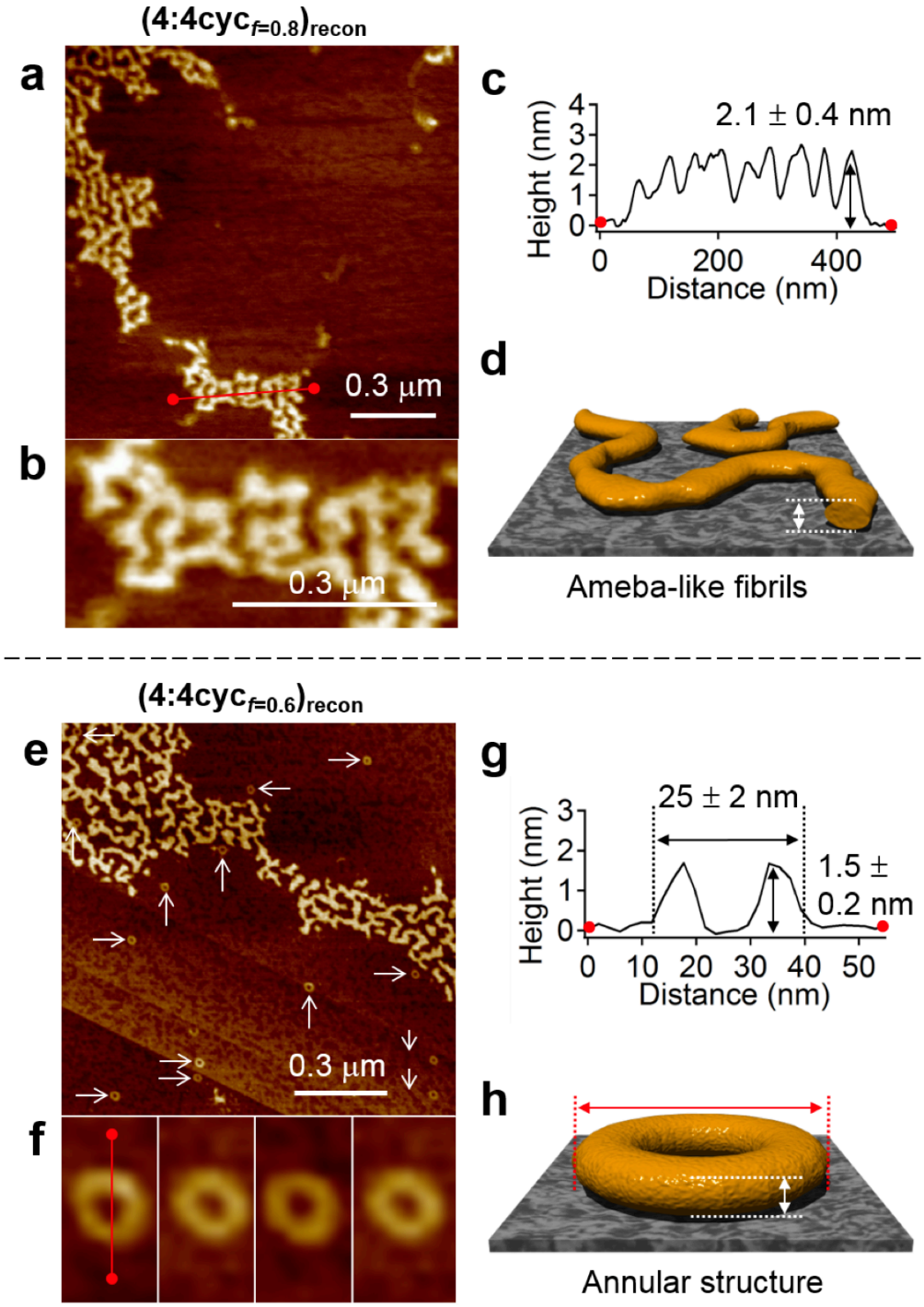

Figure 4-14. (a–c) AFM height image (a), its magnified image (b) and cross-sectional analysis between the red dots in image (a). (c) of **(4:4cyc$_{f=0.8}$)$_{recon}$**. (d) Schematic representation of the ameba-like fibrillar nanostructures of **(4:4cyc$_{f=0.8}$)$_{recon}$**. (e) AFM height image of ameba-like and annular nanostructure of **(4:4cyc$_{f=0.6}$)$_{recon}$**. (f,g) AFM height images (f) and cross-sectional analysis between the red dots in image (f). (g) of annular nanostructure of **(4:4cyc$_{f=0.6}$)$_{recon}$**. (h) Schematic representation of the annular nanostructure of **(4:4cyc$_{f=0.6}$)$_{recon}$**. Samples were prepared by spin-coating the corresponding MCH solutions ([**4**+**4cyc**] = 100 μM) onto HOPG.

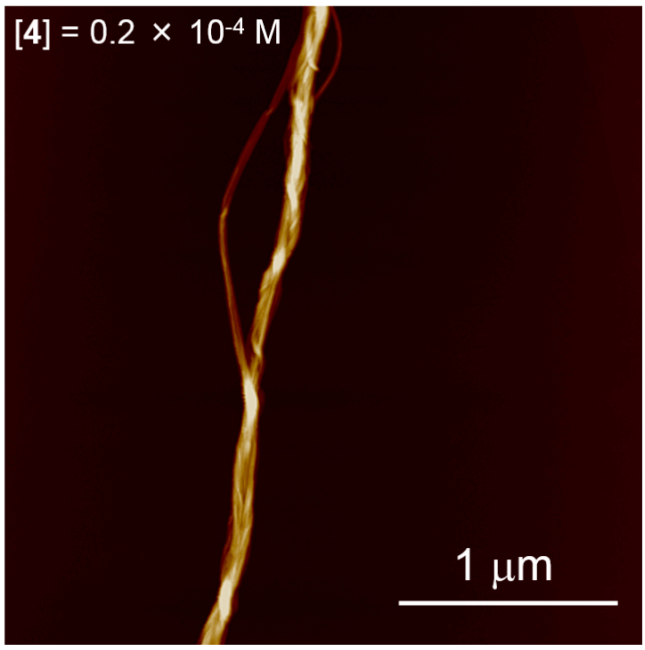

Figure 4-15. AFM height image of $\mathbf{4}_{agg}$, spin-coated from a MCH solution ([**4**] = 20 μM) at 293 K onto HOPG.

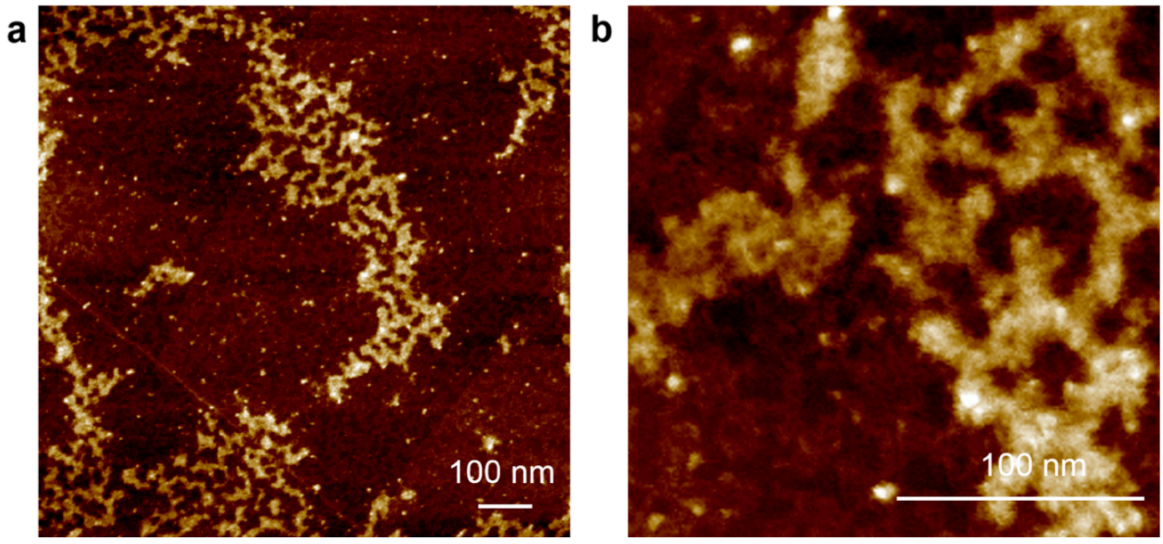

Figure 4-16. AFM height images of ill-defined aggregates of **4cyc**, spin-coated from a MCH solution ([**4cyc**] = 100 μM) at 293 K onto HOPG.

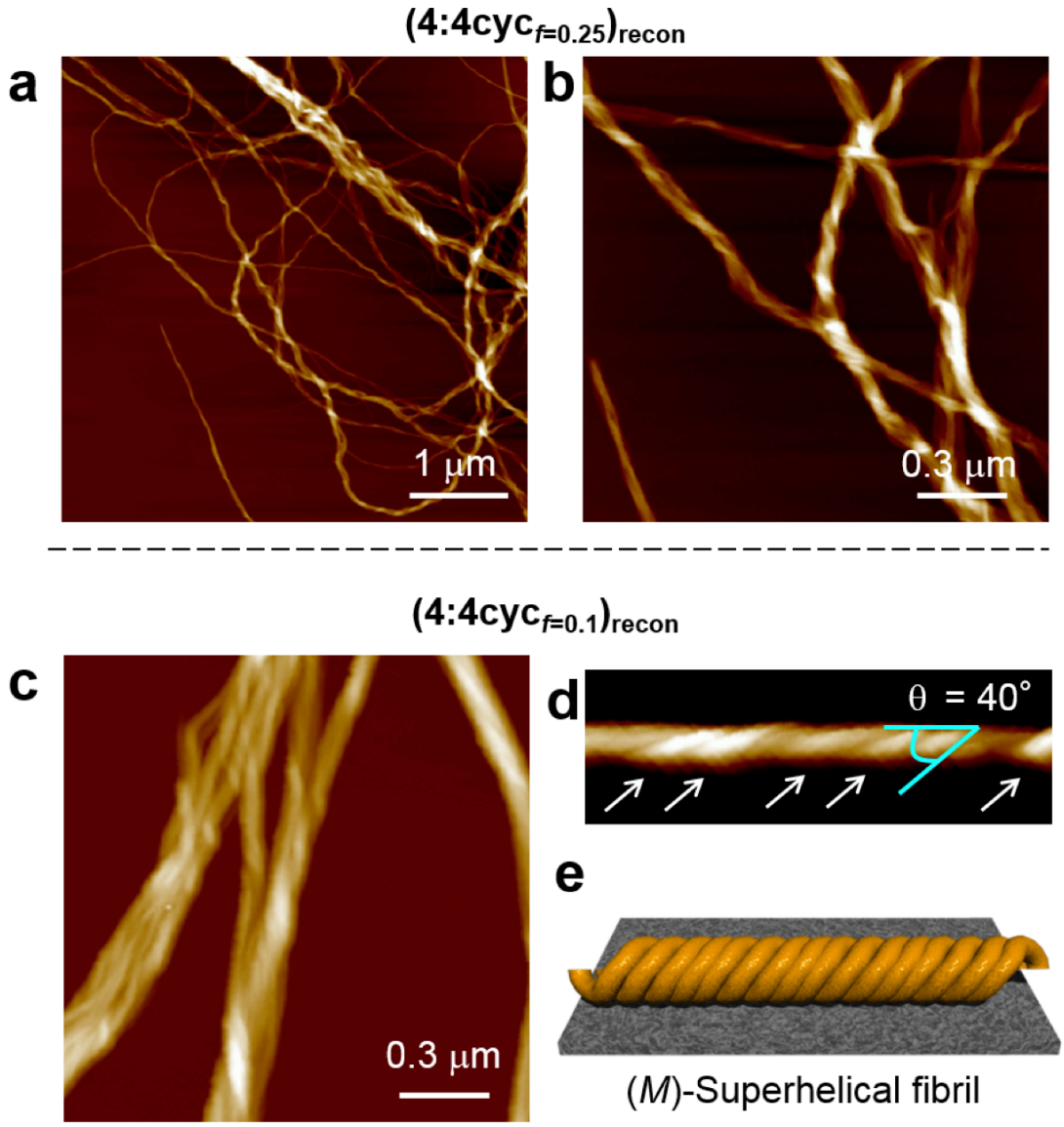

Figure 4-17. (a,b) AFM height images of (*M*)-superhelical fibrils of **(4:4cyc$_{f=0.25}$)$_{recon}$**. (c,d) AFM height images of (*M*)-superhelical fibrils of **(4:4cyc$_{f=0.1}$)$_{recon}$**. (e) Schematic representation of the (*M*)-superhelical fibril. Samples were prepared by spin-coating the corresponding MCH solutions ([**4**+**4cyc**] = 100 μM) onto HOPG.

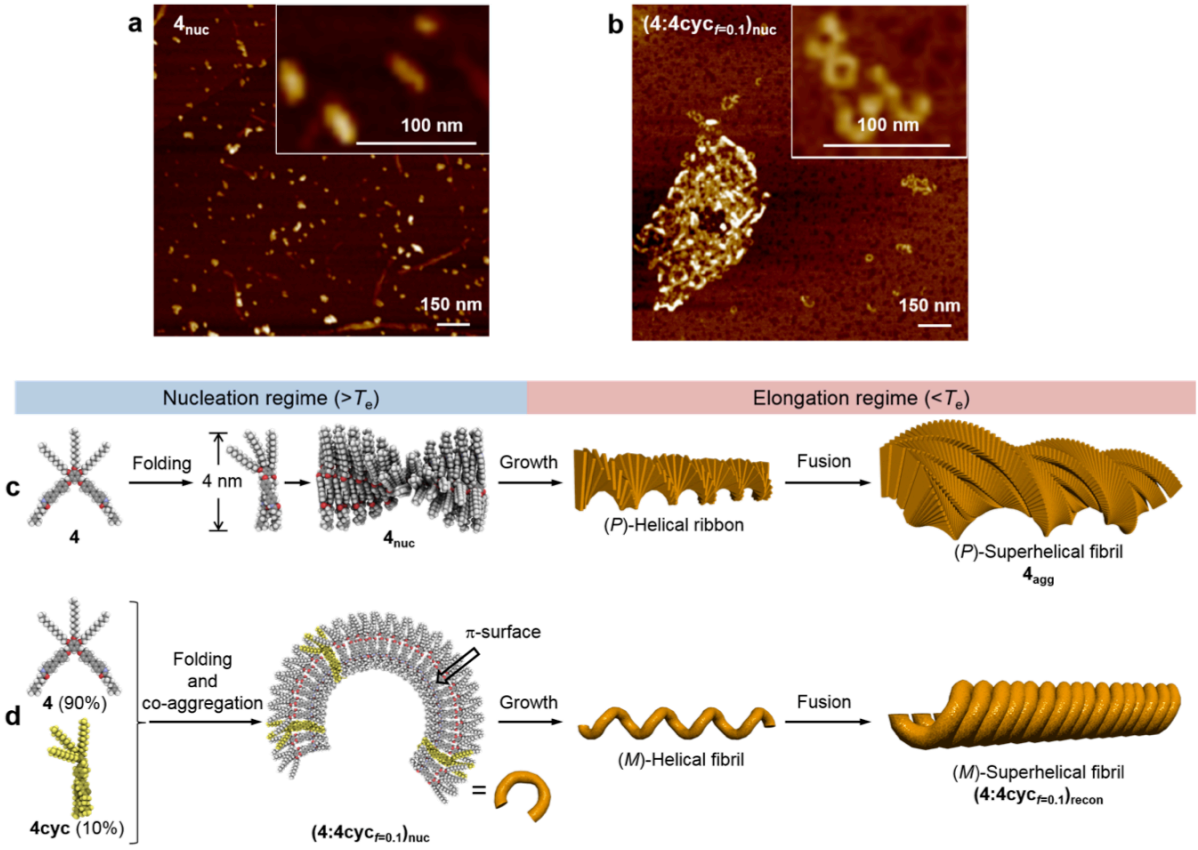

Figure 4-18. (a,b) AFM height images of nanostructures of $\mathbf{4}_{nuc}$ and $\mathbf{(4:4cyc}_{f=0.1}\mathbf{)}_{nuc}$, respectively. Samples were prepared by spin-coating corresponding MCH solutions ([**4**+**4cyc**] = 100 μM) at 328 K (T_e) onto HOPG. (c,d) Schematic representation of the proposed cooperative supramolecular polymerization processes of $\mathbf{4}_{agg}$ and $\mathbf{(4:4cyc}_{f=0.1}\mathbf{)}_{recon}$, respectively.

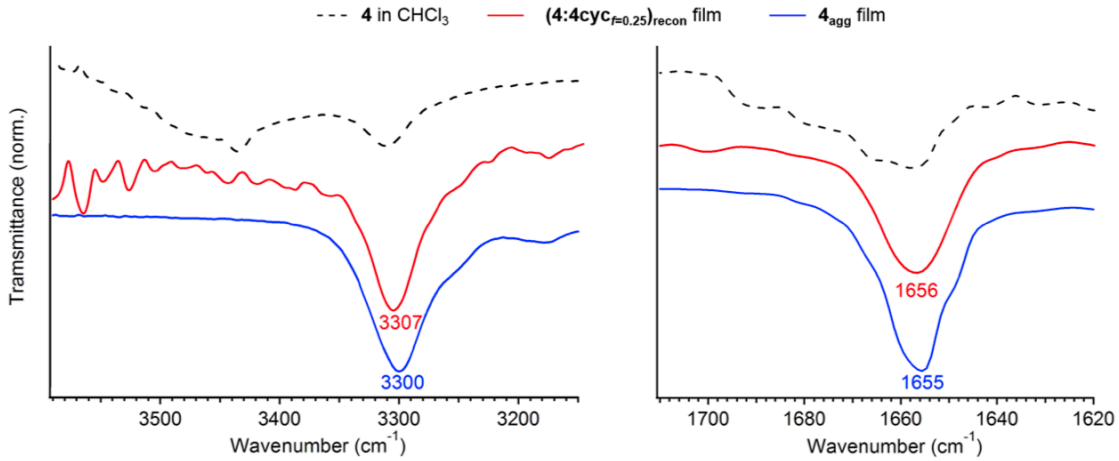

Figure 4-19. FT-IR spectra of **4** ([**4**] = 10 mM) in $CHCl_3$ (dashed curve), $\mathbf{(4:4cyc}_{f=0.25}\mathbf{)}_{recon}$ (red curve) and $\mathbf{4}_{agg}$ (blue curve).

4-8. Discussion and Conclusion

All the spectroscopic and microscopic results mentioned so far disclosed intricate supramolecular polymerization processes of the V-shaped stilbene dyad **4**, which can be controlled by coaggregation with its photoproduct **4cyc**. In Figure 4-20, self- and co-aggregation mechanisms of **4** and **4cyc** with the energetic landscapes are proposed on the basis of the spectroscopic studies. The supramolecular polymerization of **4** via intramolecular folding process and subsequent extended one-dimensional helical stacking is largely different from the curved aggregation of the V-shaped azobenzene dyad (Figure 4-20a).[9] This difference is presumably due to stronger π–π stacking force of the stilbene unit compared to the azobenzene unit. Based on the K_a and T_e values for aggregation of **4**, I calculated 3.7 kJ mol^{-1} for the free energy change of nucleation (ΔG_n) at T_e (Figure 4-20b).[24] The positive ΔG_n value indicates that this cooperative process includes an unfavorable nucleation regime, where uphill nucleation process and subsequent downhill elongation process can be definitely distinguished. In contrast, nearly pure **4cyc** only provides ill-defined aggregates because of impaired π–π stacking force as well as conformational flexibility. By coaggregation with a small amount of **4**, however, **4cyc** can form ameba-like fibrils and annular nanostructures depending on the amount of **4** (Figure 4-20c) via non-cooperative (isodesmic) supramolecular polymerization process (Figure 4-20d). The lack of cooperativity in the **4cyc**-rich systems could be rationally explained based on a dilution effect of **4** by a major amount of **4cyc**, which hampers nucleation of **4**. In the presence of minor amounts of **4cyc**, the mixtures of **4** and **4cyc** copolymerize through another cooperative process with lower cooperativity compared with that of $\mathbf{4_{agg}}$ (Figure 4-20e). The ΔG_n values of the **4cyc**-poor coaggregates were calculated from the K_a and T_e values to be −4.8 for $\mathbf{(4{:}4cyc_{\mathit{f}=0.1})_{recon}}$ and −5.6 kJ mol^{-1} for $\mathbf{(4{:}4cyc_{\mathit{f}=0.25})_{recon}}$, respectively (Figure 4-20f). The negative values of ΔG_n suggest that the cooperative polymerization process of **4cyc**-poor

coaggregates is composed of a favorable downhill nucleation.[15b] The formation of the energetically more stable nucleus is most likely due to the preferential formation of hydrogen bonds that is used for curved aggregation in the nucleation regime.

The present system is extremely remarkable because multicomponent aggregation systems often result in narcissistic self-sorting to give mixtures of thermodynamic products. Although integrative social self-sorting behaviors are well found in natural molecular assembly systems, such highly organized molecular complexes in synthetic systems depend strongly on specific noncovalent interactions. The effective integration of original molecules and their photoproducts into the same supramolecular assembly nanosystem via thermal reconstruction is presumably due to the subtle modification of molecular conformation by photochemical reaction[12]. This approach could be utilized to other photoreactive units possessing appropriate covalent linker moieties. The present results unveil multicomponent supramolecular assembly systems, wherein their morphologies and resulting properties could be controlled by modulation of the mixing ratio of two different components.

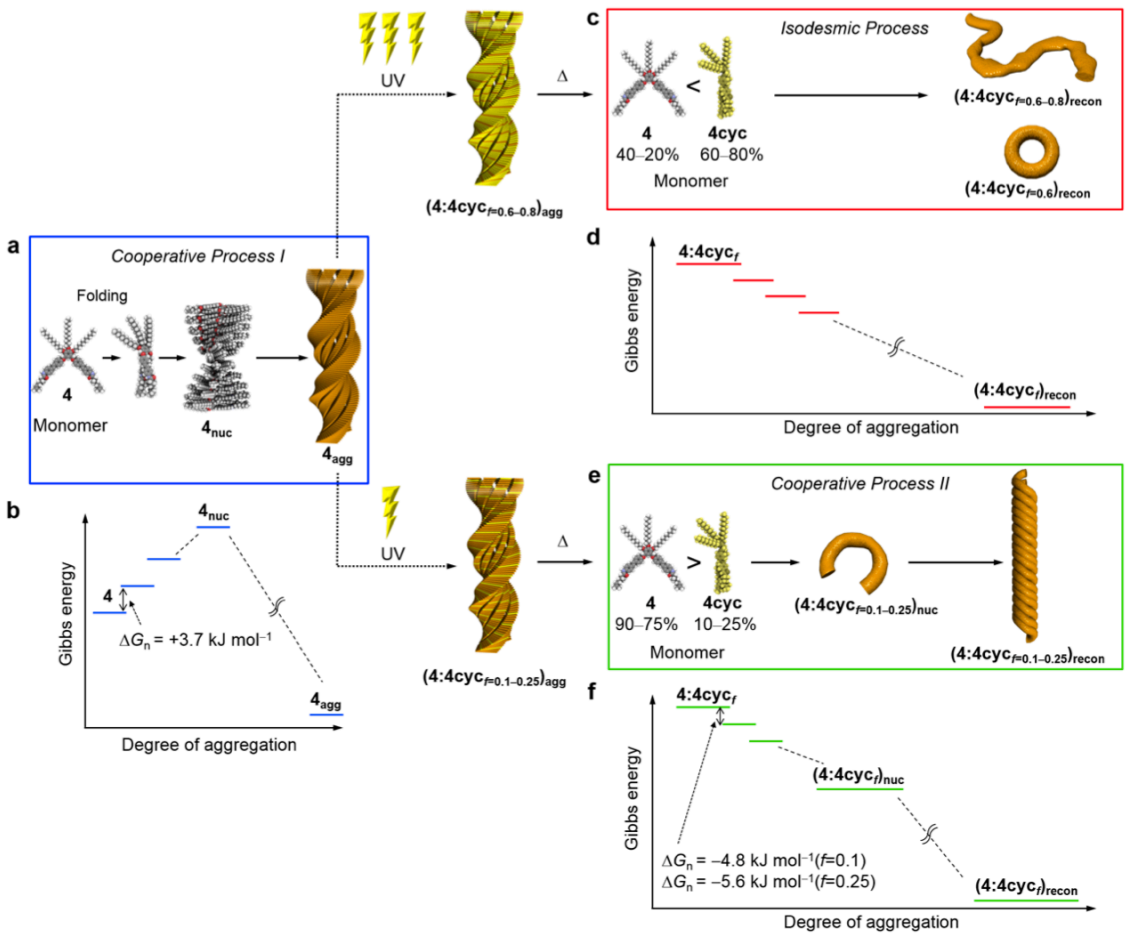

Figure 4-20. (a,c,e) Schematic representation of three (co)aggregation processes of **4** and **4cyc**. (b,d,f) Energy landscapes of three (co)aggregation processes of **4** and **4cyc**. (a,b): Cooperative supramolecular polymerization process for $\mathbf{4_{agg}}$; (c,d): isodesmic coaggregation process for $\mathbf{(4{:}4cyc_{\mathit{f}=0.6–0.8})_{recon}}$; (e,f): downhill cooperative supramolecular copolymerization process for $\mathbf{(4{:}4cyc_{\mathit{f}=0.1–0.25})_{recon}}$.

4-9. Synthesis and Characterization

Compound **4** was prepared according to Synthetic scheme 4-1.

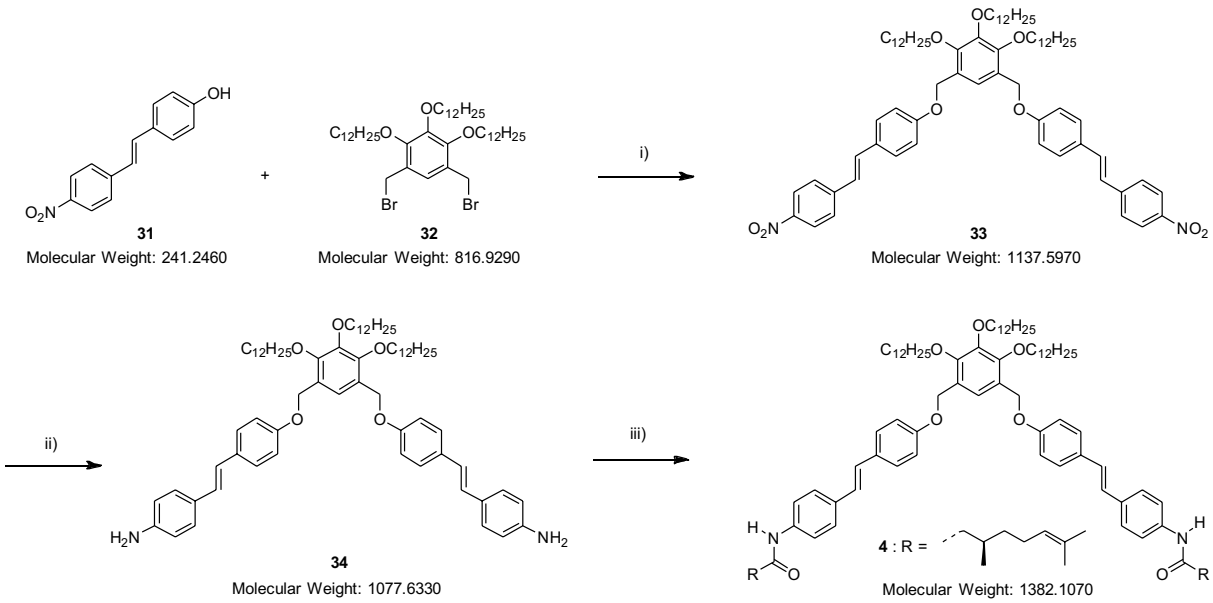

Synthetic scheme 4-1. Synthetic scheme of compound **4**. i) K_2CO_3, DMF, 70 °C; ii) Na_2S, 1,4-dioxane, H_2O, 100 °C; iii) (*R*)-(+)-citronellic acid, DCC, DMAP, CH_2Cl_2, room temperature.

Synthesis of compound 33: Compound **31** (270 mg, 1.12 mmol) was added to a suspension of K_2CO_3 (342 mg, 2.5 mmol) in dry DMF (10 mL) at 70 °C. To this solution, 1,5-bis(bromomethyl)-2,3,4-tris(dodecyloxy)benzene[25] (**32**, 457 mg, 0.56 mmol) dissolved in dry DMF (5 mL) was added dropwise and the mixture was stirred for 18 h at 70 °C under N_2 atmosphere. The reaction mixture was poured into ice-water and the resulting precipitates were purified by column chromatography over silica gel (eluent: $CHCl_3$) to give compound **33** as a yellow solid (534 mg, 84% yield).

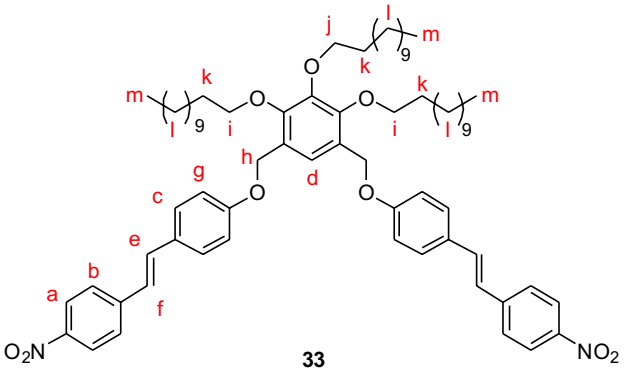

^{1}H NMR (500 MHz, $CDCl_3$, 298 K): δ (ppm) 8.19 (4H, d, J = 8.8 Hz, Ar-H_a), 7.58 (4H, d, J = 8.8 Hz, Ar-H_b), 7.48 (4H, d, J = 8.8 Hz, Ar-H_c), 7.28 (1H, s, Ar-H_d), 7.22 (2H, d, J = 16.3 Hz,

ArCH_e=CHAr), 7.00 (2H, d, J = 16.3 Hz, ArCH=CH_fAr), 6.99 (4H, d, J = 8.8 Hz, Ar-H_g), 5.06 (4H, s, Ar-CH_h), 4.08 (4H, t, J = 6.6 Hz, Ar-OCH_i), 4.02 (2H, t, J = 6.6 Hz, Ar-OCH_j), 1.79–1.69 (6H, m, CH_k), 1.48–1.22 (54H, m, CH_l), 0.89–0.84 (9H, m, CH_m).

^{13}C NMR (125 MHz, $CDCl_3$, 298 K): δ (ppm) 159.70, 152.18, 146.52, 145.92, 144.41, 133.05, 129.18, 128.56, 126.61, 125.65, 124.28, 124.19, 115.23, 74.43, 73.84, 65.45, 32.06, 30.53, 30.51, 29.88, 29.84, 29.82, 29.79, 29.70, 29.67, 29.53, 26.31, 26.29, 22.83, 14.24.

HRMS (ESI): *m/z* calculated for $C_{72}H_{100}O_9N_2Cl$ 1171.7123 $[M+Cl]^-$, found 1171.7159.

Synthesis of compound 34: Compound **33** (150 mg, 0.132 mmol) was dissolved in 1,4-dioxane (5 mL) at 65 °C under N_2 atmosphere. To this solution, Na_2S (500 mg, 2 mmol) dissolved in a mixture of water (1.0 mL) and 1,4-dioxane (5 mL) was added dropwise, and the mixture was stirred for 6.5 h at 100 °C. After the reaction mixture was cooled to r.t., 1,4-dioxane was removed by evaporation. The resulting solid was dissolved in $CHCl_3$ and washed with water. The organic layers were dried over Na_2SO_4 and evaporated to dryness. The resulting solid was reprecipitated from $CHCl_3$-MeOH mixture to give **34** as an orange solid (142 mg, *ca.* 100% yield).

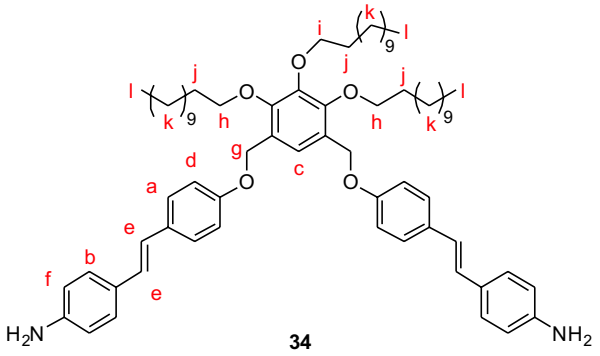

34

^{1}H NMR (500 MHz, $CDCl_3$, 298 K): δ (ppm) 7.38 (4H, d, J = 8.8 Hz, Ar-H_a), 7.30 (4H, d, J = 8.6 Hz, Ar-H_b), 7.28 (1H, s, Ar-H_c), 6.93 (4H, d, J = 8.8 Hz, Ar-H_d), 6.88–6.87 (4H, m, ArCH_e=CH_eAr), 6.66 (4H, d, J = 8.6 Hz, Ar-H_f), 5.03 (4H, s, Ar-CH_g), 4.06 (4H, t, J = 6.6 Hz, Ar-OCH_h), 4.02 (2H, t, J = 6.6 Hz, CH_i), 1.77–1.70 (6H, m, CH_j), 1.40–1.24 (54H, m, CH_k), 0.89–0.86 (9H, m, CH_l).

^{13}C NMR spectrum of this compound could not be measured due to its very low solubility.

HRMS (ESI): *m/z* calculated for $C_{72}H_{105}O_5N_2$ 1077.8018 $[M+H]^+$, found 1077.8018.

Synthesis of compound 4: Compound **34** (84 mg, 0.077 mmol), (*R*)-(+)-citronellic acid (26 mg, 0.15 mmol) and *N,N*-dimethyl-4-aminopyridine (DMAP, 2 mg, 0.018 mmol) were dissolved in dry CH_2Cl_2 (3.0 mL). A solution of *N,N′*-dicyclohexylcarbodiimide (DCC, 31 mg, 0.15 mmol) in dry CH_2Cl_2 (2 mL) was added dropwise at 0 °C, and the mixture was stirred for 17 h at room temperature under N_2 atmosphere. After the resulting white precipitates were filtered off, the filtrate was diluted with CH_2Cl_2 and washed with brine. The organic layer was dried over Na_2SO_4 and evaporated to dryness. The resulting solid was reprecipitated from $CHCl_3$–MeOH mixture and further purified by column chromatography over silica gel ($CHCl_3$:ethyl acetate = 20:1) to give compound **4** as a yellow solid (33 mg, 31% yield).

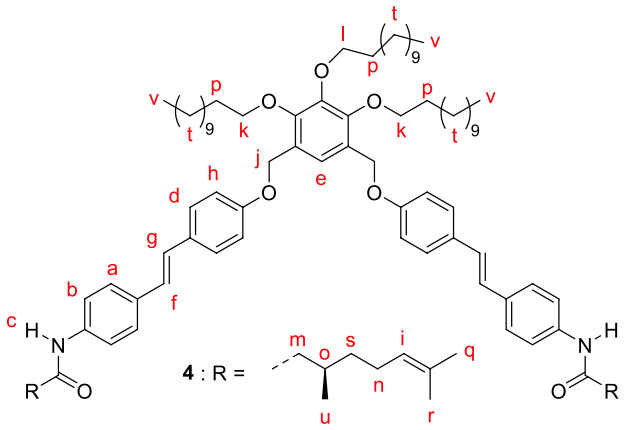

^{1}H NMR (500 MHz, $CDCl_3$, 298 K): δ (ppm) 7.45 (4H, d, J = 8.5 Hz, Ar-H_a), 7.36 (4H, d, J = 8.5 Hz, Ar-H_b), 7.36 (2H, s, amide-H_c), 7.33 (4H, d, J = 8.8 Hz, Ar-H_d), 7.20 (1H, s, Ar-H_e), 6.95 (2H, d, J = 16.3 Hz, ArCH=CH_fAr), 6.89 (2H, d, J = 16.3 Hz, ArCH_g=CHAr), 6.85 (4H, d, J = 8.8 Hz, Ar-H_h), 5.11 (2H, t, J = 7.2 Hz, CH_i=C$(CH_3)_2$), 5.07 (4H, s, Ar-CH_j), 4.05 (4H, t, J = 6.6 Hz, Ar-OCH_k), 4.01 (2H, t, J = 6.6 Hz, Ar-OCH_l), 2.42–1.98 (10H, m, C$H_{m–o}$), 1.78–1.71 (6H, m, CH_p), 1.69 (6H, s, CH_q), 1.61 (6H, s, CH_r), 1.47–1.24 (58H, m, C$H_{s,t}$), 1.02 (6H, d, J = 6.4 Hz, CH_u), 0.90–0.85 (9H, m, CH_v).

^{13}C NMR (125 MHz, $CDCl_3$, 298 K): δ (ppm) 171.08, 158.42, 151.62, 145.87, 136.99, 133.91, 131.80, 130.28, 127.68, 127.61, 126.88, 125.93, 125.91, 124.38, 120.44, 115.16, 74.28, 73.82, 65.45, 45.66, 37.06, 32.07, 30.75, 30.56, 30.53, 29.88, 29.85, 29.83, 29.80, 29.73, 29.69, 29.53, 26.29, 25.86, 25.64, 22.84, 19.75, 17.83, 14.27.

HRMS (ESI): *m/z* calculated for $C_{92}H_{137}O_7N_2$ 1382.0420 $[M+H]^+$, found 1382.0416.

Characterization of photoproduct 4cyc:

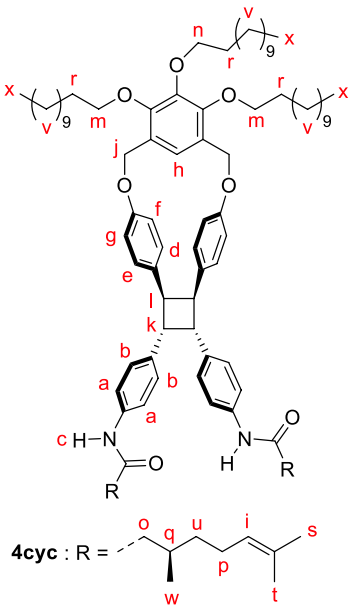

^{1}H NMR (500 MHz, $CDCl_3$, 298 K): δ (ppm) 7.28 (4H, d, J = 8.4 Hz, Ar-H_a), 7.05 (4H, d, J = 8.4 Hz, Ar-H_b), 6.96 (2H, s, amide-H_c), 6.94 (2H, dd, J = 8.6, 2.2 Hz, Ar-H_d), 6.61 (2H, dd, J = 8.4, 2.1 Hz, Ar-H_e), 6.55 (2H, dd, J = 8.5, 2.4 Hz, Ar-H_f), 6.46 (2H, dd, J = 8.4, 2.6 Hz, Ar-H_g), 6.25 (1H, s, Ar-H_h), 5.10 (2H, br, CH_i=C(CH_3)$_2$), 5.08 (4H, s, Ar-CH_j), 4.39 (2H, d, J = 5.9 Hz, cyclobutane-H_k), 4.20 (2H, d, J = 5.9 Hz, cyclobutane-H_l), 4.05 (4H, t, J = 6.6 Hz, Ar-OCH_m), 4.01 (2H, t, J = 6.6 Hz, Ar-OCH_n), 2.35–1.96 (10H, m, C$H_{o–q}$), 1.84–1.75 (6H, m, CH_r), 1.67 (6H, s, CH_s), 1.59 (6H, s, CH_t), 1.51–1.25 (58H, m, C$H_{u,v}$), 0.97 (6H, d, J = 5.9 Hz, CH_w), 0.90–0.86 (9H, m, CH_x).

HRMS (ESI): *m/z* calculated for $C_{92}H_{137}O_7N_2$ 1382.0420 $[M+H]^+$, found 1382.0449.

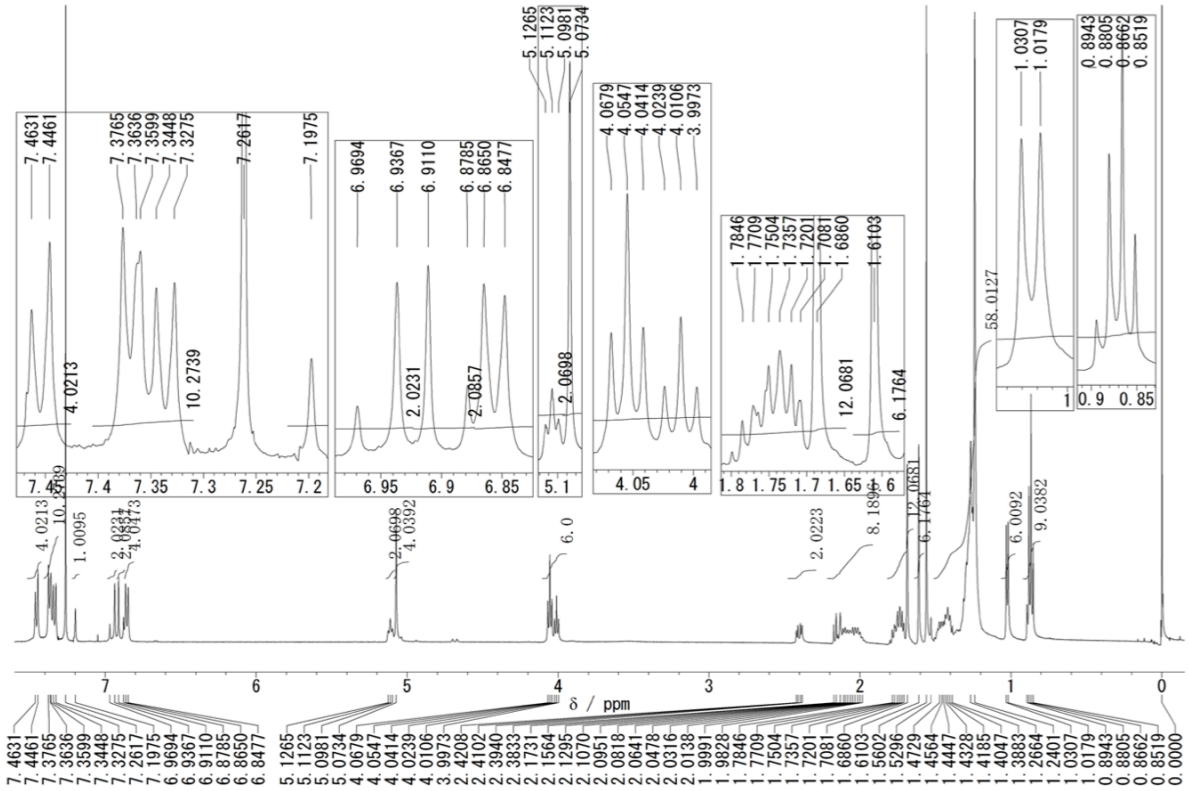

Chart 4-1. ^{1}H NMR spectrum of compound **4** in $CDCl_3$ at 298 K.

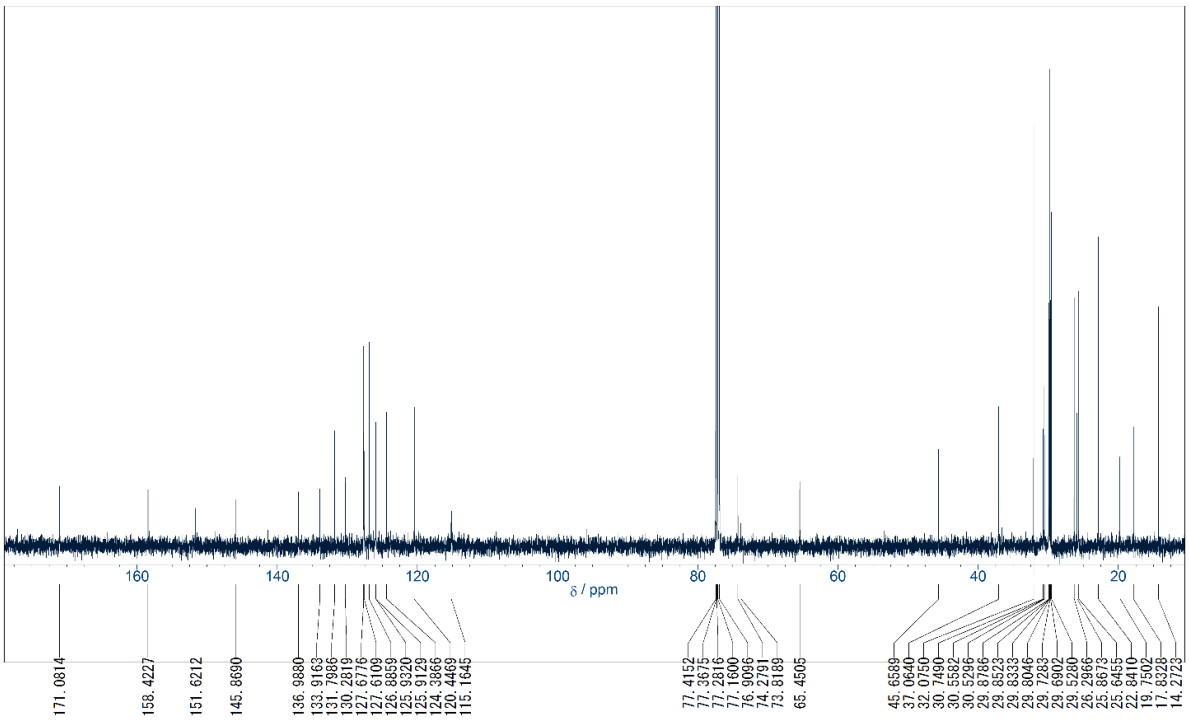

Chart 4-2. ^{13}C NMR spectrum of compound **4** in $CDCl_3$ at 298 K.

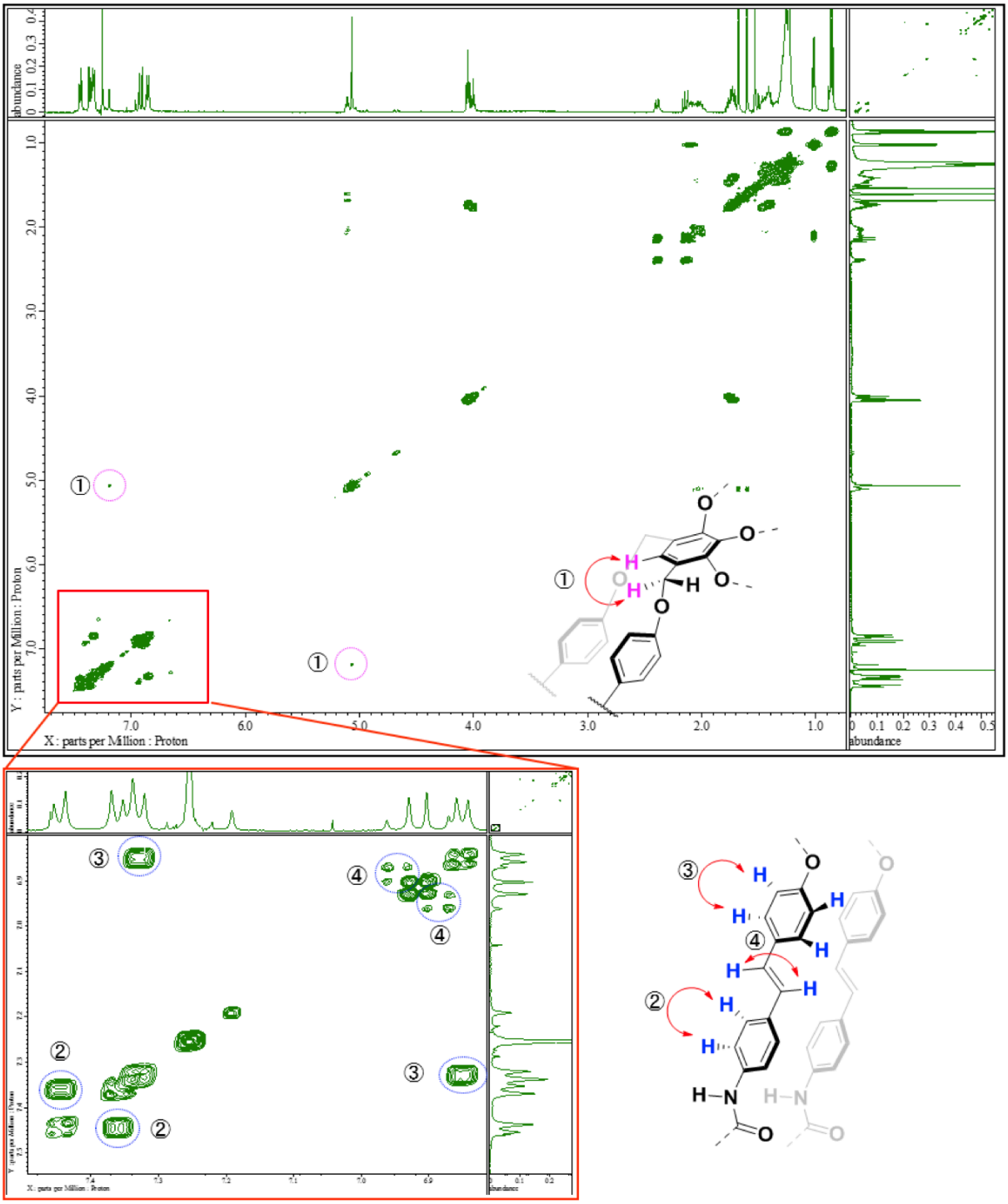

Chart 4-3. 2D COSY NMR spectrum of compound **4** in $CDCl_3$ at 298 K and partial molecular structure with assignment of corresponding cross-peaks between two different proton signals. Aromatic region was magnified at the bottom.

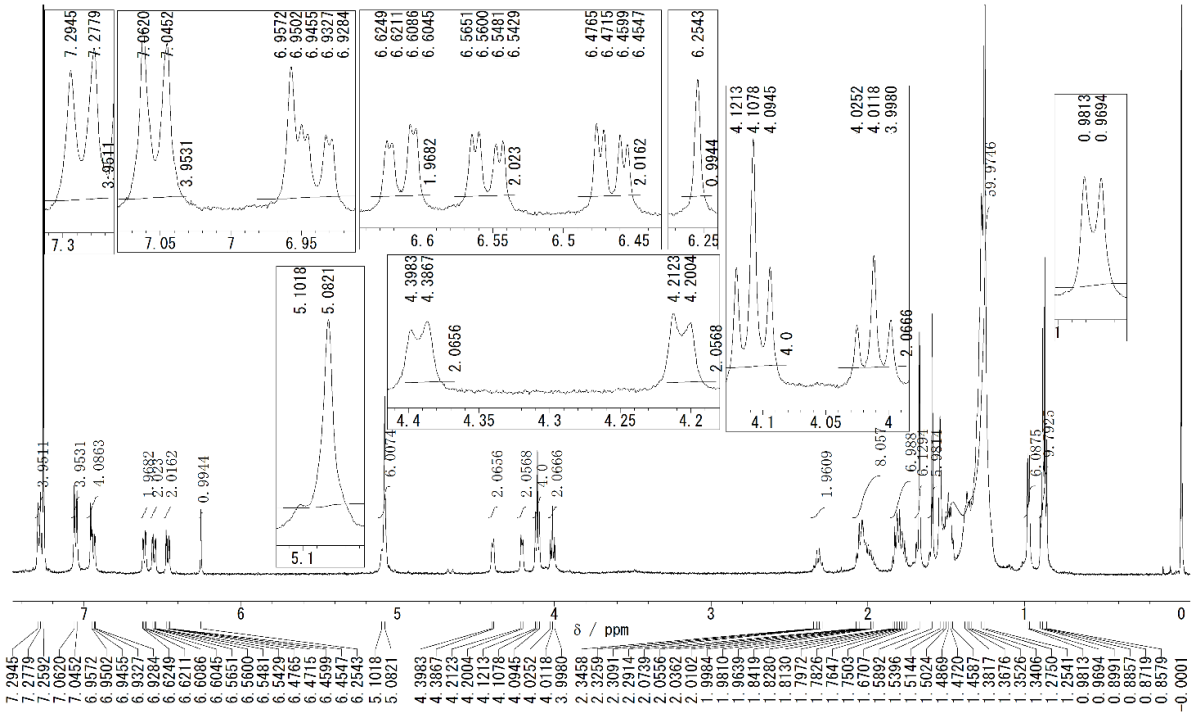

Chart 4-4. ^{1}H NMR spectrum of compound **4cyc** in $CDCl_3$ at 298 K.

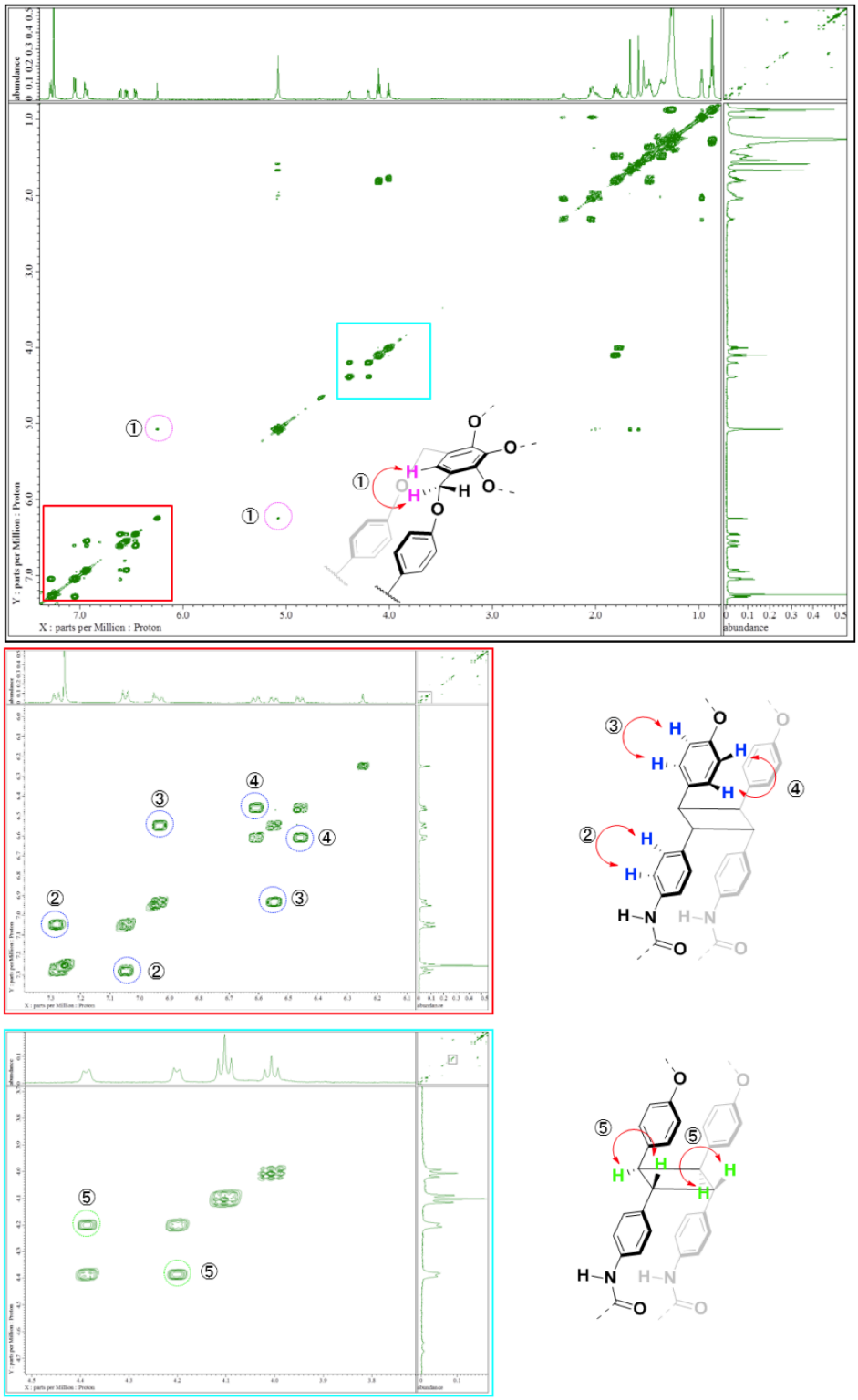

Chart 4-5. 2D COSY NMR spectrum of compound **4cyc** in $CDCl_3$ at 293 K and partial molecular structure with assignment of corresponding cross-peaks between two different proton signals. Aromatic and cyclobutane regions were magnified at the bottom.

4-10. References

1. H. Park, K. Zhang, Y. Ren, S. Nadji, N. Sinha, J.-S. Taylor, C. Kang, *Proc. Natl. Acad. Sci. U. S. A.* **2002**, *99*, 15965–15970.

2. V. Ramamurthy, Y. Inoue, *Supramolecular photochemistry*: controlling photochemical processes. (Wiley, 2011).

3. (a) F. J. M. Hoeben, P. Jonkheijm, E. W. Meijer and A. P. H. J. Schenning, *Chem. Rev.* **2005**, *105*, 1491–1546. (b) L. C. Palmer, S. I. Stupp, *Acc. Chem. Res.* **2008**, *41*, 1674–1684. (c) B. M. Rosen, C. J. Wilson, D. A. Wilson, M. Peterca, M. R. Imam and V. Percec, *Chem. Rev.* **2009**, *109*, 6275–6540. (d) S. Yagai, *Bull. Chem. Soc. Jpn.* **2015**, *88*, 28–58.

4. (a) S. Yagai, A. Kitamura, *Chem. Soc. Rev.* **2008**, *37*, 1520–1529. (b) H. J. Kim, T. Kim, M. Lee, *Acc. Chem. Res.* **2011**, *44*, 72–82. (c) E. Mattia, S. Otto, *Nat. Nanotechnol.* **2015**, *10*, 111–119.

5. (a) C.-H. Huang, D. M. Bassani, *Eur. J. Org. Chem.* **2005**, *2005*, 4041–4050. (b) S. Yagai, T. Karatsu, A. Kitamura, *Chem.—Eur. J.* **2005**, *11*, 4054–4063. (c) J. Zhang, Q. Zou, H. Tian, *Adv. Mater.* **2013**, *25*, 378–399.

6. (a) R. Iwaura, T. Shimizu, *Angew. Chem. Int. Ed.* **2006**, *45*, 4601–4604. (b) R. Iwaura, T. Shimizu, *Angew. Chem. Int. Ed.* **2006**, *45*, 4601–4604. (c) L. Li, H. Jiang, B. W. Messmore, S. R. Bull, S. I. Stupp, *Angew. Chem. Int. Ed.* **2007**, *46*, 5873–5876. (d) T. Muraoka, H. Cui, S. I. Stupp, *J. Am. Chem. Soc.* **2008**, *130*, 2946–2947. (e) Y. Yan, H. Wang, B. Li, G. Hou, Z. Yin, L. Wu, V. W. W. Yam, *Angew. Chem. Int. Ed.* **2010**, *49*, 9233–9236. (f) C. Wang, Q. Chen, H. Xu, Z. Wang, X. Zhang, *Adv. Mater.* **2010**, *22*, 2553–2555. (g) S. Mahesh, A. Gopal, R. Thirumalai, A. Ajayaghosh, *J. Am. Chem. Soc.* **2012**, *134*, 7227–7230. (h) A. Gopal, M. Hifsudheen, S. Furumi, M. Takeuchi, A. Ajayaghosh, *Angew. Chem. Int. Ed.*

2012, *51*, 10505–10509. (i) Q. Zhao, Y. Wang, Y. Yan, J. Huang, *ACS Nano* **2014**, *8*, 11341–11349. (j) S. Yagai, K. Iwai, M. Yamauchi, T. Karatsu, A. Kitamura, S. Uemura, M. Morimoto, H. Wang, F. Würthner, *Angew. Chem. Int. Ed.* **2014**, *53*, 2602–2606. (k) H.-L. Sun, Y. Chen, J. Zhao, Y. Liu, *Angew. Chem. Int. Ed.* **2015**, *54***,** 9376–9380. (l) N. Kameta, M. Masuda, T. Shimizu, *Chem.—Eur. J.* **2015**, *21*, 8832–8839. (m) K. Higashiguchi, G. Taira, J. Kitai, T. Hirose, K. Matsuda, *J. Am. Chem. Soc.* **2015**, *137*, 2722–2779. (n) E. Busseron, J.-J. Cid, A. Wolf, G. Du, E. Moulin, G. Fuks, M. Maaloum, E. Busseron, P. Polavarapu, A. Ruff, A.-K. Saur, S. Ludwigs, N. Giuseppone, *ACS Nano* **2015**, *9*, 2760–2772.

7. (a) S. Shinkai, T. Nakaji, T. Ogawa, K. Shigematsu, O. Manabe, *J. Am. Chem. Soc.* **1981**, *103*, 111–115. (b) T. Kawasaki, M. Tokuhiro, N. Kimizuka, T. Kunitake, *J. Am. Chem. Soc.* **2001**, *123*, 6792–6800. (c) M. Takeshita, M. Hayashi, S. Kadota, K. H. Mohammed, T. Yamato, *Chem. Commun.* **2005**, 761–763. (d) S. Yagai, T. Nakajima, K. Kishikawa, S. Kohmoto, T. Karatsu, A. Kitamura, *J. Am. Chem. Soc.* **2005**, *127*, 11134–11139.

8. (a) S. Yagai, T. Nakajima, T. Karatsu, K. Saitow, A. Kitamura, *J. Am. Chem. Soc.* **2004**, *126*, 11500–11508. (b) S. Yagai, S. Hamamura, H. Wang, V. Stepanenko, T. Seki, K. Unoike, Y. Kikkawa, T. Karatsu, A. Kitamura, F. Würthner, *Org. Biomol. Chem.* **2009**, *7*, 3926–3929.

9. S. Yagai, M. Yamauchi, A. Kobayashi, T. Karatsu, A. Kitamura, T. Ohba, Y. Kikkawa, *J. Am. Chem. Soc.* **2012**, *134*, 18205–18208.

10. M. Yamauchi, Y. Chiba, T. Karatsu, A. Kitamura, S. Yagai, *Chem. Lett.* **2013**, *42*, 799–800.

11. (a) S. J. George, T. F. a de Greef, R. Bovee, J. L. J. van Dongen, A. P. H. J. Schenning, E. W. Meijer, *Chem. Asian J.* **2009**, *4*, 910–917. (b) M. Ikeda, A. Momotake, Y. Kanna, K. Shimotori, T. Arai, *Photochem. Photobiol. Sci.* **2012**, *11*, 1524–1527. (c) H. Kashida, T. Doi,

T. Sakakibara, T. Hayashi, H. Asanuma, *J. Am. Chem. Soc.* **2013**, *135*, 7960–7966.

12. M. M. Safont-Sempere, G. Fernández, F. Würthner, *Chem. Rev.* **2011**, *111*, 5784–5814.

13. C. Geiger, M. Stanescu, L. Chen, D. G. Whitten, *Langmuir* **1999**, *15*, 2241–2245.

14. N. Harada, K. Nakanishi, *Acc. Chem. Res.* **1972**, *5*, 257–263.

15. (a) D. Zhao, J. S. Moore, *Org. Biomol. Chem.* **2003**, *1*, 3471–3491. (b) T. F. A. De Greef, M. M. J. Smulders, M. Wolffs, A. P. H. J. Schenning, R. P. Sijbesma, E. W. Meijer, *Chem. Rev.* **2009**, *109*, 5687–5754.

16. P. Jonkheijm, P. van der Schoot, A. P. H. J. Schenning and E. W. Meijer, *Science* **2006**, *313*, 80−83.

17. (a) D. M. Bassani, V. Darcos, S. Mahony, J. P. Desvergne, *J. Am. Chem. Soc.* **2000**, *122*, 8795–8796. (b) S. Yamada, N. Uematsu, K. Yamashita, *J. Am. Chem. Soc.* **2007**, *129*, 12100–12101. (c) L. R. Macgillivray, G. S. Papaefstathiou, T. Friščić, T. D. Hamilton, D. K. Bučar, Q. Chu, D. B. Varshney, I. G. Georgiev, *Acc. Chem. Res.* **2008**, *41*, 280–291. (d) J. M. Rivera, D. Silva-Brenes, *Org. Lett.* **2013**, *15*, 2350–2353.

18. X. Song, C. Geiger, M. Farahat, J. Perlstein, D. G. Whitten, *J. Am. Chem. Soc.* **1997**, *119*, 12481–12491.

19. S.-Y. Yang, X.-L. Deng, R.-F. Jin, P. Naumov, M. K. Panda, R.-B. Huang, L.-S. Zheng, B. K. Teo, *J. Am. Chem. Soc.* **2014**, *136*, 558−561.

20. (a) Y. Ito, T. Kajita, K. Kunimoto, T. Matsuura, *J. Org. Chem.* **1989**, *54*, 587–591. (b) H. Maeda, K. Nishimura, K. Mizuno, M. Yamaji, J. Oshima, S. Tobita, *J. Org. Chem.* **2005**, *70*, 9693–9701.

21. R. B. Martin, *Chem. Rev.* **1996**, *96*, 3043–3064.

22. (a) A. Ajayaghosh, R. Varghese, S. Mahesh, V. K. Praveen, *Angew. Chem. Int. Ed.* **2006**, *45*, 7729–7732. (b) M. J. Mayoral, C. Rest, J. Schellheimer, V. Stepanenko, G. Fernández, *Chemistry* **2012**, *18*, 15607–15611. (c) M. J. Mayoral, C. Rest, J. Schellheimer, V. Stepanenko, G. Fernández, *Chem.—Eur. J.* **2012**, *18*, 15607–15611.

23. A. Wu, L. Isaacs, *J. Am. Chem. Soc.* **2003**, *125*, 4831–4835.

24. F. García, L. Sánchez, *J. Am. Chem. Soc.* **2012**, *134*, 734–742.

25. F. Würthner, S. Yao, U. Beginn, *Angew. Chem. Int. Ed.* **2003**, *42*, 3247–3250.

Chapter 5.

Conclusion and Perspectives

Introduction of functional molecules with luminescence, conductive and stimuli-responsive properties into supramolecular self-assembly systems is a simple and powerful strategy for improvement and development of supramolecular material. However, such an approach might give rise to a complex organization and an unexpected deterioration or change in the original functionality due to the complexity in molecular structures and sensitive supramolecular system. Therefore, in-depth understanding of the self-assembly mechanism is of great important.

Control over self-assembly process from a viewpoint of the molecular structure enables us to rationally functionalize the supramolecular assemblies. In this thesis, I unveiled the key relationship between molecular structure and its supramolecular polymerization process by in-depth investigation of self-assembly of hydrogen-bonding unit-functionalized π-conjugated molecules. As a result, the degrees of conformational freedom affect the polymerization thermodynamics and kinetics, completely leading to the distinctive stacking arrangements (molecular level), morphologies (nanostructure level) and physical properties (macroscopic level). Furthermore, in the system using photoresponsive π-conjugated molecules, the degrees of conformational freedom are controlled with light irradiation, resulting in the construction of photocontrollable supramolecular polymerization processes, in which the level of cooperativity is tuned by regulating the irradiation time.

These novel findings based on molecular conformation would be useful for understanding and evaluating self-assembly mechanisms of known and new molecules in artificial systems, and can play an important role to create outstanding supramolecular materials based on precise molecular designs.

Chapter 6.

Acknowledgements

First of all, I would like to acknowledge Prof. Dr. Shiki Yagai, my thesis supervisor, for supporting my research at all time and providing an elegant guidance about how to progress my research and prepare of papers. I would like to appreciate Prof. Dr. Takashi Karatsu for the kind supports and advice in the laboratory. I would like to thank Dr. Xu Lin for the interesting, kind and direct advice in the laboratory. I am very thankful to Dr. Bimalendu Adhikari and Dr. Deepak D. Prabhu for the kind English supports and abundant advice in the laboratory. I am very thankful to the Japan Society for the Promotion of Science (JSPS) for a research fellowship for young scientists (26·7715).

I also express my great thanks to the following scientists:

Prof. Dr. Tomonori Ohba of Chiba University (Department of Chemistry, Graduate School of Science) for transmission electron microscopy (TEM) measurements.

Prof. Dr. Shin-ichi Adachi, Prof. Dr. Nobutaka Shimizu, Dr. Hideaki Takagi and Dr. Rie Haruki of High Energy Accelerator Research Organization (KEK) for small-angle X-ray scattering (SAXS) measurements.

Prof. Dr. Takanori Fukushima and Dr. Takashi Kajitani of Tokyo Institute of Technology (Institute of Innovative Research) for X-ray diffraction (XRD) measurements at SPring-8.

Finally, I am greatly thankful to the laboratory member for the kind cooperation.

Chapter 7.

Appendix

7-1. Abbreviation

AFM: Atomic Force Microscopy

CD: Circular dichroism

DLS: Dynamic light scattering

DNA: Deoxyribonucleic acid

DSC: Differential scanning calorimetry

ESI: Electron spray ionization

HOPG: Highly-oriented pyrolytic graphite

MCH: Methylcyclohexane

NOE: Nuclear Overhauser effect

NMR: Nuclear magnetic resonances

OPE: Oligo(p-phenylene ethynylene)

OPV: Oligo(p-phenylene vinylene)

POM: Polarized optical microscopy

ppm: Parts per million

SP: Supramolecular polymer

STM: Scanning tunneling microscopy

TDP: 3,4,5-Tridodecyoxyphenyl

T_e*: elongation temperature*

TEM: Transmission electron microscopy

T_m*: Melting temperature*

XRD: X-ray diffraction

7-2. List of Publications

Main Papers

1. **Mitsuaki Yamauchi**, Bimalendu Adhikari, Deepak D. Prabhu, Xu Lin, Takashi Karatsu, Tomonori Ohba, Nobutaka Shimizu, Hideaki Takagi, Rie Haruki, Shin-ichi Adachi, Takashi Kajitani, Takanori Fukushima, Shiki Yagai.

   "Supramolecular Polymerization of Supermacrocycles: Effect of Molecular Conformations on Kinetics and Morphology"

   Chemistry A European Journal (Wiley-VCH)

   Year 2017. In press. (DOI: 10.1002/chem.201605873) (Inside Cover に選定)
2. **Mitsuaki Yamauchi**, Norimichi Kanao, Bimalendu Adhikari, Takashi Karatsu, Shiki Yagai.

   "Phototriggered supramolecular polymerization of barbituric acid rosette"

   Chemistry Letters (The Chemical Society of Japan)

   Volume 46, Issue 1, pg. 111–114, Year 2017. (Editor's Choice に選定)
3. **Mitsuaki Yamauchi**, Tomonori Ohba, Takashi Karatsu, Shiki Yagai.

   "Photoreactive helical nanoaggregates exhibiting morphology transition on thermal reconstruction"

   Nature Communications (Nature Publishing Group)

   Volume 6, Article number: 8936, pg. 1–10, Year 2015.

Relevant Papers

1. Xu Lin, Mika Suzuki, Marina Gushiken, **Mitsuaki Yamauchi**, Takashi Karatsu, Takahiro Kizaki, Yuki Tani, Ken-ichi Nakayama, Mitsuharu Suzuki, Hiroko Yamada, Takashi Kajitani, Takanori Fukushima, Yoshihiro Kikkawa, Shiki Yagai.

   "High-fidelity self-assembly pathways for hydrogen-bonding molecular semiconductors"

Scientific Reports (Nature Publishing Group)

Year 2017. In press.

2. Bimalendu Adhikari, Tomoya Suzuki, Xu Lin, **Mitsuaki Yamauchi**, Takashi Karatsu, Shiki Yagai.

   "Photoresponsive supramolecular copolymers from diarylethene-perylene bisimide hydrogen bonded complexes"

   Polymer (Elsevier)

   Year 2017. In press. (DOI: 10.1016/j.polymer.2017.01.025)

3. Xu Lin, Hiroki Kurata, Deepak D. Prabhu, **Mitsuaki Yamauchi**, Tomonori Ohba, Shiki Yagai.

   "Water-Induced Helical Supramolecular Polymerization and Gel Formation of Alkylene-Tethered Perylene Bisimide Dyad"

   Chemical Communications (Royal Society of Chemistry)

   Volume 53, Issue 1, pg. 168–171, Year 2017.

4. Deepak D. Prabhu, Keisuke Aratsu, **Mitsuaki Yamauchi**, Xu Lin, Bimalendu Adhikari, and Shiki Yagai.

   "Supramolecular polymerization of hydrogen-bonded rosettes with anthracene chromophores: regiomeric effect on nanostructures"

   Polymer Journal (Nature Publishing Group)

   Year 2017. In press. (DOI: 10.1038/pj.2016.94)

5. Martin J. Hollamby, Keisuke Aratsu, Brian R. Pauw, Sarah E. Rogers, Andrew J. Smith, **Mitsuaki Yamauchi**, Xu Lin, Shiki Yagai.

   "Simultaneous SAXS and SANS Analysis Detects Toroidal Supramolecular Polymers Composed of Noncovalent Supermacrocycles in Solution"

   Angewandte Chemie International Edition (Wiley-VCH)

Volume 55, Issue 34, pg. 9890–9893, Year 2016.

6. Keisuke Aratsu, Deepak D. Prabhu, Hidetaka Iwawaki, Xu Lin, **Mitsuaki Yamauchi**, Takashi Karatsu and Shiki Yagai.

   "Self-sorting regioisomers through hierarchical organization of hydrogen-bonded rosettes"

   Chemical Communications (Royal Society of Chemistry)

   Volume 52, Issue 53, pg. 8211–8214, Year 2016.

7. Shiki Yagai, Satoru Okamura, Yujiro Nakano, **Mitsuaki Yamauchi**, Keiki Kishikawa, Takashi Karatsu, Akihide Kitamura, Akira Ueno, Daiki Kuzuhara, Hiroko Yamada, Tomohiro Seki, Hajime Ito.

   "Design Amphiphilic Dipolar Systems for Stimuli-Responsive Luminescent Materials Using Metastable States"

   Nature Communications (Nature Publishing Group)

   Volume 5, Article number: 4013, pg. 1–10, Year 2014.

8. Shiki Yagai, Kazunori Iwai, **Mitsuaki Yamauchi**, Takashi Karatsu, Akihide Kitamura, Shinobu Uemura, Masakazu Morimoto, Hao Wang, Frank Würthner.

   "Photocontrol over Self-Assembled Nanostructures of pi-pi Stacked Dyes Supported by the Parallel Conformer of Diarylethene"

   Angewandte Chemie International Edition (Wiley-VCH)

   Volume 53, Issue 10, pg. 2602–2606, Year 2014.

9. **Mitsuaki Yamauchi**, Yosuke Chiba, Takashi Karatsu, Akihide Kitamura, Shiki Yagai.

   "Self-Assembled Nanofibrils and Nanorings from Oligo(*p*-phenylene vinylene) Dimers"

   Chemistry Letters (The Chemical Society of Japan)

   Volume 42, Issue 8, pg. 799–800, Year 2013.

10. **Mitsuaki Yamauchi**, Shun Kubota, Takashi Karatsu, Akihide Kitamura, Ayyappanpillai Ajayaghosh, Shiki Yagai.

”Guided supramolecular polymerization of oligo(*p*-phenylene vinylene) functionalized bismelamines”

Chemical Communications (Royal Society of Chemistry)

Volume 49, Issue 43, pg. 4941–4943, Year 2013.

11. Michinari Kohri, Yoshihiro Shinoda, Hiroto Kohma, Yuri Nannichi, **Mitsuaki Yamauchi**, Shiki Yagai, Takashi Kojima, Tatsuo Taniguchi, Keiki Kishikawa.

    ”Facile Synthesis of Free-Standing Polymer Brush Films Based on a Colorless Polydopamine Thin Layer”

    Macromolecular Rapid Communications (Wiley-VCH)

    Volume 34, Issue 15, pg. 1220–1224, Year 2013.

12. Michinari Kohri, Hiroto Kohma, Yoshihiro Shinoda, **Mitsuaki Yamauchi**, Shiki Yagai, Takashi Kojima, Tatsuo Taniguchi and Keiki Kishikawa.

    “A colorless functional polydopamine thin layer as a basis for polymer capsules”

    Polymer Chemistry (Royal Society of Chemistry)

    Volume 4, Issue 9, pg. 2696–2702, Year 2013.

13. Shiki Yagai, **Mitsuaki Yamauchi**, Ai Kobayashi, Takashi Karatsu, Akihide Kitamura, Tomonori Ohba, Yoshihiro Kikkawa.

    “Control over Hierarchy Levels in the Self-Assembly of Stackable Nanotoroids”

    Journal of the American Chemical Society (American Chemical Society)

    Volume 134, Issue 44, pg. 18205–18208, Year 2012.

学会発表

国内（著者、題名、学会名、場所、年月、発表種類）※新しい順位に記載

1. ○**山内光陽**、矢貝史樹、『水素結合性マクロサイクルの形成を経た協同的な超分子

重合』、日本化学会第 96 春季年会、同志社大学（京都府）、2016 年 3 月、口頭発表

2. ○山内光陽、矢貝史樹、『水素結合性超分子マクロサイクルの超分子ポリマー化における螺旋の誘起』、5 回 CSJ 化学フェスタ 2015、タワーホール船堀（東京都）、2015 年 10 月、ポスター発表
3. ○山内光陽、石渡勝也、矢貝史樹、『水素結合性環状六量体の自己集合における協同性の発現』、日本化学会第 95 春季年会、日本大学（千葉県）、2015 年 3 月、口頭発表
4. ○山内光陽、矢貝史樹、『光反応を利用した集合経路及び螺旋性の制御』、第 1 回 π 造形科学若手研究会、紀州鉄道熱海ホテル（静岡県）、2014 年 11 月、口頭発表
5. ○山内光陽、矢貝史樹、『 [2 + 2]光環化付加反応を利用した集合経路の制御』、第 4 回 CSJ 化学フェスタ 2014、タワーホール船堀（東京都）、2014 年 10 月、ポスター発表
6. ○山内光陽、石渡勝也、矢貝史樹、『水素結合性環状超分子の積層における協同性の発現』、第 63 回高分子討論会、長崎大（長崎県）、2014 年 9 月、口頭発表
7. ○山内光陽、矢貝史樹、『積層型ナノリングの動的構造制御』、第 3 回 CSJ 化学フェスタ 2013、タワーホール船堀（東京都）、2013 年 10 月、ポスター発表
8. ○山内光陽、唐津孝、北村彰英、吉川佳広、矢貝史樹、『アゾベンゼン二量体からなる積層型ナノリングにおける階層構造の制御』、日本化学会第 93 春季年会、立命館大学（滋賀県）、2013 年 3 月、口頭発表
9. 矢貝史樹、○山内光陽、小林愛、唐津孝、北村彰英、吉川佳広『光応答性ナノリングの構築』、第 61 回高分子討論会、名古屋工業大学（愛知県）、2012 年 9 月、ポスター発表
10. 矢貝史樹、○山内光陽、小林愛、唐津孝、北村彰英、『積層型ナノリングの光制御』、2012 年光化学討論会、東京工業大学（東京都）、2012 年 9 月、ポスター発表

国際（著者、題名、学会名、場所、年月、発表種類）※新しい順位に記載

1. ○**Mitsuaki Yamauchi**, Takashi Karatsu, Shiki Yagai、『Cooperative supramolecular polymerization via formation of hydrogen-bonded supermacrocycles』、Joint Symposium on Chemistry、Chiba University (Chiba)、March, 2016、Oral presentation
2. ○**Mitsuaki Yamauchi**, Shiki Yagai、『Morphology transition based on photoreactive helical nanoaggregates composed of stilbene supramolecular building blocks』、CEMSuptra 2016、The University of Tokyo (Tokyo)、January, 2016、Poster presentation
3. ○**Mitsuaki Yamauchi**, Shiki Yagai、『Cooperative supramolecular polymerization of hydrogen-bonded supermacrocycles』、Pacifichem 2015、Kalia Tower (Hawaii)、December, 2015、Oral presentation
4. ○**Mitsuaki Yamauchi**, Shiki Yagai、『Controlled self-assembly pathways by photocyclized product of stilbene dyad』、Pacifichem 2015、Convention Center (Hawaii)、December, 2015、Poster presentation
5. ○**Mitsuaki Yamauchi**, Shiki Yagai、『Helical undulation of supramolecular polymer nanorods by a structural alteration from ether to ester linkages』、25th Annual Meeting of MRS-Japan 2015、Hatoba Kaikan (Kanagawa)、December, 2015、Poster presentation
6. ○**Mitsuaki Yamauchi**, Shiki Yagai、『Evolution of Cooperative Self-Assembly Pathway in Hydrogen-Bonded Cyclic Hexamers』、Workshop on Chirality in Chiba University 3rd Symposium、Chiba University (Chiba)、March, 2015、Oral presentation
7. ○**Mitsuaki Yamauchi**, Shiki Yagai、『Self-assembly Pathways Guided by Photocyclized Product of Stilbene Dyad』、The 15th IUMRS-International Conference in Asia (IUMRS-ICA 2014)、Fukuoka University (Fukuoka)、August, 2014、Oral presentation
8. ○**Mitsuaki Yamauchi**, Shiki Yagai、『Control over Self-Assembly Pathway through Photoreaction of Stilbene Supramolecular Building Blocks』、NIMS CONFERENCE 2014、Tsukuba International Congress Center (Ibaraki)、July, 2014、Poster presentation

9. ○**Mitsuaki Yamauchi**, Shiki Yagai、『Dynamic Control in the Self-assembly of Stackable Nanorings』、The 3rd Junior International Conference on Cutting-Edge Organic Chemistry in Asia、Seimei-no-mori (Chiba)、November, 2013、Poster presentation
10. ○**Mitsuaki Yamauchi**, Yoshihiro Kikkawa, Shiki Yagai、『Self-Assembly of Stackable Nanorings into Nanotubes and Superhelical Structures』、Japan–China Joint Symposium on Functional Supramolecular Architectures、Okazaki Conference Center (Aichi)、January, 2013、Poster presentation
11. ○**Mitsuaki Yamauchi**, Ai Kobayashi, Takashi Karatsu, Akihide Kitamura, Yoshihiro Kikkawa, Shiki Yagai、『Self-Assembly of Stackable Nanorings』、International Workshop on Soft Interface Sciences for Young Scientists 2012、AIST (Ibaraki)、November, 2012、Poster presentation

解説　※新しい順位に記載

1. 2016.1.15　Chem-Station（化学ポータルサイト）スポットライトリサーチ、『光刺激で超分子ポリマーのらせんを反転させる』という題目で記事を掲載しています。
   http://www.chem-station.com/blog/2016/01/photoreactive.html
2. 2015.11.20　プレスリリース（各種 Web ニュースに記載）、『世界初、千葉大学でわずかな光刺激で螺旋の巻方向が反転した分子集合体の構築に成功』という題目で記事を掲載しています。
   http://prtimes.jp/main/html/rd/p/000000030.000015177.html